LAWRENCE
LIVERMORE
NATIONAL
LABORATORY

UCRL-PROC-209115

WCRP/WGNE Workshop

The Second Phase of the Atmospheric Model Intercomparison Project (AMIP2)

Toward Innovative Model Diagnostics

Meteo-France, Toulouse, France
11–14 November, 2002

Edited by P. Gleckler

August 16, 2004

This work was performed under the auspices of the U.S. Department of Energy by University of California, Lawrence Livermore National Laboratory under Contract W-7405-Eng-48.

WCRP/WGNE Workshop

The Second Phase of the Atmospheric Model Intercomparison Project (AMIP2)

Toward Innovative Model Diagnostics

Meteo-France, Toulouse, France
11-14 November, 2002

Edited by P.J. Gleckler

Participants of the AMIP2 workshop
Meteo-France, Toulouse, France
11-14 November, 2002

Support for this workshop was provided by the U.S. National Science Foundation, the World Climate Research Programme, and Meteo-France.

CONTENTS

HYDROLOGICAL CYCLE AND LAND SURFACE PROCESSES 143

OVERVIEW AND GENERAL CIRCULATION

The AMIP Experience: Challenges and Opportunities

P. Gleckler

Program for Climate Model Diagnosis and Intercomparison
Lawrence Livermore National Laboratory

When PCMDI and the WCRP's WGNE first introduced AMIP to the climate modeling community in the early 1990s, it was truly an ambitious exercise. Many modeling groups had not integrated their atmospheric GCM for more than a couple of years, and few were using anything but climatological SSTs and sea-ice as boundary conditions. All that changed with AMIP, as modelers were inspired to consider performing integrations of 10 years (AMIP 1) with realistically varying monthly mean SSTs and sea-ice. Thanks to Larry Gates (who garnered community-wide participation), and the U.S. DOE (who not only provided support for PCMDI to lead the project, but also made computer time available to many participants), AMIP has helped inspire a wide range of climate modeling intercomparisons.

Since its inception, the WCRP's Working Group on Numerical Experimentation (WGNE) has assisted PCMDI in its leadership of AMIP by annually reviewing its progress and providing guidance via the WGNE AMIP Panel. PCMDI's close collaborations with WGNE have helped to ensure that AMIP remain a community-based exercise.

In 1995 an international AMIP conference was held in Monterey, CA, USA, where a uniquely diverse collection of model intercomparison analysis results was presented (see WCRP-92). To gauge the success of the AMIP exercise, some 150 workshop attendees were surveyed, including participants from all the contributing modeling groups. Most considered the AMIP experience to be a valuable mechanism for the community to document model strengths and weaknesses, and that somehow the process needed to continue. Not long after the conference, the AMIP Panel, the PCMDI, the WGNE, and the modeling community at large set out to improve the experimental protocol for AMIP. The refinements to the experimental design resulted in the beginning of AMIP2 (http://www-pcmdi.llnl.gov/projects/amip/NEWS/amipnl8.pdf). The primary differences between AMIP1 and AMIP2 experiment were: improved boundary conditions and their treatment, an extended integration (1979–1996, later extended to 1979–"near present"), and a greatly extended specification of standard model output.

From 1998 up until the November 2002 workshop in Toulouse, PCMDI collected a next generation of AMIP(2) simulations. A majority of the model analyses discussed at this workshop and included in these proceedings are based on AMIP2 and, like the first conference, this culmination of results represents the beginning of bringing AMIP2 toward closure.

Early on in the AMIP experience it became clear that the project was effective for identifying common model errors, but only occasionally would it directly unravel their causes. Yet a new and more solid rationale for the project had emerged: with steady improvements in computing resources, modelers began to run multi-year integrations more routinely, and the AMIP experimental protocol served as a standard test of newer model versions. AMIP evolved into a de facto benchmark for the climate modeling community. From that point on, a primary

motivator for AMIP has been to focus on increasing advanced and innovative diagnostics, and hence the theme for this workshop.

While many model deficiencies identified in AMIP1 remain present in the more recent collection of simulations, the continuity between AMIP1 and AMIP2 is enabling researchers to track how model performance has progressed. At the Toulouse workshop a need for a continuing and coordinated evaluation of AGCMs was again expressed, with many arguing for an AMIP3 in the open forum discussions. At the same time, however, it was clear that a future AMIP would have to be carefully coordinated with other priorities in the climate modeling community.

Meanwhile, coupled model evaluation has become the higher priority at PCMDI, as evidenced by its support of AMIP's sister project the Coupled Model Intercomparison Project (CMIP). Moreover, both WCRP's Working Group on Coupled Modeling (WGCM) and the WGNE maintain that AMIP's future must be designed to complement the evaluation of coupled models, most likely via ties with CMIP.

One means by which AMIP can complement coupled model diagnosis is that there remain important modeling challenges that can be addressed without the added complexity of the coupled modeling framework. Many process-oriented studies serve as an example and likely coincide with future emphasis of model diagnosis. For this reason, some effort was made to entrain into this workshop the modeling-based activities represented by the GEWEX Modeling and Prediction Panel (GMPP), including: the GEWEX Cloud System Study (GCSS), the GEWEX Land/Atmosphere System Study (GLASS), and the GEWEX Atmospheric Boundary Layer Study (GABLS). A prime example was the discussions led by Mark Webb and Steve Kreuger on possible advancements to understanding cloud-radiative effects in models by introducing the ISCCP "Simulator" into an AMIP diagnostic protocol.

These proceedings provide examples of how models are being evaluated, but in actuality the use of the AMIP database extends far beyond what was presented at the Toulouse workshop. Even as AMIP2 winds down, the AMIP database will likely be exploited for years to come. While it is not clear from the outcome of this workshop what the next step of AMIP will be, it almost certainly will serve as a supporting exercise to coupled model evaluation.

Tracking Changes in the Performance of AMIP Models

Karl E.Taylor, Peter J. Gleckler, and Charles Doutriaux
Program for Climate Model Diagnosis and Intercomparison
Lawrence Livermore National Laboratory,
P.O. Box 808, L-103, Livermore, CA 94550 USA (taylor13@llnl.gov)

AMIP simulations are now becoming a routine part of the development cycle of atmospheric models used in climate studies. Model development teams examine output from AMIP runs, along with related runs with prescribed climatological sea surface temperatures and sea ice concentrations, to help them assess how well their models simulate climate under so-called "perfect ocean" conditions. With the establishment of AMIP experiments as a benchmark for assessing model performance and with the maturing of the AMIP project itself, we can now also begin tracking how model performance is changing.

Comprehensive model evaluation requires a wide variety of tests and techniques, from the examination of individual model elements (e.g., numerical formulation, parameterized processes) to the assessment of mean climatology and modes of variability, once all the model elements have been linked together. Of particular relevance to AMIP simulations are discrepancies found between the observed and simulated global patterns of the seasonally varying mean climate. It is this aspect of atmospheric model performance that is the focus of this brief summary.

We should like to consider how well models simulate a number of different fields, and traditionally the first step is to compare numerous maps, zonal mean plots, and latitude-height cross-sections of the mean simulated and observed climate state for individual seasons. Even when a single model is considered, however, it is difficult to assimilate and synthesize some general overview of model performance and to assess whether a newer version of a model produces in fact a more "realistic looking" simulation. The task is considerably increased when a large collection of model simulations, such as that comprising AMIP, is considered.

Here we are forced to rely on statistical measures to summarize model performance, realizing that much of the most interesting and revealing information contained in the simulations will be lost when the spatially complex, seasonally varying patterns of model errors are distilled in this way. Perhaps the simplest and most common statistical measure used to quantify the errors in a simulated field is the root-mean-square difference between the simulated and observed field (i.e., the standard deviation of the difference field, which is usually referred to as the RMS error). The RMS error can be divided by the standard deviation of the observed field to yield a non-dimensional error measure. Loosely speaking, the square of this normalized RMS error can be thought of as the fraction of the total observed variance that is correctly captured by the model simulation.

Since it is not model performance itself, but the change in that performance that is the focus here, we consider only the subset of AMIP models for which results are available from both an older and a more recent model version. There are 14 modeling centers that have submitted AMIP results both in the early and also the late 1990s. We have also computed a so-called "median

model" result for each era (1992-1996 and 1997-2001). The median model is formed after regridding the model output to a common (T42) grid. For each grid cell and each season, the median of the 14 model values is selected, and the collection of these values defines the median model. We note that a mean model, computed similarly, shows very similar characteristics, except in cases when units errors have been made in reporting results from one or more models (e.g., reporting precipitation in units of mm/day rather than in kg m^{-2} s^{-1}).

For each of the models, we have analyzed seasonal maps of 13 different fields that can be compared with observations. We have calculated the RMS error for each of these fields, which involves summing the squared differences over all grid cells (with all model output first regridded to a T42 resolution grid) and over all 4 seasons. With the resulting space-time error statistics, the 30 model simulations (14 pairs of simulations from the modeling centers plus the two median model results) are then ordered such that this measure of model error decreases monotonically. With each field considered separately, each model is then given a percentile ranking, according to this ordering. Figure 1 shows the results.

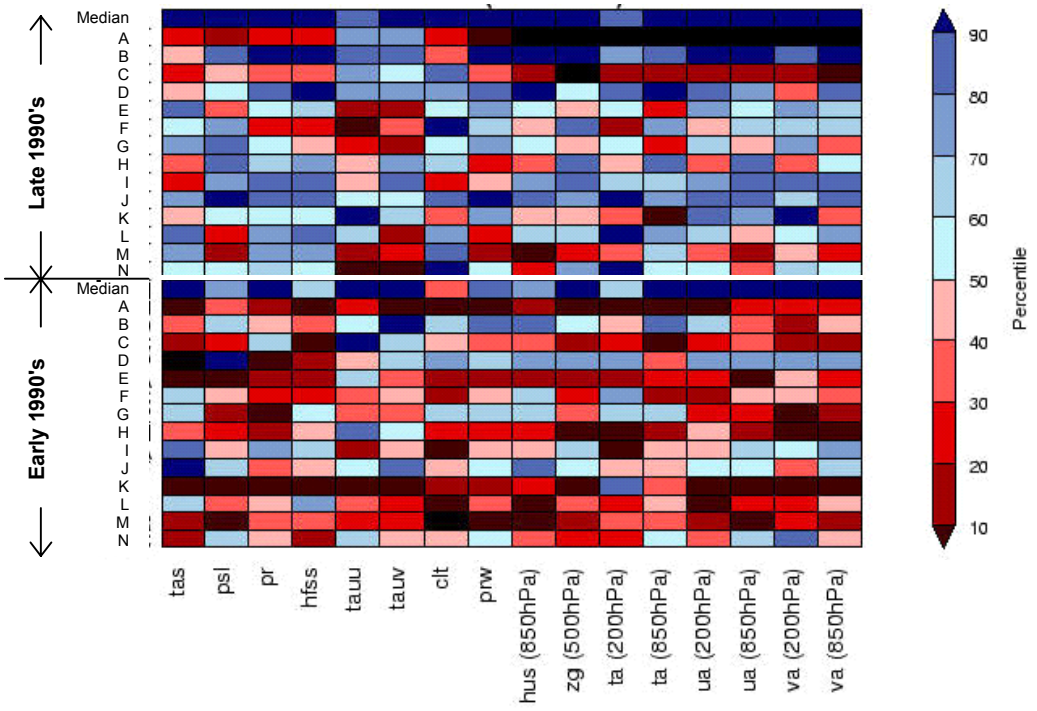

Fig. 1: The relative ranking of models (anonymously labeled by letter labels on the left) based on the RMS error in simulating the global distribution of seasonal fields. The fields analyzed were: surface air temperature (tas), mean sea level pressure (psl), precipitation (pr), surface sensible heat flux over the oceans (hfss), zonal and meridional components of surface wind stress over the oceans (tauu and tauv), cloud fraction (clt), precipitable water (prw), 850 hPa specific humidity (hus), 500 hPa geopotential height (zg), temperature (ta) at 200 and 850 hPa, and zonal (ua) and meridional (va) wind at 200 and 850 hPa. Simulated fields were compared to the European Centre Reanalysis with the following exceptions: Precipitation was compared to the Xie-Arkin data set, cloud fraction was compared to the ISCCP data, and sensible heat was compared to the UWM/COADS climatology. The black boxes indicate fields that were missing from the AMIP database.

Compared with the lower half of the figure, about twice as many boxes in the upper half are shades of blue (124 vs. 61), indicating that for the various fields considered, the more recent models tend to have smaller RMS errors. Another striking feature is that the median model tends to have smaller errors than the individual models on which it is based. This is true of both the earlier and more recent ensemble of models.

Without examining figure 1 carefully, it is difficult to determine whether an individual model has improved. The figure also fails to show how large the actual change in error has been since only the relative rankings are shown. To provide further information concerning changes in model performance, it is therefore useful to construct a so-called "Taylor diagram." Figure 2 focuses on the median model result and summarizes how model performance has changed over the last decade. As described in Taylor (2001, J. Geophys. Res., 106, 7183-7192), the statistics shown in the diagram are the correlation coefficient between the observed and simulated field (related to the azimuthal angle), the centered (i.e., mean removed), normalized root-mean-square (RMS) difference between the two fields (proportional to the distance to the point on the x-axis marked observed), and the ratio of the standard deviation (SD) of the simulated field to that observed (proportional to the radial distance). The statistics for the more recent "median" model results are plotted at the head of each arrow, and the older median model results are plotted at the tail of each arrow. A model may be judged to have improved if the correlation increases, the arrow points toward the observed point (indicating a reduction in RMS error), and the arrow moves toward the dotted arc (i.e., the simulated SD moves toward the observed). Because most of the arrows are directed in the general direction of the observed point, the impression given by the diagram is that general improvement has occurred over the past decade.

As indicated earlier, there is a wide variety of information that must be considered when assessing changes in model performance. Our analysis here has been limited to the seasonal cycle of the global distribution of more than a dozen fields of importance to climate. Despite these limitations, it is encouraging that at least some aspects of atmospheric simulations have improved over the last decade. Not only are individual models improving, but the median results of those models appear to be superior to most of the models comprising the ensemble.

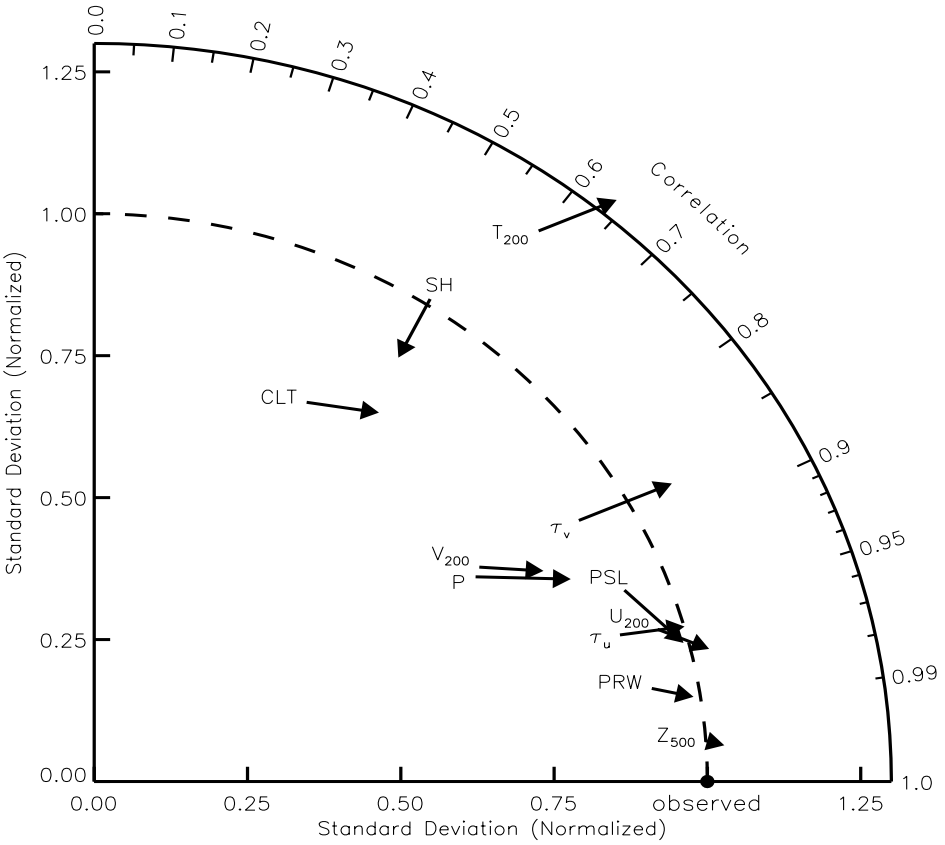

Fig. 2: Change in median model performance. A subset of the fields described in figure 1 is analyzed here.

The ERA-40 Project and Its Use for Model Evaluation

M. J. Miller, A.J.Simmons and S. Uppala
European Centre for Medium-Range Weather Forecasts

Abstract

The ERA-40 project and its current status are reviewed. Key differences and improvements since production of the ERA-15 analyses are summarized, as are additional changes developed specifically for ERA-40. New products and the improved quality of most of the ERA-40 products are discussed.

1. INTRODUCTION

The new reanalysis project ERA-40, supported by the European Union and several other organizations, is progressing at ECMWF. It covers the period from mid-1957 to 2001 overlapping the earlier ECMWF reanalysis ERA-15 (1979-1993) and complementing the NCEP reanalysis, which runs from 1947. ERA-40 uses the historical ground-based WWW observations and observations from special experiments such as the 1974 Atlantic Tropical Experiment of the Global Atmospheric Research Program GATE, First GARP Global Experiment FGGE 1979, Alpine Experiment ALPEX 1982 and the more recent 1992-1993 TOGA-COARE. The datasets have been made available to the project, principally by NCAR/ NCEP, ECMWF, JMA and the US NAVY. In addition, and to a much larger extent than in ERA-15, ERA-40 makes use of multichannel satellite radiances through a 3D-variational assimilation starting with data from the first VTPR sounding instrument in 1972 and continuing up to the present SSM/I, TOVS and ATOVS instruments. Analysis of ozone is also included. Cloud Motion Winds are used from 1979 onwards and EUMETSAT has undertaken to reprocess Meteosat winds for 1982-1988.

Ideally, reanalysis is the analysis of past observational data using a fixed, tried-and-tested, data assimilation system. In practice, however, in developing and running a reanalysis system one has to address a number of issues and make a number of compromises.

Firstly, for a data assimilation that covers a period of several decades and has to be completed within a production period of about two years, the computational cost of completing a single analysis will typically have to be substantially less than for an advanced current operational data assimilation system. Choosing an earlier, affordable operational version of the data assimilation system may mean foregoing a number of desirable recent developments.

Secondly, the best available data assimilation system is likely to be based on the use of data from current observing systems, and thus require adaptation to use data from older observing systems. Moreover, when the reanalysis system is run in production mode, its performance must be monitored carefully to identify when intervention is required to adapt to changes in any pre-processing applied by data producers.

Thirdly, a system that is tried-and-tested inevitably has a number of known deficiencies. Whilst recently developed changes may be implemented to address some of these deficiencies,

acceptable and reasonably tested solutions to others may not be available. Account needs to be taken of this in the generation of products, the validation and the documentation of the reanalysis.

Finally, errors and addressable deficiencies in formulation may well be found during the course of production of a reanalysis. Decisions have to be made as to whether to introduce corrections or refined formulations in the interest of improving later analyses, or to let the problems remain in the system in the interest of continuity of the full set of analyses.

Each of these types of issue has been faced in the development and production runs of the ERA-40 data assimilation system,

The computational cost of ECMWF's current operational four-dimensional variational data assimilation (4D-Var) and T511 horizontal resolution is too high for it to be used for ERA-40. A modified form of the three-dimensional variational analysis (3D-Var) used operationally in the ECMWF medium-range prediction system between January 1996 and November 1997 (Andersson et al., 1998) has thus been adopted. 3D-Var is today used operationally at ECMWF to produce short cut-off analyses from which forecasts are run to provide boundary conditions for the limited-area short-range forecasting systems of a number of the ECMWF Member States. It is also the method used for operational global analysis at a number of other centres (e.g. Parrish and Derber 1992; Lorenc *et al*. 2000) and was used for the NCEP/NCAR reanalysis (Kalnay et al., 1996).

The spectral representation of atmospheric fields chosen for ERA-40 has triangular truncation of the spherical harmonic expansion at total wavenumber 159. This T159 resolution is finer than the T62 resolution used for the NCEP/NCAR reanalysis, and the T106 resolution used for ECMWF's fifteen-year analysis for 1979-1993 (ERA-15; Gibson et al., 1997). Other fields are represented on a form of reduced Gaussian grid (Hortal and Simmons, 1991; Courtier and Naughton, 1994) with a quasi-uniform grid spacing of about 125km, the same as used for ERA-15. The 60-level vertical resolution is that currently used operationally at ECMWF.

A comprehensive documentation of the analysis scheme and assimilating model used for ERA-40, and which are elements of the "Integrated Forecasting System" (IFS) developed jointly by ECMWF and Météo-France may be found in the IFS documentation viewable on ECMWF's public website (http://www.ecmwf.int), and further information (including specification of the products archived from ERA-40 and details of their spatial representation) can be found in the site's ERA-40 pages.

2. THE USE OF OBSERVATIONS IN ERA-40

The first ECMWF reanalysis ERA-15 covered the period, 1979-1993, during which the observing system was relatively homogeneous. There were two sources of satellite data in ERA-15, data from the TOVS instruments in the form of Cloud Cleared Radiances (CCR) from NESDIS and the Cloud Motion Winds from geostationary satellites, both available throughout the period. The CCR data had gone through many preprocessing steps and 1d-retrievals were used in the Optimum Interpolation analysis (Gibson et al 1997). In ERA-40 the calibrated Level-

1c radiances are used directly through 3D-Var (Andersson et al, 1998). Vertical Temperature Profiler Radiometer data, 1972-1979, are used for the first time in a data-assimilation as radiances. VTPR is a 8-channel infrared instrument. All earlier data-assimilations of VTPR data including the NCEP reanalysis have been based on the old operational temperature and humidity retrievals. The use of satellite radiances in ERA-40 allow for a more observation-driven stratospheric analysis during the second half of the reanalysis.

Data from Special Sensor Microwave/ Imager (SSM/I) data are used in ERA-40. ERS Scatterometer winds over the oceans are used in the wind analysis from 1994 onwards and altimeter wave height data from 1991 onwards in the wave analysis. Cloud Motion Wind processing techniques have been improved throughout the period, (Uppala, 1997), and EUMETSAT has initiated a task to reprocess the winds 1982-1988.

The ozone observations used in the ERA-40 are TOMS total ozone and SBUV ozone layer measurements. All these observations are available from 1978 to the present time.

Conventional data for ERA-40 comes from a wide selection of sources. The ERA-40 period begins with the International Geophysical Year of 1958 when the foundation for the current conventional network was established. Most of these data have been collected by NCAR/ NCEP and are being used in ERA-40. Special datasets such as ECMWF observation archive, FGGE, ALPEX and PAOBs will also be included. A new updated Comprehensive Ocean-Atmosphere Data Set (COADS) has been provided by NCAR. Separate additional datasets have been received from JMA and US Navy archives.

The ERA-40 production is organized in three streams covering different stages in the evolution of the observing system. Stream 1 covers the most recent period, with analyses running from the beginning of January 1989 onwards. Stream 2 runs from September 1957 onwards and Stream 3 from January 1973 onwards.

3. CHANGES SINCE ERA-15

The data assimilation system used for ERA-15 was cycle 13r4 of the IFS, and was essentially the same as that used operationally by ECMWF from April 1995 to January 1996, apart from its use at lower resolution. Since then there have been between one and four changes each year to the operational forecasting system that are of relevance to ERA-40. ERA-40 is based on cycle 23r4 of the IFS, though with some modifications. Simmons and Hollingsworth (2002) discuss the substantial improvement in overall medium-range forecast accuracy that has resulted from them.

Large differences in two-metre temperature between ERA-40 and ERA-15

The change in low-level temperature from ERA-15 to ERA-40 is especially pronounced for high latitudes in winter. There are differences in surface and low-level atmospheric temperatures in the Antarctic due to model parametrization revisions, more-accurate specification of the orography, a changed modelling of sea-ice and treatment of the main permanent ice shelves as land rather than sea-ice. Fig. 1 shows differences in two-metre temperature between monthly-mean analyses for July 1989 from ERA-40 and ERA-15. The

ERA-40 analysis is substantially warmer over the Antarctic plateau, by up to 22K, generally cooler by a few degrees over sea-ice, and substantially colder, by up to 15K, over the Ronne and Ross ice shelves.

Horizontal resolution of the ERA-40 assimilation system

The assimilating model for ERA-40 uses the linear-grid option adopted operationally in April 1998. As noted earlier, the spectral resolution is T159, compared with the T106 resolution of ERA-15. The ~125 km resolution reduced Gaussian grid is however the same as that used for ERA-15. One consequence of ERA-40's use of finer spectral resolution, but the same grid-point resolution, is a very marked reduction in the amplitude of the unrealistic spectral ripples in the model orography that are most obvious over oceans or flat land close to major mountain ranges. Fig.2 compares the ERA-40 and ERA-15 orographies in the vicinity of South America. A logarithmic contour is chosen to emphasize the reduced amplitude of spectral ripples for ERA-40, which can be seen not only over the Pacific Ocean to the west of the Andes but also over the Amazon basin.

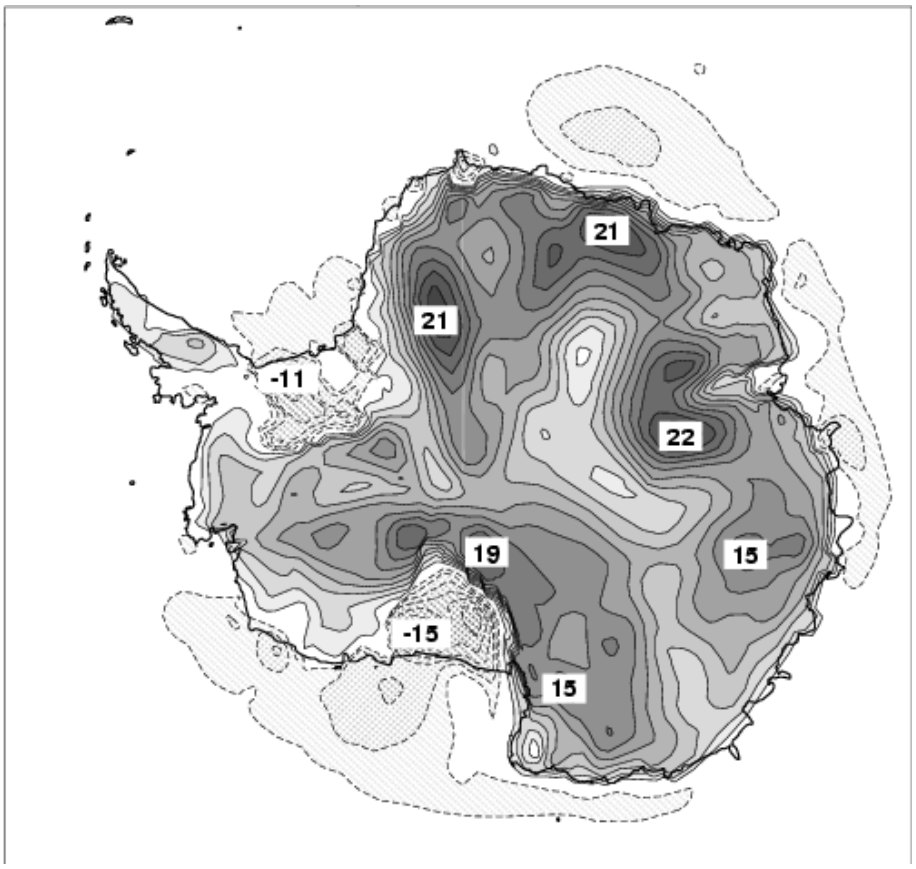

Fig. 1 Differences over the Antarctic in two-metre temperature (K) between ERA-40 and ERA-15 analyses averaged for July 1989. Contours begin at values of ±1K, with contour intervals of 2K. Continuous lines indicate where ERA-40 analyses are on average warmer than ERA-15 analyses.

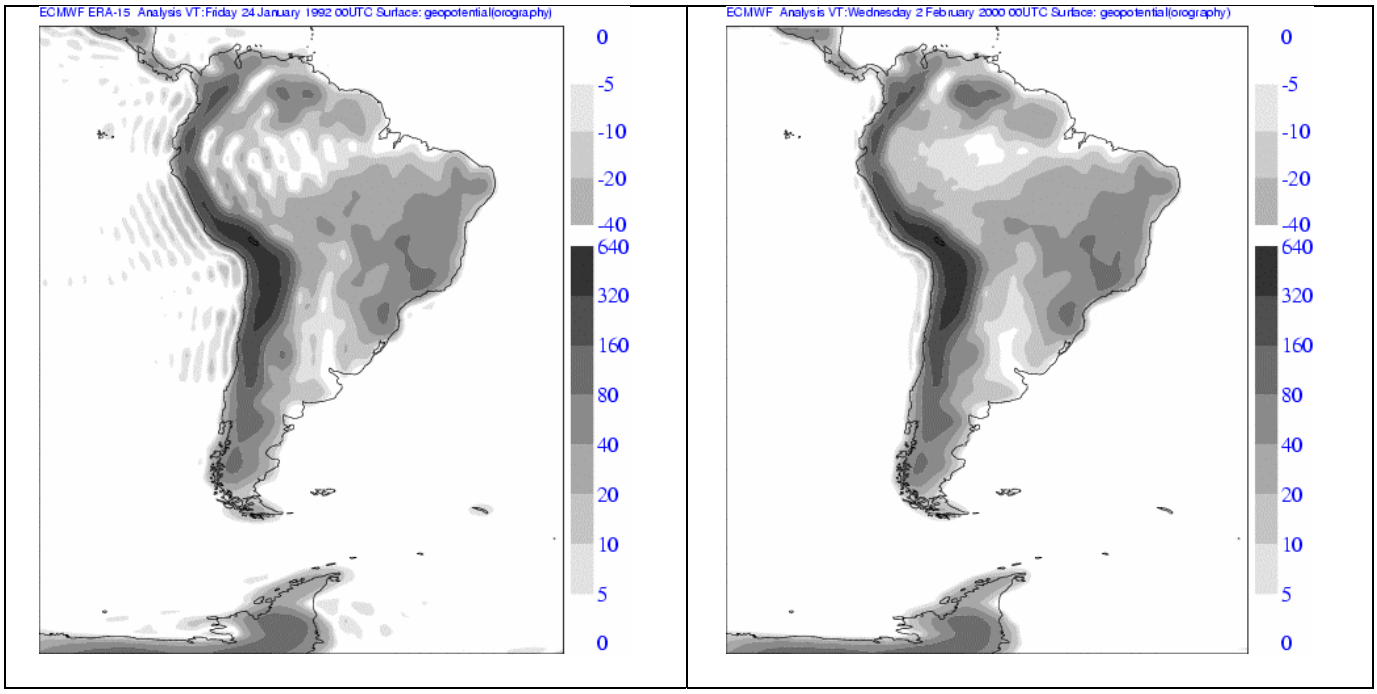

Fig. 2 ERA-15 (left) and ERA-40 (right) model orographies, plotted with contour values ±50, ±100, ±200, 400, 800, 1600 and 3200m.

Vertical resolution of the ERA-40 assimilation system

The 60-level vertical resolution used for ERA-40 is that operational since October 1999. The distribution of these 60 levels is compared with that of the 31 levels used in the ERA-15 model in Fig. 3. The greater number of levels in the planetary boundary layer can be seen, though not their precise location (for that see Jakob et al., 2000). Upper tropospheric resolution is similar for the two configurations. The improved stratospheric representation for ERA-40 is evident; the vertical layer spacing is close to 1.5km over much of the stratosphere in the 60-level model.

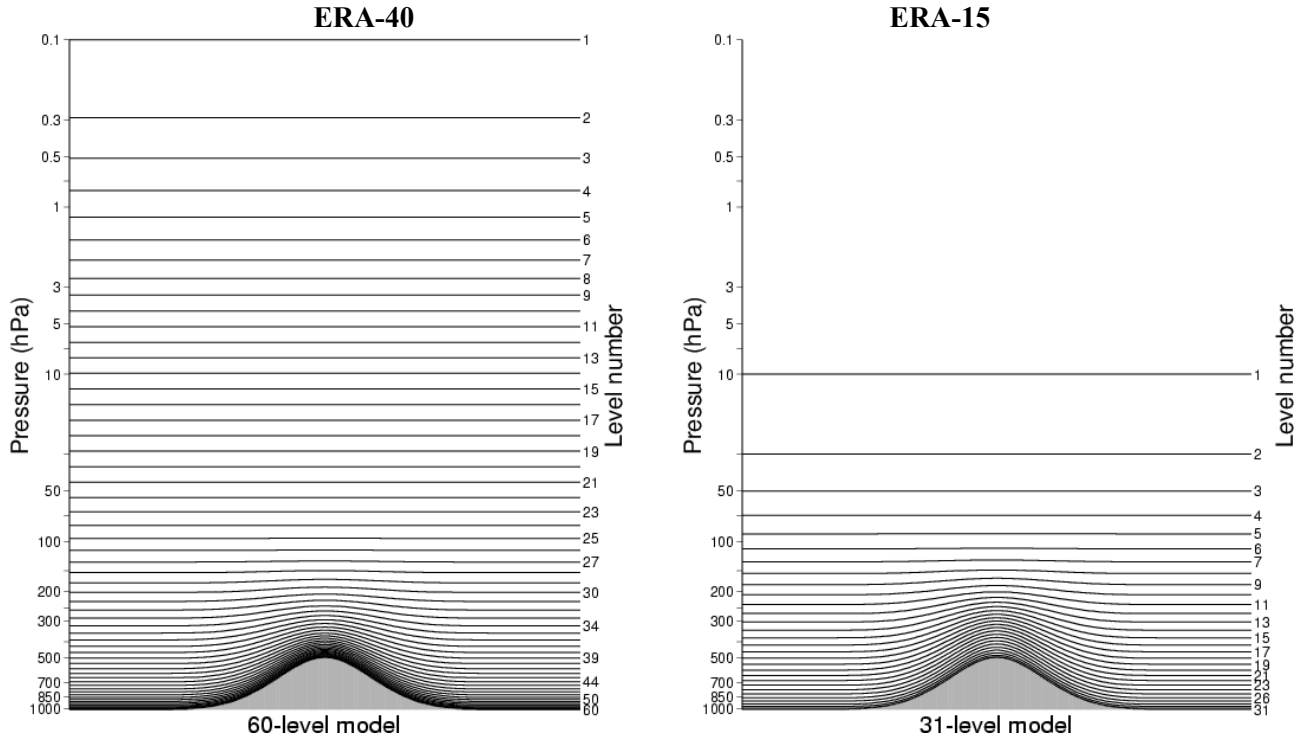

Fig. 3 The distribution of full model levels at which the basic prognostic variables are represented, for ERA-40 (left) and ERA-15 (right).

Differences in oceanic 10-metre wind speed between ERA-40 and ERA-15

Kållberg(1997) discussed the fits to observation and spin-up of oceanic 10m winds in ERA-15. He inferred that the analysed winds were too low in places due to the assimilation of 10-metre wind observations from island stations that were unrepresentative of winds over neighbouring open seas, and that winds were likely to be too high elsewhere because of the assumption that ship wind observations were at 10m rather than at the generally higher levels at which the anemometers were located. Both analysis deficiencies have been corrected for ERA-40, by blacklisting unrepresentative island winds and adopting the changed use of ship winds introduced operationally in July 1999[1].

More recent changes

Although based on cycle 23r4, several changes that became operational in later cycles were included in the ERA-40 data assimilation system. These included three changes that were

[1] In the absence of information on the actual anemometer height, ship winds are assigned to a fixed height of 25m derived from averaging a recent WMO list of reporting ships. No allowance is made for a tendency for anemometer heights to increase over the period of ERA-40. This could cause a slight spurious drift in the ocean winds over the course of the reanalysis.

introduced operationally in January 2002 in cycle 24r3: a finite-element scheme for the model's vertical discretization, removal of an error in the SSM/I bias correction (which affected stream-1 ERA-40 production up to January 1993) and a pre-conditioning of the 3D/4D-Var minimization (that has negligible impact on results but which significantly increases production efficiency). The assimilation of ozone observations introduced into operations in April 2002 as part of cycle 25r1 was based on that used in ERA-40, with assimilation of near-real-time total ozone retrievals from GOME replacing ERA-40's use of TOMS total ozone as the latter retrievals are not available in time for operational use. SBUV data are used in both ERA-15 and operations.

3. ADDITIONAL DEVELOPMENTS AND FEATURES FOR ERA-40

Several developments or parameter adjustments within the assimilation system were made specifically for ERA-40.

An FGAT (first-guess at the appropriate time) capability for the 3D-Var analysis was developed for use in ERA-40 in response to feedback received on the original plans for the reanalysis. In this approach, background (first-guess) values are compared with observed values at the observation time rather than the analysis time, and the differences are applied at analysis time. The 3D-Var configuration was also adapted to use the linear grid employed in the model, allowing analysis increments to be derived at the full T159 resolution of the assimilating model (the same resolution at which they are currently derived operationally in 4D-Var). These developments have enabled the reanalysis to fit data more accurately both in space and time.

IPCC trends for the specified, radiatively-active gases have been introduced for ERA-40 as recommended by a Workshop on Boundary Conditions and Atmospheric Composition held at ECMWF in July 1998. Aerosol variability and a trend in the stratospheric water vapour source due to methane oxidation (see later) have not been included.

Enhanced sets of post-processed products have also been developed for ERA-40, in collaboration with members of the user community. Examples are vertically-integrated fluxes, fields from the physical parametrizations for support of chemical-transport modelling, and special grid-point and catchment-basin diagnostics. They are specified in the Archive Plan included in the project's web pages.

4. SHORT-RANGE FORECAST VERIFICATION

The ERA-40 system has also been monitored by regular verification of the short-range forecasts carried out as part of the production. Annual-mean root-mean-square errors of one-day 500hPa height forecasts for the extratropical northern and southern hemispheres show that the ERA-40 errors are smaller than the errors of ERA-15 and ECMWF operational forecasts for 1989. They do not match those obtained operationally by ECMWF in 2001, when the T511 4D-Var system was in operational use and some enhancements to the observing system had occurred. They are, however, not much poorer than those from the 2001 operational systems of the Met Office and NCEP. Comparison with results for ECMWF operations presented by Simmons and Hollingsworth(2002) shows ERA-40 performance to be similar to that achieved by

ECMWF operations in 1997 for the northern hemisphere and from mid-1998 to mid-1999 for the southern hemisphere, as judged by one-day 500hPa height forecast errors.

5. GENERAL REMARKS

On the ERA-40 web pages http: //www.ecmwf.int/ research/ era, the progress of the project can be followed using various monitoring diagnostics.

Initial assessment of the ERA-40 system performance, which has thus far been mainly based on the period 1989 onwards, shows that the analysis quality is good in comparison with ERA-15 and ECMWF's operations at the time. Satellite radiances are used extensively and the analysis is responding well to the signals in the data. This also means that possible problems in the data are easily absorbed into the analysis unless noticed in the monitoring. Compared to ERA-15, the ERA-40 satellite bias corrections are valid for longer periods helping to achieve better time consistency. Concerns have been raised about high precipitation rates over the Tropics and the imbalance of P-E, and. Investigations are underway to understand the possible causes. The tropical wind observations fit the first guess better in later years indicating improving quality of the wind analysis. Also the short-range forecasts indicate very good performance in ERA-40. An evaluation of the quality of all atmospheric variables, fluxes etc will be put on the website after further validation. Details of a later rerun of the 1979 to present period which will 'clean-up' some of the problems identified during the ERA-40 validation, will be put on the website also. Nevertheless, the ERA-40 datasets will represent the most comprehensive set of atmospheric (and ocean wave) data so far available for studies of many aspects of atmospheric science.

ACKNOWLEDGEMENTS

The ERA-40 data assimilation system has benefited from the work of very many people, not only those active at ECMWF in the general development of the forecasting system and in its adaptation to ERA-40, but also those active elsewhere in the validation of experimental and production analyses, and those who earlier helped with advice and data during the planning of the project. The contributions of the project partners to the planning and validation are acknowledged in particular.

References

Andersson, E., Haseler, J., Undén, P., Courtier, P., Kelly, G., Vasiljevic, D., Brancovic, C. Cardinali, C., Gaffard, C., Hollingsworth, A., Jakob, C., Janssen, P., Klinker, E., Lanzinger, A., Miller, M., Rabier, F., Simmons, A., Strauss, B., Thépaut, J.-N., and Viterbo, P. 1998: The ECMWF implementation of three-dimensional variational assimilation (3D-Var). Part III: Experimental results. *Quart. J. R. Meteorol. Soc.,* **124**, 1831-1860.

Courtier, P., and Naughton, M. 1994: A pole problem in the reduced Gaussian grid. *Quart. J. R. Meteorol. Soc.*, **120**, 1389-1407

Gibson, J.K., Kållberg, P., Uppala, S., Nomura, A., Hernandez, A., and Serrano, E. 1997: ERA Description. ECMWF Re-Analysis Final Report Series, **1**, 71pp.

Hortal, M. and Simmons, A.J. 1991: Use of reduced Gaussian grids in spectral models. *Mon. Wea. Rev.,* **119**, 1057-1074.

Jakob, C., Andersson, A., Beljaars, A., Buizza, R., Fisher, M., Gérard, E., Ghelli, A., Janssen, P., Kelly, G., McNally, A.P., Miller, M., Simmons, A., Teixeira, J., and Viterbo, P. 2000: The IFS cycle CY21r4 made operational in October 1999. *ECMWF Newsletter*, **87**, 2-9.

Kållberg, P. 1997: Aspects of the re-analysed climate. ECMWF Re-Analysis Final Report Series, **2**, 89pp.

Kalnay, E., Kanamitsu, M., Kistler, R., Collins, W., Deaven, D., Gandin, L., Iredell, M., Saha, S., White, G., Woollen, J., Zhu, Y., Chelliah, M., Ebisuzaki, W., Higgins, W., Janowiak, J., Mo, K.C., Ropelewski, C., Wang, J., Leetmaa, A., Reynolds, R., Jenne, R., and Joseph, D., 1996: The NCEP/NCAR 40-year reanalysis project. *Bull. Amer. Meteor. Soc*., **77**, 437-471.

Lorenc, A.C., Ballard, S.P., Bell, R.S., Ingleby, N.B., Andrews, P.L.F., Barker, D.M., Bray, J.R., Clayton, A.M., Dalby, T., Li, D., Payne, T.J. and Saunders, F.W. 2000: The Met. Office global three-dimensional variational data assimilation scheme. *Quart. J. R. Meteorol. Soc.*, **126**, 2991- 3012.

Parrish, D.F. and Derber, J.C. 1992: The National Meteorological Center's Spectral Statistical-Interpolation analysis system. *Mon. Wea. Rev.*, **120**, 1747-1763.

Simmons, A.J. and A. Hollingsworth 2002: Some aspects of the improvement in skill of numerical weather prediction. *Quart. J. Roy. Meteor. Soc.,* **128**, 647-677.

On the Limitations of Prescribing Sea Surface Temperatures in Atmospheric General Circulation Model Experiments ”

James W. Hurrell[1*], Simon Brown[2], Christophe Cassou[1], and Adam Phillips[1]

[1]National Center for Atmospheric Research, Boulder, CO, USA.
[2]United Kingdom Meteorological Office, Bracknell, U.K.
[*]Corresponding author email: *jhurrell@ucar.edu*

1. INTRODUCTION

It is widely accepted that extratropical sea surface temperature (SST) variability arises primarily in response to fluctuations in surface heat fluxes driven by atmospheric variability. The back-interaction exerted by SST anomalies on the atmosphere in the real world is fundamentally different, therefore, from the one-way forcing that takes place in atmospheric general circulation model (GCM) experiments with prescribed SSTs, even if those SSTs are time dependent as in the Atmospheric Model Intercomparison Project (AMIP) framework. Several studies have shown that a primary effect of coupling is to attenuate the thermal damping exerted by the infinite heat capacity ocean in prescribed SST integrations, suggesting that extratropical atmospheric low-frequency variability will be underestimated in prescribed SST experiments.

The effects of interactive SSTs have been addressed in the literature using models of varying complexity, from linear, one-dimensional models to coupled GCM experiments. Moreover, the latter have generally employed simple mixed layer oceans and have compared the extratropical atmospheric variability of the coupled system to the uncoupled variability that arises under climatological SST conditions.

We employ a more consistent approach in the hope of a better quantification of the effect of coupling. In particular, we compare the simulated climate from a fully coupled ocean-atmosphere GCM (HadCM3) to that from the atmospheric component (HadAM3) of the same model, where the latter is forced with the sea ice and SST fields internally generated by the former. The coupled data are from a 150-year subset of a longer integration, and the uncoupled data consist of a 3-member (150-year) ensemble, where each ensemble member was initialized from slightly different conditions. Sea surface temperatures and sea ice are updated every 24 hours, the coupling frequency of HadCM3. More detailed results will be presented in a separate paper currently in preparation.

2. ATMOSPHERIC VARIABILITY *VARIANCE DISTRIBUTION*

The ratio (uncoupled/coupled) of the standard deviation of monthly near-surface (2 m) air temperature (SAT) anomalies reveals enhanced variability over the extratropical oceans in the fully coupled simulation (Figure 1). Very similar maps are obtained for 850 hPa temperature (not shown). The smallest ratios (e.g., off the east coasts of Asia and North America) in SAT are near 0.9, meaning a local increase in variance of up to 20% in the coupled simulation. Averaged over the extratropical latitudes (20-90º), there is a 13% increase in both hemispheres of SAT in the coupled simulation. Similar ratios are obtained when longer time scale variations of SAT are considered. For 3-month seasonal mean anomalies, the largest increases in hemispheric SAT

variance due to coupling are near 20% and occur during the winter seasons, while the smallest increases (~6%) occur during the summer seasons. These results are robust among all 3 members of the uncoupled ensemble. Consistent with the notion of reduced thermal damping, coupling reduces the variance of the net surface heat flux anomalies (not shown).

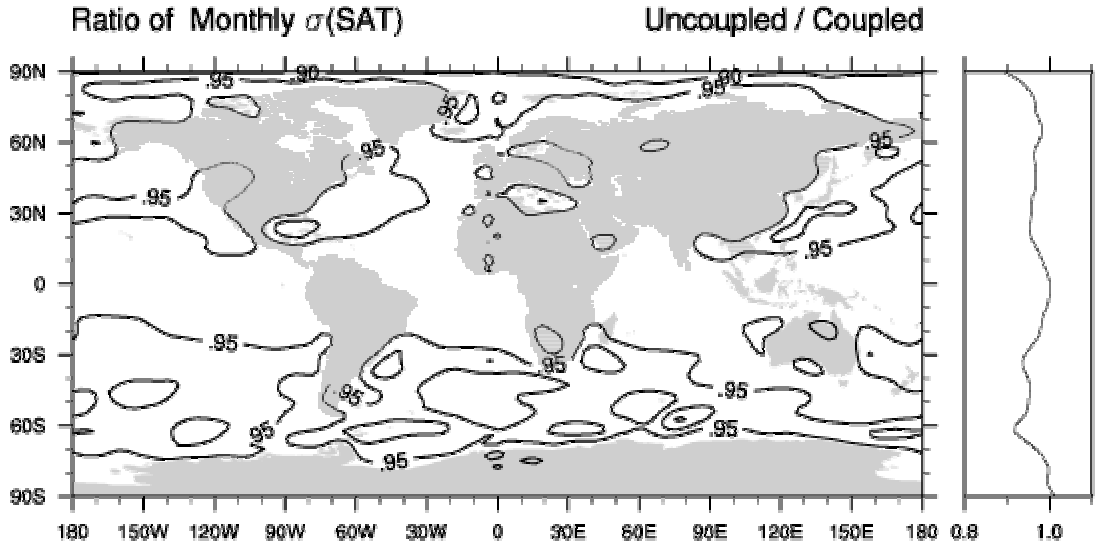

Figure 1. The ratio (uncoupled/coupled) of the standard deviation of monthly mean SAT anomalies. The contour interval is 0.05, and the 1.0 contour has been omitted.

The accompanying increase in upper-tropospheric variance is smaller (Figure 2). The variance of the boreal winter mean (DJF) 500 hPa geopotential height field is larger in the coupled simulation than in the uncoupled simulations, but not everywhere and only by about 5% when averaged over the extratropical hemispheres. The largest local differences are evident over the North Atlantic, where the variance is ~10% larger in the coupled simulation on average. Over the North Pacific, there is a reduction in variance due to coupling. While the local differences are generally not statistically significant, they are robust among the three uncoupled simulations.

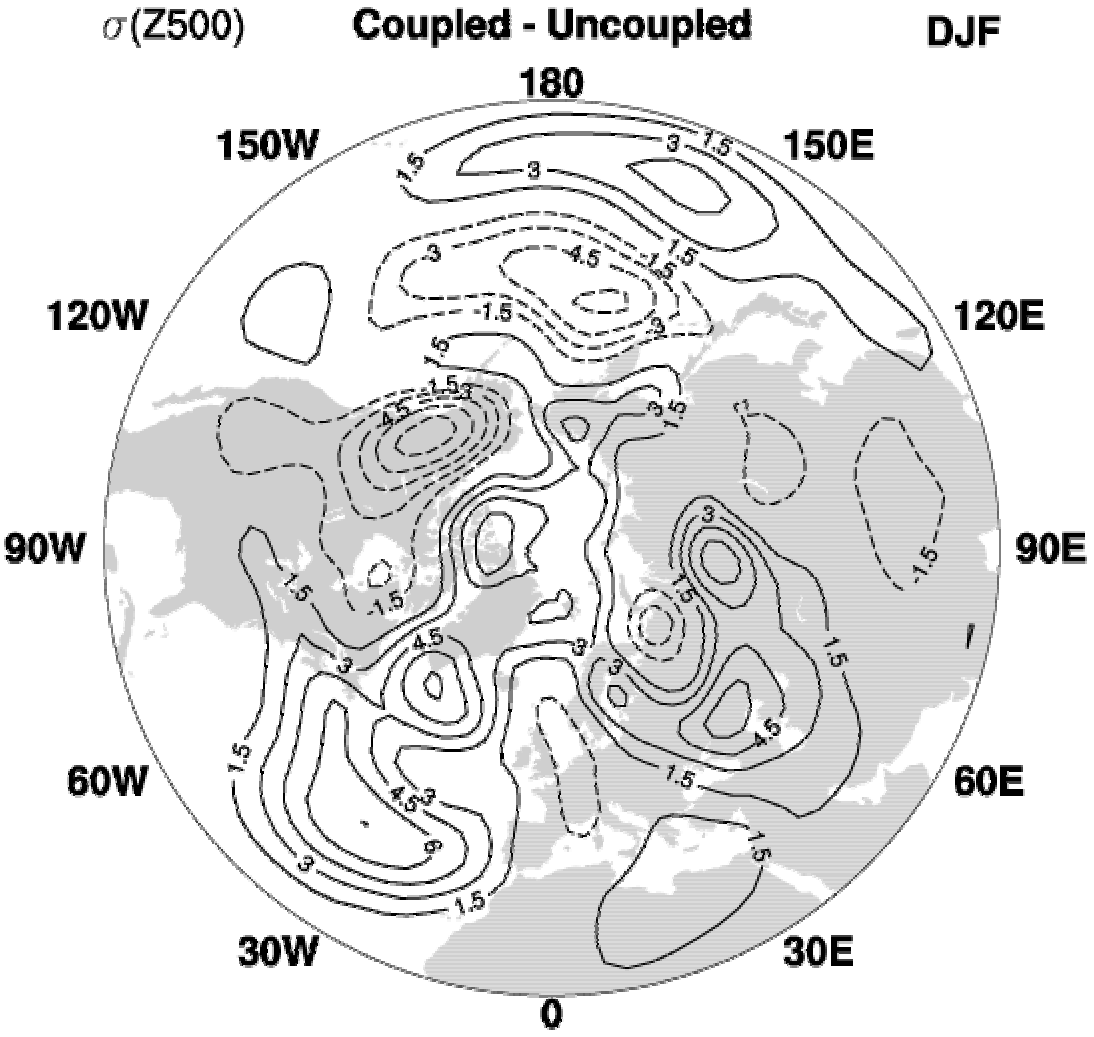

Figure 2. The difference (coupled minus uncoupled) in the standard deviation of boreal winter (DJF) 500 hPa geopotential heights. The contour interval is 1.5 gpm, and the zero contour has been omitted.

Modes of variability

We have examined hemispheric, rotated and regional empirical orthogonal functions (EOFs) of monthly and seasonal 500 hPa geopotential height anomalies. In all cases, coupling does not alter the spatial structure of the variability, but it does alter the variance associated with the leading modes. Some of these aspects are quantified in Figure 3, which shows the spatial pattern correlation and the variance ratio for the first two EOFs of 500 hPa height computed over the North Atlantic domain (20º-80ºN, 90ºW-30ºE).

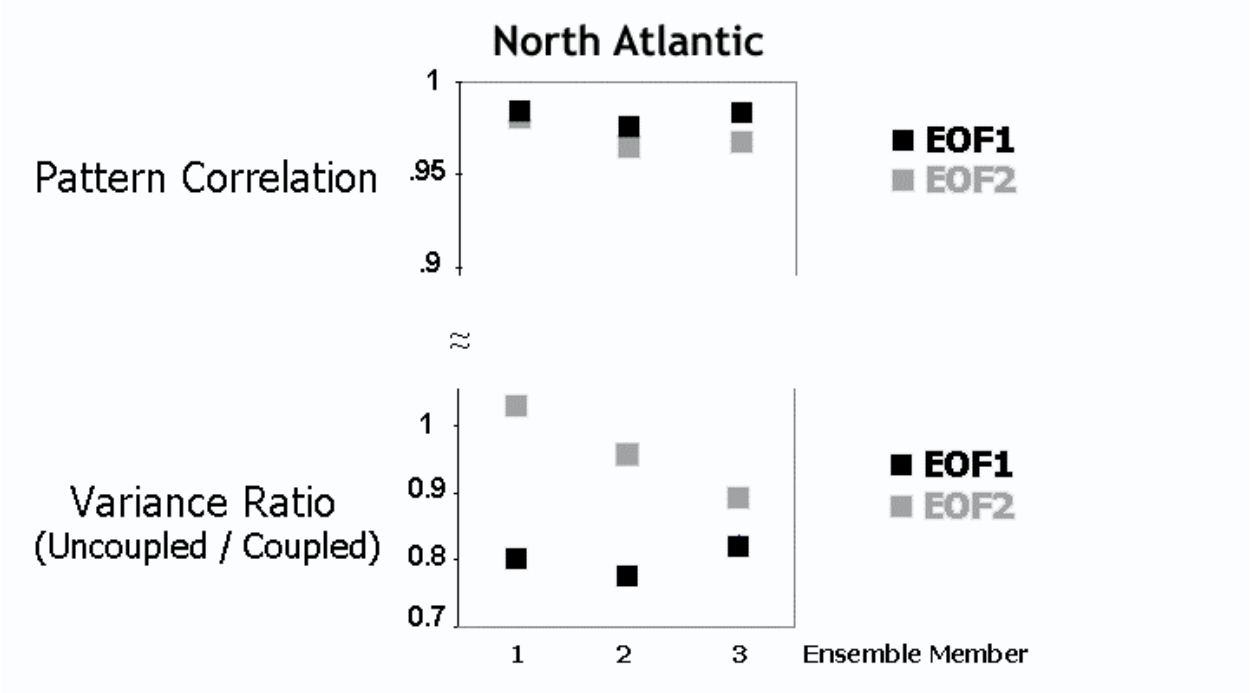

Figure 3. The spatial correlation over the North Atlantic domain (20º-80ºN, 90ºW-30ºE) of the first two EOFs of 500 hPa geopotential height (top), and the ratio of the simulated EOF variance (bottom), between the coupled and the three uncoupled simulations.

The leading EOF reflects the model's North Atlantic Oscillation (NAO), while the second EOF reflects the model's East Atlantic (EA) teleconnection pattern. In both cases, the pattern correlations between the uncoupled simulations and the coupled simulation are very high (> 0.97). The variance ratios indicate that all 3 uncoupled simulations underestimate the total variance associated with the NAO by about 20%, suggesting a modest amplification of the NAO signal in HadCM3 due to middle latitude air-sea interaction. I

One may also think of the overall effect of coupling as biasing the atmospheric circulation toward certain flow regimes by increasing their persistence. We have examined this possibility through a climate regime analysis applied to monthly mean 500 hPa geopotential height data (not shown). Coupling does not alter the geographical patterns of the regimes, nor does it impact the frequency of occurrence. There is an indication of more persistence in the coupled data, but the effect is minimal. For instance, in the coupled simulation, the regime corresponding to the negative index phase of the NAO occurred for 3 or more consecutive months in 10 (of 150) winters, but for no more than 5 winters in any of the individual uncoupled simulations.

3. SUMMARY

The results confirm that coupling enhances lower tropospheric thermal variance and reduces the variance of net surface energy flux. Coupling can also slightly alter the amplitude and persistence of dominant natural modes of middle latitude variability, such as the North Atlantic Oscillation, without altering their spatial structure. Overall, however, the effects are

smaller than most previous studies indicate, in part because most studies have compared the middle latitude atmospheric variability of the coupled system to the uncoupled variability that arises under climatological SST conditions. Under these conditions, the variance of SAT, for instance, typically doubles due to coupling on interannual and longer time scales. While our results suggest the detrimental effect of specifying middle latitude SST is small in AMIP-style integrations, advective processes in the ocean could potentially result in non-local coupling. It is expected this, however, would be most important at decadal and longer time scales.

Atmospheric Energetics in AMIP2 Models

G.J. Boer and S.J. Lambert
Canadian Centre for Climate Modelling and Analysis
Meteorological Service of Canada
University of Victoria

Model intercomparison attempts to answer, among others, the following questions: (1) how well do models reproduce the current climate, (2) do models correctly incorporate the mechanisms that control climate variability and change, (3) can models reproduce perturbed climates, (4) is simulated climate change reliable, and especially, (5) how do we improve models? Model intercomparison falls into at least three categories: the "morphology" of climate including the distribution pertinent mean structures and of first and second order climate statistics; budgets, balances and cycles such as that of energy, momentum, moisture etc.; and a rather broad category of particular climate processes such as the AO/AAO, MJO, blocking etc.

The energy cycle is and example of the second of these categories and is basic to the working of the atmosphere and of the climate system. It deals with the amounts and distributions of available potential (APE) and kinetic (KE) energies, and encapsulates the "basic rate of working" of the system as a heat engine, namely the generation of APE, its conversion to the KE that provides the transports by which the system attempts to attain equilibrium, and the subsequent dissipation of that KE. The energy cycle is a function of the distribution of both first and second order climate statistics namely the means, variances and covariances that arise in the governing equations under temporal and spatial averaging and which have robust physical meaning. Several levels of verification and intercomparison are possible under different levels of averaging and integration.

A standard global version of the energy cycle is represented by the 6-box energy diagram which gives the amounts of energy in mean zonal and mean non-zonal or stationary structures and in the transients of the flow together with the generation of, conversion between, and dissipation of these various forms of energy. Unfortunately, the AMIP data set precludes the calculation of all the terms in this version of the energy cycle owing to the lack of a number of covariance terms. We concentrate therefore on the 4-box energy budget like that of Figure 2 which is obtained by combining transient and standing components into a single "eddy" term.

Model results are compared against the NCEP objective reanalysis. In this preliminary stage, results from 14 AMIP2 models are used. One of these models is the AMIP2 "mean model", the climate statistics of which are obtained by simple ensemble averaging of the statistics of the individual models. All data are on a common 128x64 grid and on 17 standard pressure levels. Initially mean January climate mean statistics (calculated over 1979 to 1995 inclusive) are considered.

Even the 4-box energy budget incorporates a considerable number of terms which cannot be considered here. We display aspects of the dominant conversion term, C(Ae,Ke), between APE and KE in Figure 1. When integrated over the atmosphere (upper panel) the basic "rate of working of the system" is 2.25 Wm^{-2} from the NCEP data and 2.67 Wm^{-2} for the mean model. In

other words the rate of working of the models exceeds that of the system by about 20% in an average sense. Model values are generally above the NCEP value. The middle panel of Figure 1 gives the latitudinal distribution of the vertically integrated contribution to the term and the bottom panel the BLT diagram comparing the latter with NCEP. We see, as was generally the case for climate quantities in CMIP (Boer and Lambert, 2001), that the mean model is one of the best models in capturing this term.

Figure 2 displays the integrated 4-box energy cycle quantities for the mean model and the NCEP reanalysis. In particular from this (and many other diagrams similar to Figure 1 we have that: (1) as usual, no one model is the "best" for all quantities in the energy cycle and the mean model is one of the best if not the best when compared to observations; (2) the models are too active, and the basic rate of working too high, in the sense that energy cycles too quickly through the system compared to NCEP; (3) the models are still too zonal in that Az and Kz are too large and Ae, Ke too small; (4) apparently generation is not the reason for the Az, Ae difference since Ge is large while Ae is small and Gz is small while Az is large compared to NCEP; (5) dissipation could play a role since De is large for small Ke and Dz small for large Kz compared to NCEP and; (6) much more analysis is possible of terms and processes governing the energy cycle.

Although it is interesting to intercompare different aspects of model behaviour, do we really care? That is, does the study of the energy cycle offer anything new other than that models differ? In its favour, the energy cycle: (1) represents very basic physical aspects of the system; (2) invokes, depends on, and highlights the need to consider all 1st and 2nd order climate statistics and not simply means and selected variances; (3) directs attention toward the processes of energy generation, conversion and dissipation which is a step beyond documenting the distributions of basic statistics; and (4) permits a hierarchy of energetic analyses including the contributions from particular geographical areas and climate processes.

January Conversion between Ae and Ke

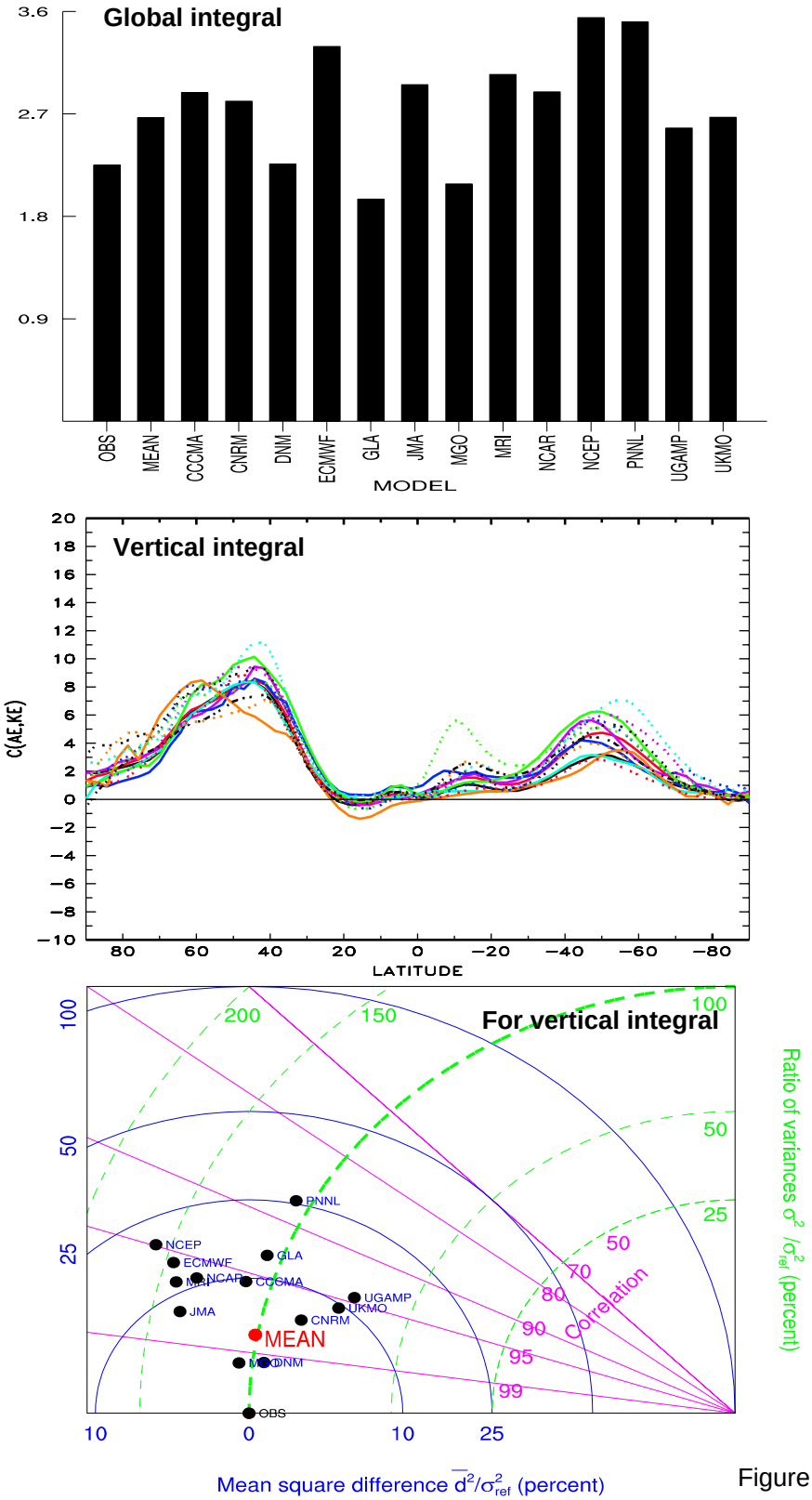

Figure 1

Atmospheric Energy Cycle - Jan

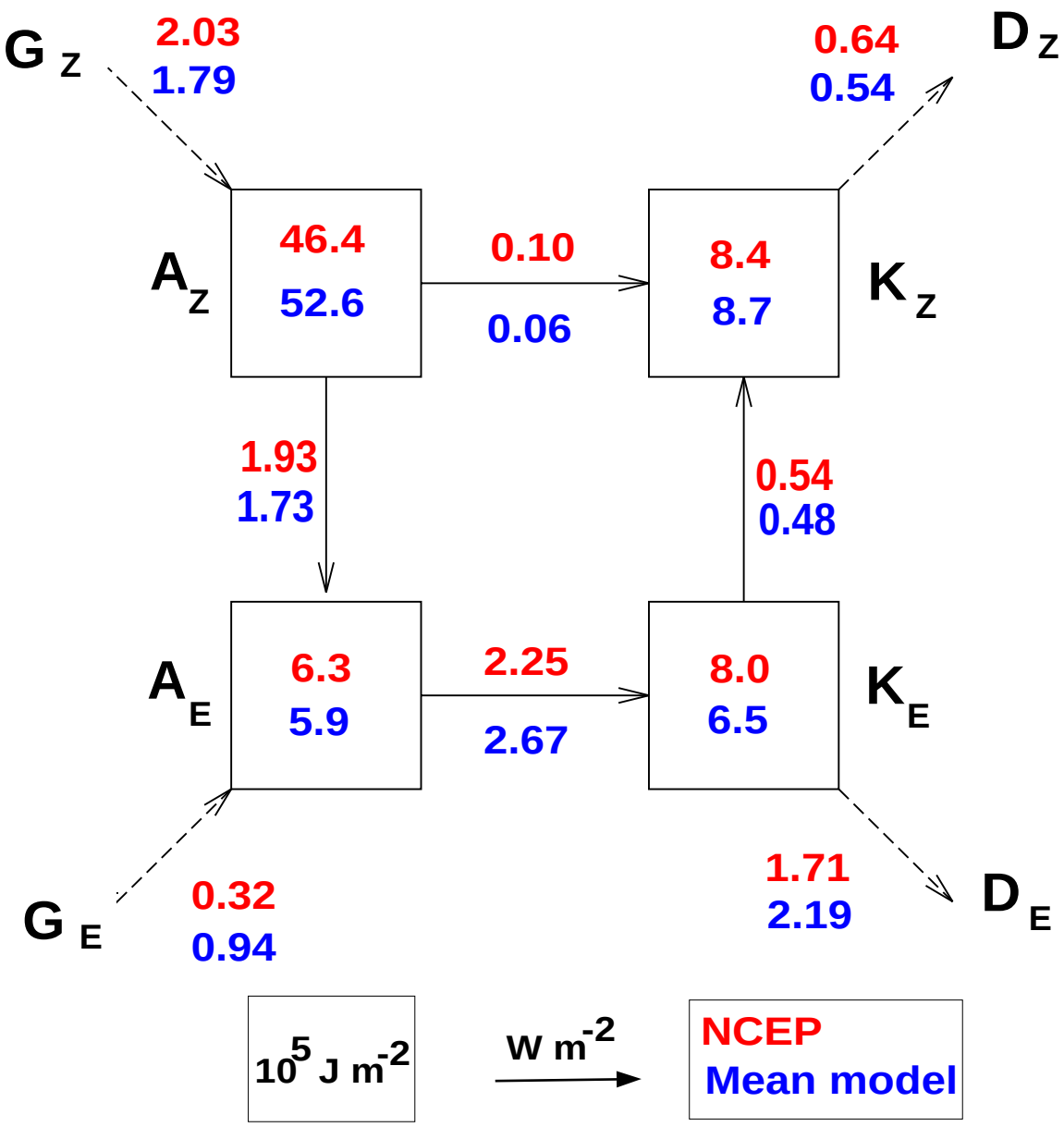

Figure 2

Assessments of Atmospheric Angular Momentum in AMIP-2 Simulations

David A. Salstein[1], Richard D. Rosen[1], Jean O. Dickey[2], and Steven L. Marcus[2]

salstein@aer.com

[1]Atmospheric and Environmental Research, Inc., Lexington, Massachusetts

[2]Jet Propulsion Laboratory, California Institute of Technology, Pasadena, California

INTRODUCTION

We are evaluating (Diagnostic Subproject 15) how well AMIP-2 models simulate the relative atmospheric angular momentum (AAM), a fundamental measure of the atmosphere's circulation that depends on the strength and distribution of the zonal winds. Also, AAM changes are compensated by solid Earth momentum, implying variations in the Earth's rotation rate, and thus in the length-of-day (l.o.d.). We focus on the spread in the mean, seasonal, and interannual components of AAM among the models, and we use the NCEP-NCAR reanalysis during 1979-95 as verification. We also compare AAM from the AMIP-2 models with that from their AMIP-1 predecessors (Hide et al. 1997). Taylor (2001) diagrams are used to depict a general improvement in simulating AAM by the current models.

MEAN, SEASONAL, AND INTERANNUAL SIGNALS

AAM is calculated between 1000 - 10 hPa from zonal wind fields of 20 currently available AMIP-2 models. Most of the model AAM mean values exceed their AMIP-1 counterparts (during the common 1979-1988 period), which themselves were larger than the NCEP-NCAR reanalysis value for this period (Fig 1; AMIP-1 and AMIP-2 being the open and solid bars, respectively). Upon analyzing the structure of the zonal winds in the reanalysis (Fig. 2, top) and the differences from it of both AMIP-1 and AMIP-2 (Fig. 2, middle, bottom), we note that the AMIP-1 errors consisted of negative biases in the subtropical upper troposphere and stratosphere, and larger positive biases in the midlatitude stratosphere of both hemispheres. In AMIP-2 the subtropical wind errors are much reduced, but those in the other regions are less so, so that the global bias, no longer mostly a balance of positive and negative errors, increases.

Figure 1

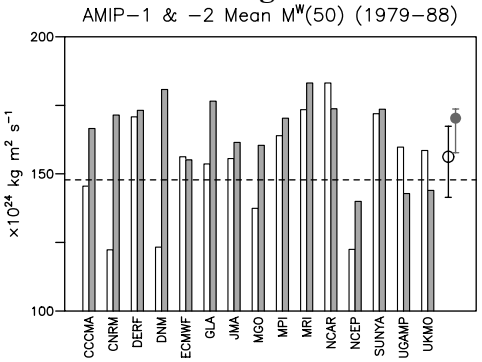

Figure 2

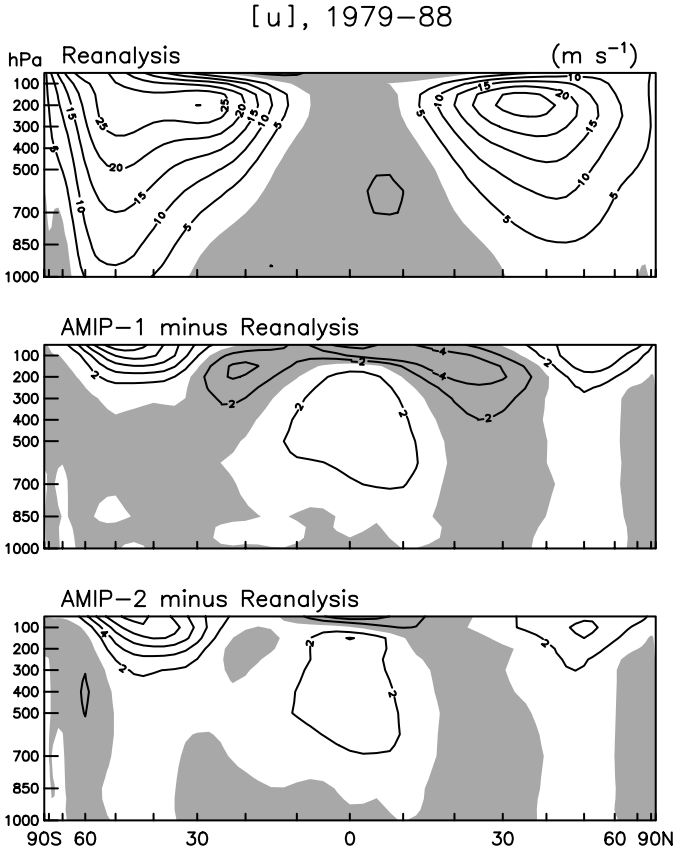

The temporal signals in the AMIP-2 AAM series are largely realistic: The median of the 20 models' 17-year seasonal signature closely resembles that of NCEP-NCAR (Fig. 3), though its annual cycle amplitude is somewhat smaller. The small underestimation of the seasonal component of AAM during northern winter, where the reanalysis falls outside spread indicated by the models' interquartile range (IQR) noted by Hide et al. (1997) continues to exist in AMIP-2. The interannual anomaly model series, like reanalysis, (Fig. 4) is strongly related to the phase of the El Nino/Southern Oscillation. AAM is greater than normal during the warm events of the period: 1983 (strong), 1987 (weak), and early 1990s (weak, but prolonged), and weaker during La Nina (1984; 1988-89). The observed AAM anomalies are somewhat better matched by the AMIP-2 median than by that of AMIP-1 in the years the experiments overlap; however, the very low value in 1984 is not fully reproduced in either.

Figure 3

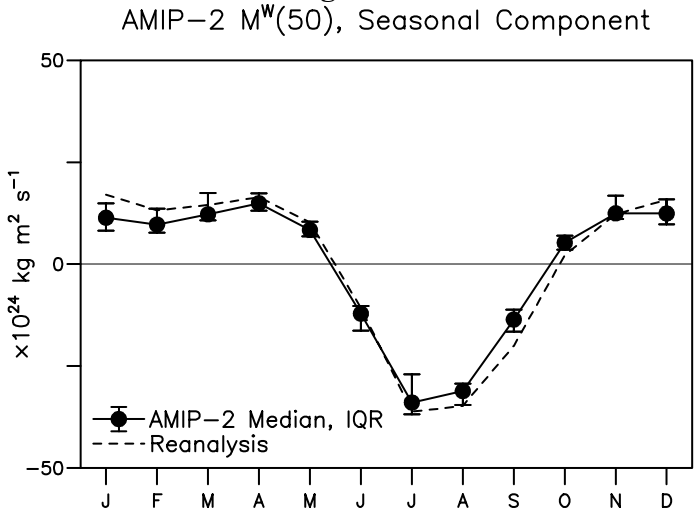

Figure 4

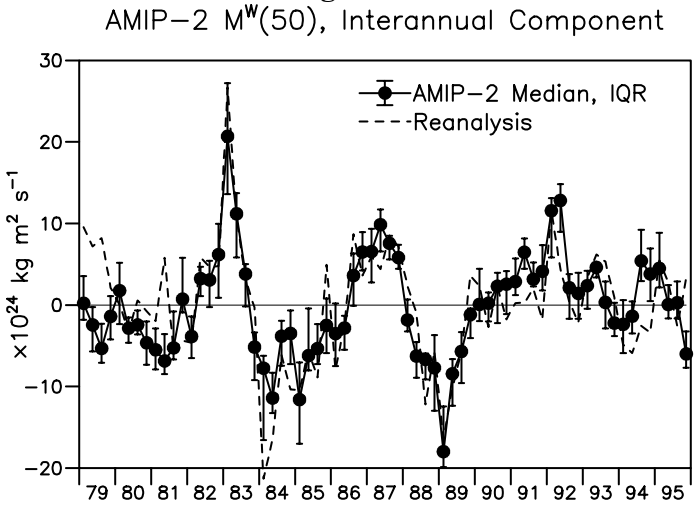

Using Taylor (2001) diagrams of correlation coefficient/standard deviation, we show the rms error levels in both the seasonal (Fig. 5) and interannual (Fig. 6) bands. In nearly all cases, the AMIP-2 (light symbols) values are nearer reanalysis than AMIP-1 (dark symbols). Note too that model ensemble medians (numbered circles) in all cases are closer to observations than their respective members. The AMIP-2 seasonal statistic is noteworthy with model median/observations correlated at 99%, although the overall amplitude is lower, by 10%, than that of reanalysis.

Figure 5

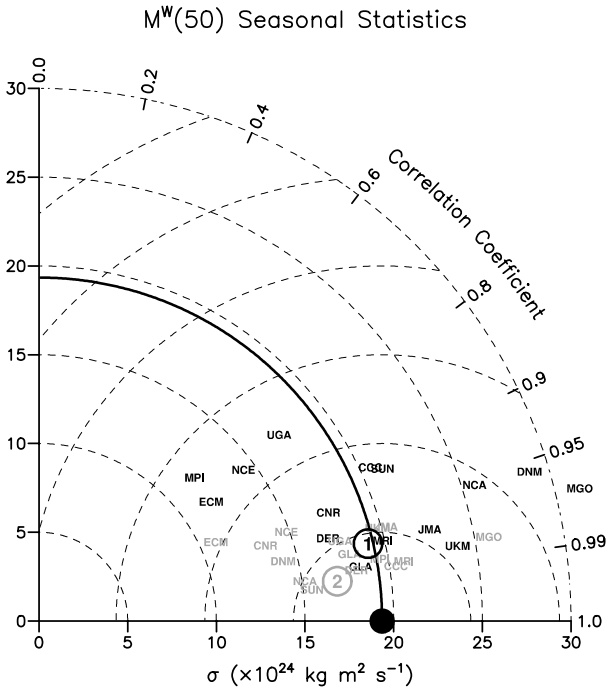

Figure 6

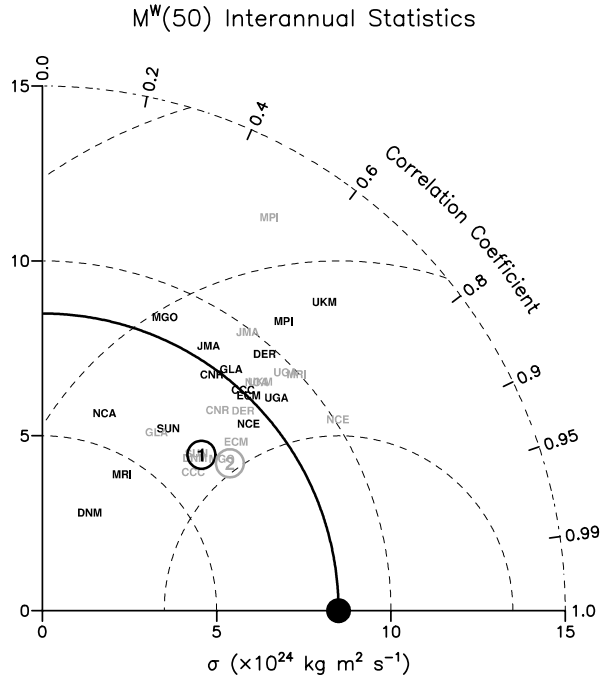

In analyzing AAM in the stratosphere (100-10 hPa; Fig. 7, top), we note that the strong semiannual signature in AAM in the reanalysis is duplicated by the AMIP-2 model median. The semiannual signature in angular momentum appears to result from annual peaks in each hemisphere six months out of phase (not shown here): although this behavior appears to be captured by the models in general, the stratospheric interannual signal, featuring a quasi-biennial signal due to tropical zonal wind anomalies, is not reproduced by the AMIP-2 models (Fig. 7, bottom). Rather, the model interannual signals appear to be a vestige of the ENSO-related tropospheric one. This signal is present in the reanalysis as well, but it is masked by the quasi-biennial behavior (in 1983-1984, for example, the signal is large when the QBO maxima and minima coincide with the El Nino/La Nina forcings (Dickey et al., 1992)

Figure 7

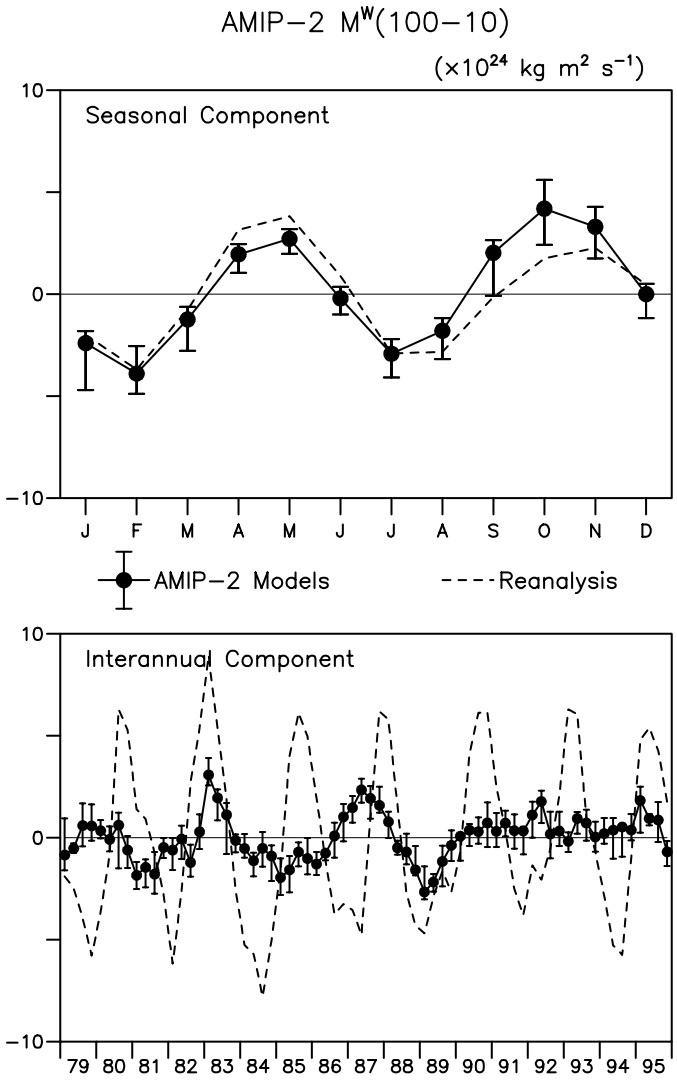

CONNECTION WITH LENGTH OF DAY

Because of conservation of angular momentum in the Earth system, changes in AAM are associated with proportional ones in l.o.d. on time scales of several days to years (Rosen et al., 1983). On longer scales, l.o.d. changes are also associated with solid Earth-fluid core coupling. To examine subdecadal scales, the first five low-order polynomials were removed from an l.o.d. series determined from a combination of several geodetic techniques (Gross et al. 2002), and the residual is compared with AAM (Fig. 8). Clearly the signals are very highly correlated, with both seasonal and interannual signals well captured.

Figure 8
AAM and Length of Day

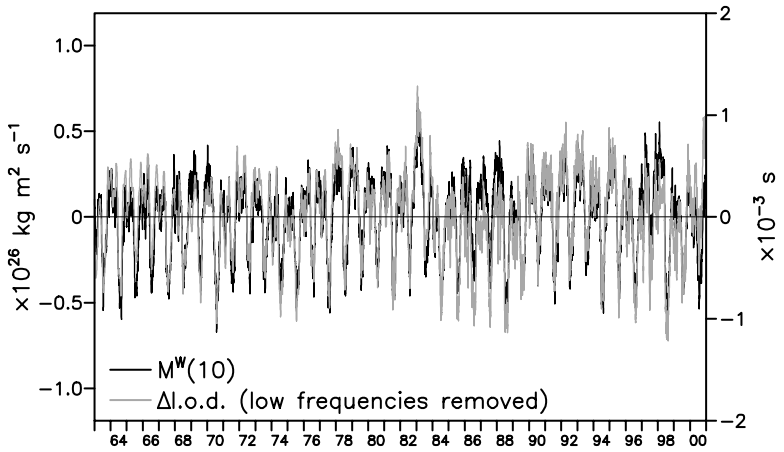

REFERENCES

Dickey, J. O., S.L. Marcus, and R. Hide, 1992: Global propagation of interannual fluctuations in atmospheric angular momentum. *Nature*, **357**, 484-488.

Gates, W. L., et al., 1999: An overview of the results of the Atmospheric Model Intercomparison Project (AMIP I). *Bull. Amer. Meteor. Soc.,* **80**, 29-55.

Gross, R., 2002: Combination of Earth orientation measurements: SPACE2001, COMB2001, and POLE 2001, JPL Pub, 02-08, 27 pp, Jet Propulsion Laboratory, Pasadena, California.

Hide, R., J. O. Dickey, S. L. Marcus, R. D. Rosen, and D. A. Salstein, 1997: Atmospheric angular momentum fluctuations during 1979-1988 simulated by global circulation models. *J. Geophys. Res*., **102**, 16423-16438.

Rosen, R.D., and D.A. Salstein, 1983: Variations in atmospheric angular momentum on global and regional scales and the length of day. *J. Geophys. Res*., **88**, 5451-5470.

Taylor, K.E., 2001: Summarizing multiple aspects of model performance in a single diagram. *J. Geophys. Res.,* **106**, 7183-7192.

ACKNOWLEDGMENTS. Grant ATM-0002688 from NSF and contract NAS5-01124 to AER supported the work reported here. The work of JOD and SLM was performed at the Jet Propulsion Laboratory, California Institute of Technology, under contract with NASA.

Use of AMIP Data Sets for FSU Superensemble Modeling of Seasonal Climate Predictions

W.T. Yun[1,2], L. Stefanova[2], T.S.V. Vijaya Kumar[2], N. Cubukcu[2], Y. S. Lee[1] and T. N. Krishnamurti

[1]Korea Meteorological Administration, [2]Florida State University

wtyun@io.met.fsu.edu

1. INTRODUCTION

A considerable amount of research is necessary to address the seasonal forecast issue. Can one provide useful guidance on whether during the coming season a given region will be wetter or drier, or warmer or colder than usual? Except for some dynamical modeling and empirical statistical studies on the seasonal guidance of ENSO scenarios, such forecasts have, in general, rather low skills. Our experience shows that Multi-Model Superensemble (MMS) skills, while better than those of a multi-model bias removed ensemble, are still generally only slightly higher than those of climatology, except for some isolated seasonal case studies. That being the state of real-time seasonal climate forecasting, it is necessary to gradually improve not only the model's data assimilation, physics, resolution, surface parameterizations, and ocean-atmospheric coupling, but also the statistical post-processing methods. This paper is one such effort to improve the forecast skills of Atmospheric General Circulation Models (AGCMs). In this paper, we use the term MMS in the sense of Krishnamurti et al. (1999, 2000). The following chapters illustrate concept of linear and non-linear MMS methods that produced best forecast and can be usefully applied.

2. DATASETS

We use datasets from several model simulations of the January 1979 - December 1988 period that were produced for the Atmospheric Model Intercomparison Project (AMIP). The observed analysis fields used in the study are based on the ECMWF reanalysis.

3. CONSTRUCTION OF LINEAR MULTI-MODEL SUPERENSEMBLE PREDICTION MODEL

Multi-Model Superensemble, developed by Krishnamurti et. al. (1999, 2000) at Florida State University, takes output from multiple operational deterministic forecasts.

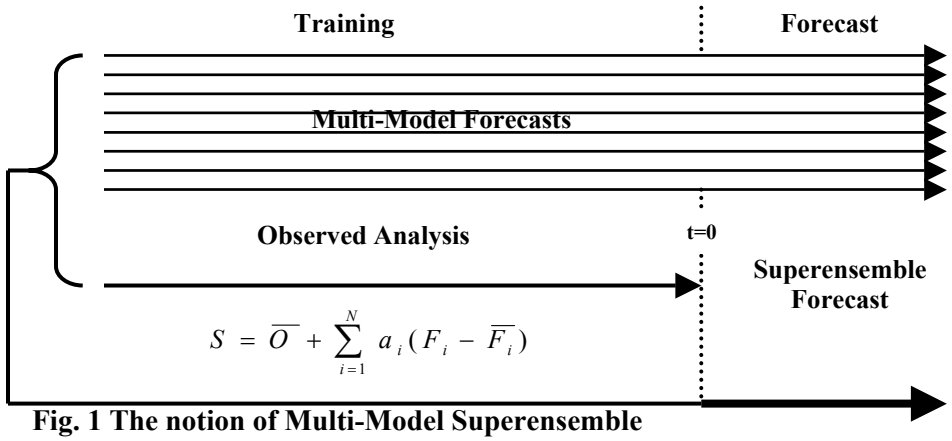

Fig. 1 The notion of Multi-Model Superensemble

Instead of treating the combination of models as an ensemble, MMS performs a statistical combination of the forecasts, based on past performance, to obtain the best deterministic forecast. The superensemble is first trained using a dataset of past forecasts and observations. The training of linear superensemble model consists of a linear multiple regression of the different models against the observations to determine the statistical weights for each model. In the forecast phase these regressions and weights are used to determine the best estimate of the forecast at each grid point from the output of all the models. For a single model this process is equivalent to making a simple bias correction at each grid-point, but for multiple models it applies bias corrections to all models and applies different weights to each model according to its past skill. The conventional multi-model superensemble forecast constructed with bias-corrected data is given by

$$S_t = \overline{O} + \sum_{i=1}^{n} a_i (F_{i,t} - \overline{F_i}) . \qquad (1)$$

Where, $F_{i,t}$ is the i^{th} model forecast for time t, $\overline{F_i}$ is the appropriate time mean of the i^{th} forecast over the training period, $\overline{O}$ is the observed appropriate time mean over the training period, a_i are regression coefficients obtained by a minimization procedure during the training period, and n is the number of forecast models involved. The MMS forecast in equation (1) is not directly influenced by the systematic errors of forecast models involved because the anomalies term $(F_{i,t} - \overline{F_i})$ in the equation accounts for each model's own seasonal climatology. At each grid point for each model of the MMS the respective weights are generated using pointwise multiple regression technique based on the training period.

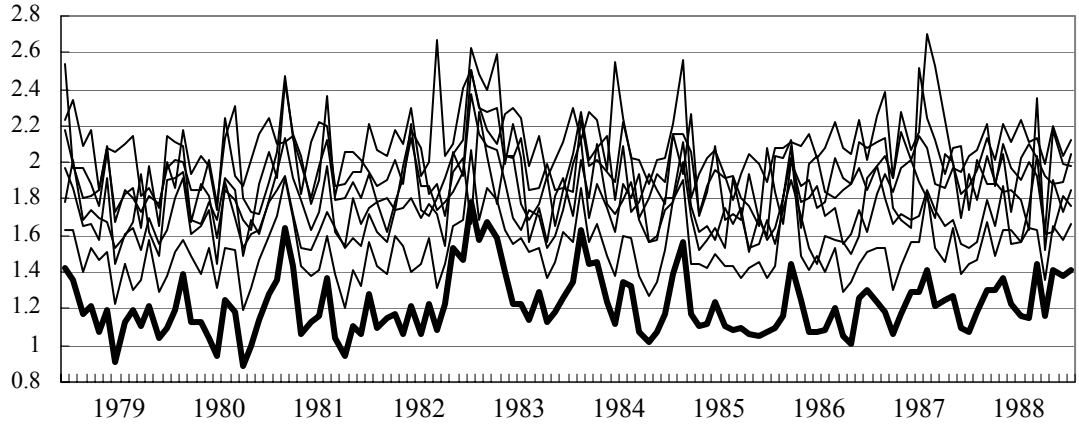

Fig. 2 Cross-validated RMS errors of global precipitation forecasts. Thin lines indicate the cross-validated RMS error of each member models and thick line is cross-validated RMS error of superensemble forecast based on SVD technique. Only the RMS errors of forecasts over the training period are shown here.

It is crucial that new techniques are developed to extract more useful forecast information from the multi-model dataset. To extract the forecast information we applied various techniques such like Singular Value Decomposition (SVD), Principal Correlation Analysis (PCA). After our experiment, the MMS model based on SVD produced best forecast under linear MMS model since SVD technique reduces the uncertainties in the solution vector of covariance matrices by computing weights. For obtaining the weights, the covariance matrix is built with the seasonal cycle-removed anomaly (F')

$$C_{i,j} = \sum_{t=0}^{Train} F'_{i,t} F'_{j,t} \ , \tag{2}$$

where, *Train* denotes the training period, and i and j – the i^{th} and j^{th} forecast models, respectively. The SVD is applied to the computation of the regression coefficients for a set of different model forecasts. The SVD of the covariance matrix C is its decomposition into a product of three different matrices. The covariance matrix C can be rewritten as a sum of outer products of columns of a matrix U and rows of a transposed matrix V^T, represented as

$$C_{i,j} = (UWV^T)_{i,j} = \sum_{k=1}^{n} w_k U_{ik} V_{jk} \ . \tag{3}$$

U and V are (nxn) matrices that obey the orthogonality relations. W is an (nxn) diagonal matrix, which contains rank k real positive singular values (w_k's) arranged in decreasing magnitude. Since the covariance matrix C is a square symmetric matrix, $C^T=VWU^T=UWV^T=C$. This proves that the left and right singular vector U and V are equal. The decomposition can be used to obtain the regression coefficients

$$x = V \cdot \left[diag(\frac{1}{w_j}) \right] \cdot (U^T \cdot \tilde{o}') \tag{4}$$

The pointwise regression model using the SVD method removes the singular matrix problem that can't be entirely solved with the Gauss-Jordan elimination method. Moreover, solving equation (4) with zeroing of the small singular values gives better regression coefficients

than the SVD solution where the small w_j's are left nonzero. If the small w_j's are retained as nonzero, it usually makes the residual $|C \cdot x - \tilde{o}'|$ larger (Press et. al., 1992). This means that if we have a situation where most of the singular values w_j's of a matrix C are small, then C will be better approximated by only a few large singular values w_j's in the sum of equation (3).

4. CONSTRUCTION OF NON-LINEAR MULTI-MODEL SUPERENSEMBLE PREDICTION MODEL USING ARTIFICIAL NEURAL NETWORK

The concept of Artificial Neural Network (ANN) models is a statistical strategy that can be used if a superposition of any forcing mechanisms leads to any effects. In comparison to multiple linear regression analysis, the main advantage is that the ANN models can catch useful information in case of non-linear cause-effect relations. The ANN learns from observations which reflect feedbacks implicitly. The disadvantage, of course, is that the physical background is neglected and results of ANN is sensitively dependent from the network architecture like the number of hidden neurons or the initialization of learning parameters. Our nonlinear Superensemble model uses the back propagation-updating rule for computing weights.

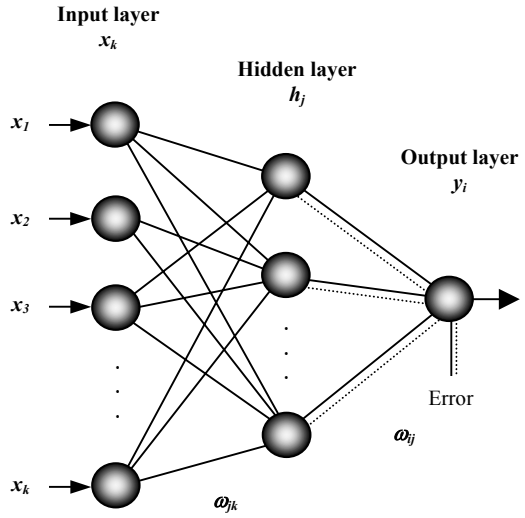

Fig. 3 A back propagation network with one hidden layer feed-forward flux (solid line) and backward directed error flux (dashed line) architecture. The ω indicates weight.

Fig. 3 illustrates a feed-forward neural network with one hidden layer, where the *j*th neuron in this hidden layer is assigned the value h_j.

$$h_j = \tanh\left(\frac{1}{T}\sum_k \omega_{kj} x_k + \theta_j\right) \tag{5}$$

Where ω_{ij} and θ_j are the weight and bias parameters, respectively. A bias term can be treated as a connection weight from a special unit with a constant, nonzero activation value. Sigmoid hidden and output units usually use a bias or threshold term in computing the net input

to the unit since networks without output biases usually ill-conditioned and harder to train than networks that use output biases. The temperature T sets the slope of the response function $g(x)=\tanh(x)$. The contribution for positive ω_{ij} is considered as an excitation and for negative ω_{ij} as inhibition.

The ANN is trained by finding the optimal values of the weights and bias parameters, which will minimize the cost function

$$E = \frac{1}{2P}\sum_{p=1}^{P}\sum_{i}(y_i^p - Y_i^p)^2 . \qquad (6)$$

It is simply the mean square error between networks output and observed data. P denotes patterns. The cost function is minimized by means of gradient descent and weight is updated according to the back propagation learning rule.

5. SUMMARY

We have introduced some concept of linear and non-linear MMS climate prediction models. In the area of seasonal climate forecasts, one of the most important questions being asked is whether it is going to be warmer, colder, wetter or dryer over the next season and where. The current state of the art leaves much to be desired for the practical utility of the seasonal forecast products. Our evaluation with stringent skill scores shows that nearly all member models perform worse than climatology. Thus, one might conclude that we are better off not running a model for seasonal forecasts since the climatology is always available. However, we did note that construction of a MMS did provide a product that was slightly superior to climatology. We strongly feel that this small edge of the superensemble can be strengthened further from various refinements of the strategies for its construction. The superensemble technique is also applied successfully to short-term numerical weather prediction, hurricane track prediction and unified model physics.

References

Krishnamurti, T. N., C. M. Kishtawal, T. E. LaRow, D. R. Bachiochi, Z. Zhang, C. E. Williford, S. Gadgil, and S. Surendran, 1999: Improved weather and seasonal climate forecasts from multimodel superensemble. *Science*, **285**, 1548-1550.

Krishnamurti, T. N., C. M. Kishtawal, Z. Zhang, T. E. LaRow, D. R. Bachiochi, C. E. Williford, S. Gadgil, and S. Surendran, 2000: Multi-model ensemble forecasts for weather and seasonal climate. *J. Climate*, **13**, 4196-4216.

Press, W. H., S. A. Teukolsky, W. T. Vettering, B. P. Flannery, 1992: Numerical Recipes in Fortran, 2nd ed., *Cambridge Univ. Press,* 963pp

TROPICAL VARIABILITY AND MONSOONS

Analysis of the West African Monsoon in Forced and Coupled Simulations

J.F. Royer, H. Douville and F. Chauvin
Meteo-France, CNRM, Toulouse
Email: jean-francois.royer@meteo.fr

Introduction

The fluctuations of the West African Monsoon and the associated interannual rainfall fluctuations are of great importance for the agriculture and economy of West African countries. Modelling studies have shown evidence of the importance and influence of surface boundary conditions (SSTs and land surface) on the atmospheric circulation and rainfall. The purpose of the present study is to document the capacity of a state-of-the-art GCM in reproducing the main characteristics of the West African monsoon by comparing a forced (AMIP type) and coupled ocean-atmosphere simulations, so as to identify the impact of the significant SST biases in the coupled simulations on the mean West African climate and on its global teleconnections.

Description of the simulations

The simulations reported here have been performed with the ARPEGE-Climat model (Déqué et al, 1994), version 3, with a T63 truncation and linear grid 128x64 points, 45 vertical levels with prognostic ozone. The land surface process scheme is the ISBA scheme. The main greenhouse gases (CO2, CH4, N20, O3, CFC-11 and CFC-12) are taken into account into Morcrette's radiation scheme, as well as the direct and indirect effect of sulfate aerosols. In the coupled simulations the ARPEGE-Climat model has been coupled to the OPA ocean GCM of IPSL/LODYC and the sea ice model GELATO (Salas y Melia, 2002). No flux correction is used in these coupled simulations. Two coupled simulations SG0 and SG1 starting in 1950 have been performed until 2100 according to scenario SRES-B2 of IPCC (Royer et al., 2002). The response of the African climate and hydrologic cycle have been reported by Maynard et al (2002) and Douville et al. (2002). Here we analyse only the first 50 years of the simulations which use the observed annual concentrations of greenhouse gases. They are very similar and differ only in the parameterization of ozone and in the albedo of clouds over sea-ice. A forced simulation (SF1) has been made with exactly the same version of ARPEGE-Climat as used in the coupled simulations, with the same concentrations of GHG, sulfate aerosol and ozone parameterization, but using as prescribed boundary conditions over the ocean the observed record of monthly mean SSTs and sea-ice from the Reynolds analysis over the period 1960-1999. An additional forced simulation (FC1) has been done with SSTs from the coupled simulation (SG0) over 1980-1993 for comparison.

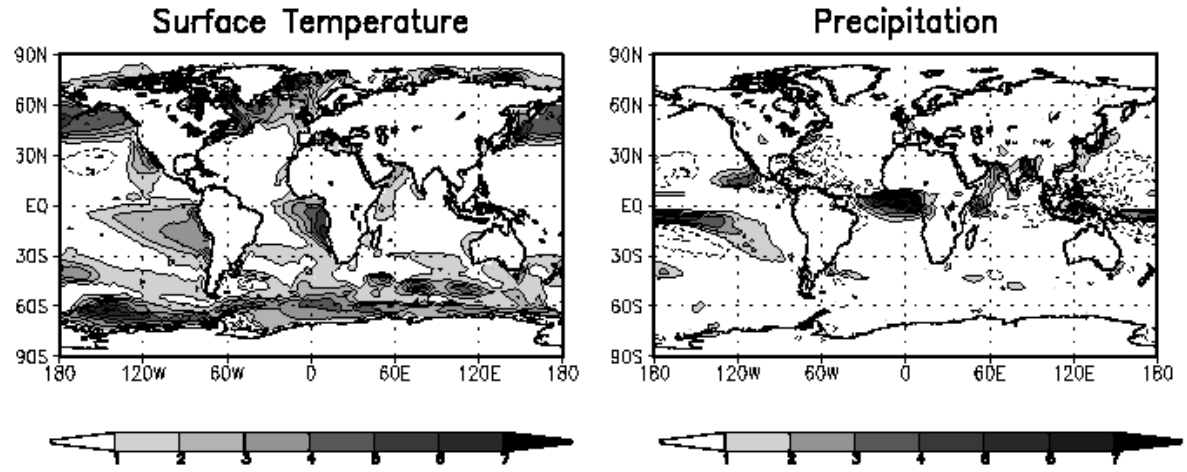

Figure 1: Difference between the coupled simulation (SG0) and the forced simulation (SF1) for sea surface temperature in K (left) and precipitation in mm/day (right) in boreal summer (June July August). Negative values are represented by dashed isolines

The surface temperature from the coupled simulation SG0 compared to the forced simulation (SF1) shows the SST bias of the coupled model (Figure 1 a). In summer the coupled model has a positive SST bias in the high latitudes of the northern hemisphere and around the Antarctic, and a wedge-shaped anomaly south of the equator in the tropics in the eastern parts of the Pacific, which looks similar to a warm El Nino anomaly, and in the tropical Atlantic in the Gulf of Guinea. These positive anomalies in the coupled model appear to be related to the overall lack of stratocumulus clouds over the oceans. This difference in the SSTs of the coupled and forced simulations produces regional differences in the distribution of precipitation (Figure 1 b), which is decreased in the western part of the Atlantic and Pacific oceans in the northern hemisphere. The precipitation maximum associated with the ITCZ is intensified south of the equator in the Pacific and over the warm anomaly over the Gulf of Guinea.

Validation of the summer climatology over Africa

The mean climate for the summer monsoon season (JJAS) for the 30-year mean 1970-1999 in the different simulations has been computed and validated by comparison to observed databases (NCEP reanalyses, CRU climatology). Besides the mean climate the interannual variability, represented by the interannual standard deviation has been studied. The main conclusions from the validation of the mean summer monsoon are the following. The model produce a rather realistic geographical distribution of the mean fields over Africa, with some biases in certain fields such as a larger lower tropospheric temperatures over the desert areas, an excessive northward penetration of the monsoon rainfall over the orographic areas of the central Sahara, and a large SST bias in the Gulf of Guinea in the coupled simulation has an impact on the position of the ITCZ which stays over the ocean and extends northwards instead of shifting northward. This can be seen in the annual cycle of the precipitation over the longitude band 10°E-10°W (figure 2) in which the “jump” in the precipitation maximum from 5°N to 10°N at the end of June observed in the CRU climatology is reproduced by the model forced by the observed SSTs (SF1), while the coupled model (SG0) and the model forced with its SSTs (FC1)

produce a broader ITCZ and a more intense precipitation maximum which moves gradually northward. The annual cycle over the Sahel region (figure 3) is well reproduced, with a small overestimation of the surface temperature, and a small underestimation of the maximum precipitation, with precipitation increasing too early in June.

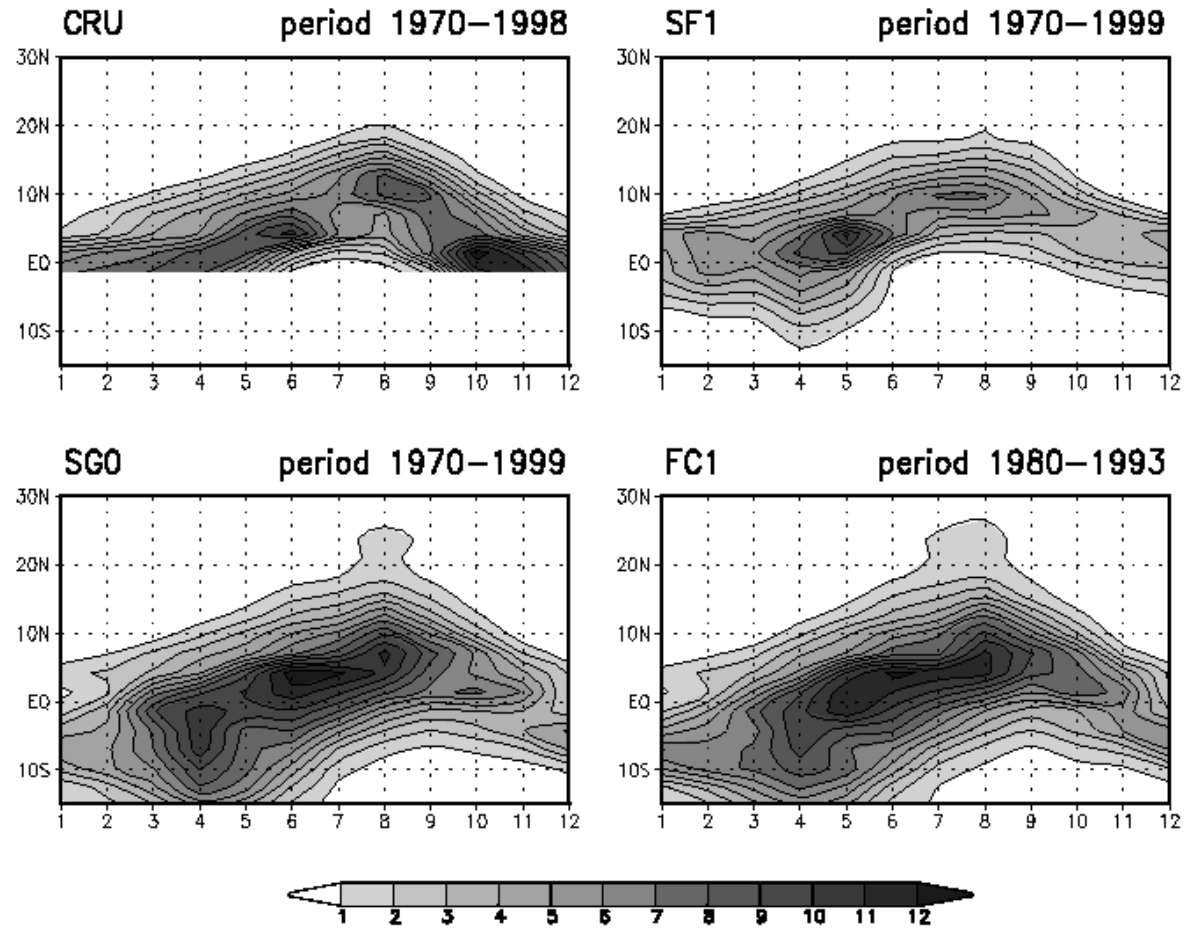

Figure 2: Distribution as a function of month (horizontal scale) and latitude (vertical scale) of the annual cycle of monthly mean precipitation (mm/day) averaged over 10°W-10°E, for the CRU climatology, the forced simulation SF1, the coupled simulations SG0 and the forced simulation FC1.

Interannual variability: Correlations of the WAMI index

The interannual variability of the African monsoon has been studied by computing the correlation fields of several indices with various large-scale fields describing various aspects of the atmospheric circulation and climate. As indices of precipitation we have used the Sudan Sahel Rainfall (SSR) index averaged over [10°N-20°N, 20°W-40°E], and the West African Monsoon Index (WAMI) defined as the vertical shear between 850 hPa wind speed and 200 hPa zonal wind over [20°W-20°E, 3°N-13°N] (Fontaine et al, 1995). The WAMI index is a dynamical index which is well correlated with monsoon precipitation over Sahel. The correlation patterns of both the SSR and WAMI indices show similar coherent large-scale structures in the

coupled and forced simulations which underscore the link between the African monsoon precipitation and the global tropical circulation. As an example we show on figure 4 the correlation map of WAMI with the sea level pressure over the globe. The correlation pattern for the NCEP reanalysis shows a characteristic distribution very similar the Southern Oscillation pattern showing positive correlation with pressure in the East Pacific and negative ones over the West Pacific, Indian Ocean extending over Africa and the North Atlantic. A similar pattern is found in the simulations but with weaker correlations especially with the East Pacific. This points out to weaker ENSO correlations with African circulation and precipitation in the simulations, which is confirmed by the correlation maps with the Southern Oscillation Index (SOI).

Figure 3: Annual cycle over the Sudan Sahel region [10-20oN, 20oW-40oE] for temperature at 2m in oC (left) and precipitation in mm/day (right) for CRU climatology (solid line with filled circles), coupled simulations SGO and SG1 (solid and dotted lines) and forced simulation SF1 (solid line with empty circles)

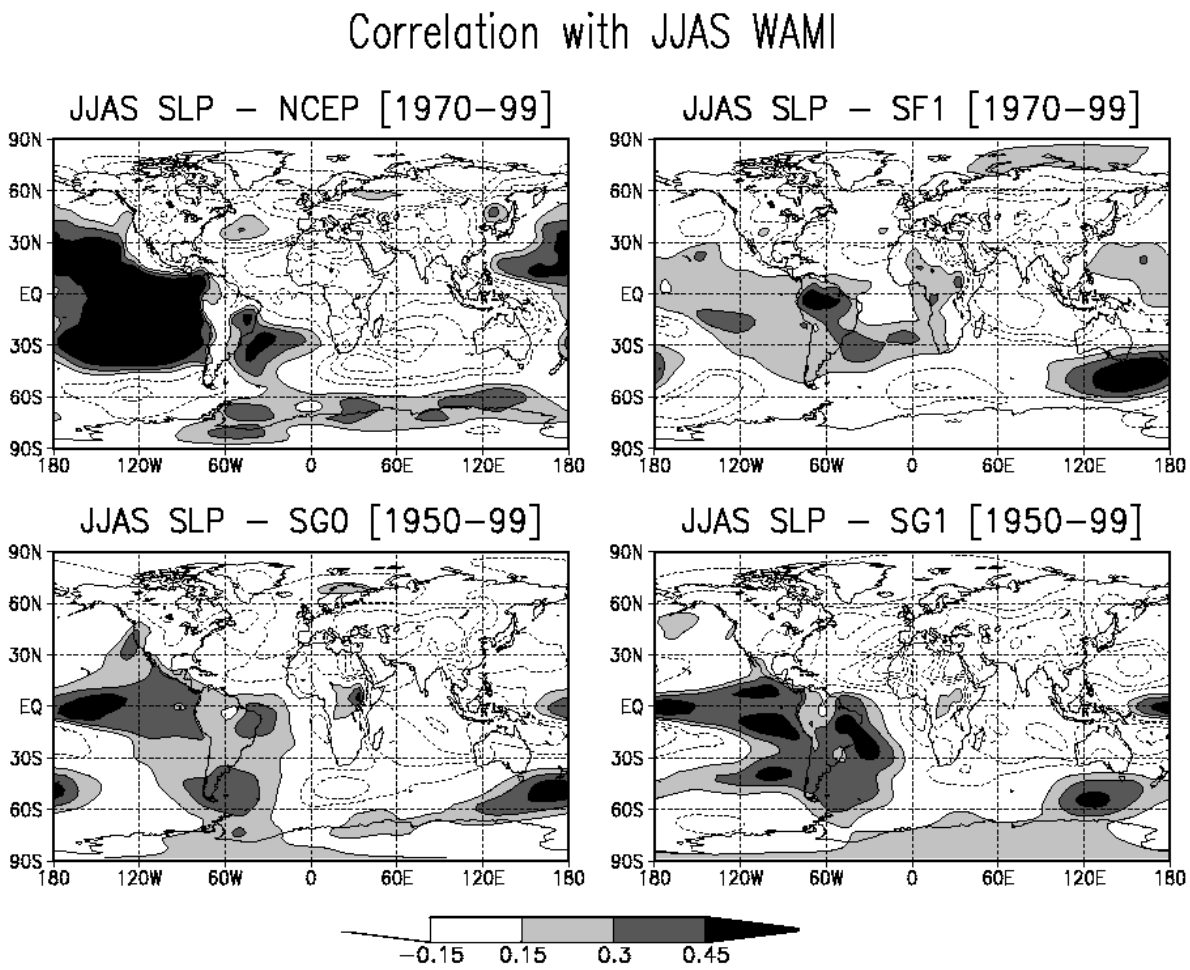

Figure 4: Correlation coefficients computed over the 40 year period 1950-1999 between the WAMI index and sea level pressure averaged over the 4 months June July August September for the NCEP reanalysis (top left) , the forced simulation SF1 (top right) and the coupled simulations SG0 and SG1 (bottom).

Conclusions

Overall the seasonal evolution and distribution patterns of the forced and coupled simulation reproduce the main features of the West African monsoon. The coupled simulations have a strong warm SST bias in the Gulf of Guinea. This produces a permanent presence of convection over the ocean with a broadening and northward extension of the ITCZ during the summer monsoon. Despite this bias in precipitation over the ocean the seasonal cycle over the subsaharan continental area appears realistic. The correlation patterns of the WAMI index of Sudan Sahel rainfall with various large scale fields are broadly reproduced. However the influence of ENSO is less prominent both in the forced and coupled simulations than in the observations. The El Nino in the coupled simulation is more frequent and more narrowly concentrated around the equator than in the observations. The Sahelian rainfall in the coupled simulation is mainly responding to Atlantic SST patterns which modulate the input of moisture in the monsoon flow. Some interdecadal variability of the correlations is also apparent. The correlations appear slightly more stable in the coupled simulations, but this may be due in part to the larger biases in the SST patterns.

References:

Déqué, M., C. Dreveton, A. Braun and D. Cariolle, 1994: The ARPEGE/IFS atmosphere model: A contribution to the French community climate modelling. Climate Dyn., 10, 249-266.

Douville H., F. Chauvin, J.F. Royer, D. Salas y Mélia, S. Tyteca, 2002 : Sensitivity of the hydrological cycles to increasing amounts of greenhouse gases and aerosols. Climate Dynamics, 20, 45-68.

Fontaine, B., S. Janicot and V. Moron, 1995: Rainfall anomaly patterns and wind field signals over West Africa in August (1958-1989). J. Climate, 8, 1503-1510.

Maynard K., J.F. Royer, F. Chauvin, 2002 : Impact of greenhouse warming on the West African summer monsoon. Climate Dynamics, vol 19, pp 499-514.

Moustaoui M., J.F. Royer, F. Chauvin, 2002 : African easterly wave activity in a variable resolution GCM. Climate Dynamics, vol 19, pp 289-301.

Royer J.F., D. Cariolle, F. Chauvin, M. Déqué, H. Douville, R.M. Hu, S. Planton, A. Rascol, J.L. Ricard, D. Salas y Mélia, F. Sevault, P. Simon, S. Somot, S. Tyteca, L. Terray, S. Valcke, 2002: Simulation des changements climatiques au cours du 21-ème siècle incluant l'ozone stratosphérique (Simulation of climate changes during the 21-st century including stratospheric ozone). Comptes Rendus de Geoscience, vol 334, n° 3, pp 147-154.

Salas y Mélia D., 2002 : A global coupled sea ice-ocean model. Ocean Modelling, vol 4, n° 2, pp 137-172.

Ackowledgements: This study has been supported by European Union 5th Framework Programme (PROMISE contract EVK2-CT-1999-00022)

Water and Energy Budgets in the JMA AMIP Simulation

Hiroto Kitagawa
Japan Meteorological Agency
kitagawa@naps.kishou.go.jp

Water and energy budgets produced in the AMIP simulation with the JMA Global Spectral Model (GSM) are validated through comparisons with the ECMWF re-analysis (Gibson et al. 1997) and observations. The validation was done focusing on a representation of the water and energy budgets and their seasonal cycles in the model, and a reproduction of their interannual variabilities in the tropics.

The model used for the AMIP experiment has T63 resolution in the horizontal and 30 vertical levels, and its vertical domain extends from surface to 1hPa. The simulation was performed according to the AMIP experimental specification. The model includes following physical parameterizations; orographic GWD, SW/LW radiations, the Arakawa-Schubert cumulus convection, diagnostic cloud cover and water content, PBL processes based on the local-K approach and the Simple Biosphere land surface model.

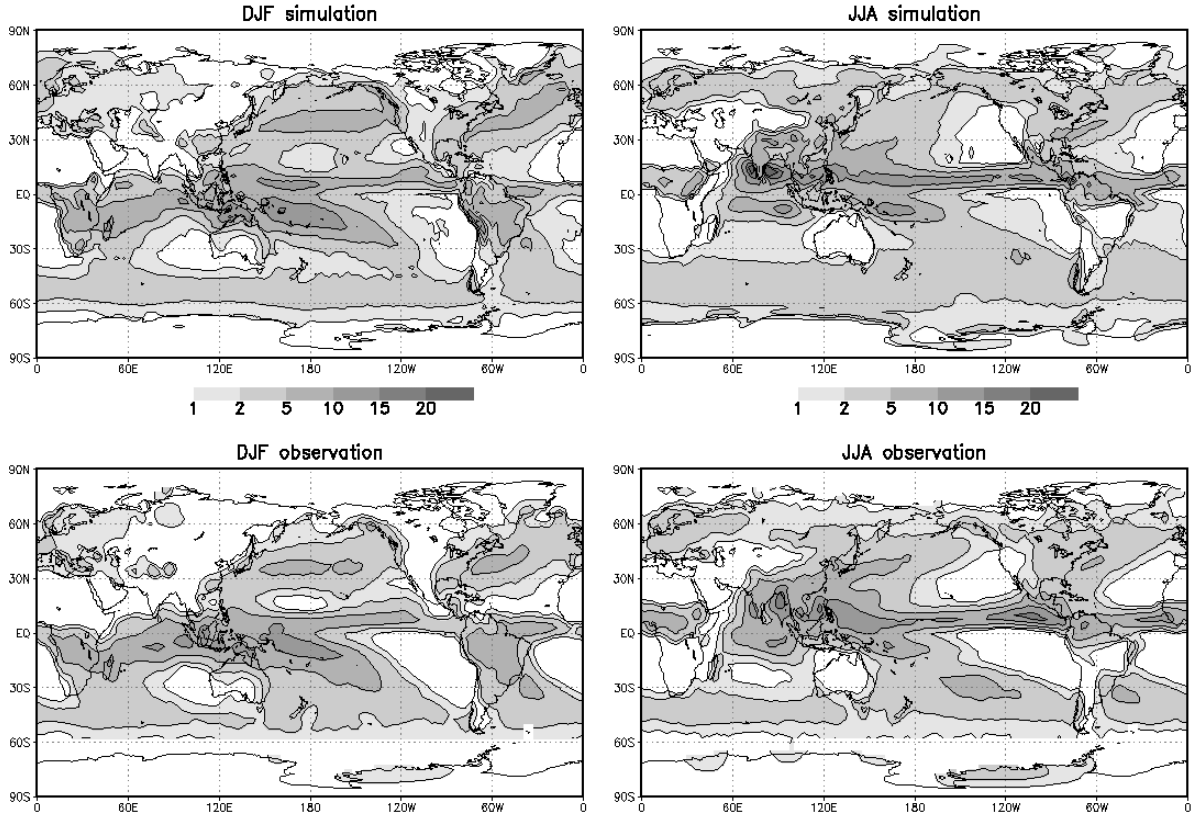

Fig. 1 DJF/JJA mean total precipitation. Simulated precipitations (upper) and the Xie-Arkin observational climatologies (lower) for DJF (left) and JJA (right). Contours are 1, 2, 5, 10, 15, 20mm/day.

Fig. 1 shows geographical distributions of total precipitation simulated by the model and the observational precipitation climatologies derived from the CPC Merged Analysis of Precipitation (CMAP) database (Xie and Arkin 1997). The precipitation and its seasonal cycle are overall well reproduced in the simulation although some systematic errors are seen in the specified regions. For example, there is a failure of model precipitation associated with the Indian summer monsoon. The model also tends to express a splitted (double) ITCZ precipitation, and somewhat overestimates precipitations over the Pacific and Atlantic wintertime storm tracks where a large amount of convective (sub-grid scale) condensation is calculated in the model.

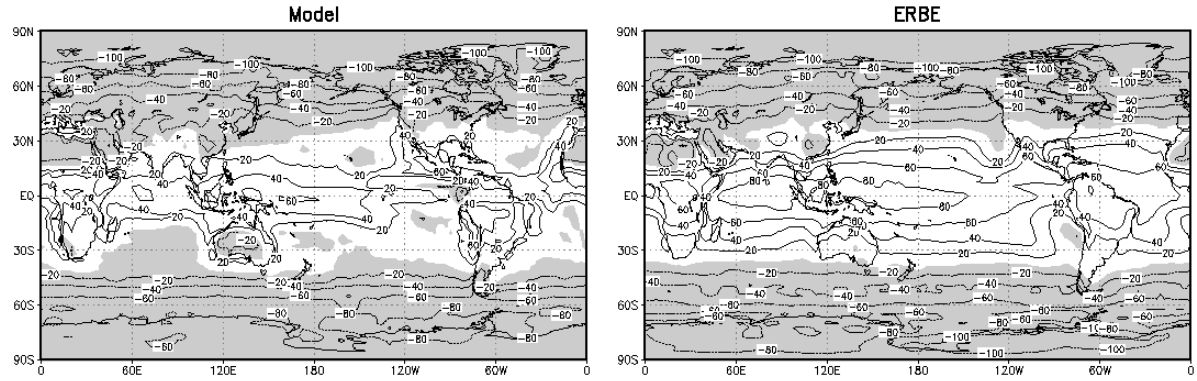

Fig. 2 Annual mean (1987-1988) TOA net downward radiation. Simulated field (left) and the ERBE observation (right). Contours are every 20W/m^2 and negatives in shaded.

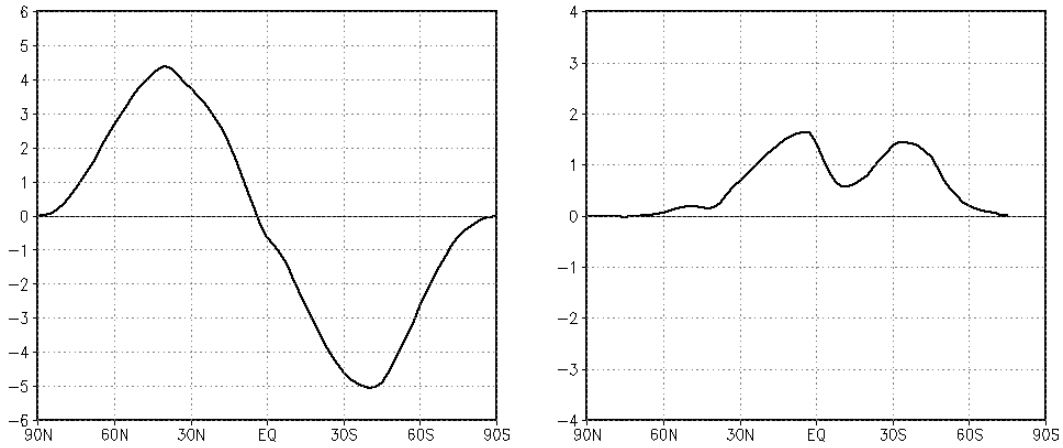

Fig. 3 Annual mean global northward meridional energy transport implied by the simulation. Atmospheric transport (left) and oceanic transport (right). Unit is in 10^{15}W.

On earth's energy budgets, the model realistically simulates both net surface energy exchange and TOA net energy balance. Here the simulated TOA energy (radiation) balance is compared with the Earth Radiation Budget Experiment (ERBE) data (Barkstrom 1984). In low-latitudes, except for the marine stratocumulus areas, net downward radiative flux is substantially underestimated by the model because of excessive shortwave reflections due to too much ice

water content diagnosed in high-level clouds (Fig. 2). This deficiency also significantly affects a representation of meridional gradients in the simulated surface heat flux field, and as a consequence, an oceanic meridional energy transport implied by the simulation seems to be systematically too small (Fig. 3).

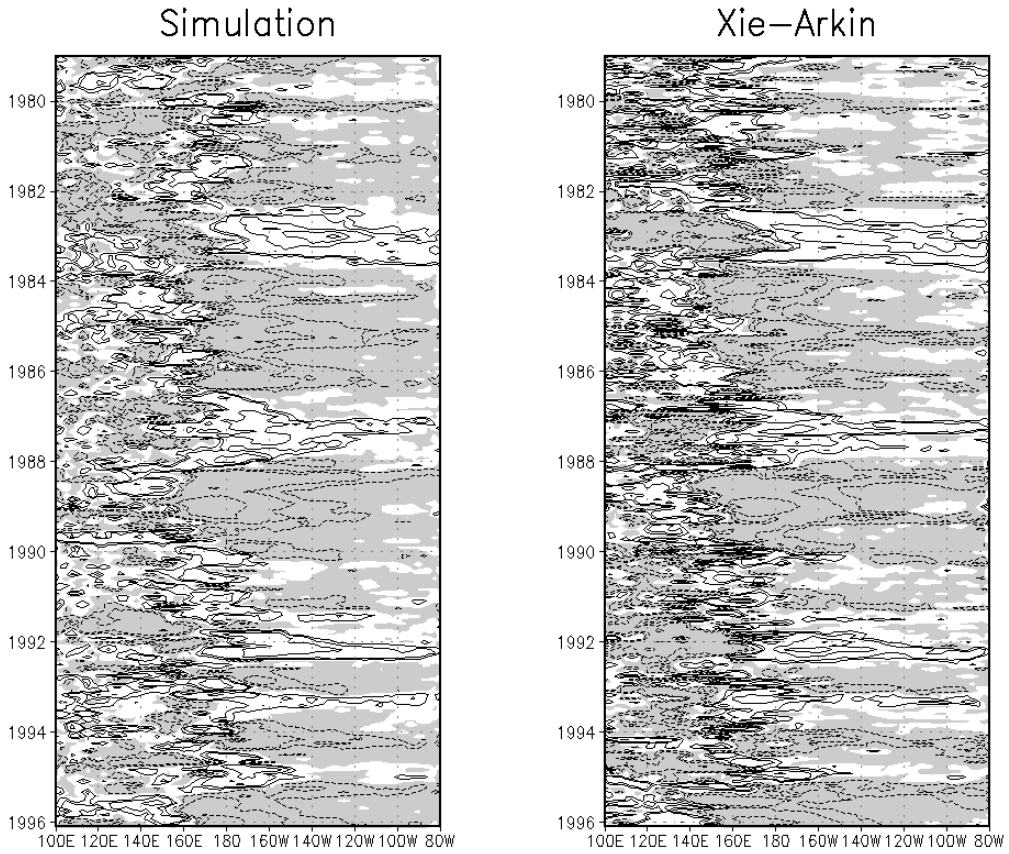

Fig. 4 Hovmoeller diagrams of monthly mean precipitation anomaly in the tropical Pacific. Simulated anomalies (left) and the anomalies from the Xie-Arkin data (right). Contours are 1, 2, 5, 10, 15mm/day and negative anomalies in shaded.

In the equatorial Pacific, the interannual variations in precipitation (Fig. 4) and OLR (not shown) are reasonably reproduced by the model, corresponding to the major El Nino and La Nina events. This suggests that the model can accurately represent the responses of local convective activity to the SST changes in the tropics. However, interannual variations in the simulated surface heat flux, total cloudiness and surface wind stress differ a little from those in the re-analysis (not shown). This discrepancy may come from insufficient reproducibilities of the model for an atmospheric boundary layer structure and accompanied low-level clouds and for a response of large-scale atmospheric circulation and flow to the SST variation.

ACKNOWLEDGEMENTS

The author gratefully thanks ECMWF and its re-analysis project for use of the re-analysis product (ERA15) and Drs. P. Xie and P. A. Arkin for use of the CMAP dataset.

REFERENCES

Barkstrom, 1984: The Earth Radiation Budget Experiment (ERBE). *BAMS*, **65**, 1170-1185.
Gibson et al., 1997: ERA description, ECMWF Re-Analysis Project Report Series, 72pp.
Xie and Arkin, 1997: Global Precipitation: A 17-Year Analysis. *BAMS*, **78**, 2539-2558.

Potential Intensity of Tropical Cyclones in a Subset of AMIP 2 Models: Results from Diagnostic Subproject 31

Kendal McGuffie[1] and Greg J. Holland [2]

[1]Department of Applied Physics
University of Technology, Sydney
PO Box 123, Broadway NSW 2007
[2]Aerosonde Ltd
Melbourne

Introduction

Thermodynamic estimates of tropical cyclone intensity have provided a good tool for both understanding and predicting the factors that affect the intensification of tropical cyclones. These estimates employ the available energy existing in the atmosphere, together with that which becomes available from air-sea interactions, to provide an objective estimate of the maximum intensity that can be achieved. Published approaches either view tropical cyclones as a heat engine (Emanuel 1988, 1999) or treat them as a balance between moist adiabatic heating and buoyancy forcing (Holland, 1997). Using observed monthly SST and real-time radiosonde sounding data near the tropical cyclones location, Tonkin *et al.* (2000) evaluated both Emanuel and Holland's Maximum Potential Intensity (MPI) models against observed maximum intensity for a large number of tropical cyclones. Results obtained by Tonkin et al (2000) suggest that the thermodynamic model provides a good estimation (+- 20 hPa) of maximum intensity achieved by tropical cyclones. Holland's (1997) approach was used by Henderson-Sellers *et al* (1998) for estimating the potential changes of cyclone intensity associated with anthropogenic climate change. The thermodynamic model of tropical cyclone development therefore provides an objective method of evaluating the climatology of the MPI and any changes of MPI that might be caused by climate change. AMIP II experiments provide good opportunities to both extend the work of Henderson-Sellers *et al.* (1998) and to evaluate additional parameters that may inhibit intensification.

Maximum Potential Intensity (MPI) models work on the principle that it is possible to specify the available energy for the intensification of a tropical cyclone in the atmosphere/ocean system. Given a set of environmental conditions, it is possible to evaluate analytically the "worst case" cyclone. Two such models currently exist, and they provide similar answers for a given environmental condition and are summarised in Emanuel (1999) and Holland (1997). These models can be used to place a physical bound on the maximum intensity that can occur in a tropical cyclone.

Schade (2000) summarises two theoretical frameworks for calculating the maximum potential intensity of tropical cyclones: static theories and dynamic theories. Dynamic theories such has that of Emanuel (1988), where the assumption of slantwise convective neutrality leads to a thermodynamically defined outflow consider the motion of a parcel along trajectories through the storm and can be considered loosely as a 'heat engine' approach. In contrast, static theories derive the MPI based on the thermodynamic structure of the environment within which the storm develops, along with some knowledge of the likely thermal structure of the eye and

eye-wall. Earliest appearances of this static approach are Miller (1958), though it has recently been enhanced by Holland (1997) and tested by Tonkin *et al.* (2000). Miller's (1958) approach is based on a parameterisation of the eye-region subsidence, whereas Holland's development of this approach utilises a separate development of warming through ascent in the eyewall and through descent in the eye (which develops if the ascent produces a pressure drop beyond a defined threshold).

Analysis

The AMIP 2 output fields used in the computation of maximum potential intensity (or simply potential intensity) are shown in Table 1. This study used only monthly average data. Eleven 'points' were selected corresponding to the regions of maximum tropical cyclone activity in the major tropical cyclone basins of the world. As there is a range of resolutions in the AMIP models, the thermodynamic models of Holland and Emanuel were applied to the nearest model grid point and values for the MPI were calculated for each month of the 17 years. Both models have been compared with observational radiosonde data and have been found to give reasonable characterisations of tropical cyclone intensity for a range of geographic locations (Tonkin *et al.,* 2000). The following AGCMs were examined in this study: ccsr-98a, cnrm-00a, cola-00a, dnm-98a, ecmwf-98a, gla-98a, jma-98a, ncar-98a, ncep-99a, pnnl-97a, sunya-99a, ukmo-98a, uiuc-98a, ugamp-98a, yonu-98a.

Table 1: AMIP 2 data required for calculation of hurricane potential intensity.

Upper-air data:	Air temperature
	Specific humidity
Surface data:	Ground temperature
	Surface pressure

Results

The results of the MPI analysis was analysed on the basis of seasonality of tropical cyclone intensity together with interannual variability. Figure 1 shows the results of the MPI analysis of the seasonal cyclone of MPI for model grid points near a nominal location roughly 200km NW of Darwin, Australia. An important characteristic of the results is the failure of one of the potential intensity schemes for some of the AGCMs. Most AGCMs give a reasonable pattern of potential cyclone intensity (corresponding with the observed cyclone season), but some AGCMs show substantial disagreement in the predicted intensity for the two models. There is no clear indication of a 'best' model of thermodynamic intensity. Note that the relative characteristics of the two schemes can be reversed for adjacent AGCM plots.

In the simulation of variability, it was much easier to pick poorly performing models. Some models display very little variability and in some cases, the expected influence of ENSO on MPI in the Australian Region was reversed. Based on preliminary comparisons with available data, most AGCM-MPI combinations exhibited variability consistent with observations of cyclone activity. The reasons for some notable exceptions are currently being explored. The

MPI schemes of Holland and Emanuel provide a useful independent validation of one aspect of the tropical simulation of AMIP AGCMs.

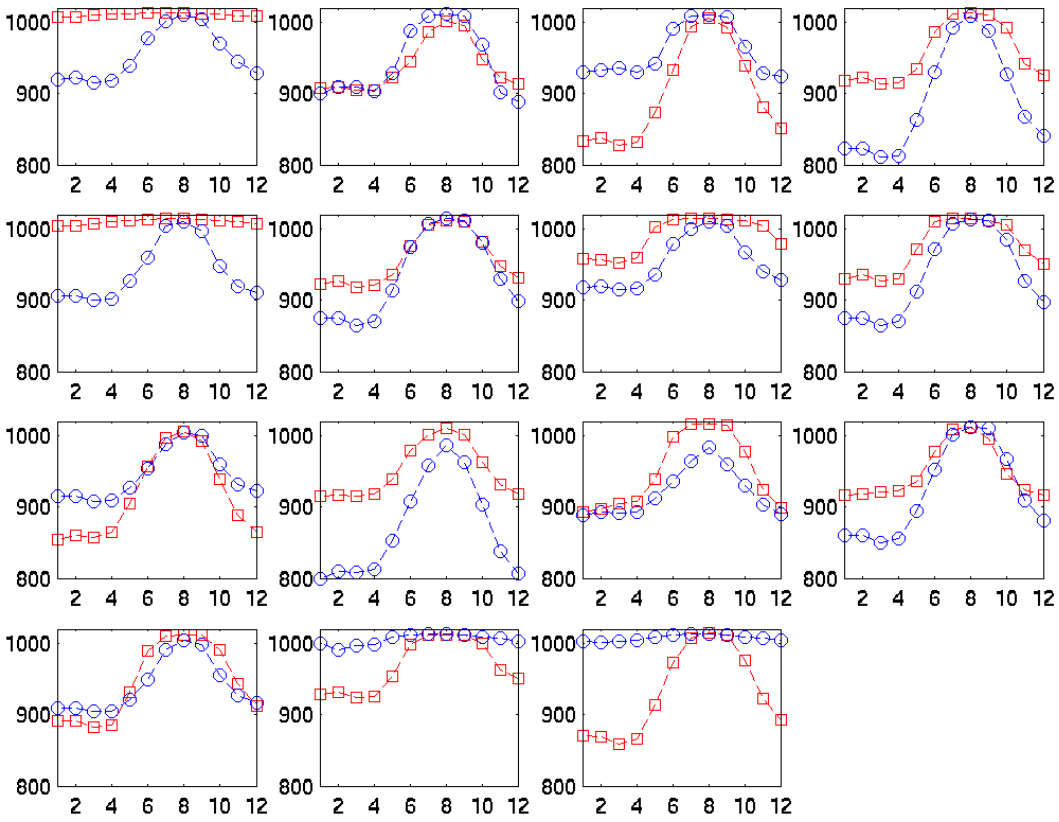

Figure 1: Mean Potential intensity of tropical cyclones in (hPa) as a function of month (1-12) for 15 AMIP2 AGCMs (not in order listed above) computed using the potential intensity models of Emanuel (squares) and Holland (circles). The upper bound of the MPI is the mean surface pressure.

References

Camp, J.P. and Montgomery, M., 2001, Hurricane maximum intensity: past and present, *Mon. Weath. Rev.,* **129**, 1704–1717.

Emanuel, K.A., 1988, The maximum intensity of tropical cyclones, *J. Atmos. Sci*, **45**, 1143–1155.

Emanuel, K.A., 1999 Thermodynamic control of hurricane intensity, *Nature*, **401**, 665–669.

Henderson-Sellers, A., Zhang, H., Berz, G., Emanuel, K., Gray, W., Landsea, C., Holland, G., Lighthill, J., Shieh, S.-L., Webster, P. and McGuffie, K. 1998. Tropical cyclones and global climate change: A post-IPCC assessment. *Bulletin of the American Meteorological Society* **79**: 19-38.

Holland G.J., 1997, The maximum potential intensity of tropical cyclones, *J. Atmos. Sci*. **54**, 2519-2541

Miller, B.I., 1958, Tropical cyclone intensity and sea surface temperature, *J. Meteor*., **15**, 184–195.

Schade, L.R., 2000, Tropical cyclone intensity and sea surface temperature, *J. Atmos. Sci.,* **57**, 3122–3130.

Tonkin, H., Holland, G.J., Holbrook, N. and Henderson-Sellers, A., 2000, An evaluation of thermodynamic estimates of climatological maximum potential tropical cyclone intensity, *Mon. Weath. Rev.,* **128**, 746–762.

The Australasian Region Wintertime Double Jet as Simulated in AMIP2 Models

Mark Harvey and Bryant McAvaney
Bureau of Meteorology Research Centre, Melbourne , Australia

Abstract

In this study, we are examining the ability of models participating in AMIP2 to simulate the behavior of the Australasian region wintertime split jet. Results are intercompared and compared with observations. Most models do not successfully simulate a realistic wintertime double jet. The subtropical component tends to be too intense. The polar component of the double jet, conversely, tends to be too weak. The deficiency in the strength of the subtropical jet appears to be related to in some models to difficulties in simulating diabatic processes in the tropics. An added difficulty in simulating a realistic subtropical jet that is evident in AMIP2 models concerns the simulation of eddies. Both eddy heat and momentum fluxes tend to be overstated, particularly in midlatitudes.

Introduction

A distinctive feature of the climatological flow in the Southern Hemisphere troposphere is the existence of a split jet in the Australasian region during winter (refer to figure 1). The split jet consists of a subtropical component between 25^{o} and 30^{o} S, and a poleward branch centred on 60^{o} S. The subtropical component of the jet extends zonally across the Australian continent and across the central South Pacific. The polar front jet (PFJ) curves poleward to the south of the Australian continent before tracking the Antarctic coastline. The subtropical jet (STJ) is a quasi-steady feature throughout the winter months, whilst the polar front jet (PFJ), exhibits a greater degree of variability in strength. Between the two jets lies a region of weak westerlies.

The dominant mechanism maintaining the subtropical component of the double jet system appears to be cross-equatorial divergent outflow from the Southeast Asian monsoon that is then fed into the subtropical jet via Coriolis torques. The mechanism responsible for the polar front jet is less clear. Bals-Elsholz *et al*, 2001, relate the variability of the polar front jet to periodic cold surges from the Antarctic region. They further relate a strong PFJ to cold air being bottled up over the Antarctic region, hence increasing the meridional tropospheric thickness gradient between high and low latitudes and so strengthening both the thermal wind and the PFJ.

The study introduced here has as its focus an examination of the ability of models submitted to AMIP2 to reproduce the physics of the subtropical jet (and in particular the wintertime double jet). This work comprises an AMIP2 diagnostic subproject. Monthly data from 16 models is used in the course of this study, with results intercompared and compared with both the Bureau of Meteorology Atmospheric Model (BAM) as well as "observations" in the form of NCEP reanalyses.

Data and Methodology

Data used in this study have come from three sources, these being (i) output from models participating in AMIP2, (ii) output from the Bureau of Meteorology Atmospheric Model (BAM) and (iii) NCEP reanalyses.

The AMIP2 data employed in this study has been monthly fields of zonal and meridional winds, temperature and outgoing longwave radiation obtained via ftp from the Program for Climate Model Diagnosis and Intercomparison (PCMDI) database. Data from some 16 models were downloaded and used in preparation of the statistics presented here.

The BAM run utilised here for the purpose of comparison with AMIP2 models and observations was an AMIP1 experiment (Gates, 1995). Initial conditions were taken from the end of a 3 year integration forced with 10 year mean sea surface temperatures and sea ice extents, varying seasonally. These boundary conditions were the mean from the ten years of the AMIP experiment.

NCEP-NCAR reanalyses were used as "observations" in this study for the purpose of assessing the ability of models to simulate the Australasian region split jet. The reanalyses are a global dataset on a 2.5 degree latitude-longitude grid. 17 years of daily data from 1979-96 were utilised.

Results

Polar stereographic plots of JAS mean zonal wind for the Australasian region at 500hPa are presented in Figure 1.The AMIP2 mean subtropical component of the double jet has a maxima to the northeast of New Zealand which compares favourably to observations. A minima in the New Zealand region with a further zone of weak westerlies poleward of New Zealand is also apparent in the AMIP2 mean. However, these features are less intense than is seen in observations. BAM performs more poorly than the AMIP2 mean when compared to observations. The BAM climatological subtropical component of the jet is too weak and is displaced to the east. The polar front jet is too weak and also very poorly defined. **T**he region of weak westerlies in the New Zealand region is similarly ill defined in BAM.

Given that the jets must reflect the underlying thermodynamic structure of the atmosphere, we will now examine plots of the meridional temperature gradient at 500hPa for JAS. In figure 2 we note that the AMIP2 mean has a too intense baroclinic zone extending from the central South Indian ocean over Australia. This reflects the too-strong subtropical jets that are typical of the majority of subtropical jets simulated by individual AMIP2 models (not shown here) which tend to vary quite markedly in their geographical location. The AMIP2 mean subtropical jet (refer to Figure 1) performs better than any individual model in terms of both strength and location. BAM (Figure 2), however, is one of several models with particularly weak baroclinicity over Australia itself and this is reflected in subtropical jets that are displaced eastward from observations. The baroclinic zone at the periphery of the Antarctic continent south of Australia that is seen in NCEP reanalyses is not simulated well in most models. Those models that do show a region of high meridional temperature gradient in this region are those with distinct polar front jets (see Figure 2), indicating that poleward warm-air advection is a key factor in the maintenance of the polar front jet.

Mean AMIP2 JAS 500hPa U

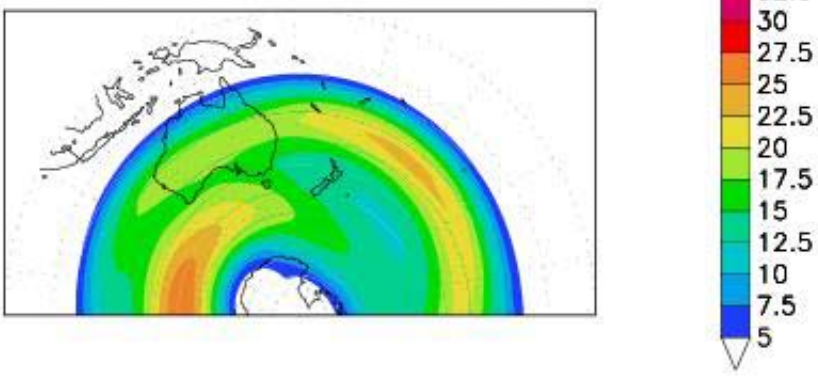

NCEP Reanalyses JAS 500hPa U

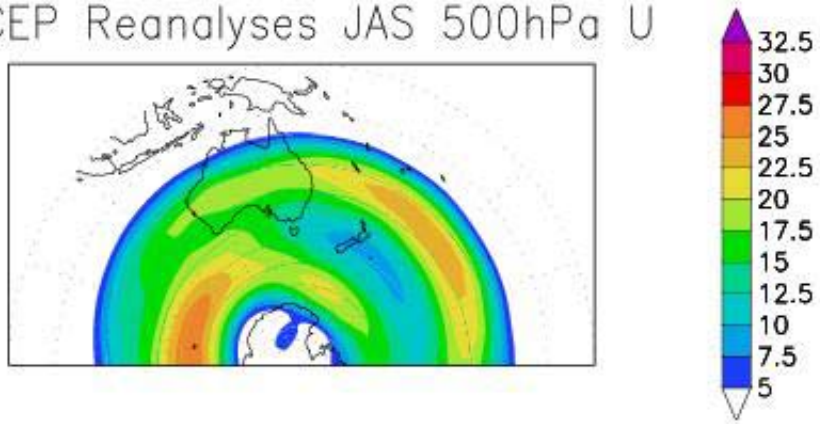

1979–1988 BAM JAS 500hPa U

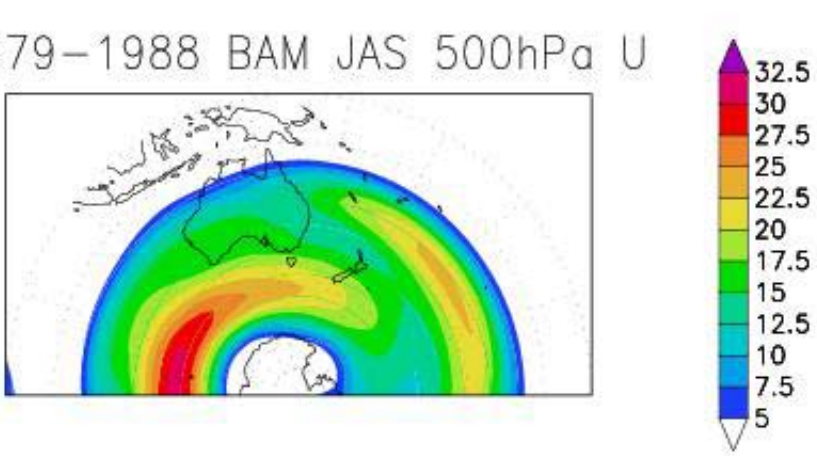

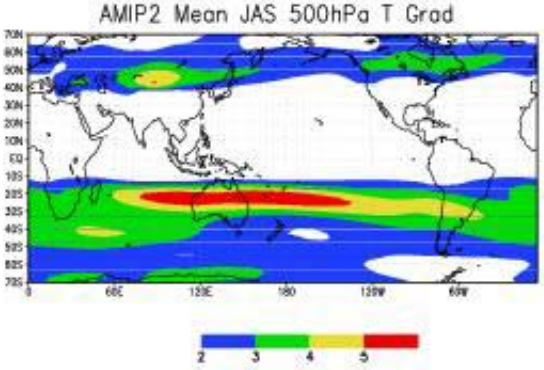
AMIP2 Mean JAS 500hPa T Grad
2 3 4 5

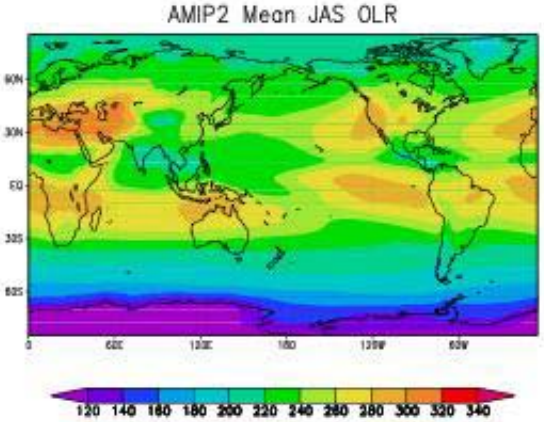
AMIP2 Mean JAS OLR
120 140 160 180 200 220 240 260 280 300 320 340

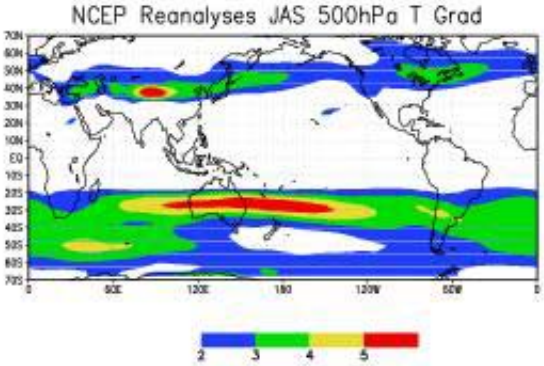
NCEP Reanalyses JAS 500hPa T Grad
2 3 4 5

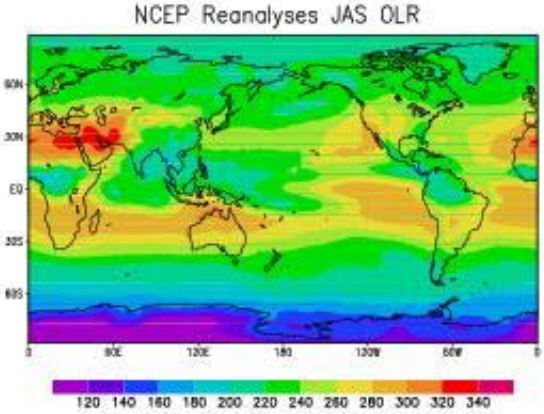
NCEP Reanalyses JAS OLR
120 140 160 180 200 220 240 260 280 300 320 340

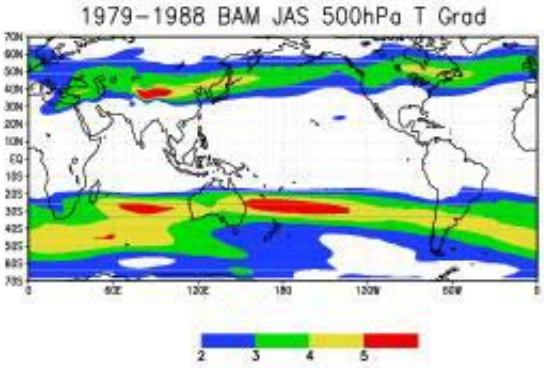
1979-1988 BAM JAS 500hPa T Grad
2 3 4 5

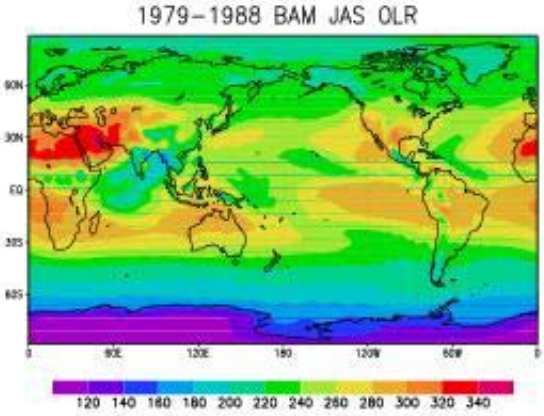
1979-1988 BAM JAS OLR
120 140 160 180 200 220 240 260 280 300 320 340

Given that cross equatorial flow from the northern monsoon season, followed by Coriolis torquing, is considered to be an important mechanism in maintaining the subtropical component of the double jet (refer, for instance, to Bals-Elsholz *et al*, 2001), we will now examine plots of outgoing longwave radiation (OLR) as a measure of deep convective activity at low latitudes and to gauge the relationship between the simulation of tropical convection and the production of a realistic subtropical jet in model output. Figure 2 shows maps of OLR for the AMIP2 mean model, as well as for BAM and NCEP reanalyses. We note that the intense baroclinic zones over Australia are associated with extensive convective activity in the tropics for both the AMIP2 mean and NCEP reanalyses.

Comparing BAM's simulation tropical convection in the Australian winter as depicted by the OLR field in Figure 2 with observations, we note that the extended region of tropical convection to the north of Australia does not appear in the model. Convective activity associated with the Indian monsoon is however well represented. This result suggests the model is not adequately capturing the extent of convective activity in the region immediately to the north of Australia. Consequently, the meridional temperature gradient will be perturbed and this will result in the strength and placement of the subtropical jet being poorly represented.

We turn now to consider transient eddy fluxes calculated from both NCEP reanalyses and model output. These fluxes represent meridional transport of heat and zonal momentum to satisfy the global balance of these quantities. The meridional transport of westerly momentum by the eddies primarily maintains the westerly winds in the southern hemisphere (Meehl, 1991) and determines the position and strength of midlatitude jets, including the subtropical jets (Trenberth, 1986). Figure 3 shows transient eddy momentum (left) and heat (right) fluxes. Results are shown for the AMIP2 mean (black), NCEP reanalyses (red), BAM (green) and the individual AMIP2 model (DNM, blue) that performed the most creditably in its simulation of climatological eddy activity.

We note that the tendency is for simulated eddies to be too intense, particularly in midlatitudes. This is especially so at 200hPa in the region of the subtropical jet core, where eddies (both heat and momentum fluxes) exceed observations by approximately 100% for both BAM and the AMIP2 mean. At 500hPa, the AMIP2 mean performs reasonably. In all cases other than eddy momentum flux at 500hPa, BAM performs more poorly than the AMIP2 mean. These results indicate that current AGCMs consistently produce excessive eddy activity in the midlatitudes of the Southern Hemisphere, particularly in the Australasian region that is the focus of this study.

Given the crucial role eddy activity plays in maintaining the strength and position of midlatitude jets (Meehl, 1991; Trenberth, 1986), the simulated midlatitude eddies would appear to be playing a role driving the too-strong subtropical jet in models.. Inadequate dissipation of eddies in the model could also be a contributing factor and further work, including the testing of other eddy dissipation schemes would be required to explore this issue in depth.

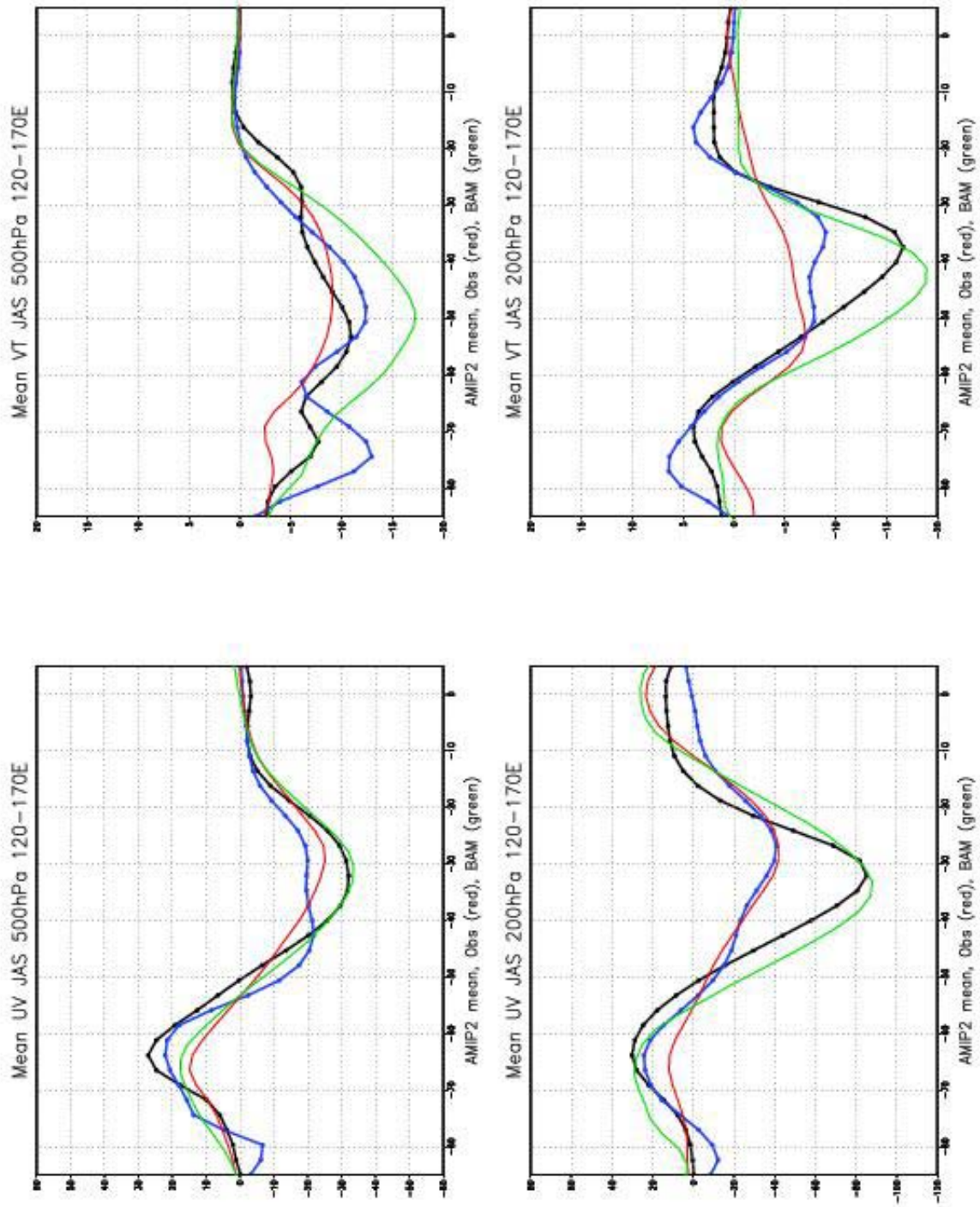
Mean VT JAS 500hPa 120–170E
AMIP2 mean, Obs (red), BAM (green)
Mean VT JAS 200hPa 120–170E
AMIP2 mean, Obs (red), BAM (green)
Mean UV JAS 500hPa 120–170E
AMIP2 mean, Obs (red), BAM (green)
Mean UV JAS 200hPa 120–170E
AMIP2 mean, Obs (red), BAM (green)

Discussion and Conclusions

We have observed that current AGCMs participating in AMIP2 do not tend to adequately capture the wintertime double jet. The subtropical component of the split jet tends to be too strong and is often significantly displaced from the location seen in observations. Further study indicates there are significant problems with the meridional temperature gradient in the model, and the cause of this appears to be diabatic processes in the tropics.

The Asian monsoon produces a gigantic heat source in the atmosphere which impacts the global circulation. Model simulations are often unable to reproduce key aspects of variability because of errors in diabatic forcing. The underlying mechanism responsible for the generation and maintenance of the quasi-steady subtropical component of the wintertime double jet would appear to be divergent cross-equatorial outflow from the northern hemisphere monsoon. Hence, the shortcomings in the simulation of diabatic processes in the tropics appear to impact the ability of models to reproduce an acceptable meridional temperature gradient and a realistic subtropical component of the double jet.

Eddy diagnostics reveal that models are consistently overstating eddy activity in mid latitudes in the Australasian region. Further experimentation would be required to determine whether the simulated eddies are a further consequence of poorly simulated diabatic processes in the tropics, or whether the excessive eddy values are a result of deficiences in the modeling of eddies themselves. If the latter is considered, the treatment of eddy dissipation in models may be a significant contributing factor in some cases.

The polar front jet is also poorly simulated in AMIP2 models, as well as BAM. The PFJ tends to be too weak and significantly displaced from its realistic geographical location. We noted above that the baroclinic zone at the periphery of the Antarctic continent is poorly simulated in most of the AMIP2 models studied here, as well as in BAM. These significant problems associated with the meridional temperature gradient at the periphery of the Antarctic continent may have several explanations, or may be due to a combination of factors. Among these possible factors would be the resolution of Antarctic topography in the model, shortcomings in modelling sea-ice albedo and possibly (at lower altitudes) the subsurface extrapolation used in extracting the temperatures (given that from the edge of the continent, Antarctica quickly rises to levels above 850hPa in altitude).

References

Bals-Elsholz, T.M. *et al*, 2001: The Wintertime Southern Hemisphere Split Jet: Structure, Variability and Evolution. *J. Climate*, **14**, 4191-4215.

Gates, W.L., 1995: *Proceedings of the first International AMIP Scientific Conference*. World Meteorological Organisation, 1995.

Kitoh, A., K. Yamazaki and T. Tokioka, 1990: The Double Jet and Semi-Annual Oscillations in the Southern Hemisphere Simulated by the Meteorological Research Institute General Circulation Model. Met. Soc. Japan, **68**, 251..

Meehl, G.A., 1991: A Reexaminatin of the Mechanism of the Semiannual Oscillation in the Southern Hemisphere. *J. Climate*, **4**, 911.

Trenberth, K.E. and K. C. Mo, 1986: Blocking in the Southern Hemisphere. *Mon. Wea. Rev*., **113**, 3-21.

Linearity in ENSO's Atmospheric Response

Sumant Nigam[1] and Eric DeWeaver[2]
[1]University of Maryland, College Park; nigam@atmos.umd.edu
[2]University of Wisconsin, Madison; deweaver@aos.wisc.edu

I. Innovative AMIP Diagnostics – Pitch for diagnosis of mechanisms

The authors would like to encourage and contribute to the enhancement of routine diagnostics performed on AMIP simulations. In this context, a review of AMIP's goals would be helpful to see if they truly reflect current community sentiments. An important original goal, as stated in Gates et al. (1999), is:

> *"It is expected that AMIP II will become an accepted community protocol for the continued diagnosis, validation, and improvement of the atmospheric GCMs, and will serve as a benchmark reference for the atmospheric component of coupled models."*

The statement is broad and inclusive, and as such, accommodative of various project activities. However if the AMIP diagnostic activity is to become more innovative – as this workshop would like it to be – then this AMIP goal needs to be sharpened. We argue that in addition to the traditional analysis of simulated *structure*, the veracity of dynamical and thermodynamical *mechanisms* of variability (from diurnal-to-decadal) in the AMIP simulations ought to be ascertained. Analysis of both structure and mechanisms should lead to improved simulations of present-day climate, and to more accurate projections of regional climate change. (George Boer and Brian Hoskins suggested as much in their presentations; Boer, arguing for the importance of budget studies, while Hoskins advocating analysis of dynamical and physical processes.)

The authors would thus like Larry Gates, Peter Gleckler, and the AMIP team to consider adding the following sentence to the above stated AMIP goal:

> *"Analysis of the structure **and** mechanisms of variability will enhance the simulation accuracy and our confidence in model projections of climate change.*

The issue of sharpening the goals is not an academic one: Subscribing to the modified goal will involve changes in the AMIP protocol, including archival of additional output to enable evaluation of dynamical and thermodynamical budgets and mechanisms.

DIAGNOSTIC STRATEGY

A two-step diagnostic strategy consisting of **error identification** and **error attribution** is being advocated by the authors. The strategy emphasizes analysis of the dynamical and thermodynamical mechanisms of variability, in addition to the canonical analysis of variability structure. Note, that realistic simulation of variability structure and underlying mechanisms is a necessary, but not sufficient, condition for obtaining reasonable simulations in a more interactive environment, as climate modelers well know.

Error Identification: From *a posteriori* objective analysis of errors in the structure of simulated variability (e.g., ENSO's circulation response) **and** its potential forcing. (e.g., ENSO heating anomalies, sub-monthly transient flux anomalies). What constitutes potential forcing depends on the definition of variability. For example, if ENSO circulation and precipitation variability were of interest, then SSTs and surface fluxes, rather than tropical diabatic heating, would be considered potential forcing. Validation targets (along with uncertainties) for both structure and potential forcing should be developed from atmospheric and oceanic reanalysis data sets, and satellite observations (e.g., TRMM) when feasible.

Error Attribution: Relate the identified circulation errors to specific features of the forcing error, from dynamical modeling. For meaningful attribution, the diagnosing models should have a) simpler dynamical structure (e.g., linear), b) resolution comparable to the general circulation model (GCM), and c) controlled/constrained diabatic forcing. Attribution can however be difficult in the presence of robust climate feedbacks, and guidance provided by simpler dynamical models must be reevaluated from GCM experiments in such situations.

II. ENSO'S ATMOSPHERIC RESPONSE

The pre and post-TOGA views of ENSO's atmospheric response (or teleconnection) in winter are depicted in *Figure 1*. The pre-TOGA view was shaped by seminal analysis of Wallace and Gutzler (1981) and Horel and Wallace (1981), and modeling studies of Hoskins and Karoly (1981). Observational findings found theoretical/modeling support, and lead to schematic depictions of the ENSO teleconnection, as a stationary Rossby wave train emanating from the region of enhanced precipitation in the central Pacific (figure 1a). The simple, elegant picture got refined in the following years, especially the TOGA decade (1985-95), from extensive analysis and modeling of the ENSO response: *First*, the importance of the climatological upper-tropospheric flow, particularly, the Asian-Pacific jet, in shaping the extratropical response was recognized: The jet-shear (2D barotropic instability) was shown to be an important energy source for wave perturbations, and to contribute to the development of ENSO's midlatitude response (Simmons, Wallace, and Branstator 1991). Vorticity gradients of the Asian-Pacific jet, on the other hand, were found important in both defining the anomalous vorticity forcing ('Rossby wave source'; Sardeshmukh and Hoskins 1988) and in modulating wave propagation into the midlatitudes (Branstator 1985). *Second*, the Pacific stormtracks were found altered in El Nino winters (Lau 1988); southeastward extension of the Asian-Pacific jet, arising from a regional Hadley response to central equatorial Pacific heating, is implicated in the displacement of stormtracks. The attendant transient vorticity fluxes were shown to be quite important in forcing the ENSO-related extratropical circulation anomalies (Held, Lyons, and Nigam 1989). Despite advances in understanding and modeling of the ENSO response in the intervening years, the post-TOGA schematic (called the teleconnection "protomodel" in Trenberth et al. 1998; figure 1b, here) remains too closely tied to the pre-TOGA view; the intermediary interaction with stormtracks is the only notable modification in the revised schematic.

POST-TOGA SCHEMATIC: IS IT ACCURATE?

The post-TOGA schematic falls short in conveying the improved understanding of dynamical and thermodynamical processes that shape ENSO's wintertime response in the

northern extratropics. *Principal shortcomings:* The ENSO response is depicted as too much wave-like; confusion with the intraseasonal PNA pattern is the issue here. The origin of the ENSO teleconnection is incorrectly depicted to be the heating monopole in the Tropics; the role of diabatic *cooling* anomalies in shaping the response is not acknowledged. Finally, the schematic doesn't advance the notion of response-insensitivity to the longitudinal position of the equatorial heating/cooling anomalies – an important finding of the TOGA period; to the contrary, by depicting the extratropical response as a wave train emanating from tropical heating, *Figure 1b* reinforces earlier notions of sensitivity and the 'directly forced from the Tropics' view.

Claim of 'Nonlinearity' of the Extratropical Response: Tenable?

Some of the aforementioned concerns are at the heart of a recent claim by Hoerling et al. (1997, hereafter referred to as HKZ) regarding the 'nonlinear' nature of ENSO's midlatitude response. HKZ suggest that the nearly opposite SST anomalies of El Nino and La Nina events could drive very different midlatitude circulations because the anomalies are superimposed on a longitudinally varying SST climatology (with warmer SSTs in the western Pacific). Since the necessary condition for occurrence of deep tropical convection is SSTs in excess of ~27C, the El Nino and La Nina convection anomalies could not be expected to be anti-symmetric, i.e., linear, on this count. This nonlinearity in SST-convection relationship causes negative La Nina heating anomalies to be displaced to the west of their positive El Nino counterparts, and HKZ suggest that this longitudinal shift may be reflected in the midlatitude circulation responses to the events. Their observational composites show a 35° shift between the 500mb North Pacific eddy height anomalies for warm and cold events.

The shift in convection between El Nino and La Nina events is a robust and easily documented feature of ENSO. However, it is not clear that this modest shift in equatorial convection should produce a substantial shift in the extratropical response. In particular, GCM experiments of Geisler et al. (1985) demonstrated a remarkable *insensitivity* of the extratropical response to the location of ENSO convection. The new insights gained during the TOGA decade (discussed above), including, role of Pacific stormtrack interactions and associated transient vorticity fluxes in establishing the ENSO teleconnection, suggest that these dynamical and thermodynamical interactions can bestow a degree of insensitivity on the upper-level height response. At the very least, they thwart attempts to establish a direct link between the position of equatorial heating and the longitudes of key teleconnection features in the higher latitudes.

Here, the linearity in ENSO's response is examined in both the tropics and midlatitudes, using data from the NCEP reanalysis and composites based on the traditional Nino 3.4 SST index (figure 2). Despite a significant zonal shift between the equatorial El Nino and La Nina heating/convection anomalies (not shown for reasons of space; see figures 6-7 in DeWeaver and Nigam 2002, which closely analyses the 'nonlinearity' claim), we find only a modest difference of about 10° in the corresponding upper-level height patterns over the northeast Pacific. If the shift is due to convection, one might expect to see a stronger shift in the height response over the tropical Pacific, in the vicinity of the heating. But our El Nino and La Nina height composites are in almost exact opposition in that region (figure 5 in DeWeaver and Nigam 2002). While these results are consistent with previous findings of insensitivity, they are clearly at odds with the observational composites of HKZ. The simplest explanation for this discrepancy is sampling

error in the presence of decadal variability. Examination of the warm and cold ENSO events used in the HKZ composites (their table 1) reveals an inequitable distribution of events with respect to the 1976/77 climate transition (e.g. Trenberth 1990, Wang 1995): 5 of the 9 warm years, but only 1 of the 9 cold years are in the post-transition period. This distribution raises the possibility that decadal climate variability, rather than nonlinearity, may account for the differences between their El Nino and La Nina composites. The issue of decadal variability is particularly significant in light of HKZ's claim that the La Nina response projects strongly onto the PNA pattern. The studies of Deser and Blackmon (1995), Dai and Nigam (1995), Zhang et al. (1997), and Mantua et al. (1997) find the PNA pattern in the 500mb height anomalies accompanying decadal variability in Pacific SSTs. One might thus expect to find elements of the PNA pattern in the HKZ La Nina composite, which is largely chosen from the early years of the record, but not in their more evenly distributed El Nino composite.

The insensitivity in the tropical height response is a somewhat unexpected finding, since studies of insensitivity have generally emphasized the extratropical ENSO response. However, the issue of nonlinearity in the tropical response is not addressed by the observational composites of HKZ, who, like many authors, identified the ENSO response using height data poleward of 20°N. Also, their analysis is carried out at the 500mb level, which is near the nodal line for the baroclinic tropical response; we have examined the height anomalies at the 200mb level, where both tropical and extratropical responses are robustly expressed.

REFERENCES:

Branstator (1985): *J. Atmos. Sci.*, **42**, 2225-2254.

Dai and Nigam (1995): *Proceedings of the XXth Annual Climate Diagnostics Workshop*, pages 25-28, NOAA/NCEP/CPC.

Deser and Blackmon (1995): *J. Climate*, **8**, 1677-1680.

DeWeaver and Nigam (2002): *J. Climate*, **15**, 2446-2461.

Gates et al. (1999): *Bull. Amer. Meteor. Soc.*, **80**, 29-56.

Geisler et al. (1985): *J. Atmos. Sci.*, **42**, 1037-1049.

Held, Lyons, and Nigam (1989): *J. Atmos. Sci.*, **46**, 163-174.

Hoerling, Kumar, and Zhong (1997): *J. Climate*, **10,** 1769-1786.

Horel and Wallace (1981): *Mon. Wea. Rev.*, **109**, 813-829.

Hoskins and Karoly (1981): *J. Atmos. Sci.*, **38**, 1179-1196.

Lau (1988): *J. Atmos. Sci*., **45**, 2718-2743.

Mantua et al. (1997): *Bull. Amer. Meteor. Soc.*, 1069-1079.

Simmons, Wallace, and Branstator (1991):

Sardeshmukh and Hoskins (1988): *J. Atmos. Sci.*, **45**, 1228-1251.

Trenberth et al. (1998): *J. Geophys. Res.*, **103**, C7, 14,291-14,324.

Trenberth (1990): *Bull. Amer. Meteor. Soc.*, **71**, 988-993.

Wallace and Gutzler (1981): *Mon. Wea. Rev*, **109**, 784-812.

Wang (1995): *J. Climate*, **8**, 267-285.

Zhang et al. (1997): *J. Climate*, **10**, 1004-1020.

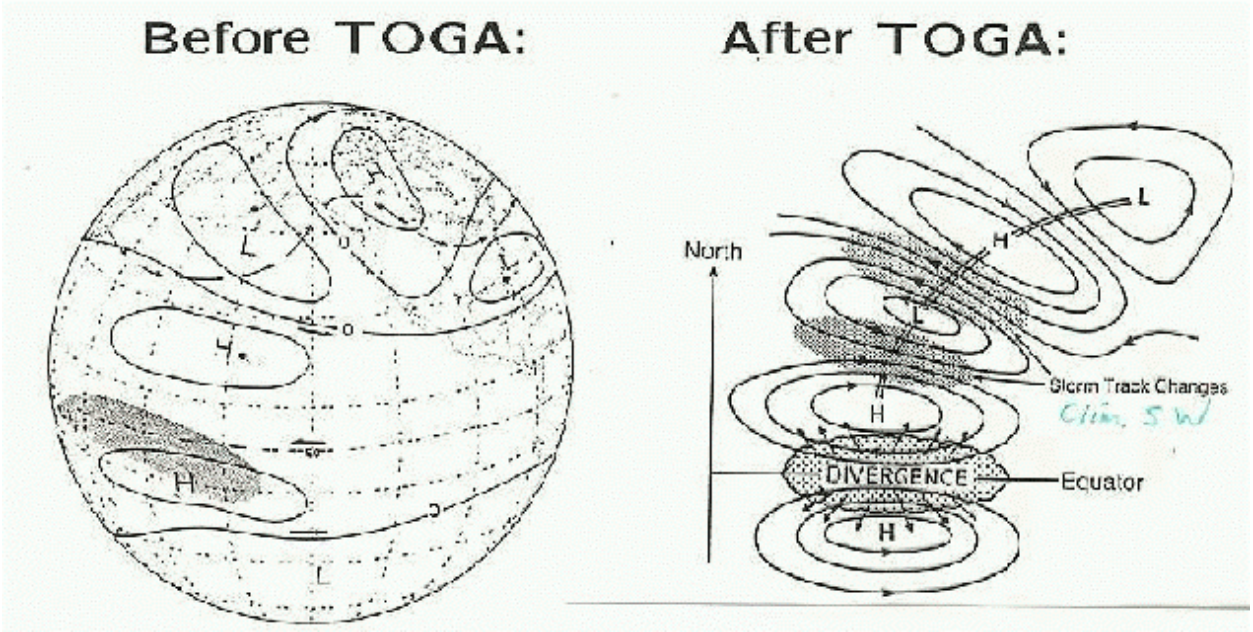

Fig 1: Pre and post-TOGA view of ENSO's atmospheric response (or teleconnection) in winter.

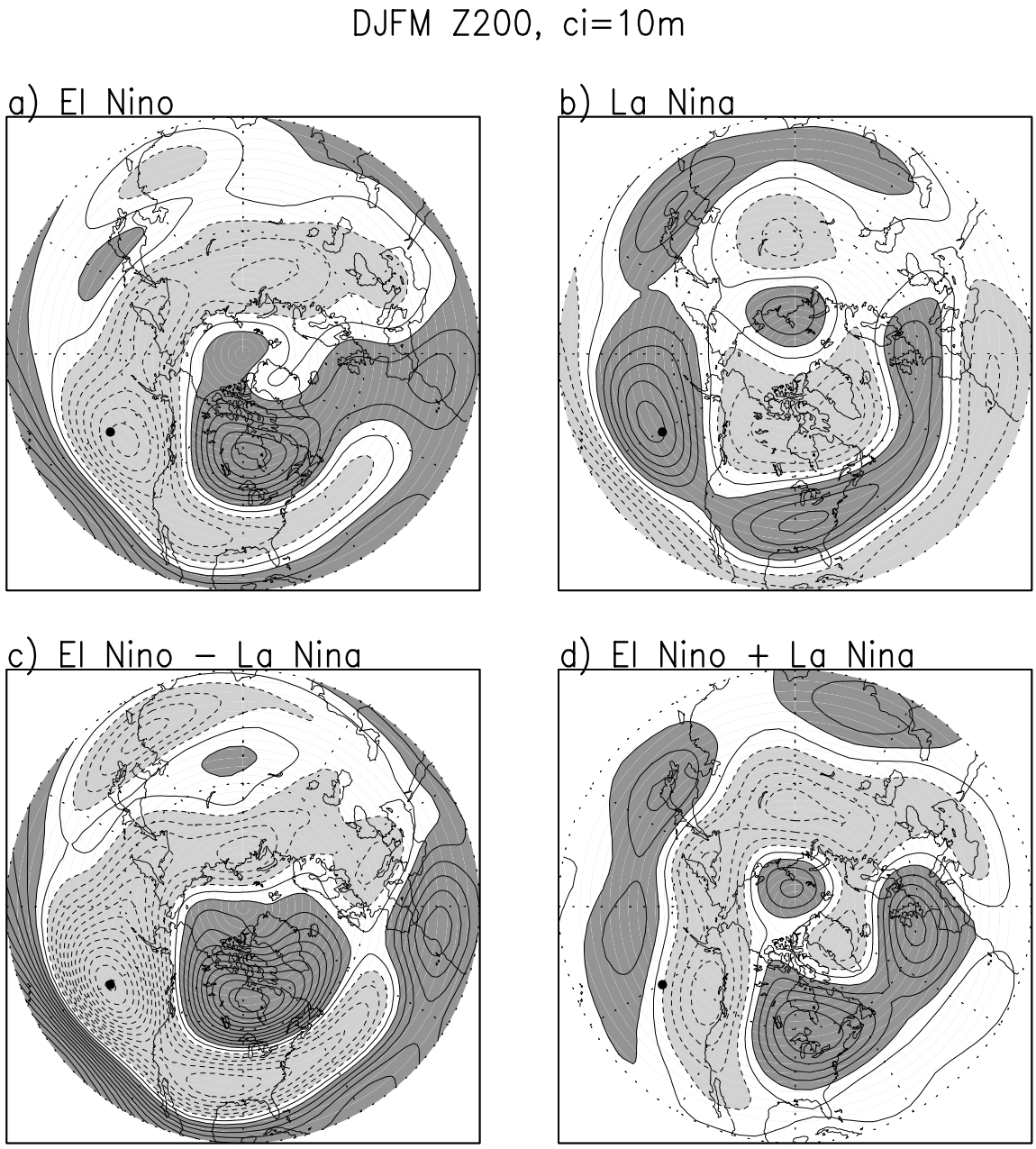

Fig 2: The 200mb height anomalies averaged for the 8 El Nino (a) and 8 La Nina (b) winters during 1950-2000; the winter is considered warm (cold) when Dec-Mar average of the Nino3.4 SST index exceeds +1 (-1) standard deviation. (c): difference of the composites in (a) and (b), used to represent the "linear" component of the ENSO response which changes only in sign between the warm and cold composites. (d): sum of (a) and (b), used to represent the "nonlinear" component of the response, which contains qualitative differences between warm and cold event responses. The sold dot represents the center of the northeast Pacific low in (c). Contour interval is 10m, with dark (light) shading for positive (negative) values in excess of 10m.

The Middle-Cloud Downstream the Tibetan Plateau

Rucong Yu

LASG, Institute of Atmospheric Physics, Chinese Academy of Sciences, Beijing 100029

ABSTRACT

Based on ISCCP data, it is found that one of the maximum coherent middle cloud cover occurs downstream the Tibetan Plateau. In February, the averaged middle cloud fraction downstream the Tibetan Plateau exceeds 50%, which is the globally maximum. Based on the ECMWF reanalysis products and data from the Earth Radiation Budget Experiment ERBE, it is found that the column atmosphere downstream the Tibetan Plateau have to obtain about $10Wm^{-2}$ energy flux from the moist static energy transport to compensate the net radiative loss responding to the strong negative cloud radiative forcing, and the low troposphere downstream the Tibetan Plateau is the coldest in same latitude. Diagnostic analysis shows that the middle cloud might be responsible for the strong radiative cooling.

The effects of the Tibetan Plateau on the westerly produce the permanent convergence below 700hPa and divergence around 600hPa, which provide the large scale circulation to maintain the high amount of middle cloud cover downstream the Tibetan Plateau. This study reveals profound effects of the middle cloud and suggests that it is worthful to understand the impacts and sustentation of the middle cloud downstream the Tibetan Plateau.

1. INTRODUCTION

The high amount of deep convective high clouds plays an important role in the maintenance of high sea surface temperature over the equatorial west Pacific (Arking and Ziskin, 1993). The marine stratus over the eastern tropical Pacific has strong impacts on the formation of the cold tongue and the asymmetric inter-tropical convergence zone (Philander et al., 1996; Yu and Mechoso, 1999). Based on the data from the International Satellite Cloud Climatology Project (ISCCP) (Rossow and Schiffer 1991), one of the maximum coherent middle cloud cover is found downstream the Tibetan Plateau. Klein and Hartmann (1993) mentioned that all the regions with high amounts of stratus clouds are over the oceans with the exception of the Chinese region. Yu et al (2001) concluded that there are distinctive cloud radiative properties in the eastern China. Based on available climate data and the previous studies, this paper will further diagnose the middle cloud radiative interactions downstream the Tibetan Plateau, and discuss their impacts on the local climate.

2. MIDDLE CLOUD DOWNSTREAM THE TIBETAN PLATEAU

Based on the ISCCP products, the low level stratus clouds are found to be limited along the southeast coast of Chinese mainland and the high level clouds mainly occur in summer monsoon season. The distinguishing cloud cover downstream the Tibetan Plateau is the middle cloud, the top-cloud pressure is between the 680hPa and 440hPa, especially in winter and spring, the averaged middle cloud fractions are about 50%. Figure 1 shows the middle cloud fractions in February. The coherent fractions exceed 50% and are the globally maximums.

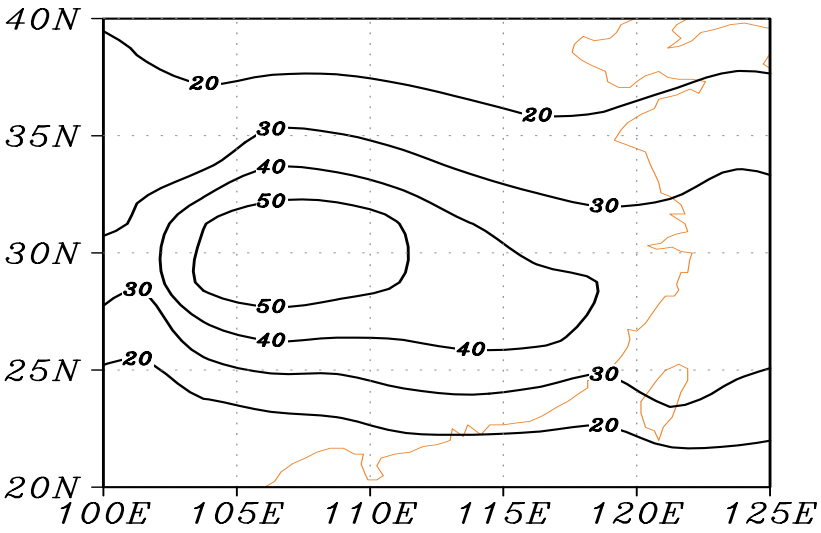

Fig.1 The percentage of middle cloud fractions downstream the Tibetan Plateau in February.

The unique persistent middle clouds over the subtropical East Asia could result from the blocking and frictional effects of the Tibetan Plateau on the dominated westerly circulation. The plateau blocks the low-level westerly and forces them to bifurcate, flow around the plateau, and converge downstream, and in addition, decelerates the westerly flow over the mountainous by friction in the middle troposphere. The lower level convergence forces a large scale ascent motion and middle level divergence limits the vertical lifting to be gentle and within the low troposphere. From Figure 2, it is clear that the zonal wind speeds, derived from the European Center for Medium-Range Weather Forecasts (ECMWF) reanalysis products (Gibson et al., 1997), are serious reduced when passing through the Tibetan Plateau, which induces a strong divergence on the middle troposphere in the leeward of Tibetan Plateau. In addition, the averaged annual cycle of middle cloud is well matched to the averaged annual cycle of divergence and zonal wind speed around 600hPa (not shown). The middle layer divergence, together with the lower layer convergence induced by westerly going round the Tibetan Plateau and converging in the leeward, provides a suitable large scale general circulation for the maintenance of middle level clouds.

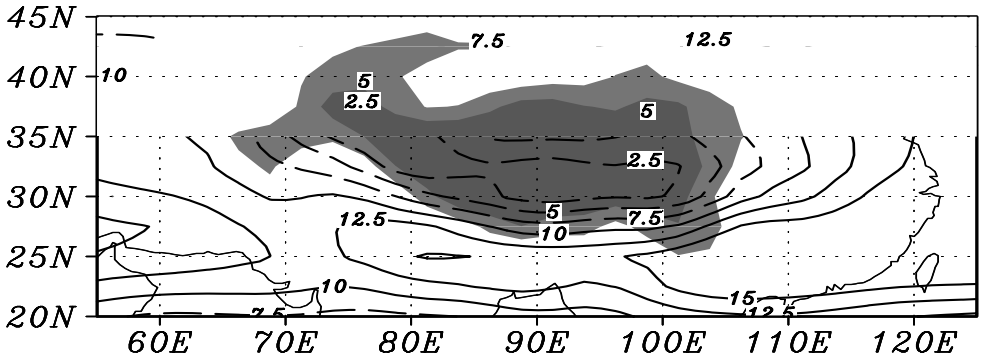

Fig.2 The shades represent the height of topography, in which the edges of light and dark regions are the contours of 2000m and 3500m respectively, and the contours represent the westerly wind speed around the 600hPa in February in units of ms^{-1} with 2.5 ms^{-1} interval and dashed lines for less than 10 ms^{-1}.

3. IMPACT ON THE CLIMATE

Because of the large cloud optical thickness from the thick middle stratus cloud, the maximum negative short wave (SW) cloud radiative forcing (CRF) and net CRF, are found downstram the Tibetan Plateau, although the total cloud fractions are obvious less than that in the west Pacific warm pool and others. Figure 3 compares the annual mean net downward radiative fluxes at the TOA with that in clear sky only downstram the Tibetan Plateau, derived from ERBE data (Barkstrom, 1984). In clear sky, the annual mean net downward radiative fluxes are around 40Wm^{-2}, but, because of the CRF, the real net downward radiative fluxes in the TOA are around -15 Wm^{-2}. Thereby the clouds induce over 55Wm^{-2} radiative cooling and change the atmosphere from energy source to energy sink downstram the Tibetan Plateau. To equilibrate the energy budget, the column atmosphere have to get averagely about 15Wm^{-2} energy flux from the atmospheric moist static energy transport to compensate the radiative loss.

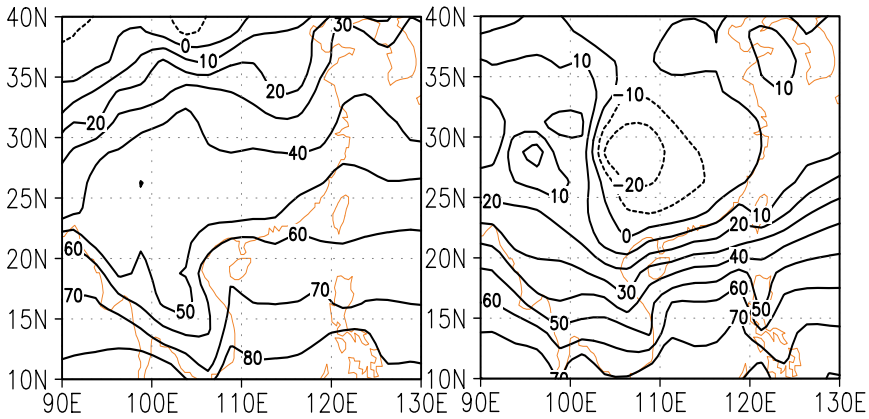

Fig.3 The annual mean net downward radiative fluxes at the TOA in clear-sky (a) and all-sky (b), in units of Wm^{-2}.

As response to the strong radiative cooling, the atmosphere of the low troposphere downstream the Tibetan Plateau are colder than that in same latitude, especially in the winter and spring seasons as shown in Figure 4. Below the 600hPa, the temperatures in February are serious lower than that in same latitude.

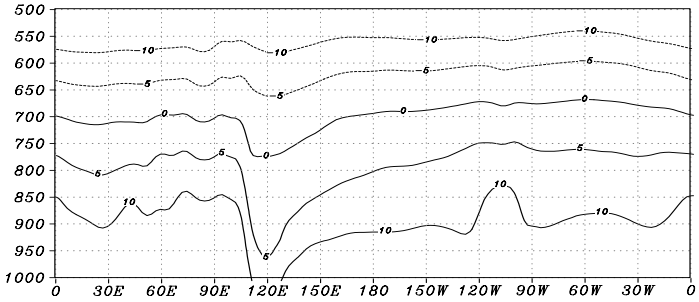

Fig.4 Zonal-height cross section of temperature (in units of ^{o}C) along 30^{o}N in February, derived from the ECMWF reanalysis products.

4. DISCUSSIONS

Some motivations are expected from this study in future modeling and observation studies, concerning the cloud parameterizations and climatic simulations. For modeling studies, much attention currently have paid to low cloud parameterization over clod ocean and deep convective cloud parameterization over the west Pacific warm pool, to improve the simulations on the tropical air-sea interactions. In fact, the Tibetan Plateau plays very important roles in global climate system, but the current climate models did not well capture the effects of the Tibetan Plateau on the real climate, especially the related cloud radiative properties, which definitely affected globally climate modeling. It is absolutely worthful to pay more attention on the physical mechanisms and climate impacts of the middle cloud sustentation down stream the Tibetan Plateau.

Acknowledgments: This work was supported by Chinese Academy of Sciences (CAS) under grant “hundred talents” for “Validation of Coupled Climate system models” and the “Innovation Program of CAS” under Grant ZKCX2□SW□210.

REFERENCES

Arking, A. and D. Ziskin, 1993: Relationship between clouds and sea surface temperatures in the western tropical pacific. J. Climate, vol.7, 988-1000.

Barkstrom, B. R., 1984: The Earth Radiation Budget Experiment (ERBE). Bull. Amer. Meteor. Soc., Vol.65, 1170-1185.

Gibson, J.K., P.Kallberg, S.Uppala, A.Hernandez, A.Nomura and E.Serrano, 1997: ERA description. ECMWF Reanalysis Project Report Series 1, European Center for Medium Range Weather Forecasts, Reading, UK, 66pp.

Klein, S. A. and D. L. Hartmann, 1993: The seasonal cycle of low stratiform clouds, J. Climate, Vol.6 1587-1606.

Philander, S.G.H., D. Gu, G. Lambert, T. Li, D. Halpern, N.-C. Lau, R.C. Pacanowski, 1996: Why the ITCZ Is Mostly North of the Equator. J. Climate: Vol. 9, No. 12, pp. 2958–2972.

Rossow, W. B. And R. A. Schiffer, 1991: ISCCP cloud data products. Bull. Amer. Meteor. Soc., Vol.72, 2-20.

Yu, J.-Y., and C. R. Mechoso, 1999: Links between annual variations of Peruvian stratocumulus clouds and of SST in the eastern equatorial Pacific. J. Climate, 12, 3305-3318.

Yu, R.C., Y.Q. Yu and M.H. Zhang, 2001: Comparing cloud radiative properties between the eastern China and the Indian monsoon region. Advances in Atmospheric Sc

Diagnosis of Diabatic Heating Errors in the NCMRWF Global Model Simulations

S.C. Kar, G.R. Iyengar, S.V. Singh and Sumant Nigam*

National Centre for Medium Range Weather Forecasting (NCMRWF), New Delhi- 110 003, India
* Department of Meteorology, University of Maryland, College Park, Maryland, MD 20742-2425, USA

ABSTRACT

Multi-year simulations of recent climate, using the NCMRWF operational model (T80/L18 resolution) and AMIP surface boundary conditions have begun. In this report, the model climate from 10-year (1979-88) simulations is described briefly. It is seen that the model has a reasonably good climate, particularly over the Indian region; the model simulates the primary zone of rainfall associated with the monsoon trough, and the orographic rainfall along the west coast reasonably well. The model correctly responds to the ENSO SST anomalies, however the remote response of these SST anomalies on the Indian monsoon is not simulated realistically during the period of simulation presented in this report. The total diabatic heating fields at various levels were compared against those diagnosed from NCEP Re-analyses. The model simulated mean pattern of heating during the summer monsoon season agrees well with the observed pattern, but three are differences in the magnitude of heating. It is proposed to examine the sources of these diabatic heating fields after an ensemble of mutli-year simulations have been carried out.

1. INTRODUCTION

Diabatic heating fields are important for the maintenance of the tropical energy budget and mean flow, and also as the primary energy source for tropical disturbances. Correct representation of the interactions between the large-scale circulations and the major heat sources is an essential aspect of the modelling of the atmospheric general circulation. Asian monsoon produces a gigantic heat source in the atmosphere, which impacts the global circulation during both summer and winter seasons. Model simulations are often unable to reproduce key aspects of seasonal and inter-annual variability because of errors in diabatic forcing. Diagnosis of the diabatic heating errors in the simulations will be helpful in understanding the deficiencies of the model physics. Multi-year simulations of recent climate, using the National Centre for Medium Range Weather Forecasting (NCMRWF) operational model (T80/L18 resolution) and AMIP surface boundary conditions have begun. The simulations conform to the standards of AMIP-II. The main objective of these simulations, in addition to participate in the model inter-comparison under the AMIP, is to diagnose the reasons for deficiencies in weather forecasts produced by the NCMRWF weather prediction model, and develop amelioration strategies. Analysis of the ensemble-mean multi-year simulation and their comparisons with the corresponding period observations will allow one to focus on the deficiencies in model's physics.

2. AMIP-II SIMULATIONS AT THE NCMRWF

The global model is operationally run at T80 horizontal resolution (triangular truncation with 80 waves) and 18 vertical levels to prepare the medium range weather forecasts. The model has

been upgraded to T170L28 (Kar, 2002) and is being run parallel to the T80L18 version of the model. This T80L18 model was adapted from the NCEP medium-range weather forecast model (Kanamitsu, 1989), and operational forecasts since 1994 show that the model has reasonable accuracy over India and the adjoining regions. The model has been improved by implementing the non-local K closure (NLC) for PBL parameterization (Basu et al. 2001) and short wave radiation parameterization scheme of Harshvardhan et. al. (1987) was implemented in the model (John, 2001). The model has been integrated using AMIP-II boundary forcing (SST and Sea-Ice) starting from 1979 to 1988. The model integrations are continuing, however, in the present report, results of 10-integration are presented.

3. RESULTS AND DISCUSSIONS

Fig. 1 (a) shows the model simulated mean rainfall distribution for the Northern Hemisphere summer season (June, July, and August, JJA). In the observed mean pattern of rainfall during the summer season (figure not shown), the zone of maximum rainfall is observed in the vicinity of ITCZ north of the equator. Besides this primary zone of rainfall, a secondary zone of rainfall occurs over the equatorial Indian Ocean region. Over the Indian subcontinent, during the monsoon months (JJA), heavy rainfall associated with orography occurs over the west coast of India and the Himalayan region. It is seen that the model has a reasonably good climate. In particular over the Indian region, the model is able to simulate reasonably well the primary zone of rainfall associated with the monsoon trough, and the orographic rainfall along the west coast. The model overestimates rainfall amounts over the African region and underestimates the rainfall amount over the west Pacific region. The model is also able to simulate the rainfall associated with the migration of the ITCZ to the south of the equator during the Northern winter season.

The model response to the ENSO SST anomalies have been examined and was found that the model responds locally to 1982-83, and 1987-88 SST anomalies rather well. However the remote response of these SST anomalies on the Indian monsoon is not simulated realistically during the period of simulation presented in this report. Therefore, the intreannual variability of the Indian monsoon is not simulated well by the model.

In Fig. 1 (b), we show the total diabatic heating (shortwave, longwave, deep convective, shallow convective, large-scale and heat-transfer due to vertical diffusion) at 400 hPa for the JJA months from all the 10-year run. The total diabatic heating fields at verious levels were compared against those diagnosed from NCEP Re-analysesIn the observed mean pattern of heating during the summer monsoon season (figure not shown), a broad area of heating extends from the Arabian sea to the west Pacific. The maximum heating occurs over the Bay of Bengal. In the tropics,

The total diabatic heating computed from model simulations has been compared with the observed diabatic heating at 400 hPa diagnosed from NCEP reanalysis data for the same period (Nigam et al., 2000), figure not shown. It was found that the mean structure of the diabatic heating from the model agrees reasonably well with the observed pattern, however, the model has large heating errors in the Indian monsoon region. Over the north-eastern parts of India and near foot hills of Himalayas, the model over-estimates the heating. Since the monsoon process is essentially convective, the total diabatic heating is dominated by deep cumulus convective heating. The amount of heating over the west Pacific region is comparatively less in the model climatology.

4. CONCLUSIONS

It is the first time that the NCMRWF global model has been integrated with AMIP II surface boundary conditions for 10 years. The model climate has been examined and it was found that the model simulates well the basic features of global circulation and rainfall climatology. The model correctly responds to the ENSO SST anomalies, however the remote response of these SST anomalies on the Indian monsoon is not simulated realistically during the period of simulation presented in this report. Examination of the diabatic heating fields reveals that the structure of the total diabatic heating field at 400hPa compare well with that diagnosed from re-analyses data. However, the magnitude of heating does not agree well with the observational counterpart. It is proposed that the structure and variability of diabatic heating in the simulation will be compared with the observational counterparts (diagnosed from NCEP and ECMWF re-analyses). Detailed intercomparisons will help establish the strengths and deficiencies of the model's physical parameterizations. Strategies for model improvement will then be developed from diagnostic modeling, which can reveal the impact of heating errors on circulation.

REFERENCES:

Basu, S., G.R. Iyengar and A. K. Mitra (2002) Impact of non-local closure scheme in simulation of Monsoon system over India", Mon. Wea. Rev.**,** 130 (1), 161-170.

John P. George (2001) Implementation of a Short wave Radiation Parameterization Scheme in the NCMRWF Operational Global Model, *WMO/TD No. 1064*, p. 4.3-4.4

S.C. Kar (2002): Description of a high-resolution Global Model (T170/L28) developed at NCMRWF. *Research Report* 1/2002, NCMRWF, 28pp.

Kanamitsu, M., (1989) Description of the NMC global data assimilation and forecast system. *Weather Forecasting*, 4, 335-342.

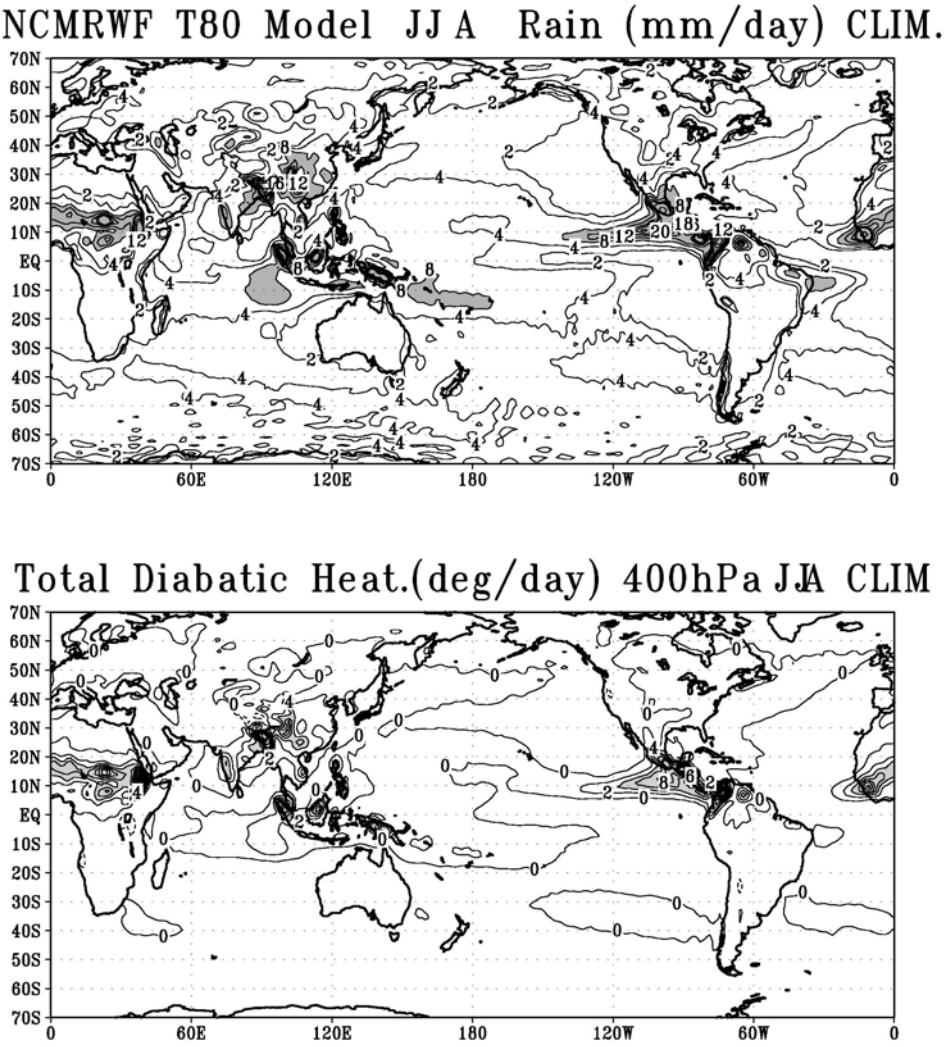

Fig. 1 (a) Model simulated climatology (10 years) (a) simulated rainfall (mm/day) for (a) JJA months, (b) DJF months, and (c) Total diabatic heating (deg/day) at 400hPa.

The Madden-Julian Oscillation in GCMs

Kenneth R. Sperber[1], Julia M. Slingo[2], Peter M. Inness[2], Silvio Gualdi[3], Wei Li[4], Peter J. Gleckler[1], and Charles Doutriaux[1]

[1]Program for Climate Model Diagnosis and Intercomparison,
Lawrence Livermore National Laboratory,
P.O. Box 808, L-103, Livermore, CA 94550 USA
(sperber1@llnl.gov)
[2]NERC Centre for Global Atmospheric Modelling,
Dept. of Meteorology, University of Reading,
P. O. Box 243, Reading RG6 6BB, England
[3]National Institute of Geophysics and Volcanology,
Via Gobetti 101, 40129 Bologna, Italy
[4]LASG,
Institute of Atmospheric Physics,
P.O. Box 9804, Beijing 100029, China

1. INTRODUCTION

The Madden-Julian Oscillation (MJO) dominates tropical variability on timescales of ~30-70 days (Madden and Julian 1971, 1972). It is manifested through large-scale circulation anomalies in conjunction with eastward propagating convective anomalies over the eastern hemisphere. Here we analyze intraseasonal variability in AMIP models and coupled ocean-atmosphere models to determine the extent to which the MJO is simulated, and the influence that air-sea interaction has on the representation of the MJO. All data are bandpassed with a 20-100 day Lanczos filter. The validation data include daily NCEP/ NCAR reanalysis (Kalnay et al. 1996), and AVHRR OLR (Liebmann and Smith 1996).

2. THE MJO AND ITS PROPAGATION

Sperber (2003) identified seven years when the boreal winter MJO was notably active as a well-defined eastward propagating mode. Using these periods, the eastward propagation of convection was isolated via EOF analysis of filtered AVHRR OLR. In the present study, filtered OLR from satellite data and the models is projected onto the afore-mentioned EOF's. Thus, all models are evaluated relative to a common metric. The analysis is confined to the months November-March, for 1979/80-1994/95 for the observations and the AMIP II models, and for 9-19 winters from the coupled models.

Figure 1 shows the lag 0 regression of the PC time series on to the filtered OLR from observations and for the ECHAM4 AMIP II model, and the SINTEX coupled ocean-atmosphere model (which used ECHAM4 as the atmospheric component). The simulated and observed anomalies are consistent, reaching approximately +/-20Wm^{-2}. However, just north of the Maritime Continent the models have more enhanced convection in EOF-1, and in EOF-2 the reduced convection is stronger north of the equator just west of the dateline. Furthermore, the convective maximum north of the Maritime Continent extends further east in ECHAM4 relative to SINTEX.

The amplitude of the OLR perturbations are directly proportional to the standard deviations of the PC's (Table 1). For the AVHRR OLR data, the standard deviations of PC-1 and PC-2 are

211.3 and 205.6, respectively. The vast majority of models have much weaker MJO convective signals. Also given is the maximum positive correlation, R, between PC-2 and PC-1, and the time lag at which it occurred. For the AVHRR data, on average, PC-2 leads PC-1 by 12 days with a maximum positive correlation of 0.67. For all models, R is smaller than observed indicating that eastward propagation is not as coherent as observed. The characteristic timescale of propagation exhibits a wide-range of variability, with some models being incorrectly dominated by westward propagation (PC-1 leads PC- 2 as denoted by negative time lags). Comparing AMIP II and AMIP I we find that HADAM3 has a weaker MJO amplitude and less coherent eastward propagation compared to HADAM2. Importantly, air-sea interaction has a beneficial influence. Three of the coupled models have an AMIP II atmospheric component. In each case the coupled models have a larger R, indicating that the MJO convection has a more realistic propagating structure. That coupling to an ocean yields improvement to the representation of the MJO is consistent with Waliser et al. (1999) and Inness and Slingo (2003).

Figure 2 shows the propagation of 5^{o}N-5^{o}S filtered OLR and 850hPa zonal wind. Both models exhibit difficulty in representing eastward propagation of enhanced convection into the central Pacific Ocean. SINTEX has more realistic convection anomalies over the Indian Ocean than does ECHAM4. However, SINTEX tends to have a standing oscillation in the central Pacific, and from day -5 to day 10 the enhanced convection does not extend as far east as for ECHAM4. The latter difference is related to systematic error of the mean state low-level winds. For the SINTEX model, the low-level near-equatorial westerlies do not extend as far eastward as for the ECHAM4 AMIPII integration. Rather the mean easterlies penetrate to 150^{o}E (not shown), and inhibit further eastward propagation of the MJO convection. This link between the convection and systematic error of the mean state is consistent with Inness and Slingo (2003) and Inness et al. (2003) based on their study using HADAM3 and HADCM3. Over much of the eastern hemisphere, the 850hPa westerlies lag the leading edge of the convection more so in the observations.

CONCLUSIONS

The simulation of the MJO proves to be a critical test of a models ability to simulate the tropics. Additional regressions and examination of space-time spectra indicate that (1) the models typically fail to represent the intraseasonal dominance of the large-scale circulation, (2) within a family of models ocean-atmosphere coupling leads to an improved lag/ lead MJO structure, and (3) eastward propagation is limited by systematic error of the mean state. Other variables are being analyzed to examine the mechanism of propagation in the models, and a more comprehensive peer-reviewed journal article will be prepared.

Table 1: Observed and simulated MJO characteristics. The columns give the observation/ model designation (the last 4 entries are from the coupled models), the standard deviations of PC-1 and PC2, the maximum positive correlation, R, between PC1 and PC-2, and the time lag at which it occurred. Positive time lags correspond to eastward propagation. Entries with an asterisk highlight models for which an AMIP II integration and a coupled ocean-atmosphere simulation using the same atmospheric model are available.

Model	PC-1	PC-2	R	Lag (days) PC-2 leads PC-1 (positive)
AVHRR	211.3	205.6	0.67	12
CCCMA-99a	100.3	107.0	0.26	11
CCSR-98a	106.4	91.7	0.30	13
CNRM-00a	155.1	143.3	0.42	14
COLA-00a	100.5	85.7	0.16	26
DNM-98a	63.0	67.1	0.16	>25
ECMWF-98a	102.5	97.5	0.20	-11
ECMWF-98b	121.8	105.7	0.29	-13
GFDL/DERF-98a	159.0	182.1	0.36	12
GISS-98a	64.0	54.6	0.23	-7
GISS-02a	37.1	37.1	0.17	-15
HADAM2 (AMIP I; 1979/ 80-1987/88)	166.5	130.9	0.40	18
*HADAM3 (L58) (UGAMP-98a)	117.1	102.8	0.28	14
JMA-98a	165.3	155.3	0.29	10
*MPI-98a (ECHAM4)	222.2	215.8	0.35	12
MRI-98a	174.2	164.1	0.31	9
NCAR-98a (CCM3)	91.9	100.2	0.18	10
*NCAR-02a (CAM2)	95.3	95.8	0.19	-24
NCEP-99a	108.9	108.6	0.24	12
NCEP-99b	104.1	98.4	0.22	24
*HADCM3 (L30)	104.4	96.0	0.45	8
IAP/LASG GOALS	123.8	129.2	0.42	9
*NCAR CCSM2	91.5	115.9	0.28	20
*SINTEX (ECHAM4/OPA8.1)	231.2	201.5	0.44	12

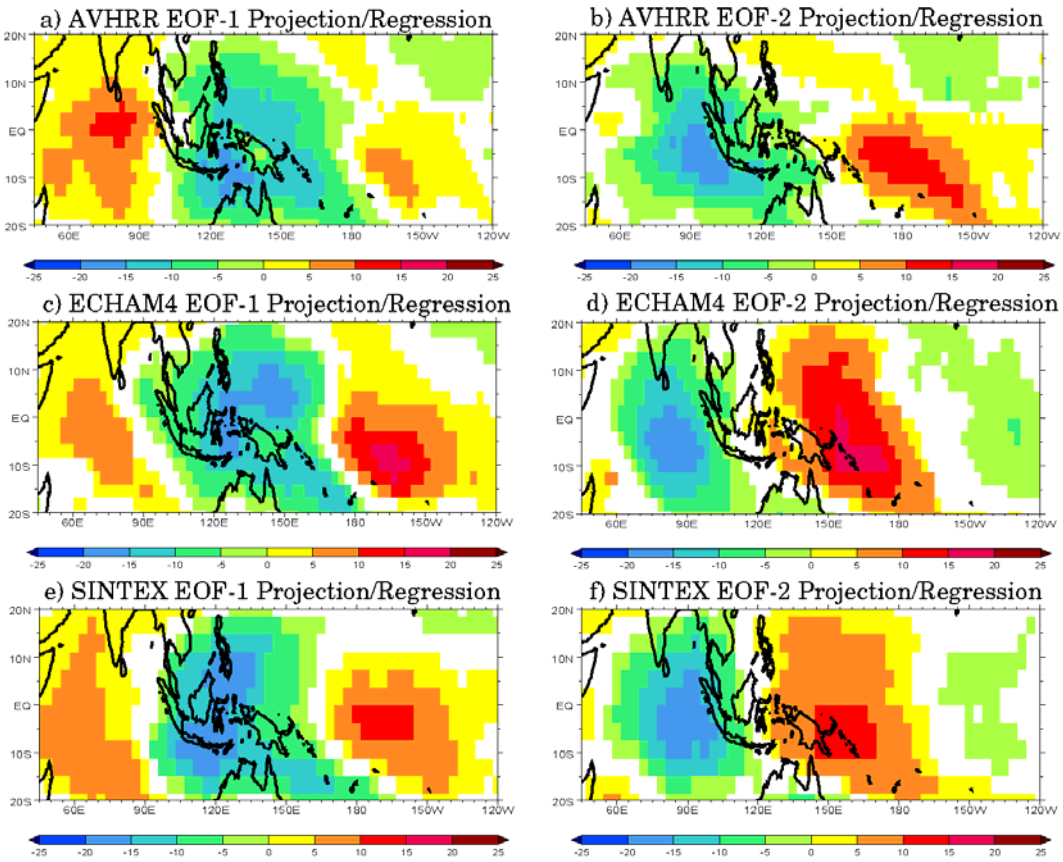

Figure 1. Linear regressions of PC-1 and PC-2 with filtered OLR for November-March: (a) and (b) 1979/80-1994/95 AVHRR OLR, (c) and (d) 1979/80-1994/95 ECHAM4 AMIP II integration, (e) and (f) years 21/22-39/40 from the SINTEX (ECHAM4+OPA8.1) coupled ocean-atmosphere model. The regressions have been scaled by a one standard deviation perturbation of the respective PC's. Negative values correspond to enhanced convection (Wm^{-2}).

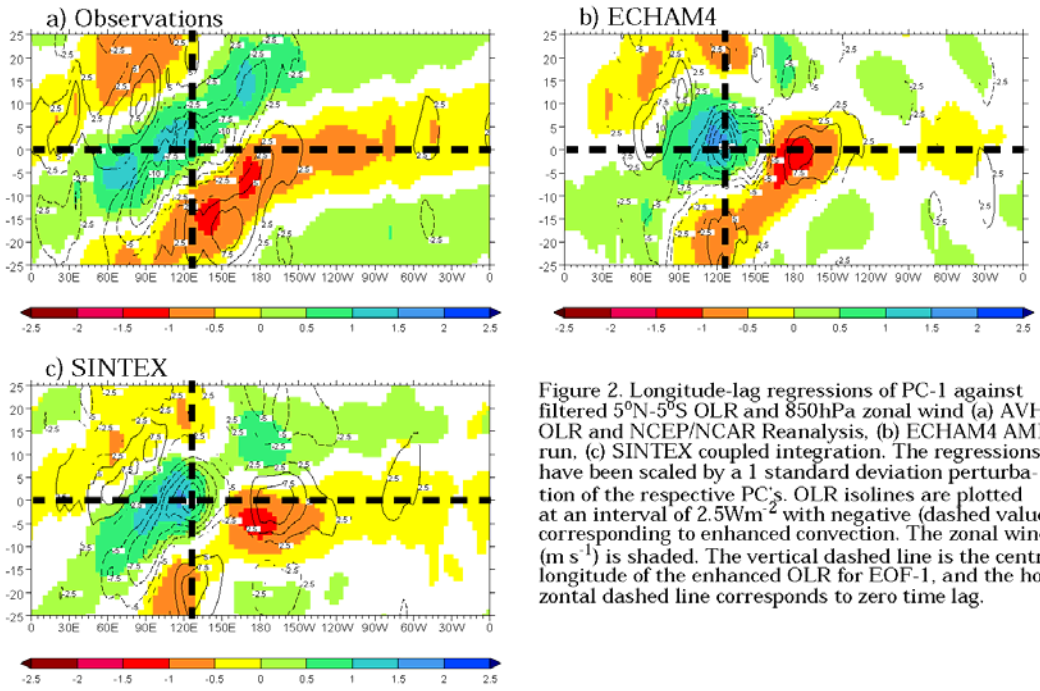

Figure 2. Longitude-lag regressions of PC-1 against filtered 5^0N-5^0S OLR and 850hPa zonal wind (a) AVHRR OLR and NCEP/NCAR Reanalysis, (b) ECHAM4 AMIP II run, (c) SINTEX coupled integration. The regressions have been scaled by a 1 standard deviation perturbation of the respective PC's. OLR isolines are plotted at an interval of 2.5Wm^{-2} with negative (dashed values) corresponding to enhanced convection. The zonal wind (m s^{-1}) is shaded. The vertical dashed line is the central longitude of the enhanced OLR for EOF-1, and the horizontal dashed line corresponds to zero time lag.

Acknowledgments. This work was performed under the auspices of the U.S. Department of Energy at the University of California Lawrence Livermore National Laboratory under contract No. W-7405-Eng-48. This is contribution UCRL-JC-150900-EXT-ABS.

References

Inness, P. M.,and J. M. Slingo, 2003: J. Clim., 16, 345-364.

Inness, P. M., J. M. Slingo, E. Guilyardi, and J. Cole, J. Clim., 16, 365-382.

Kalnay, E, M. et al, 1996: BAMS, 77, 437-471.

Liebmann, B., and C. A. Smith, 1996: Bull. Amer. Meteorol. Soc., 77, 1275-1277.

Madden, R. A. and P. R. Julian, 1971: JAS, 28, 702-708.

Madden, R. A. and P. R. Julian, 1972: JAS, 29, 1109-1123.

Sperber, K. R., 2003: Mon. Wea. Rev. (submitted)

Waliser, D. E., K. M. Lau, and J.-H. Kim, 1999: J. Atmos. Sci., 56, 333-358.

Analysis of Propagating Modes in the Tropics in Short AMIP Runs

Huug van den Dool and Suranjana Saha
NCEP/NWS/NOAA Washington DC E-mail: huug.vandendool@noaa.gov

1. Introduction and summary.

NCEP has produced in early 2002 a large set of 1-year AMIP runs of candidate next generation NWP models that may become operational, see companion paper in this volume by Saha and Van den Dool. A total of about fifteen 1-year AMIP runs were made with variation in horizontal and vertical resolution, and aspects of the physics, such as the convection scheme. The initial condition was Dec 15, 2000, and the 1 year we studied, discarding the 1st two weeks of the runs, covers Jan, 1 to Dec, 31 of 2001. A few runs were extended to 5 years, and two runs all the way out to 25 years. We here analyze the behavior of these models in the large scale tropical troposphere, primarily the MJO, the tides and the zonal mean zonal wind. Tides are studied in terms of surface pressure, while MJO is gauged by 200mb velocity potential (□). An analysis technique, named Empirical Wave Propagation (EWP), explained in section 2, is applied to model data and the results in terms of amplitude and phase speed of □ anomalies are compared to observations (~analyses from CDAS). Depending on the physical packages and the resolution, there are clear differences in strength and phase speed of large scale tropical disturbances in the models. Compared to AMIP I, when we and most other researchers concluded that the MJO was very weak in amplitude and much too fast, the current global NCEP model is better in producing stronger divergence anomalies which move in the right direction, but too slow. Model versions with better □ anomalies also tend to be better in the streamfunction □. With regards to the tides in the tropics - they are much too strong in all model runs. There are worrisome changes in the systematic error in the mean and the variance of the zonal mean zonal wind in response to changing convection scheme, but the path to model improvement, given such large sensitivity, is not clear.

2. Empirical Wave Propagation

Given is a data set X, for instance 200 mb velocity potential, once daily 0Z, on a 2.5 by 2.5 lat/lon grid, denoted as X (□ , □, t). Remove a suitable climatology (a function of day of the year and hour of the day) and retain anomaly data X'. For any given time t : project X' along a latitude circle onto the sin m□ / cos m□ orthogonal pair. This yields two coefficients (a and b), or, alternatively, amplitude (A) and phase (□) for each zonal wavenumber m, m=0 to 72, i.e.

$$X'(\square, t) = A_0 + \sum_m A_m \cos m(\square - \square_m) \quad (1)$$

(1) is just an ordinary Fourier transform. First a few comments about the amplitude A.

Note that the space-time variance $= \sum_t \sum_s X'^2 = \frac{1}{2} \sum_t \sum_m A^2_m$

$$= \frac{1}{2} \left(\sum \langle A_m \rangle^2 + \sum \langle A'^2_m \rangle \right), \text{ where } \langle\ \rangle \text{ is the time mean.}$$

$$\sum_m \quad \sum_m$$

or approximately $\frac{1}{2} \left(\sum_m <A_m>^2 \right)$

To about 75% accuracy the variance in the atmosphere can be thought of as being associated with anomaly waves with a constant time mean amplitude ($<A_m>$). The amplitude of anomaly waves, thus defined, is surprisingly constant.

These waves move! Now a few comment about the phase speed.

Take a single wave m_0 . Question: will wave m_0 on average move east or west???

At time t: $A \cos m_0(\lambda-\lambda) = a \cos m_0\lambda + b \sin m_0\lambda$ (2)

At time t+1: $A_1 \cos m_0(\lambda-\lambda_1) = a_1 \cos m_0\lambda + b_1 \sin m_0\lambda$ (2a)

Move the crest of the wave on the leading day (t) to a reference longitude (like Greenwich), this is done by phase shifting over $+\lambda$. Move the wave on the next day (t+1) over the exact same λ - this maintains the relative positioning, but in a new framework. This yields:

At time t: $A \cos m_0\lambda = A \cos m_0\lambda + 0 \sin m_0\lambda$ (3)

At time t+1: $A_1 \cos m_0(\lambda- (\lambda_1 - \lambda)) = c_1 \cos m_0\lambda + d_1 \sin m_0\lambda$ (3a)

Now do this for all pairs t/t+1!! The r.h.s. coefficients A, c_1 and d_1 are a function of time, with time means $<A>$, $<c_1>$ and $<d_1>$.{ The time mean of coefficients a and b would be zero.} The amplitudes of time averaged phase shifted wave at the leading time is simply $<A>$, while the phase angle difference t vs t+1 is given by $\lambda_{p1} = \arctan(<d_1> / <c_1>)$, and the phase speed by:

$$c(\lambda, m_0) = \lambda_{p1}(\lambda, m_0) \cdot 6375000 \cdot \cos(\lambda) / 86400 / m_0 \quad (4)$$

EWP is related to spectral analysis but uses only 1-day lagged data to determine wave speeds (and amplitude) under quasi linear conditions.

3. Results

We applied the above EWP analysis to λ anomalies for the year 2001, and show in Fig 1 the phase speed (top), amplitude (middle), and period (bottom), as a function of latitude and zonal wavenumber in the tropical strip. Clearly, λ anomalies propagate eastward, with considerable dispersion as shorter waves have little phase speed. Maximum speed and amplitude

is seen for wavenumber 1. The period is the amount of time for wave m to travel 360/m degrees of longitude. So a speed of 9 to 10 m/s for wave 1 yields the familiar MJO period of about 45 days. Fig.1 is as observed according to CDAS. Similar diagrams were made for some 15 model AMIP runs for 2001. They are not shown for lack of space, but can be viewed in http://wwwt.emc.ncep.noaa.gov/gmb/ssaha/exps/chi/spd/ . The results show the current NCEP model and its perturbation in terms of resolution etc have decent amplitude but a too low phase speed. Only the model versions with RAS convection have reasonable speed, both in and in .

In October 2002, a model was selected to be the new operational model. A 23 year AMIP run was made that allows us to discuss seasonality of anomaly behavior in that new model. In this case a 23 year climatology was removed month by month and the EWP analysis was done for each month separately. Focusing only on wave #1 along the equator, Fig 2. shows the phase speed and amplitude of zonal wave #1 as a function of month. In the analyses, CDAS (top), the phase speed is seen to vary twice a year with a maximum (~10-11 m/s) in May and November, and minima near 6 m/s in February and August-September. The amplitude has a single maximum in March and a single minimum in December. The middle (phase speed) and lower panel (amplitude) of Fig.2 show that the model (labeled prx_28/64) has little reality in its annual cycle, neither in T62L28 nor in T62L64 resolution. Waves are progressive in all seasons, but the speed is too low, especially from Oct to Jan. The amplitude may be too strong in the model, especially with 64 levels. On the whole the current model is better than at the time of AMIP I, when the amplitude was much too weak and the phase speed much too fast. Still, there is much room for improvement.

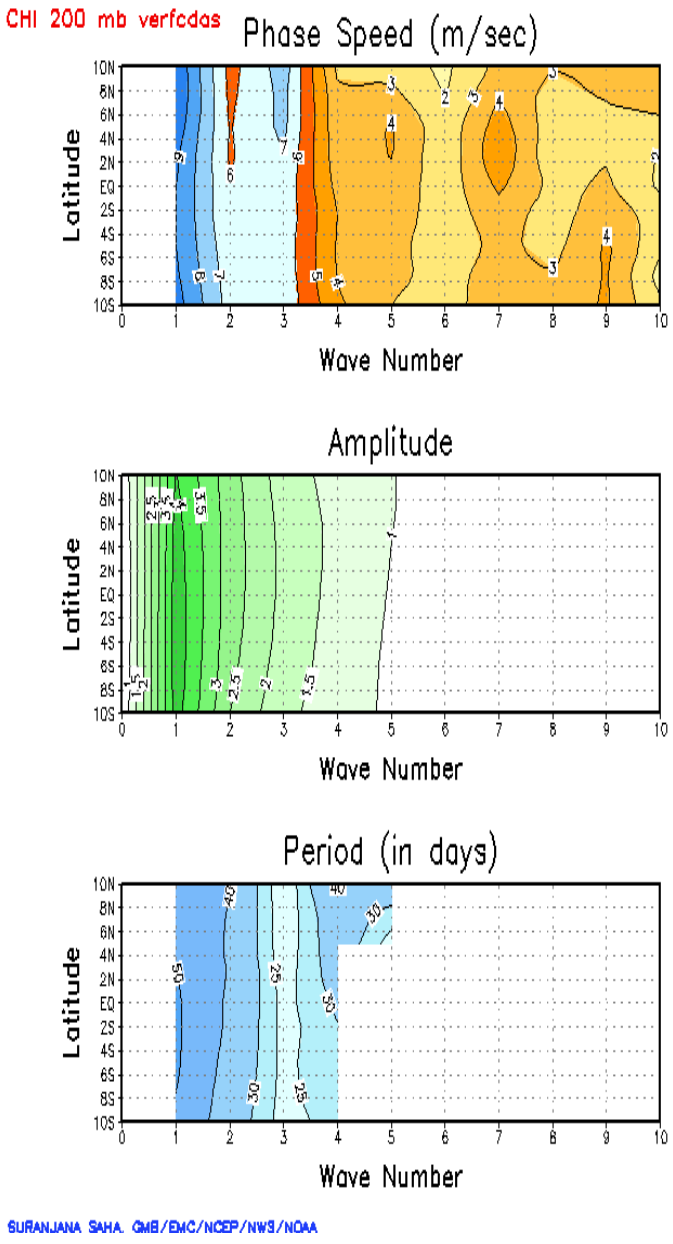

Fig. 1. The phase speed (top, m/s), amplitude (middle, 10**6 m**2/s) and period (days) of anomalies at 200mb as a function of latitude and zonal wavenumber. Calculations done with verifying analyses during 2001.

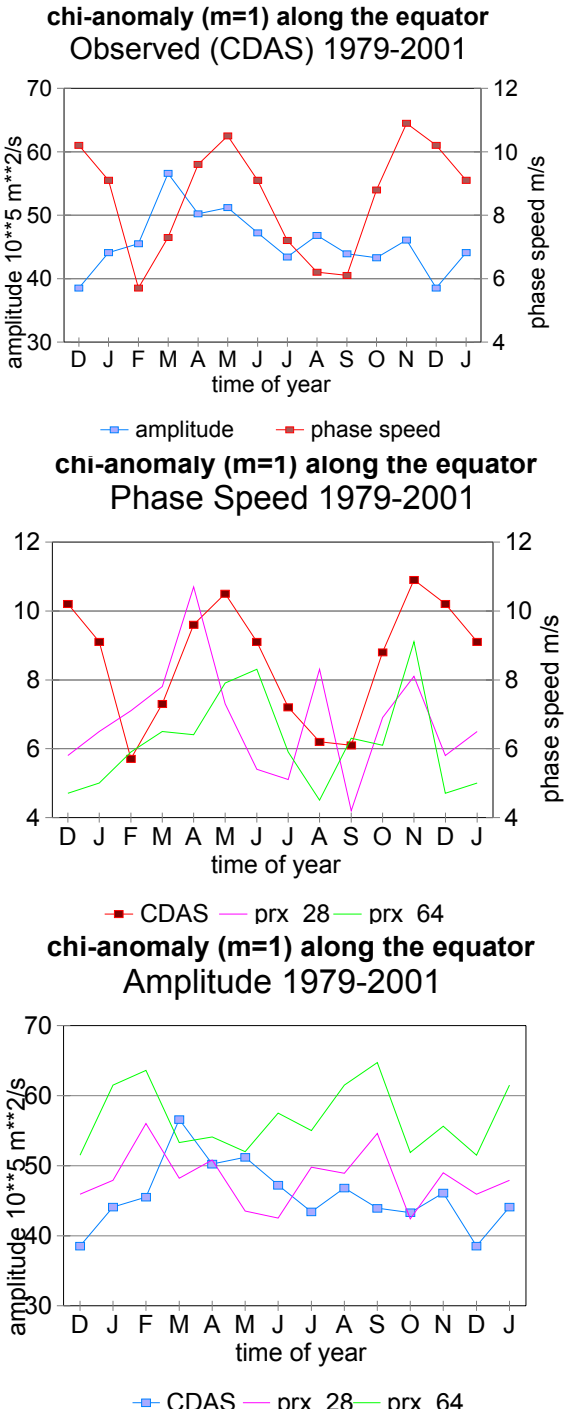

Fig.2 The phase speed (m/s), and amplitude of anomaly wave # 1 at 200mb along the equator as a function of month during 1979-2001. Top for CDAS (observed), middle and bottom the phase speed and amplitude in two model runs compared to CDAS.

Forcing of the Quasi-Biennial Oscillation from a Broad Spectrum of Atmospheric Waves

M. A. Giorgetta, E. Manzini, and E. Roeckner
Max Planck Institute for Meteorology, Bundesstr. 55, 20146 Hamburg, Germany
Email: giorgetta@dkrz.de

ABSTRACT.

The circulation of the stratosphere, and its influence on the trace constituent distribution, is an important component of the climate system, which must be included in simulations of global climate change. However, the ability to simulate a dominant stratospheric phenomenon, the Quasi-Biennial Oscillation (QBO) in equatorial zonal wind (Fig. 1a), is an outstanding challenge in climate modeling. Although confined to the tropics, the QBO affects the circulation and the interannual variability of the entire stratosphere, parts of the mesosphere and possibly also of the troposphere [*Baldwin et al.,* 2001]. Here we show that the QBO is successfully simulated in a general circulation model (GCM) of the newest generation. Key factors are a sufficient spatial resolution, a realistic simulation of tropical convection, and the consideration of the effects of gravity waves. From this simulation it is inferred that a broad spectrum of atmospheric waves is necessary to generate the QBO in the model.

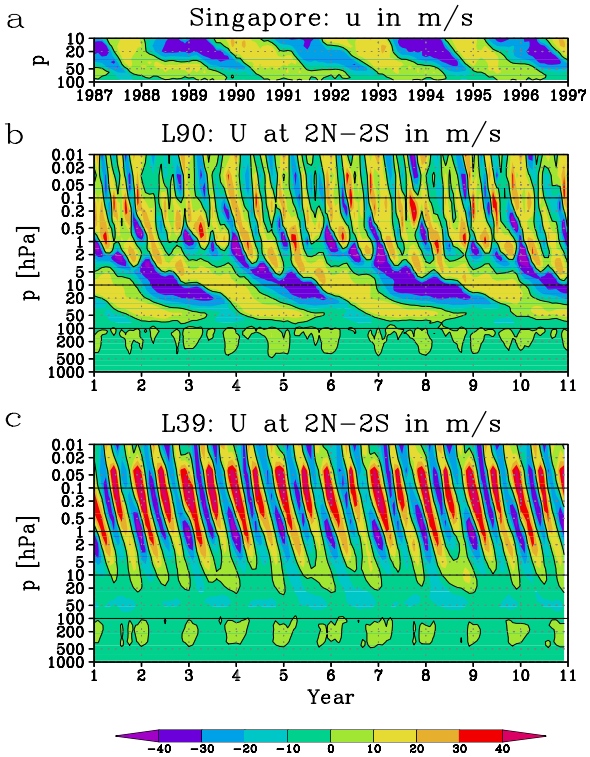

Figure 1. Singapore monthly mean zonal wind (m/s) in the lower stratosphere from 1987 to 1996 (a). Monthly and zonal mean zonal wind (m/s) at the equator in experiment L90 (b) and experiment L39 (c). The zero contour is shown in bold.

EXPERIMENTS

The GCM employed for these experiments is MAECHAM5, the Middle Atmosphere configuration of ECHAM5. With respect to its predecessor [*Roeckner et al.*, 1996; *Manzini et al.*, 1997] this new middle atmosphere GCM differs mainly in the treatment of radiation processes [*Morcrette et al.*, 1998], surface fluxes [*Schulz et al.*, 2001], and cloud physics [*Lohmann and Roeckner*, 1996]. The GCM includes parameterizations for deep convection [*Tiedtke*, 1989; *Nordeng*, 1996] and for momentum flux deposition from a spectrum of gravity waves [*Manzini et al.*, 1997].

Two experiments have been carried out, which differ by the vertical resolution only. Experiment L39 represents the control experiment using the standard vertical grid of the model, which resolves the atmosphere by 39 layers from surface up to 0.01 hPa or approximately 80 km altitude. The vertical resolution in the stratosphere decreases continuously from typically 1.5 km at the tropical tropopause to 3 km at the stratopause. Experiment L39 is integrated for 10 years starting from an initial state that does not contain a QBO structure.

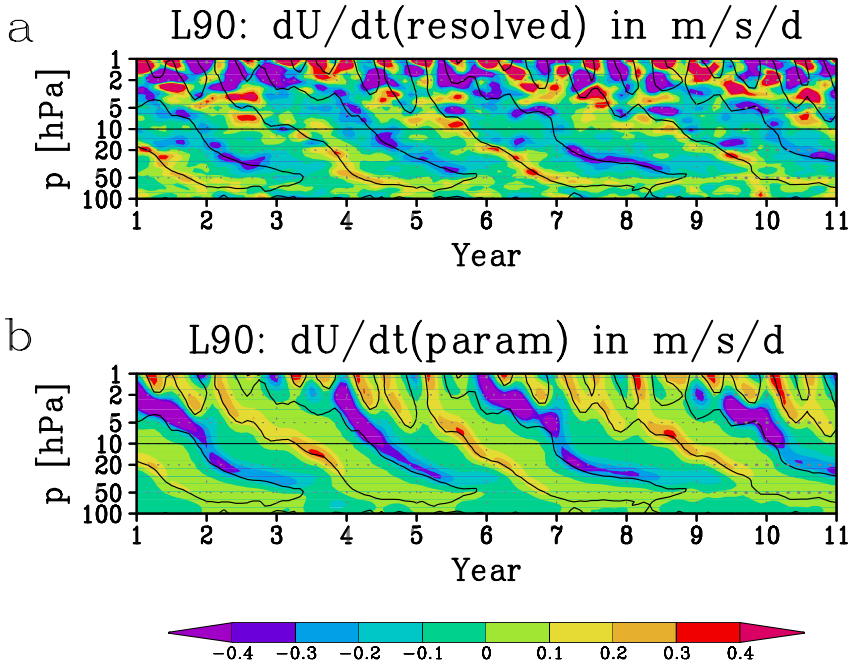

Figure 2. Monthly and zonal mean tendency of zonal wind (m/s/d) at the equator by resolved waves diagnosed as divergence of EP-flux (a) and by parameterized gravity wave dissipation (b). The zero contour of the zonal mean wind is shown in bold.

Experiment L90 resolves the atmosphere by 90 layers from surface to 0.01 hPa. The lowermost 5 layers are identical to those of L39 in order to avoid differences in turbulent vertical fluxes near the surface. The vertical resolution in the stratosphere is approximately 700 m between the tropopause and 42 km altitude, and better than 1 km up to the stratopause. This resolution is sufficient to resolve waves with vertical wavelengths of 2.8 km or longer.

Experiment L90 is integrated for 17 years starting from initial conditions without any representation of the QBO, as in experiment L39. The first 7 years of the L90 integration show a transition from the initial no-QBO state to a realistic QBO structure. Only the last 10 years of this integration are shown and discussed below.

Horizontal resolution: spectral T42 in dynamics, Gaussian grid 2.8°x~2.8° in physics.Sea surface temperature and sea ice distribution are prescribed equally in both experiments and follow the climatological annual cycle, averaged for the period 1979 to 1995.

RESULTS AND CONCLUSIONS

The simulated QBO (Fig. 1b) exhibits the typical properties of the observed QBO. Amplitudes of eastward and westward jets, the period of the QBO, the propagation characteristics of both phases as well as the differences in the latitudinal extent of both phases are realistically captured in the simulation. The QBO is obtained in an experiment that differs only by the substantially increased vertical resolution of the model (700 m in the lower and middle stratosphere) compared to the control experiment (Fig. 1c). This vertical resolution has been selected in order to allow for a better representation of the vertical structure of tropical atmospheric waves that are resolved at the given horizontal resolution [*Boville and Randel*, 1992]. Thus, the QBO wave mean-flow interaction can be resolved in the model, provided that the simulated convective heating excites a realistic spectrum of tropical waves in the troposphere. The analysis of the wave-induced zonal mean forcing due to the resolved and parameterized portions of the wave spectrum (Fig. 2) shows that both parts are relevant for the QBO forcing, in agreement with current estimates of tropical wave activity and wave mean-flow interaction in the tropical stratosphere [*Bergmann and Salby*, 1994] . Resolved waves provide, however, the largest tendencies for the downward propagation of the QBO in the lower stratosphere.

REFERENCES:

Baldwin, M. P., L. J. Gray, T. J. Dunkerton, K. Hamilton, P. H. Haynes, W. J. Randel, J. R. Holton, M. J. Alexander, I. Hirota, T. Horinouchi, D. B. A. Jones, J. S. Kinnersley, C. Marquardt, K. Sato, and M. Takahashi, The quasi-biennial oscillation, *Rev. Geophys*., *39*, 179-229, 2001.

Bergman, J. W., and M. L. Salby, Equatorial wave activity derived from fluctuations in observed convection, *J. Atmos. Sci.*, *51*, 3791-3806, 1994.Lohmann, U., and E. Roeckner, Design and performance of a new cloud microphysics scheme developed for the ECHAM general circulation model, *Climate Dyn.*, *12*, 557- 572, 1996.Manzini, E., N. A. McFarlane, and C. McLandress, Impact of the Doppler spread parameterization on the simulation of the middle atmosphere circulation using the MA/ECHAM4 general circulation model, *J. Geophys. Res.*, *102*, 25751-25762, 1997.

Morcrette, J.-J., S. A. Clough, E. J. Mlawer, and M. J., Iacono, Impact of a validated radiative transfer scheme, RRTM, on the ECMWF model climate and 10 day forecasts, ECMWF Research Department Tech. Memo. No. 252, ECMWF, Reading, 1998.

Nordeng, T. E., Extended versions of the convective parametrization scheme at ECMWF and their impact on the mean and transient activity of the model in the tropics, ECMWF

Research Department Techn. Memo 206, ECMWF, Reading, 1996.Roeckner, E., K. Arpe, L. Bengtsson, M. Christoph, M. Claussen, L. Dümenil, M. Esch, M. Giorgetta, U. Schlese, and U. Schulzweida, The atmospheric general circulation model ECHAM-4: Model description and simulation of present day climate, MPI-Report 218, Max Planck Institute for Meteorology, Hamburg, 1996.

Schulz, J.-P., L. Dümenil, and J. Polcher, On the land surface atmosphere coupling and its impact in a single-column atmospheric model, *J. Appl. Meteor.*, *40*, 642-663, 2001.

Tiedtke, M., A comprehensive mass flux scheme for cumulus parameterization in large-scale models, *Mon. Weather Rev.*, *117*, 1779-1800, 1989.

FLUXES, CLOUDS AND RADIATION

Using ARM Data for Model Diagnostics

Jean-Jacques Morcrette
European Centre for Medium-Range Weather Forecasts
Shinfield Park, Reading Berkshire RG2 9AX, United Kingdom
e-mail: Jean-Jacques.Morcrette@ecmwf.int

Abstract:

The cloud and radiation fields produced by the operational ECMWF forecasts are assessed using observations from the Atmospheric Radiation Measurement Program (ARM) South Great Plains (SGP) site over the April-May 1999 period. Over the first 36 hours of the forecasts, most of the model fields, taken over a 24-hour time window (either 0-24, 6-30, or 12-36-hour) are generally consistent with each other. Comparisons of model fields taken from any such 24-hour time window with observations are therefore representative of the quality of the ECMWF model physical parameterizations. The surface radiation fluxes are assessed separately for clear-sky, overcast, and whole-sky situations. For clear-sky fluxes, differences between model and observations are linked to differences in humidity and temperature profiles, the characterization of aerosols, and systematic errors in the shortwave radiation scheme. Model cloud occurrences and boundaries over the Central Facility are compared with similar quantities derived from radar and micropulse lidar observations. Model cloud water is tentatively assessed through comparisons with the radar reflectivity measurements. Systematic deficiencies in the surface radiation fields in presence of clouds are discussed with respect to differences between the model and observed cloud characteristics. Given the T_L319 resolution of the ECMWF model at the time of the comparisons, both the day-to-day and temporal variability within-the-day are reasonably well captured by 24-hour forecasts including cloud-radiation interactions with 1-hour time resolution. However, most of the differences with observations can be traced back to either deficiencies in the clear-sky shortwave radiation scheme, or problems in the cloud fraction and/or cloud water content. A full version of this study is available in Morcrette (2002).

1. Methodology

The study covers the whole months of April and May 1999. A spring period was preferred because spring had, in the past, not been a particularly good period for ECMWF forecasts. Moreover, for somewhat average conditions of temperature and humidity, a large temporal variability can be expected at the latitude of the ARM-SGP site (Lamont, Oklahoma, 36.605 ^{o}N, 97.485 ^{o}W), depending on the flow direction of the prevalent air mass. In the following, use is made of measurements by the observational systems located at the Central Facility.
The ECMWF fields correspond to outputs every one hour for all 36-hour forecasts starting 24-hours apart between 19990331 12UTC and 19990531 12 UTC. The analyses from which the forecasts were started are obtained through a 4-D variational assimilation of all the observations during a 6-hour window centered around the analysis time. The model used in this study is the so-called cycle 23R1 of the ECMWF Integrated Forecast System, operational between 27 June and 11 November 2000. Among the modifications introduced with cycle 23R1 are the replacement of the previous longwave (LW) scheme (Morcrette, 1991) by the Rapid Radiation Transfer Model (Mlawer et al., 1997) and the introduction of a tiling scheme for the surface

processes. The M91 scheme included cloud effects using maximum-random overlap of effective cloud layers through an effective emissivity approach. The ECMWF version of the RRTM LW scheme also includes a maximum-random overlap assumption but keeps the cloud fraction and cloud optical thickness as two separate quantities.

The rest of the package of physical parameterizations follows Gregory et al. (2000). All cloudy fluxes are computed from cloud optical thicknesses derived from the prognosed liquid and ice cloud water content weighted by a 0.7 inhomogeneity factor following Tiedtke (1996). The dynamical part of the model includes the two-time-level semi-lagrangian scheme (Hortal, 2000) on a linear grid of Hortal and Simmons (1991), which keeps roughly the same dimension going towards the poles.

In the study presented here, the T_L319 L60 model (about 60 km horizontal resolution and 60 levels in the vertical) is run with a 20-minute time-step. The 60-level vertical resolution includes about twelve levels between the surface and the average top of the planetary boundary layer (PBL). The full radiation computations (i.e., those using updated cloud fraction and cloud water) are called every hour.

2. Comparisons at the Central Facility

2.1. Total column water vapor and cloud water

The model total column water vapor (TCWV) and total column cloud water (TCCW) are compared over April 1999, with quantities derived from Microwave Radiometer (MWR) observations in Figure 1 (top and bottom, respectively). The agreement in TCWV is quite good, especially for the low values. For the highest values, some uncertainty might exist in the observations, due to moisture condensing on the observing device. The periods over which such a problem occurs are given by the wet index at the bottom of Figure 1a, and top of Fig 1b.

The total column cloud water (TCCW) (Fig. 1 bottom) is much more difficult to assess. The model TCCW includes both the liquid and ice water, whereas the retrieved TCCW based on the difference between observations at 23.8 and 31.4 GHz is really cloud liquid water only. The peaks in the observations obviously correspond to clouds above the MWR. They are also usually flagged as wet, so the observations are likely to include precipitation.

Figure 1 (top)

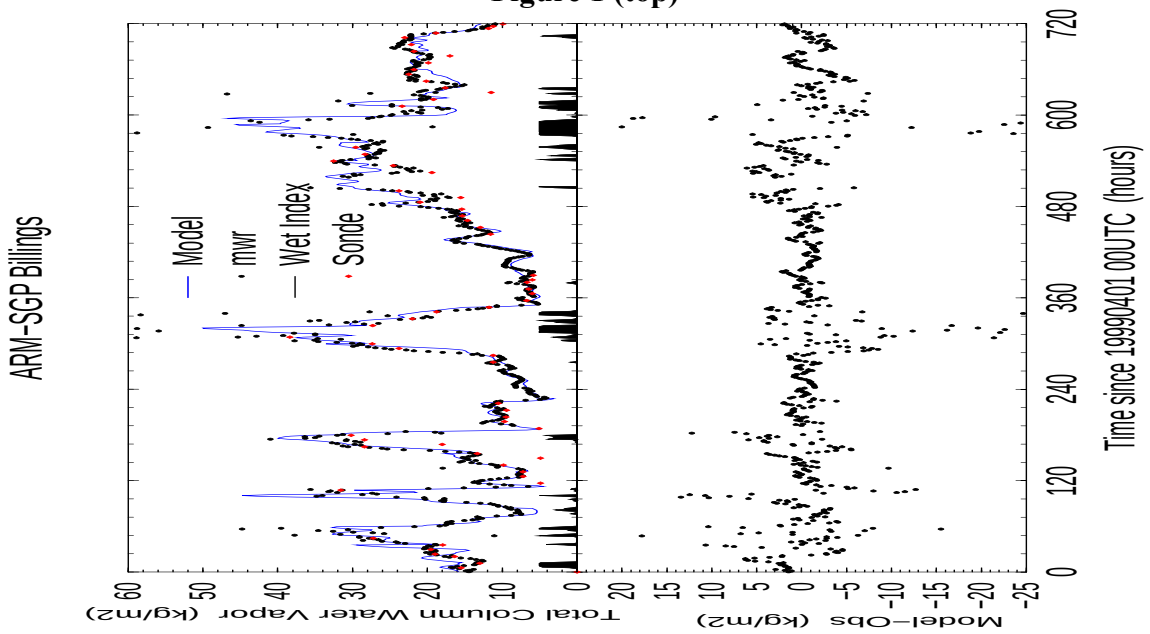

Figure 1 (bottom)

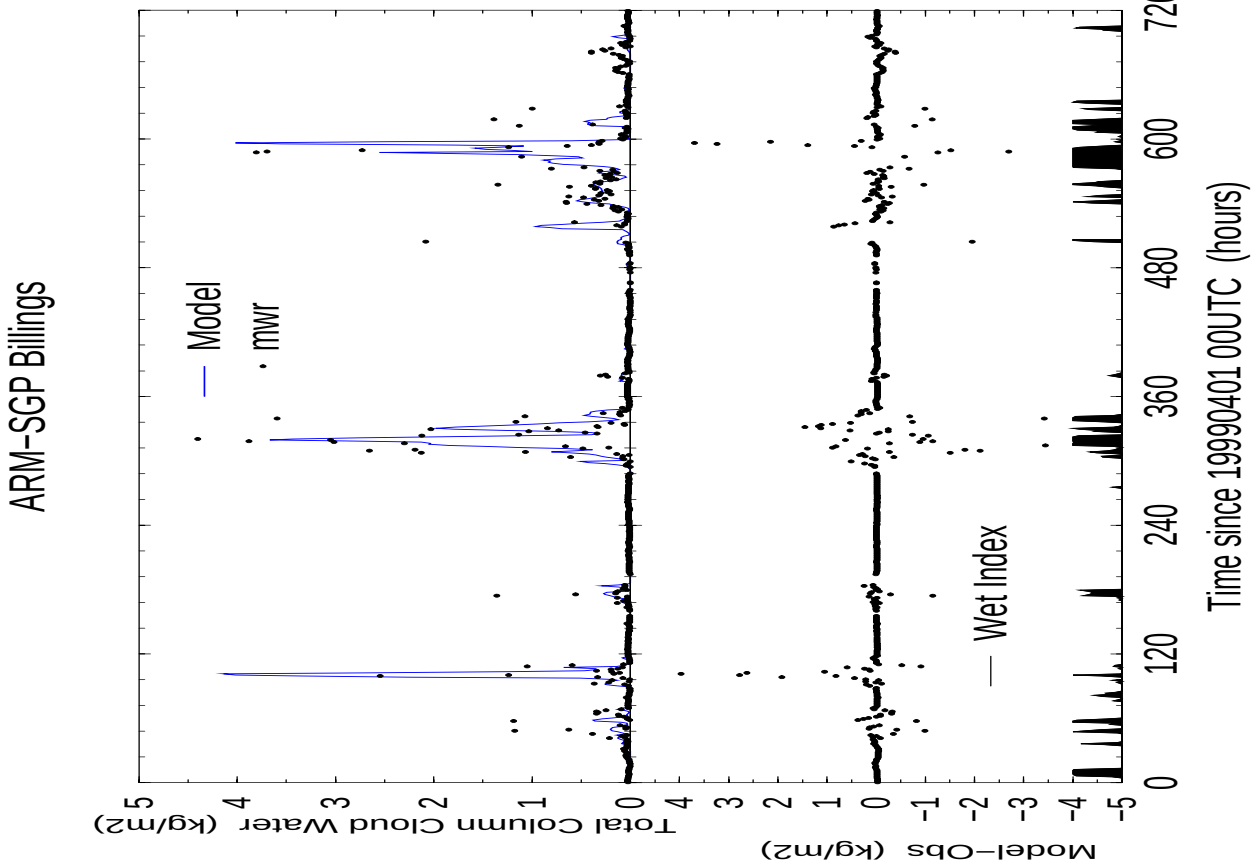

2.2. Downward radiation

The corresponding surface downward SW and LW radiation (referred to as SSRD, and STRD, within the ECMWF model and archive) are presented in Figure 2 (top for SSRD, bottom for STRD) as measured from two sets of radiometers located at the Central Facility (C1 and E13) and as represented by the model forecasts. For all the time slots for which both the E13 and C1 measurements are available over the April-May period, the correlation between the two stations is better than 0.999 for both SSRD and STRD. Some uncertainty arises from the (small) negative values usually reported by the pyranometers during nighttime. Statistics for SSRD were computed in three different ways, the first set corresponding to all observations during the period, the second set to all observations with nighttime values set to zero, and the third set to daytime observations only. Over the 2-month period of the observations, the difference between the first two approaches is at most 2.5 Wm^{-2}. In both cases, the correlation is practically unity, and the slope higher than 0.998. Therefore, the slight disagreement between these two approaches is unlikely to be of concern for evaluating the model behavior.

In clear-sky atmosphere, the STRD is between 240 and 290 Wm^{-2}. Only when clouds are present, does STRD get over 300 Wm^{-2}, with the values over 360 Wm^{-2} corresponding to the presence of low level cloudiness. There is a reasonable agreement between model and observed STRD (Fig.2, bottom), reflecting the ability of the model to produce the cloud events at the right time, with cloud base close to the proper height.

From the 1464 (=61 days x 24) one-hour slots in April-May 1999, 168 clear-sky situations have been extracted (only 164 such situations are for daytime conditions, and are thus used for the SW). This extraction is based on the following set of conditions: a model total cloud cover < 1%, no return from the Multi-Mode Cloud Radar (MMCR), no cloud base from the Micropulse Lidar (MPL), and a zero wet index from the Microwave Radiometer (MWR). Over this set of profiles, there is a very good agreement between the MWR-observed and model TCWV and STRD. The agreement for STRD is within the range obtained when comparing C1 and E13 SIRS measurements. In contrast, even on these selected clear-sky cases, the model SSRD overestimates the observed SSRD by 31.2 Wm^{-2} over the 164 daytime situations. This reflects a likely bias in the SW radiation scheme and with possibly a small contribution from an improper specification of the aerosol optical thickness.

Figure 2 (top)

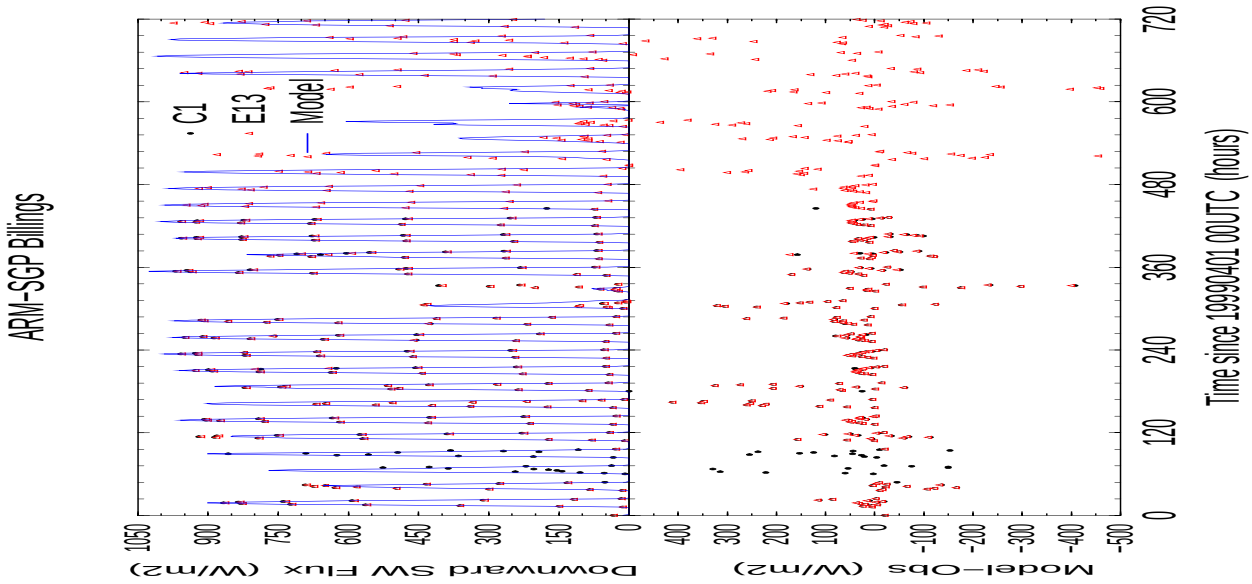

Figure 2 (bottom)

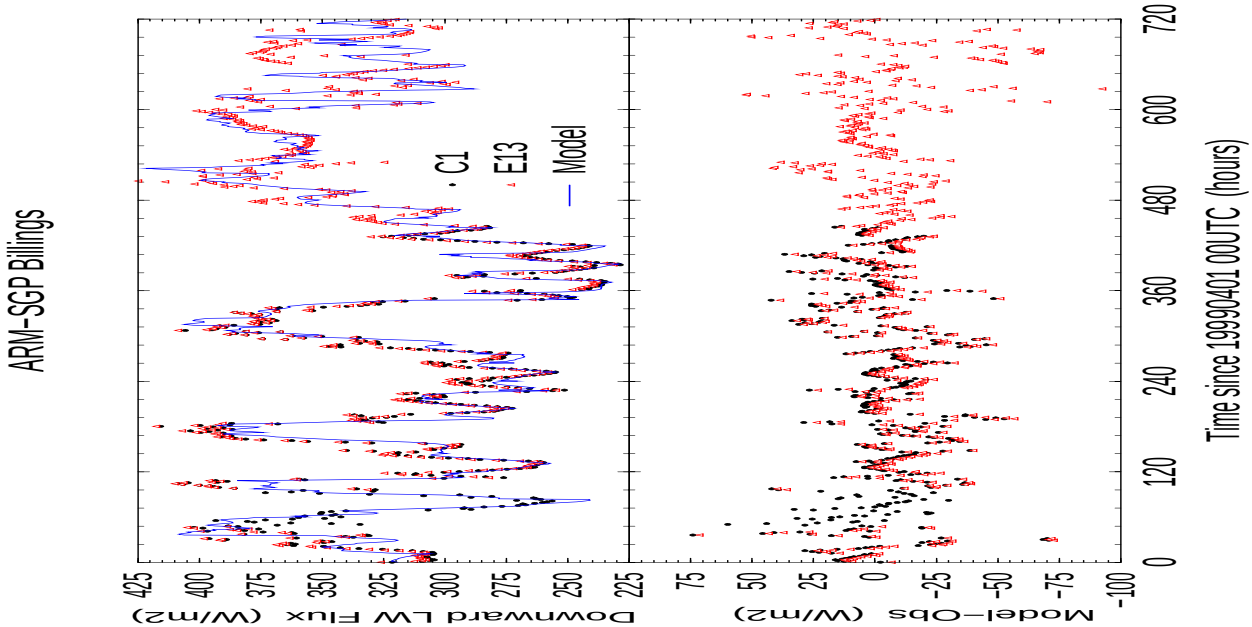

In the presence of cloudiness, the discrepancies between model and observed surface radiation fluxes are as likely to come from incorrect atmospheric profiles, incorrect definition of the cloud parameters (cloud base height and optical properties) produced by the forecasts as from the radiation schemes used in the model. Therefore a set of 59 overcast situations (25 during daytime are used for SSRD) has been extracted, for which the model total cloud cover (TCC) is > 99%,

with presence of clouds during all intervals making the one-hour slot in the MMCR, BLC and MPL observations. These cases show an agreement on both the cloud cover and the cloud base height. However, the comparison between MWR-observed and model TCWV is certainly affected by moisture condensating (dew) or precipitating on the observing device. The agreement in STRD is again good (with a 2 Wm^{-2} model overestimation). Again, the model SSRD overestimates the observed SSRD by 26.4 Wm^{-2}. The overestimation is consistent with the deficiency already seen for the SW radiation scheme in clear-sky conditions, but problems in the definition of the cloud optical parameters (optical thickness in particular) cannot be ruled out and are as likely to increase as decrease the clear-sky error.

Over the 1436 LW comparisons, the model underestimates the observations by 2 Wm^{-2}. The SW comparisons are restricted to 821 daytime comparisons and show a 17 Wm^{-2} overestimation by the model.

The net radiation (SWdown - SWup + LWdown -LWup), for April 1999, as produced by the model, was compared to observations by the Energy Balance Bowen Ratio system at station E13. In the model, the often large overestimation of the SSRD, the slight underestimation of STRD, and the too large skin temperature at night all contribute to the model producing too much energy input to the surface during daytime, and too much energy output from the surface at night.

2.3. Cloudiness

The temperature and humidity in the first 3000 m above the surface forecasted by the ECMWF model were compared to the temperature and humidity derived from the AER interferometer (AERI). There is an overall good agreement between model and observations, with the range of differences going from -11.0 to 11.6 K for temperature and from -5.2 g kg-1 to 8.3 g kg^{-1} for humidity. However, the average bias over the first 3000 m of the atmosphere varies between -1.6 K at the surface and 0.7 K at 3000 m for temperature, and between -0.2 g kg^{-1} at 300 m and 0.3 g kg^{-1} at 1800 m.

The capability of the ECMWF model to produce cloudiness at the proper time and height can be also judged by comparing the model cloud fraction with a so-called cloud mask produced from radar measurements and/or the height of clouds detected by the micropulse lidar (MPL) or the Beaufort Laser Ceilometer (BLC). When a large amount of clouds, with substantial low-level cloudiness, is present (2-3, 7, 13-14, 24-25 April), the agreement for cloud base height between BLC measurements and the model is generally good. At other times, the agreement is much poorer, and the cloudiness derived from MMCR measurements often does not support the BLC measurements. A Ze-reflectivity simulated using IWC-Ze and LWC-Ze relationships from the model IWC and LWC fields, is presented in Figure 3 (top panel). Details of the procedure follows Beesley et al. (2000). The corresponding Ze-reflectivity derived from MMCR measurements by Clothiaux et al. (2000) are presented in the bottom panel of Figure 3. The effect of heavy precipitation on the radar reflectivity data can be seen on the 2nd, 7th, 13th and 24th of April. The observed reflectivity saturates at these times corresponding to a wet index of 1 in the MWR measurements.

The comparison of the two panels in Fig. 3 shows that, in terms of reflectivity, the model is in the ball park of the measurements, particularly for the higher-level (ice) clouds. The results are

obtained using the IWC-Ze relationship of Atlas et al. (1995) for a 100 mm equivalent particle diameter Do, within the range 60-120 mm diagnosed by the model from temperature following Matveev (1984). However, as seen in an intercomparison of Ze-reflectivities derived from the same model ice content, differences up to several dBZ exist between the various IWC-Ze relationships or when Do is allowed to vary between 100 and 900 mm in Atlas et al.'s relationships. So the obtained agreement between model and observations cannot be taken as a sure proof of the adequacy of the model cloud ice water content.

For liquid water clouds, the agreement between the various theoretical relationships is much better, so a disagreement between model and observations is likely to indicate a problem in the distribution of the model cloud liquid water content. As seen in a similar intercomparison of Ze-reflectivities from the same model liquid water content, the LWC-Ze curves remain within 2 dBZ of each other. The agreement is down to 1 dBZ for Frisch et al.'s relationships when the particle number concentration varies between 150 and 900 cm-3, which correspond to the concentrations implicitly assumed for ocean and land in the ECMWF model. A comparison of the lower parts of clouds in Figure 3 indicates that, for liquid water clouds, the model reflectivity is generally too low.

Acknowledgments:

Dr. Clothiaux is gratefully thanked for providing the radar and micropulse lidar measurements used in this study. Thanks to Robin Perez for help in acquiring all the other observational data and pointing to the relevant documentation. These observational data were obtained from the Atmospheric Radiation Measurement (ARM) Program sponsored by the U.S. Department of Energy, Office of Science, Office of Biological and Environmental Research, Environmental Sciences Division.

REFERENCES

Atlas, D., S.Y. Matrosov, A.J. Heymsfield, M.-D. Chou, and D.B. Wolff, 1995: Radar and radiation properties of ice clouds. J. Appl. Meteor., 34, 2329-2345.

Beesley, J.A., C.S. Bretherton, C. Jakob, E.L. Andreas, J.M. Intrieri, and T.A. Uttal, 2000: A comparison of cloud and boundary layer variables in the ECMWF forecast model with observations at the Surface Heat Budget of the Arctic ocean (SHEBA) ice camp. J. Geophys. Res., 105D, 12337-12350.

Clothiaux, E.E., T.P. Ackerman, G.C. Mace, K.P. Moran, R.T. Marchand, M.A. Miller, and B.E. Martner, 2000: Objective determination of cloud heights and radar reflectivities using a combination of active remote sensors at the ARM CART sites. J. Appl. Meteor., 39, 645-665.

Frisch, A.S., C.W. Fairall, and J.B. Snider, 1995: Measurement of stratus cloud and drizzle parameters in ASTEX with a Ka-band Doppler radar and a microwave radiometer. J. Atmos. Sci., 52, 2788-2799.

Gregory, D., J.-J. Morcrette, C. Jakob, A.C.M. Beljaars, and T. Stockdale, 2000 : Revision of convection, radiation and cloud schemes in the ECMWF Integrated Forecasting System. Quart. J. Roy. Meteor. Soc., 126, 1685-1710.

Hortal, M., 2000: The development and testing of a new two-time-level semi-Lagrangian scheme (SETTLS) in the ECMWF forecast model. Quart. J. Roy. Meter. Soc., in press.

Hortal, M., and A.J. Simmons, 1991: Use of reduced Gaussian grids in spectral models. Mon. Wea. Rev., 119, 1057-1074.

Matveev, Yu. L., 1984 : Cloud dynamics. D. Reidel Publishing Co., Dordrecht, 340 pp.

Mlawer, E.J., S.J. Taubman, P.D. Brown, M.J. Iacono, and S.A. Clough, 1997: Radiative transfer for inhomogeneous atmospheres: RRTM, a validated correlated-k model for the longwave. J. Geophys. Res., 102D, 16,663-16,682.

Morcrette, J.-J., 1991: Radiation and cloud radiative properties in the ECMWF operational weather forecast model. J. Geophys. Res., 96D, 9121-9132.

Morcrette, J.-J., 2002: Assessment of the ECMWF model cloudiness and surface radiation fields at the ARM-SGP site. Mon. Wea. Rev., 130, 257-277. (also, 2001: ECMWF Technical Memorandum No. 327, 43 pp.)

Tiedtke, M., 1993: Representation of clouds in large-scale models Mon. Wea. Rev., 121, 3040-3061.

Tiedtke, M., 1996: An extension of cloud-radiation parameterization in the ECMWF model: The representation of sub-grid scale variations of optical depth. Mon. Wea. Rev., 124, 745-750.

Using the ISCCP Simulator to Assess Cloudiness in GCMs

Mark Webb[1] and Stephen Klein[2]

[1]Hadley Centre, Met Office, UK, mark.webb@metoffice.com
[2]NOAA/GFDL, Princeton, New Jersey, USA, sak@gfdl.noaa.gov

The International Satellite Cloud Climatology Project (ISCCP - Rossow &Schiffer 1999) provides near-global cloud retrievals from operational weather satellite radiances, with gridded statistical summaries of cloud occurrence in various categories of cloud top pressure (Pc) and column cloud optical thickness (tau) available from 1983 to 2001. Although widely used in the validation of GCMs, it is not possible to make a quantitative comparison between multi-level ISCCP data and unprocessed GCM output due to various inconsistencies i.e.: 1) ISCCP's view from above means that low clouds are obscured when high clouds are present - what is retrieved is a single column cloud top pressure rather than a cloud profile. 2) Comparing with unprocessed GCM cloud variables does not include the effects of the cloud overlap assumptions in the GCM radiation code. 3) ISCCP optical property assumptions and those in the GCM are usually inconsistent.

In theory a radiance code in a GCM could simulate synthetic versions of the operational radiances (including satellite track information, viewing angles, etc.) The exact ISCCP retrieval algorithm could then be applied to produce synthetic ISCCP data, and any systematic differences between the model derived ISCCP diagnostics and the real ISCCP retrievals would be proof of deficiencies in the GCM. This 'ideal' approach would remove all inconsistencies, but would require the simulation of sampling from various satellites within the GCM, which is not considered practical at present.

Instead, a more practical approach was taken initially by Yu et al (1996) (LMD GCM) and Del Genio et al. (1996) (GISS GCM) which was to simulate the key features of the ISCCP retrieval that lead to inconsistencies with GCMs. This 'practical' approach is similar to that outlined above, but neglects angular effects and does not reproduce the sampling features seen in the ISCCP data between the regions viewed by different satellites (e.g. over the Indian ocean.)

A number of more recent studies have applied this approach using the Klein and Webb ISCCP simulator (Klein and Jakob, 1999 and Webb et al 2001), also known as (ICARUS/SCOPS). SCOPS (Subgrid Cloud Overlap Profile Sampler, developed by Mark Webb) samples the subgrid cloud overlaps from the GCM gridbox to give cloud profiles on scales more comparable with ISCCP pixels. ICARUS (ISCCP Clouds And Radiances Using SCOPS, developed by Stephen Klein) then converts the profiles sampled by SCOPS into ISCCP-like retrievals by: 1) Calculating a VIS cloud optical thickness for each subgrid profile sample by summing the optical thickness on model levels. 2) Calculating a nadir IR radiance and 'retrieving' a radiative cloud top using a single-level cloud retrieval model with a VIS adjusted emissivity. 3) Applying an optical thickness cut off at a level consistent with the lower limit of the ISCCP cloud detection scheme.The joint code requires instantaneous values cloud fraction, cloud optical thickness and cloud emissivity for each cloud type (e.g.stratiform, convective), as

well as temperature and water vapour, on radiation timesteps. It is written in FORTAN77 and can be built into a GCM/CRM or run on high frequency

Model output.

Webb et al (2001) ran the ISCCP simulator on model output generated as part of an EU Project (FP IV) on Cloud Feedbacks and Validation, an intercomparison of UKMO (HadAM4), ECMWF (cycle 16r2) and LMD (LMDZ 2.0) model versions. The figure shows distributions of cloud occurrence in the ISCCP C1 cloud categories for the observations and the three models, as well as a composite breakdown of the ERBE shortwave and longwave cloud radiative forcing into contributions from low, mid-level and high top clouds. This comparison shows that the UKMO and ECMWF model versions compared here both underestimate mid-level top cloud, but that the associated lack of shortwave cloud radiative forcing from mid levels is compensated for in the UKMO model by extra cloud forcing from the low clouds. The LMD model version has the best distribution of mid-level top clouds, and so has a better simulation of the longwave cloud radiative forcing than the other two in this region.

Other more recent studies have used compositing to relate ISCCP diagnostics to the local dynamical environment:

Klein & Jakob (1999) applied the method of Lau and Crane (1995) to the ECMWF model and showed that in mid-latitude cloud systems the ECMWF low clouds were too optically thick, the high clouds too optically thin, and that mid-level top cloud was missing from some areas.

Tselioudis et al (2000) Proposed that dynamical changes under climate change can drive cloud feedbacks and devised a 'cloud survey' compositing technique to focus on all clouds rather than just those which are strongly dynamically forced (as with Lau & Crane, Klein &Jakob)

Norris and Weaver (2001) Modified the 'cloud survey' technique and showed that errors in NCAR CCM3 cloud amounts in subsidence regimes can lead to errors in coupling of interannual cloud variations with SST.

Bony et al (1997) and Williams et al (2002) have suggested that compositing may allow some cloud feedbacks to be related to present day cloud variability.

A recently announced proposal from WGCM (WCRP Working Group on Coupled Modelling) by Bryant McAvaney (BMRC) and Herve Le Treut (LMD) plans to build the simulator into different GCMs and to examine cloud feedbacks in more detail in Cess et al style +/-2K experiments, and equilibrium 2CO2 slab ocean experiments. The ISCCP simulator is available for free from http://gcss-dime.giss.nasa.gov.

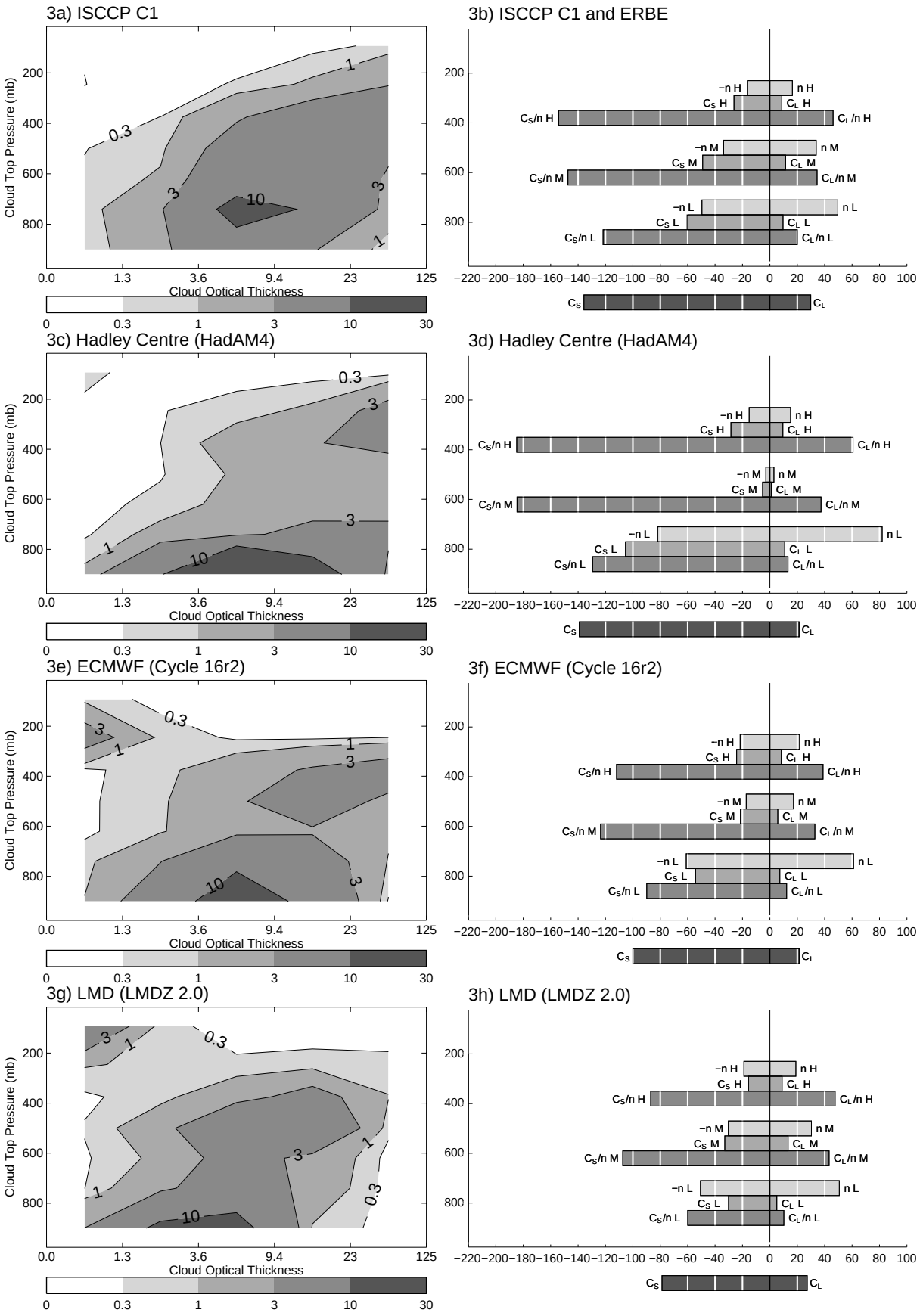
3a) ISCCP C1
3b) ISCCP C1 and ERBE
3c) Hadley Centre (HadAM4)
3d) Hadley Centre (HadAM4)
3e) ECMWF (Cycle 16r2)
3f) ECMWF (Cycle 16r2)
3g) LMD (LMDZ 2.0)
3h) LMD (LMDZ 2.0)
Cloud Top Pressure (mb)
Cloud Optical Thickness
0.0 1.3 3.6 9.4 23 125
0 0.3 1 3 10 30
200 400 600 800
−220 −200 −180 −160 −140 −120 −100 −80 −60 −40 −20 0 20 40 60 80 100
−n H
n H
CS H
CL H
CS/n H
CL/n H
−n M
n M
CS M
CL M
CS/n M
CL/n M
−n L
n L
CS L
CL L
CS/n L
CL/n L
CS
CL

Figure: July 1988 monthly averaged ISCCP-like cloud distribution in the mid-latitude north Pacific 160-235E, 40-60N (a,c,e,g)) and breakdown of the longwave and shortwave cloud radiative forcing Cl and Cs as a function of nL, nM and nH, the percentages of occasions where the daily mean is dominated by low, mid-level and high top cloud respectively (b,d,f,h).

BIBLIOGRAPHY:

Bony S., K.-M. Lau and Y.C. Sud, 1997: Sea-Surface Temperature and Large-Scale Circulation Influences on Tropical Greenhouse Effect and Cloud Radiative Forcing, J. Climate, 10, 2055-2077.

Del Genio, A.D., 1996: A prognostic cloud water parameterization for global climate models. J. Climate, 9, 270-304.

Klein, S. A., and C. Jakob, 1999: Validation and sensitivities of frontal clouds Simulated by the ECMWF model. Monthly Weather Review, 127(10), 2514-2531.

Norris J.R., Weaver C.P, 2001 Improved techniques for evaluating GCM cloudiness applied to the NCAR CCM3. J Climate, 14, 2540-2550.

Rossow W.B, Schiffer, R.A.,1999 Advances in understanding clouds from ISCCP. Bulletin of the American Meteorological Society, 80(11),2284-2287

Tselioudis, G., Zhang Y.-C., Rossow W.B., 2000, Cloud and radiation variations associated with Northern Hemisphere midlatitude low and high sea level pressure regimes, J. Clim., 13, 312-327.

Webb, M., C. Senior, S. Bony, J.-J; Morcrette, 2001, Combining ERBE and ISCCP Data to assess clouds in the Hadley Centre, ECMWF and LMD atmospheric climate Models, Climate Dynamics, 17, 905-922.

Williams, K.D., M.A. Ringer and C.A. Senior, 2003 Evaluating the cloud response to climate change and current climate variability. Accepted by Clim. Dyn.

Yu, W., Doutriaux, M., Seze, G., Le Treut, H., Desbois, M., 1996 A methodology study of the validation of clouds in GCMs using ISCCP satellite observations. Climate Dynamics, 12, 389-401.

Evaluation of Radiative Fluxes in AMIP-type GCM Experiments Based on Surface Observations

Martin Wild

Swiss Federal Institute of Technology, Institute for atmospheric and climate sciences,
Winterthurerstr. 190, CH-8057 Zurich, Switzerland , email: wild@geo.umnw.ethz.ch

ABSTRACT

Surface and atmospheric radiation budgets from 20 GCMs are assessed in the framework of the AMPI II Diagnostic Subproject No. 32 „surface and atmospheric radiative fluxes“, based on direct observations at the surface. Common biases in the AMIP II GCMs include a tendency towards excessive surface insolation, due to a lack of atmospheric absorption, and a too small longwave downward radiation at the surface.

INTRODUCTION

Substantial uncertainty still exists regarding the distribution of radiative energy within the global climate system, and its representation in General Circulation Models (e.g., Gleckler et al. 1993, Wild et al. 1995, 1998, 2002). Radiative flux fields from 20 different models participating in AMIP II were made available for this study, reflecting the status of the AMIP II database as for October 2002. The observational data for the assessment of the GCM-calculated radiative fluxes have been retrieved from two databases established at the Swiss Federal Institute of Technology: The Global Energy Balance Archive (GEBA, Gilgen and Ohmura 1999) and the database of the Baseline Surface Radiation Network (BSRN, Ohmura et al. 1998).

RESULTS

The global mean absorbed shortwave radiation at the earth's surface calculated by the 20 AMIP II GCMs are displayed in Fig. 1. Large differences in the range of more than 30 Wm^{-2} in the global mean are found amongst the GCMs. Most values are also substantially larger than two additional estimates given in Fig. 1 which incorporate direct surface observations from GEBA (Ohmura and Gilgen 1993, Wild et al. 1998). The excessive radiation at the surface is not so much related to biases in the total shortwave absorption of the climate system, since the top of atmosphere balances are often tuned to match the satellite values (cf. Table 1). Rather, a lack of absorption of solar energy in the atmosphere is responsible for the excessive radiation at the surface. The large discrepancies in the GCM-calculated absorption of solar radiation in the atmosphere become apparent in Fig. 2 and Table1, covering a range of almost 30 Wm^{-2}. The lack of an adequate representation of aerosols (Wild 1999) as well as underestimated water vapor absorption (Wild et al. 1998, Wild 2000) have been suggested as contributors to the excessive insolation at the surface and the associated lack of atmospheric absorption.

Figure 1

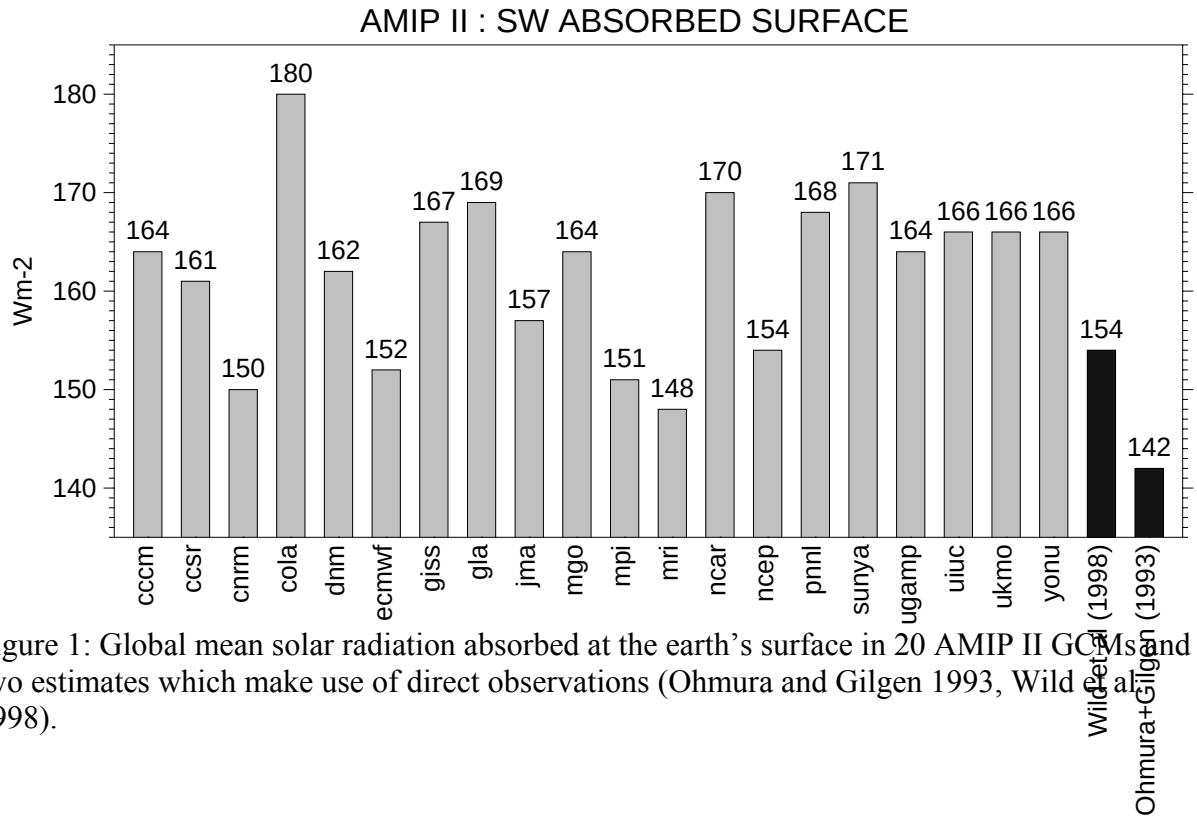

Figure 1: Global mean solar radiation absorbed at the earth's surface in 20 AMIP II GCMs and two estimates which make use of direct observations (Ohmura and Gilgen 1993, Wild et al. 1998).

Figure 2

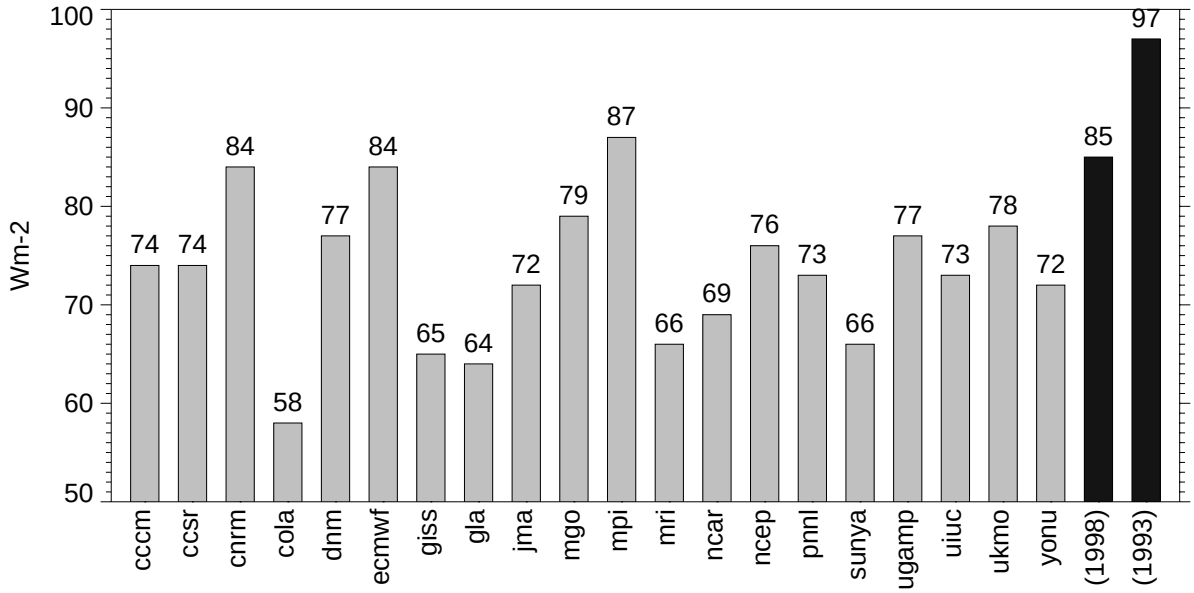

Figure 2: As Figure 1, but for absorption of the solar radiation in the atmosphere.

For the separate assessment of the insolation under cloud-free conditions, clear-sky climatologies at selected sites from BSRN have been constructed, based on composites of cloud-free episodes. This shows that the AMIP II version of the Hadley Centre Model (HadAM3) is in excellent agreement with observations, while the AMIP I representative of the same model series

(HadAM2) reveals a significant overestimation of the clear sky fluxes at the surface, related to a lack of absorbtion in the cloud-free atmosphere. A similar improvement is found in the AMIP II version of the Max Planck Institute for Meteorology (ECHAM4), compared to their AMIP I version ECHAM3. This indicates that the clear sky fluxes in the AMIP II models have significantly improved compared to the AMIP I models. Yet, a comparison of the global mean insolation under cloud free conditions of the 20 AMIP II models shows, that a significant overestimation is still present in some of the other models compared to a best estimate derived from the observed clear sky climatologies (cf. Fig. 3).

Figure 3

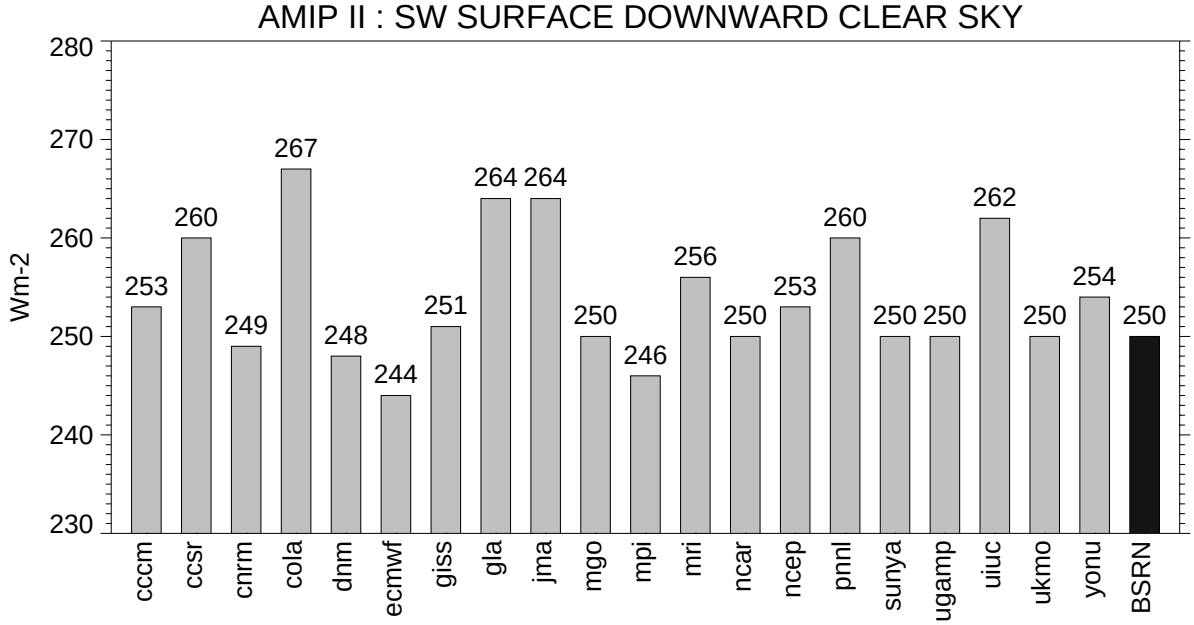

Figure 3: Global mean solar radiation incident at the surface under cloud free conditions in 20 AMIP II GCMs and an estimate which makes use of direct observations (BSRN).

In the longwave budgets, the most difficult component to simulate is the downward longwave radiation at the surface (cf. standard deviations in Table 1). Global mean values of downward longwave radiation of the 20 AMIP II GCMs are given in Fig. 4. Again large differences, up to 40 Wm-2 become apparent between the GCMs. Interestingly enough, the standard deviation of the model values of this component is larger under clear sky conditions than under all sky conditions (cf. Table 1). This indicates that the clouds mask some of the discrepancies caused by different emission of the cloud free atmosphere in the various models. The difficulties in accurately simulating the longwave emission under cloud-free conditions, particularly from cold and dry atmospheres, have been pointed out by Wild et al. (2001). Figure 4 also includes a best estimate derived from the GEBA/BSRN observations (Ohmura and Gilgen 1993, Wild et al. 1998, 2001) which exceeds most of the GCM values. This indicates, that several of the AMIP II models may significantly underestimate the downward longwave radiation.

Figure 4

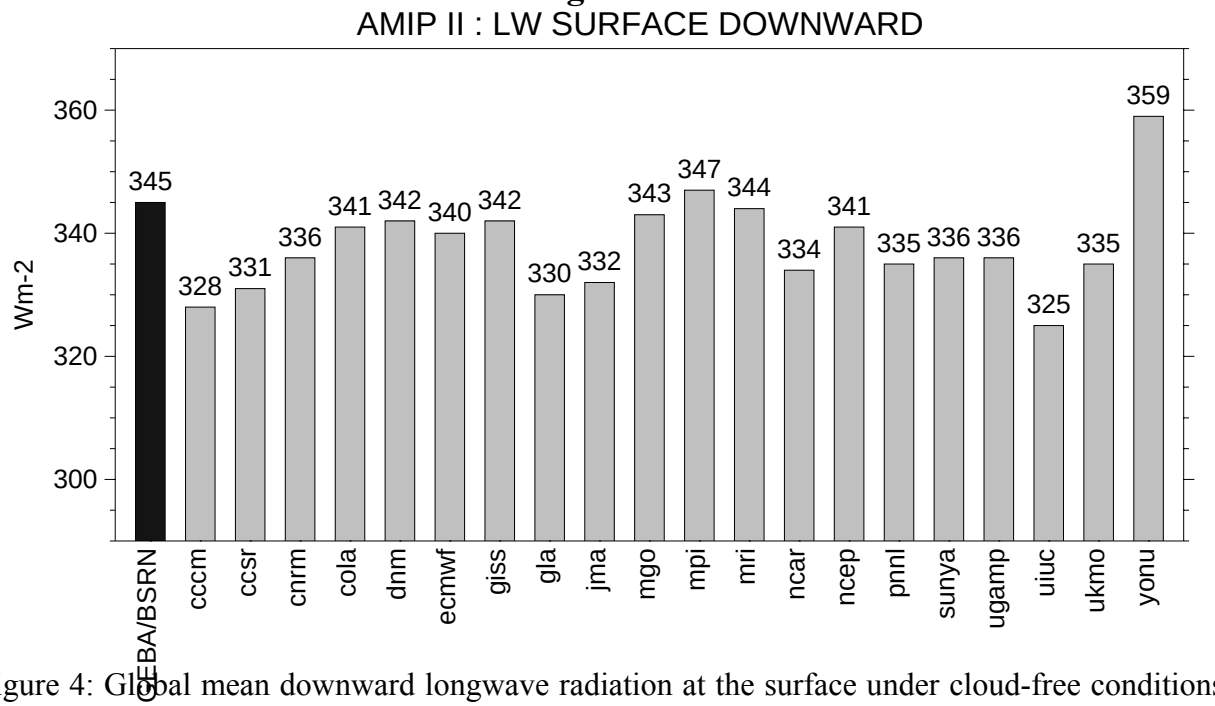

Figure 4: Global mean downward longwave radiation at the surface under cloud-free conditions in 20 AMIP II GCMs and an estimate which makes use of direct observations from GEBA/BSRN (Ohmura and Gilgen 1993, Wild et al. 1998, 2001).

CONCLUSIONS

AMIP II models largely differ in their global mean radiation budgets, particularly at the surface (cf. larger standard deviations of the 20 models in their surface budgets compared to their TOA equivalent in Table 1). Observations from GEBA and BSRN can help to identify and constrain systematic biases within AMIP models. Compared to these observations, GCMs tend to overestimate the surface insolation, due to a lack of solar absorption in the atmosphere. The overestimation of surface insolation under cloud-free conditions and a lack of adequate aerosol forcing contribute to the biases. Improvements compared to AMIP I were found at least in some of the AMIP II models (e.g., HadAM3, ECHAM4/5) with significantly reduced biases in the clear-sky fluxes. The longwave downward fluxes in GCMs, on the other hand, are typically smaller than observed, particularly at high latitudes and under cold climates.

***ACKNOWLEDGEMENTS*:** The author is indebted to Dr. Peter Gleckler, Dr. Jerry Potter and the staff of the PCMDI for their effective support to access and analyze the AMIP II data. This study is supported by the Swiss National Center for Competence in Climate Research (NCCR Climate) funded by the Swiss National Science Foundation.

Table 1: Means and standard deviations of various components of the global mean radiation budgets as calculated in 20 GCMs participating in AMIP II, together with independent estimates derived from observations.

Component	Mean of 20 GCMs	Standard Dev.	Independent estimates
SW absorbed surface	163	8.4	154 [1] 142 [2]
SW absorbed atmosphere	73	7.3	85 [1], 98 [2]
SW absorbed TOA	236	6.5	235 [3]
LW outgoing TOA	236	6.5	235 [3]
LW downward surface (all sky)	338	7.6	345 [1] [2]
LW downward surface (clear sky)	310	9.4	

1) Wild et al. (1998)
2) Ohmura and Gilgen (1993)
3) Barkstrom et al. (1990)

REFERENCES:

Barkstrom BR, Harrison EF, Lee III RB (1990) Earth Radiation Budget Experiment. EOS 71: 297-305.

Gilgen, H., and A. Ohmura, 1999: The Global Energy Balance Archive *Bull. Amer. Meteor. Soc.*, **80**, 831-850.

Gleckler, P. J., and K. E. Taylor, 1993: The effect of horizontal resolution on ocean surface heat fluxes in the ECMWF model. *Climate Dynamics,* **9**, 17-32.

Ohmura, A, and H. Gilgen, 1993: Re-evaluation of the global energy balance. *Geophysical Monograph 75,* IUGG Volume **15**, 93-110.

Ohmura, A., E. Dutton, B. Forgan, C. Froehlich, H. Gilgen, H. Hegner, A. Heimo, G. Koenig-Langlo, B. McArthur, G. Mueller, R. Philipona, R. Pinker, C. Whitlock, and M. Wild, 1998: Baseline Surface Radiation Network (BSRN/WCRP), a new precision radiometry for climate research, *Bull. Am. Meteorol. Soc.*, **79**, 2115-2136.

Wild M., Ohmura A., Gilgen H. and Roeckner E., 1995: Validation of GCM simulated radiative fluxes using surface observations. *J. Climate*, **8**, 1309-1324.

Wild M., Ohmura A., Gilgen H., Roeckner E., Giorgetta M. and Morcrette, J.J., 1998: The disposition of radiative energy in the global climate system: GCM-calculated versus observational estimates. *Climate Dynamics*, **14**, 853-869.

Wild M., 1999: Discrepancy between model-calculated and observed atmospheric shortwave absorption in areas with high aerosol loadings. *J. Geophys. Res*., **104** (D22), 27361-27371.

Wild M., 2000: Absorption of solar energy in cloudless and cloudy atmospheres over Germany and in GCMs. Geophys. Res. Let**. 27**, 959-962.

Wild M., Ohmura A., Gilgen H., Morcrette J.J. and Slingo A., 2001: Evaluation of downward longwave radiation in GCMs. *J. Climate*, **14**, 3227-3239.

On the Sensitivity of Poleward Heat Transport in AMIP Simulations to the Dominant Terms of the Surface Energy Balance

Peter Gleckler

PCMDI/LLNL, Livermore, California, USA (e-mail: pgleckler@.llnl.gov),

Background

The oceanic meridional heat transport (T_o) implied by an AGCM can help evaluate its readiness for coupling with an ocean model. In this study we examine the T_o from AMIP2 simulations and evaluate its sensitivity to the dominant terms of the surface energy balance. Gleckler et al. (1995, hereafter referred to as G95) demonstrated that in AMIP1 the T_o implied by AGCMs was critically sensitive to the simulated cloud radiative effects. In many models excessive shortwave cloud-radiative cooling in the low latitudes led to insufficient surface heating, resulting in wildly different profiles of T_o in the Southern Hemisphere (SH). Many of the models in fact had a global ocean heat transport in the SH mid-latitudes that was northward. While heat transport in the South Atlantic is believed to be northward, estimates for the global ocean suggest a maximum transport in both hemispheres of greater than 1PW toward their respective poles (Trenberth, 1994).

G95 exploited ERBE measurements (Barkstrom et al, 1990) to construct a hybrid $\widetilde{T}_o$, which was a cross between the simulated net ocean surface heating with corrections in the observed top-of-atmosphere (TOA) energy balance. Specifically, deficiencies in the simulated TOA shortwave cloud radiative effects (or forcing) were corrected with estimates derived from ERBE radiances. The resulting T_o looked much more realistic, with most hybrid-adjusted models revealing the expected southward T_o in the SH. The results from this study led many to conclude that deficiencies in shortwave cloud radiative effects were the dominant problem in the implied T_o of AGCMs, and hence key to improving coupled model integrations (IPCC, 1995).

Several years after the G95 study, Hack (1998) diagnosed T_o more closely to better understand the improvements in CCM3 over CCM2. Somewhat contrary to the findings of G95, Hack (1998, hereafter referred to as H98) demonstrated that the improvements in CCM3 were largely due to a reduction in the tropical latent heat fluxes that were primarily attributable to a deep formulation for parameterized moist convection. Considering the findings of G95 and H98 collectively, it is easy to imagine how a models meridional distribution of net surface heating (and thus T_o) could be plausible but for the wrong reasons. For coupled ocean-atmosphere models each terms of the surface energy budget must be realistically simulated, not just their net effect.

In this study we revisit the implied T_o in AMIP2 simulations and apply the diagnostic of G95. We then extend the hybrid T_o concept (model corrected by observations) to adjust the dominant terms of the surface energy balance instead of the TOA cloud radiative effects. This approach is less robust than the test of G95 because the observationally based TOA clear-sky shortwave

measurements (from which cloud radiative forcing estimates follow, Cess and Potter, 1990) are more reliable than ocean surface flux estiamtes. However, by correcting for the dominant surface terms (incoming solar heating and latent heat cooling) we can revisit the results of G95 in the context of the findings of H98 for the suite of AMIP2 simulations. In what follows we use much of the terminology introduced in G95. The ocean heat transport (T_o), implied by a model is calculated from the net ocean surface energy balance:

$$T_o(\phi) = 2\pi a^2 \int_{-\pi/2}^{\phi} \langle N - \alpha \rangle(\phi) \cos(\phi') d\phi' \qquad (1)$$

where *a* is the radius of the earth, φ is the latitude (in radians), N is the net surface heat flux and the brackets $\langle\ \rangle$ denote a zonal average that is weighted by the fraction of ocean in each zone. The area-weighted global ocean average N is represented by α. Inclusion of α in the T_o diagnostic calculation ensures a physically plausible result of no transport at the endpoint pole of integration. The choice of subtracting α uniformly in latitude is conventional but in fact rather arbitrary. The terms of the net surface heat balance are defined as:

$$N = SW + LW + LH + SH \qquad (2)$$

with SW and LW respectively representing the net surface shortwave and longwave radiation at the ocean surface, LH the latent heat flux, and SH the surface sensible heat flux (all defined as + downward). In G95, the total atmospheric and ocean implied heat transport (T_{A+O}) was partitioned into clear-sky and cloudy-sky effects (T_{clr} and T_{CRF} respectively). To was then computed as a residual of T_{A+O} - T_A (the implied atmospheric transport) from which the following relation was derived:

$$\widetilde{T}_O \cong T_O + \delta T_{CRF}, \qquad (3)$$

yielding an adjustment to a model's implied ocean transport corresponding to the T_{A+O} differences between the model and observations ($T_{CRF}^{Model} - T_{CRF}^{ERBE}$). In G95 it was argued (and re-confirmed in this study) that the clear-sky model biases ($T_{clr}^{Model} - T_{clr}^{ERBE} = \delta T_{clr}$) were of secondary importance to the implied heat transport, hence the approximate relation of (3).

Data: Models and Observations

The subset of models in the AMIP2 database used here include only those for which all terms surface and TOA energy budgets are available. All of the terms introduced below are defined as long term 'climatological' means, which for the case of the AMIP2 simulations is roughly 17 years in length. Observationally-based estimates of TOA (top of atmosphere) radiative fluxes are taken from ERBE (Barkstrom et al, 1990). For the surface fluxes, we focus on the dominant terms of surface shortwave radiation (SW) and latent heat flux (LH). Estimates of SW are taken from the Southampton Oceanographic Centre (SOC) climatology (Josey, 1999) as well as two satellite derived estimates originating as part of the GEWEX SRB (Darnell et al., 1992 and Pinker, 1992). The SOC climatology estimate of the latent heat flux is also be used along with

the UWM/COADS estimate (daSilva, 1992). Finally, transport estimates global ocean T_o are taken from Trenberth (1994).

Results

The time mean (AMIP integration average) of T_o for 20 models is shown in Figure 1, and the ERBE corrected hybrid calculation (Eq 3) is shown for this newer set of models in Figure 2.

Figure 1

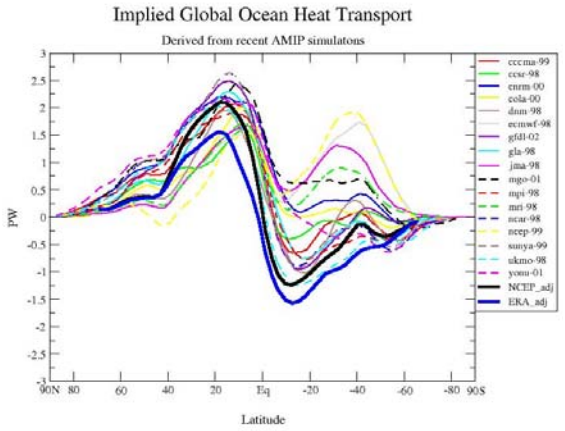

Figure 2

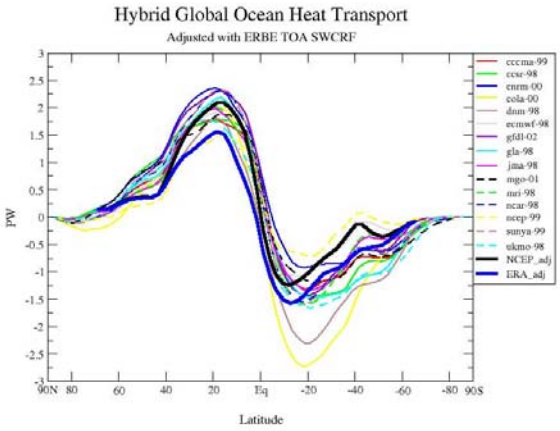

The cause of this dramatic correction for many of the models results from excessive SW cloud radiative forcing (as defined be Cess et al., 1990) is the lower latitudes (Figure 3). The situation has improved somewhat from the earlier generation of AMIP1 models. Not surprisingly, there is a strong relationship (R = .74) between $CRF_{SW,\,TOA}$ and the surface SW as seen in Figure 4.

Figure 3

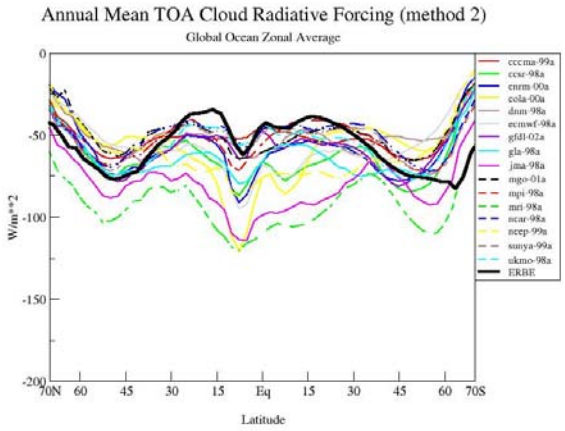

Figure 4

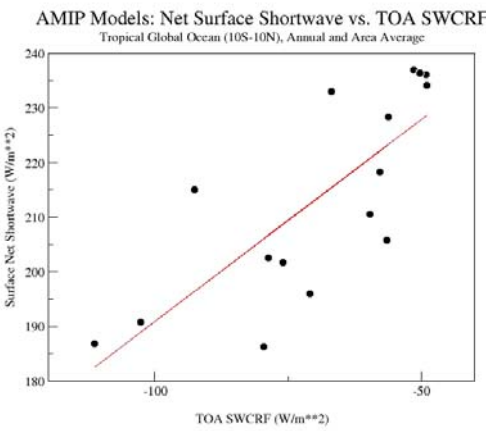

which is directly in the implied T_o in Eq (2). Note that SW is directly part of the T_o calculation as defined in Eq (2) whereas the $CRF_{SW,\,TOA}$ is not. In light of the results of H98, we are compelled to investigate the relative important of the surface terms SW and LH on the implied T_o.

The time mean (AMIP integration average) of the SW is shown in Figure 5. The observational dataset used for comparison is derived from ISCCP data with two algorithms, one from that of Pinker (1992) and the other Staylor (Darnell et al., 1992). While these observationally-based estimates are less reliable are less reliable than the ERBE TOA counterparts, they suggest (Figure 5) that most models underestimate the low latitude SW which is consistent with the CRF_{SW},top seen in Figure 3. The comparison of the simulated LH with the in-situ based estimates is however also intriguing. Most all models have much more evaporation in the tropics than either of the COADS based climatologies. Once more however, we must reiterate the uncertainty of these surface flux estimates. Reanalysis products (ERA and NCEP) are not shown but for both terms agree much more closely with the collection of AMIP models. Whether or not the reanalysis surface fluxes are more realistic than the data we use here is a subject of debate (Taylor et al, 2000). However, the implied T_o from the reanalysis suggests they suffer from similar deficiencies to the AGCM's.

Figure 5

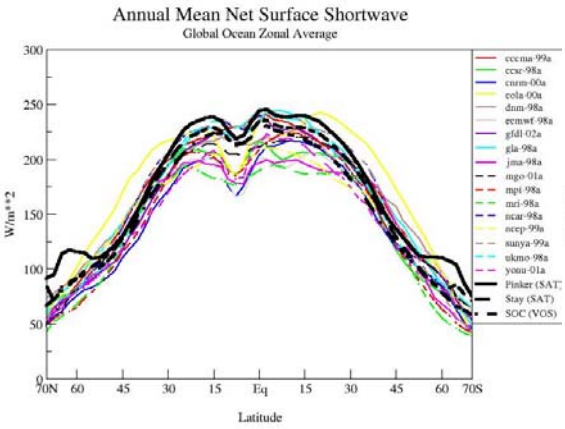

Figure 6

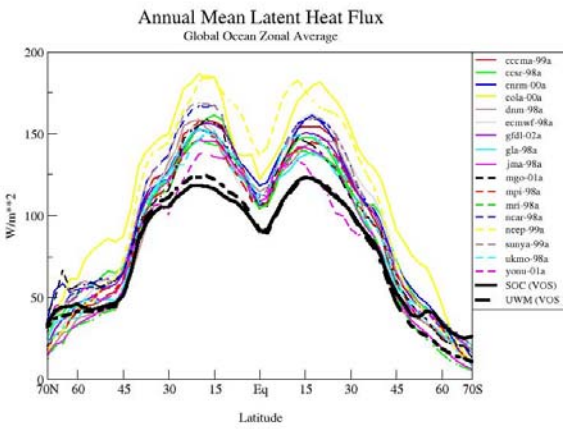

To investigate the findings of H98 in the broader context of the suite of AMIP2 simulations, we construct a two new hybrid implied T_o's as in Eq (3) but this time making adjustments with the observationally-based surface flux estimates rather than ERBE at the TOA. This is simply accomplished via Eq. (2) as follows: $\widetilde{T}_{o,SW}$ = SW_{obs}+LW+LH+SH and $\widetilde{T}_{o,LH}$ = SW+LW+LH_{obs}+SH. One concern with this approach might be that the observational corrections, not being true to the model, can result in much larger global ocean heating imbalances (α's from Eq 1). They do, with $\left|\widetilde{\alpha}_{o,SW}\right|$ and $\left|\widetilde{\alpha}_{o,LH}\right|$ being > 10 Wm^{-2} for many models. However the point is the following: Global average imbalances are removed in the T_o diagnostic calculation via α. It is the SW and LH meridional distributions that are being corrected by observations in $\widetilde{T}_{o,SW}$ and $\widetilde{T}_{o,LH}$, the result of which are shown in Figures 7 and 8.

Figure 7

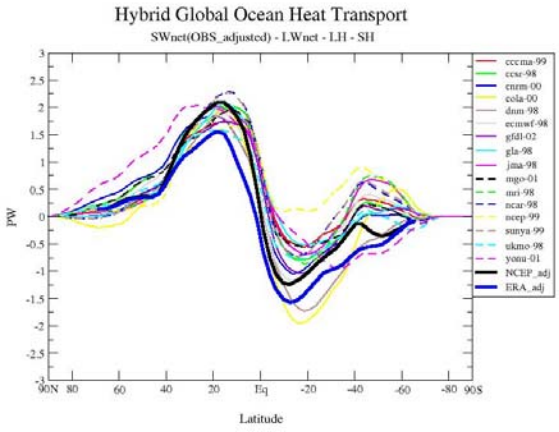

Figure 8

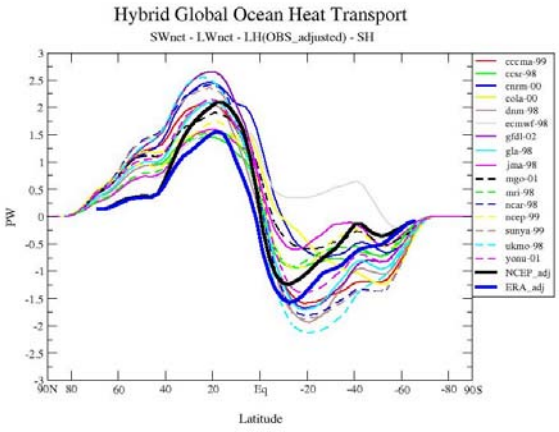

Conclusions

Our results confirm the findings of Hack (1998), that indeed the simulated latent heat flux can be as much a culprit in meridional heat transport problems as can cloud-radiative effects. They are of course intimately intertwined, and unraveling their interrelated processes may depend very much on the combination of parameterizations, perhaps only to be resolved on a model-by-model bases. But routine use of a collection of hybrid implied T_o diagnostics may prove useful in the model development process. While the uncertainties in the observed surface flux terms are large, it is possible that further tests may help us to establish more faith in their meridional distributions than we have in their absolute values. Moreover, the tests introduced here provide additional clues as to whether or not a realistic implied T_o is obtained for the right reasons at the air-sea interface.

References

Barkstrom, B., H. Harrison, and R. Lee, the earth radiation budget experiment, EOS, 71, No. 9, 297, 1990

Cess, R.D., et al., Intercomparison and interpretation of climate feedback processes in 19 atmospheric general circulation models, *J. Geophys.Res*, **95**, 16,601, 1990

Darnell, W.L., W. F. Staylor, S.K. Gupta, N.A. Ritchey, and A. C. Wilber, 1992: Seasonal variation of the surface radiation budget derived from ISCCP-C1 data. *J.Geophy.Res*., 97, 15741-15760.

Gleckler, P.J., D.A. Randall, G. Boer, R. Colman, M. Dix, V. Galin, M. Helfand, J. Kiehl, A. Kitoh, W. Lau, X.-Z. Liang, V. Lykossov, B. McAvaney, K. Miyakoda, S. Planton, and W. Stern, 1995: Cloud-radiative effects on implied oceanic energy transports as simulated by atmospheric general circulation models. *Geophys. Res. Letts* ., 22, 791-794.

Hack, J., 1998: Analysis of the Improvement in the Implied Meridional Ocean Energy Transport as Simulated by the NCAR CCM3, J.Clim., 11, 1237-1245

IPCC, 1995

Josey, S. A., E. C. Kent and P. K. Taylor, 1999: New insights into the ocean heat budget closure problem from analysis of the SOC air-sea flux climatology *J.Clim,* **12(9)**, 2856 - 2880.

Pinker, R. T. and I. Laszlo, 1992 . Modeling of surface solar irradiance for satellite applications on a global scale. *J. Appl. Meteor., 31, 194-211.*

Final report of the Joint WCRP/SCOR Working Group on Air-Sea Fluxes, Ed. P. Taylor, 2000, WCRP-112, WMO/TD-No. 1036.

Trenberth, K. and A. Solomon, The global heat balance: heat transports in the atmosphere and ocean, Clim.Dyn., **10**, pp. 107-134, 1996

Comparison of AMIP II Cloud Layer Properties with ISCCP D2 Estimates

Bryan C. Weare
Atmospheric Science Program
Department of Land, Air and Water Resources

University of California, Davis Atmospheric Model Intercomparison Project (AMIP) II has made available cloud amounts, liquid and ice contents at each model level from five models. This paper will discuss a preliminary analysis of the monthly mean three-dimensional cloud structure for those models. This output will be compared with the global cloud products from the monthly International Satellite Cloud Climatology Project (ISCCP) D2 analysis. In order to make the comparisons are direct as possible the AMIP II GCM outputs are transformed to the D2 high, mid and low data types as described below. The comparisons will concentrate on an evaluation of the main space-time variability of cloud properties. Significance is assessed at the 95% confidence level.

The model outputs are transformed to the ISCCP D2 data types following the method shown schematically in Fig. 1.

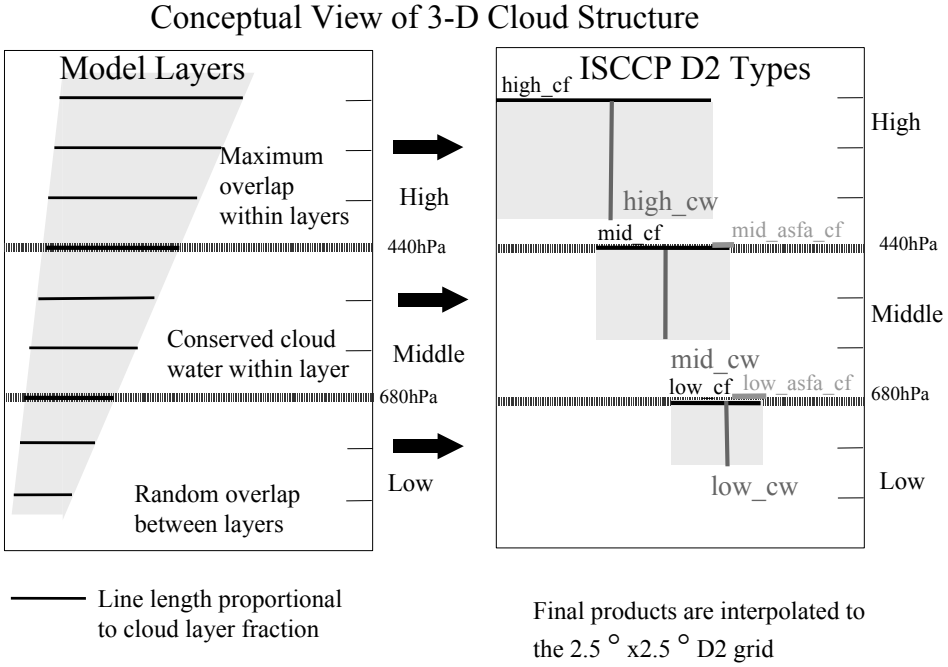

Fig. 1

The radiative effects of clouds depend upon a complex nonlinear interaction between cloud amounts and cloud properties, which are partly determined by cloud liquid and ice amounts. In order to understand better these interactions in both the D2 observations and the model outputs a simple model is utilized, which is derived from the ISCCP radiative transfer model relating reflected solar radiation to cloud optical depth. In this case the cloud albedo above a black surface associated with the mid cloud as seen from above by a satellite α_mid is given by

$$\begin{aligned} \alpha\_mid &= r\_mid * mid\_asfa\_cf = (1.1 - e^{-\tau\_mid/15}) * 0.84 * mid\_asfa\_cf \\ \tau\_mid &= mid\_asfa\_ice / 10.5 + mid\_asfa\_liquid / 6.292 \end{aligned} \quad (1)$$

The high and low cloud albedos are determined in a similar manner. Monthly mean albedos are calculated in this way not only for all of the models, but also for the ISCCP D2 data.

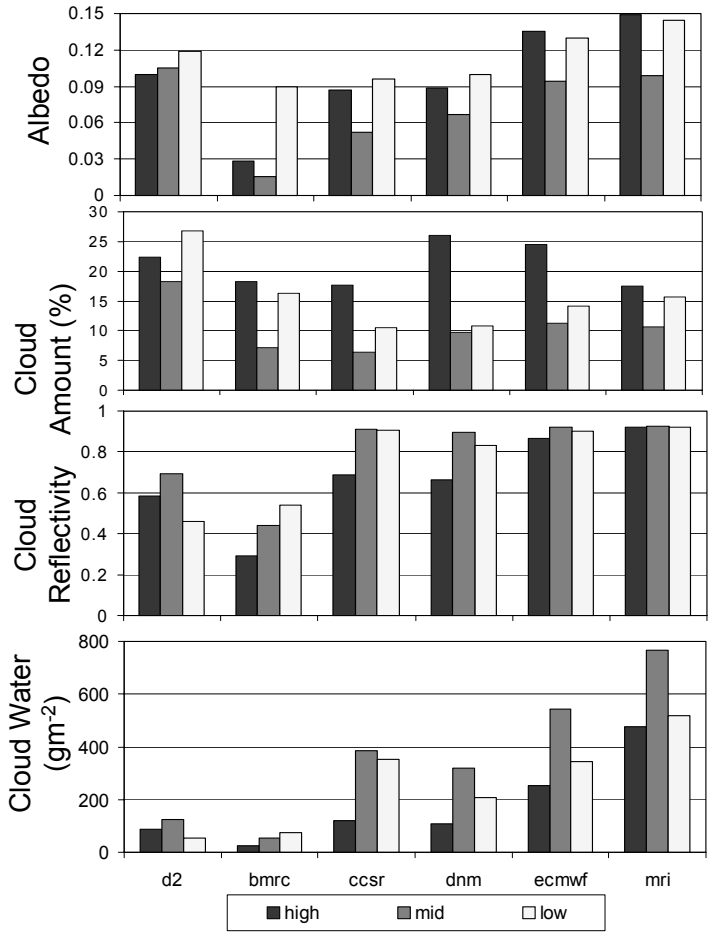

Fig. 2

Fig. 2 shows a summary of the annual mean albedos averaged between 60°N and 60°S separately for α_high, α_mid and α_low clouds for the D2 observations and the models. It should be emphasized that these means are based on averages of albedos at each point and for each month. Fig. 2 also shows the corresponding 60°N-60°S annual mean cloud fractions, reflectivities, and water depths (ice plus liquid) for the high, mid and low clouds. The near-global annual mean model high cloud albedos range from less than a third of the D2 value to about 50% greater. The two models with the largest values, ECMWF and MRI, both have considerably larger high cloud reflectivties and water contents, than do the observations or other models. It also should be noted that water contents vary between models much more than do the other three variables. Also, some models seem to account for an apparent underestimate of mid and low cloud amounts by having relatively large cloud water, hence reflectivity, values

Fig 3 shows a summary of the near-global means of the seasonal standard deviations of the departures of monthly mean values of cloud amount and water relative to the annual mean values. From Fig. 3a, all models have seasonal variability of high cloud amounts which are statistically comparable to that of the D2 observations. Three model have mid or low cloud variability, which is significantly (identified by hatching) smaller than the observations. Fig. 3b shows that the model cloud water variabilities are statistically larger in most cases from those of D2. Overall, models seem to slightly underestimate mid and cloud amount seasonal variability and overestimate that for cloud water at all levels.

Another key feature of the vertical structure of clouds is a description of how cloud layers overlap each other. The general nature of the overlap may be inferred by deriving the annual mean total cloud cover using the random overlap assumption using.

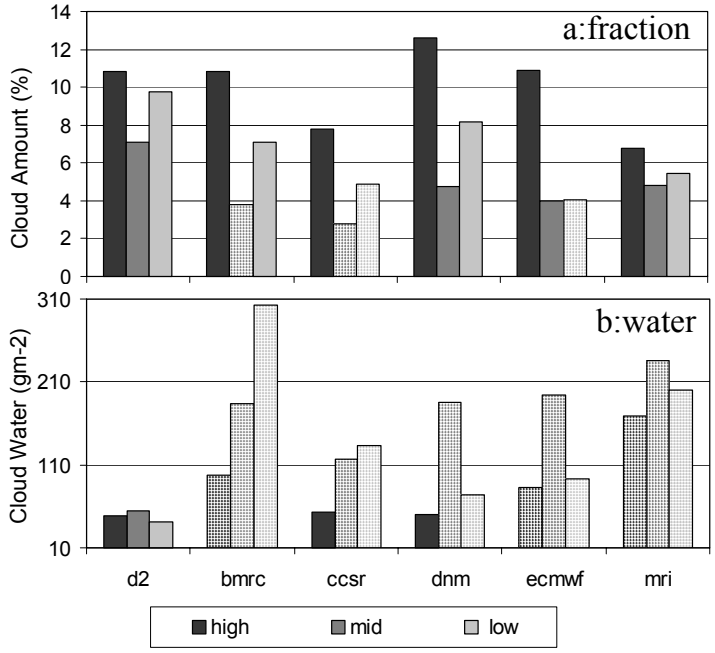

Fig. 3

$$\text{total (random)} = 1 - \prod_{i=1}^{3} (1 - layer_i\_cf) \qquad (2)$$

This may be compared to the annual mean of modeling group's reports of total cloud amounts used in radiative transfer calculations. Fig. 4 illustrates the differences between these two annual means for four models (the BMRC total cloud information is not available) and observational estimates from monthly mean analyses of D2 and surface observer cloud amounts. The estimated observed total cloud amount using a random overlap assumption is greater nearly everywhere than the directly estimated value, implying that in the real atmosphere monthly mean clouds generally are more closely stacked in the vertical than is implied by the random overlap assumption. However, the reverse is true in most places for the models. This implies that for the globe monthly mean model clouds tend to be more spread horizontally than assumed by the random assumption

Overall, most of the five AMIP II models agree with observational estimates of global mean cloud amounts and spatial and seasonal variability of cloud albedo and amounts for the three levels. However, the models tend to greatly overstate these quantities compared with observations for the water content of the clouds, especially for the mid and low levels. Finally, monthly mean model clouds may be less vertically stacked than observations. This work will proceed with the analysis of output.

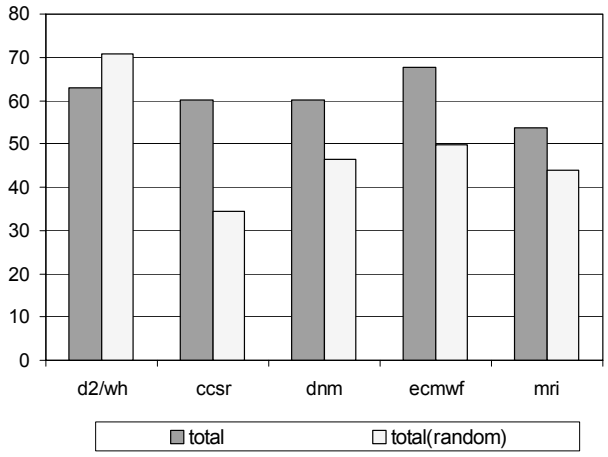

Fig. 4

Validation of CRMs and GCM Cloud Parameterizations Using CERES Data

Zachary A. Eitzen[1,2], Kuan-Man Xu[1], B.A. Wielicki[1], T. Wong[1], and L. Parker[3]

1 - NASA Langley Research Center email: z.a.eitzen@larc.nasa.gov

2 - Colorado State University

3- SAIC

Introduction

Cloud systems have important effects on the dynamical, hydrological and radiative budgets of the global atmosphere. For many years, researchers have used cloud-resolving models (CRMs) to simulate these cloud systems. Until now, these CRMs have primarily been validated by comparing their results to observations from field experiments (Xu and Randall 1996, 2001). While this technique is useful, it is helpful to have as many cases as possible over as long a time period as possible to verify the robustness of model improvements. With the launch of the Tropical Rainfall Measuring Mission (TRMM) satellite, researchers have been given the opportunity to simultaneously obtain observations of the radiative and microphysical properties of clouds using the CERES (Clouds and the Earth's Radiant Energy System) instrument and observations of the hydrological properties of the same clouds using the TRMM precipitation radar (PR) and TRMM Microwave Imager (TMI) instruments.

Our approach is as follows: First, diagnose the cloud systems using CERES SSF (Single Scanner Footprint) cloud and radiative data. The time and location of the system can be matched to an ECMWF analysis at the same time, to evaluate the ECMWF model's cloud and radiative transfer parameterizations. To initialize the CRM, we use vertical profiles of the temperature, moisture, wind, cooling tendencies and moistening tendencies obtained from ECMWF analyses at the same time and place. By applying this procedure to dozens of cloud systems, we can be more confident that improvements to the model are real than if we used a single case study.

Although this work currently focuses on deep tropical convection, selection criteria have also been developed for several other kinds of cloud systems that are also of interest from a climatological standpoint, as shown in Table 1.

Table 1 : Cloud Selection Criteria

Category	Latitude Range	Eff. Height	Cloud Fraction	Optical Depth
Tropical deep convection	25° S - 25° N	*ztop* > 10 km	1.0	$\tau > 10$
Trade cumulus	40° S - 40° N	*ztop* < 3 km	0.1-0.4	N/A
Transition stratocumulus	40° S - 40° N	*ztop* < 3 km	0.4-0.99	N/A
Solid stratus	40° S - 40° N	*ztop* < 3 km	0.99-1.0	N/A

Description of the Models

At LaRC, we are currently using two CRMs. The first, denoted by LaRC-A (the "a" stands for anelastic), is the UCLA/CSU CRM (Krueger 1988; Xu and Randall 1995). The second, denoted by LaRC-C (the "c" stands for compressible), is based on the Advanced Regional Prediction System (ARPS; Xue et al. 2000).

The LaRC-C simulations were performed in 2-D, with a periodic horizontal domain 700 km wide using $\Delta x = 1$ km. The vertical domain was 25 km high (the top 8 km was a sponge layer) and stretched, with an average Δz of 500 m. The initial state of the model atmosphere is horizontally homogeneous, with a vertical profile that is calculated from an average over a 7° by 7° box surrounding the center of each cloud system to obtain vertical profiles of wind, temperature, moisture, and the cooling and moistening tendencies from the ECMWF analyses that are matched to the same location and time. The LaRC-A simulations were set up in a similar (though not identical) manner.

In order to compare the results of the ECMWF model to those of the satellite and CRMs, each 0.5625° x 0.5625° ECMWF grid cell was split into 30 subgrids. Then, the maximum-random overlap assumption (Klein and Jakob 1999) was used to distribute the ECMWF cloud fields in the vertical and horizontal directions.

Results

In this section, we will compare the ECMWF, LaRC-A, and LaRC-C simulations to the CERES observations of 29 cloud systems that were observed over the tropical Pacific Ocean in March 1998. Each of these cloud systems had a surface area that was larger than an equivalent circle with a diameter of 300 km. In these figures, we are looking at the probability density functions (PDFs) of various fields. These PDFs are calculated among the individual satellite pixels or model columns that fit the selection criteria described in Table 1. Using the PDFs allows us to see how well the variability of fields within each system is simulated by the CRMs and the ECMWF model.

In Fig. 1, we see that the two CRMs produce PDFs of cloud optical depth that are similar to that of the observations in the range from $20 < \tau < 100$. LaRC-C produces more cloudy columns with $10 < \tau < 20$ than are observed, and both CRMs produce at least some cloudy columns that have $\tau > 120$, which is the highest optical depth that the CERES instrument can measure. The ECMWF model produces a PDF that is flatter than is observed throughout the range of cloud optical depths.

In Fig. 2, we see that the two CRMs produce PDFs of outgoing longwave radiation (OLR) that are fairly similar to the observations, although LaRC-A produces more cloudy columns with OLR around 135 W m^{-2} than observed, and both CRMs produce PDFs that are more broadly peaked than is observed. The PDF from the ECMWF model shows that its cloud systems have values of OLR that are lower than those observed.

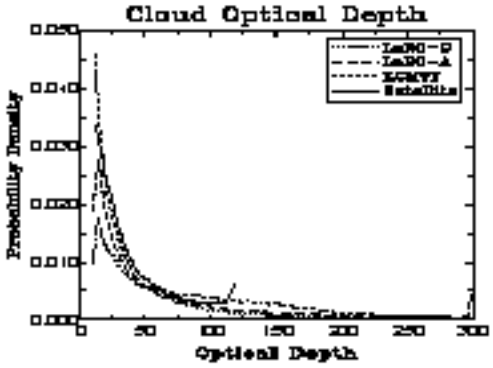

Fig. 1. PDFs of cloud optical depth.

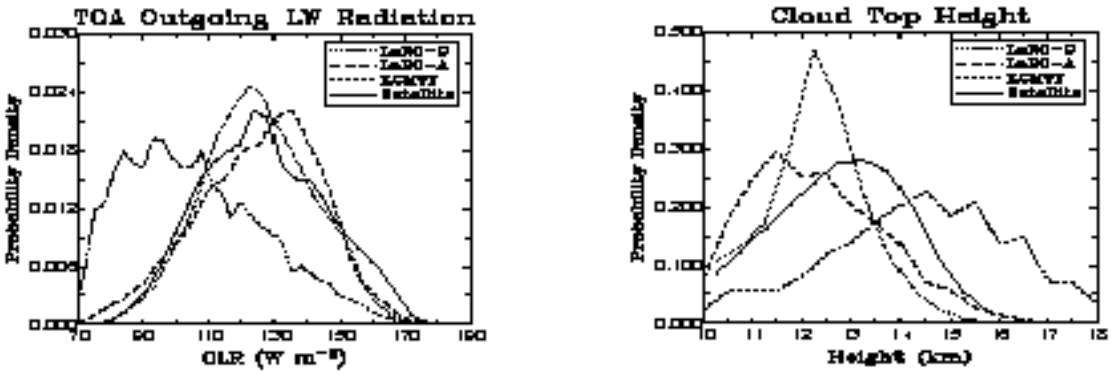

Fig. 2. PDFs of outgoing longwave radiation (left) and cloud top height (right).

Consistent with our results for OLR, the PDFs of effective cloud top height (the height at which τ first exceeds 2, integrating from the top) show that the CRM cloud systems tend to be somewhat shallower than those observed, while the ECMWF cloud systems tend to be deeper.

In the another plot (not shown), we see that the PDF of the albedo simulated by LaRC-C model produces a PDF that is fairly broad, but is centered at a value much lower than that of the observations. This indicates that there is a problem with the treatment of shortwave radiation in LaRC-C that needs to be addressed

Summary and Future Work

The CERES and TRMM instruments have proven to be useful tools for identifying different types of cloud systems, and for diagnosing the variability of their radiative, microphysical and hydrological properties. The cloud systems simulated by the CRMs and ECMWF model are broadly similar to the satellite observations of the systems. However, there is certainly room for

improvement. One of the first things that we plan to do is to refine the initialization technique for the CRM simulations of cloud systems. We plan on eliminating cases in which the ECMWF model does not simulate a cloud system that is in approximately the same location as observed. Also, we will scale the size of the averaging box surrounding each cloud system to be proportional to the size of the system.

One of the conclusions of this work is that there is a significant problem with the shortwave radiation above optically thick ice clouds in LaRC-C. We are currently performing experiments where the effective diameters of the ice crystals in the model are adjusted, to see if this alleviates the problem.

In the future, we will perform simulations of the March 2000 cloud systems, to see if the CRMs can replicate the observed interannual variability in cloud systems. In addition, we will diagnose (using the criteria in Table 1) and simulate shallow cloud systems, as well.

Acknowledgment. This work has been supported by the NASA EOS Interdisciplinary Study program.

References

Klein, S. A., and C. Jakob, 1999: Validation and sensitivity of frontal clouds simulated by the ECMWF model. *Mon. Wea. Rev.,* **127,** 2514-2531.

Krueger, S. K., 1988: Numerical simulation of tropical cumulus clouds and their interaction with the subcloud layer. *J. Atmos. Sci.*, **45,** 2221-2250.

Xu, K.-M., and D. A. Randall, 1995: Impact of interactive radiative transfer on the macroscopic behavior of cumulus ensembles. Part I: Radiation parameterization and sensitivity tests. *J. Atmos. Sci.*, **52,** 785-799.

Xu, K.-M., and D. A. Randall, 1996: Explicit simulation of cumulus ensembles with the GATE Phase III data: Comparisons with observations. *J. Atmos. Sci.*, **53,** 3710-3736.

Xu, K.-M., and D. A. Randall, 2001: Updraft and downdraft statistics of simulated tropical and midlatitude convection. *J. Atmos. Sci.*, **58,** 1630-1649.

Xue, M., K. K. Droegemeier, V. Wong, 2000: The Advanced Regional Prediction System (ARPS) - A multi-scale nonhydrostatic atmospheric simulation and prediction tool. Part I: Model dynamics and verification. *Meteorol. Atmos. Phys.*, **75,** 161-193.

First Results of the AMIP2 GCMs Evaluation Using Meteosat Water Vapor Data

Hélène Brogniez, Rémy Roca, Laurence Picon
Laboratoire de Météorologie Dynamique, Ecole Polytechnique, 91128 Palaiseau, FRANCE
brogniez@lmd.polytechnique.fr

1 Introduction

The humidity of the mid and upper troposphere has an important role in the tropical climate because of the non-linear relationship between the vertical distribution of the water vapor and the radiation budget (Spencer and Braswell, 1997). Therefore, to have a good representation of the atmospheric system, General Circulation Models (GCMs) should reproduce the correct moisture of the upper levels.

In the frame of the subproject 34 (Roca and Picon, 1999), the Meteosat water vapor data are used to evaluate the distribution of upper level moisture and of convection as well as their links. The proposed evaluation was first based on a model-to-satellite approach which consists in a direct comparison of Meteosat-5 radiances simulated from GCMs and the observed radiances (Roca *et al.*, 1997). Because no cloud profile was available at the beginning of this work, the present work focuses on the clear sky areas. For this purpose, the observed and simulated clear sky water vapor brightness temperatures (BTs) are inverted in terms of a mean relative humidity of a tropospheric layer and compared.

2 The retrieval of the mean relative humidity

The Meteosat Water Vapor (WV) channel is centered on 6.3µ m and, in clear sky, is sensitive to the humidity and temperature of a large layer of the troposphere. In previous works (Soden and Bretherton, 1993; Schmetz *et al.*, 1995) the clear sky WV BTs are inverted in terms of Upper Tropospheric Humidity (UTH). These methods developed for different WV radiometers (Meteosat-6.3µ m, GOES-6.7µ m ...) define the UTH on different layers of the troposphere. The parameters for the retrieval are also computed in different ways.

Roca *et al.* (2002) define the Free Tropospheric Humidity (FTH) which is derived from Meteosat-6.3µm clear sky BTs from:

$$ln\left(\frac{p_0 FTH}{cos\theta}\right) = aBT_{6.3\mu.} + b$$

where p_0 describes the thermal structure of the column and θ is the satellite viewing angle. a and b are obtained for each pixel from a look-up table computed with a radiative transfer code (Morcrette and Fouquart, 1985; Roca, 2000) for two profiles of constant relative humidity (5% and 50%). Because there is an important contribution of the whole 800-100hPa layer to the observed WV radiance, the FTH is defined as the mean relative humidity of the free troposphere weighted by the corresponding weighting function. This algorithm was validated with radiosondes of the INDOEX experiment and revealed a small bias of 2.7% and a standard deviation of 6% (Roca *et al*, 2001). A sensitivity study showed that low clouds, with a cloud top pressure greater than 700hPa, have a small impact on WV BTs (Roca *et al*, 2002). The ISCCP

DX product (Rossow and Garder, 1993) is used to select the clear and low clouds areas. Then, the FTH algorithm is applied on the selected BTs over the Africa and Tropical Atlantic region. The spatial resolution of the FTH is a regular mesh of 0.625. This product is built using the Meteosat database of LMD containing a homogeneous set of Meteosat-5 radiances (07/1983-02/1994, every 3 hours) (Picon *et al.*, 2002). Monthly means of FTH are produced over 1984-1993 in order to allow AMIP comparisons. On Figure 1 are represented the mean BT (left) and the mean FTH (right) for July 1992. We see two particularly dry areas: one in the North East of Africa and one covering a large region in the South Hemisphere (SH). Those two regions correspond to warm BTs and are linked to large subsiding areas.

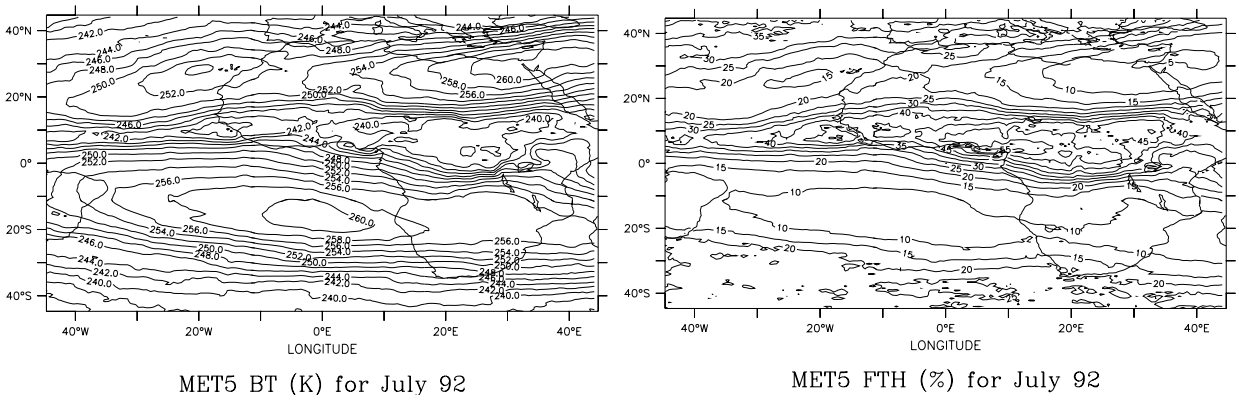

Figure 1: MET5 BT (left) and FTH (right) for July 1992. Intervals are 2K and 5%.

Note that an uncertainty is introduced by the calibration of the Meteosat-5 WV channel. Bréon and Jackson (2000) have estimated an absolute bias of -1.5K with a calibration study between Meteosat-5 radiances and NOAA/HIRS radiances. The impact of this bias is small in dry regions (bias of 1.5% for a FTH equal to 10%).

3 The FTH used for the intercomparison

The radiative transfer code mentioned above is used to compute the simulated WV BTs from humidity and temperature profiles for each GCM. A local look-up table containing the parameters of the retrieval (a, b and p_0 in eq(1)) is also calculated in the same way than for the observations. Then, the error due to the retrieval method is not considered in the comparisons.

The FTH is then retrieved for each of the 16 evaluated GCMs (available profiles of q and T). Because there was no available information about the simulated clouds, only dry regions without high or medium cloud can be compared. These regions are determined with a threshold of 25% in FTH. Figure 2 shows the mean seasonal cycle of this dry FTH in the SH and the simulated mean seasonal cycles. The mean GCM is in good agreement with the observed mean seasonal cycle and get the maximum of dryness of July. However, there is a large spread (9% in July) between all seasonal cycles simulated by the models.

4 The JJA distribution of dry FTH (25%)

Figure 3 shows the driest regions of the observed FTH for JJA (FTH 25%) (left) and two illustrations of extreme simulations (centre and right). In the observed JJA, there is one large dry area in the South and two areas of low FTH in the North with an extreme dryness in the East of the Mediterranean Sea.

First, some GCMs have a good location of the dry structures in both hemispheres (Fig. 3 centre). However, a few GCMs do not simulate the spread of the dryness in the SH (Fig. 3 right).

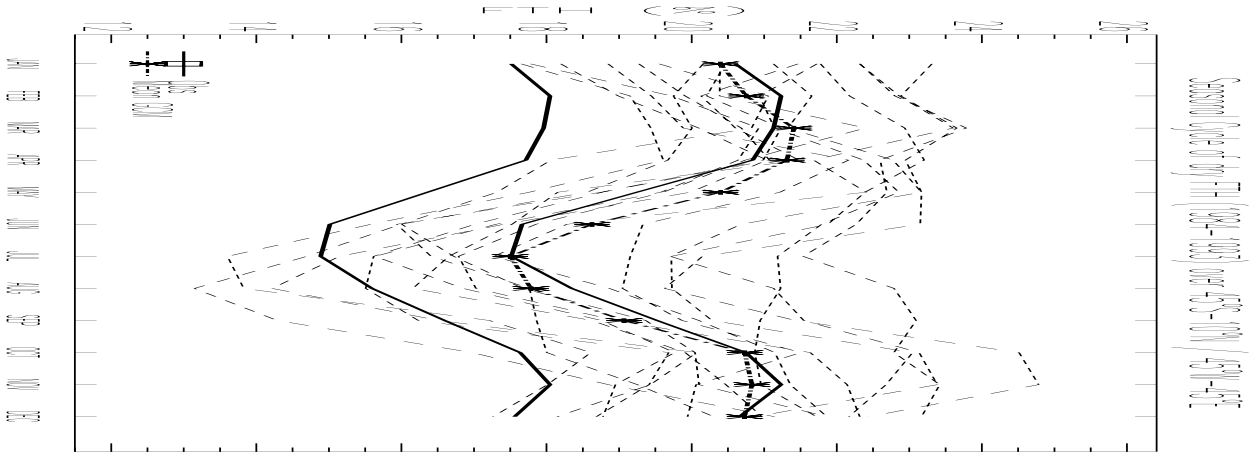

Figure 2: Mean seasonal cycles of FTH (25%). Average over 45°S-10°N/45°W-45°E. Full lines are for the observed dry FTH with the uncertainty. Dotted line with stars is for the FTH of the mean GCM. Dashed line is for each evaluated GCM.

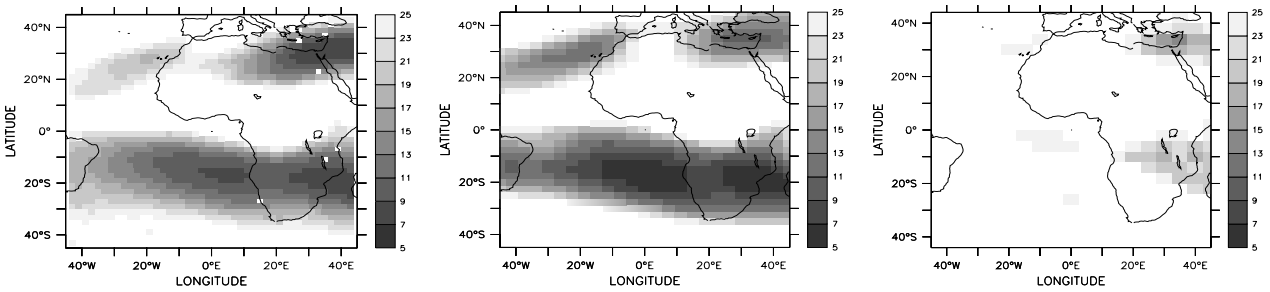

Figure 3: Dry FTH (25%) for JJA. Observation (left) and 2 GCMs (centre and right).

To avoid the problem of location of the structures, we focused on each simulated dry area of the SH. For each GCM, we evaluated the mean and the standard deviation over their dry region (Fig. 4). The driest grid point of the SH is also computed to test the minimum of FTH reached by the models in the area. The studies of the observed and simulated means are similar (around 18%, left) when considering the mean GCM and the uncertainty of calibration. However, on Figure 4 (right) is indicated that the mean GCM has a standard deviation small compared to the observation over this dry region and shows that some GCMs have a too weak variability. The GCMs are further classified according to the minimum of FTH encountered over their dry area.

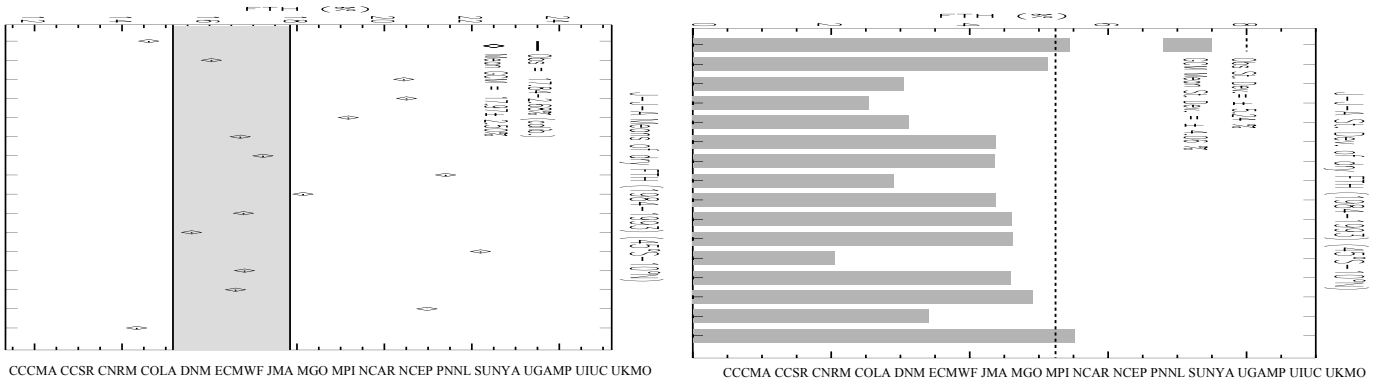

Figure 4: Mean (left) with the uncertainty of calibration (grey area) and standard deviation (right) over the dry SH for JJA.

Table 1 shows that six GCMs do not reproduce the observed extreme dryness. They are too moist by more than 5% and these models have a small spatial variability. Three models are more than 2% too dry but their spatial variation over the region agrees with the observed variation. Finally, seven GCMs reach the correct extremum of the SH and have a good spatial variability compared to the observed one.

Too moist (□ 5%)	*Too dry (□ 2%)*	*In agreement*
CNRM, COLA, DNP, MGO, PNNL, UIUC	CCCMA, CCSR, UKMO	ECMWF, JMA, MPI, NCAR, NCEP, SUNYA, UGAMP

Table 1: Classification of the 16 GCMs according to their minimum of FTH over the Southern Hemisphere.

5 Summary and Future work

The simulated dry regions for each GCM are considered in this study. The results show that the mean GCM describes well the observed mean seasonal cycle over the SH. In this preliminary study, 7 models out of 16 models agree with the observed FTH both in their representation of the minimum and in their spatial variability during JJA. The other models reproduce well the mean over the region but their simulated minimum of FTH is either too dry by more than 2% or too moist by more than 5%. These latter models exhibit too weak a variation over the studied region. A similar analysis over the northern Hemisphere nevertheless indicates that some models can be too moist in the N.H. whereas they are too dry in the SH. Next step of this work is the extension of this analysis to the interannual variability over the 1984-1993 period. The availability of cloud profiles from some models could allow to broaden our comparisons to the convective areas and to further evaluate the relationships between the variability of the dry regions and the convective ones.

References

Bréon F-M and D. Jackson, 2000: Calibration of the METEOSAT water vapor channel using collocated NOAA/HIRS 12 measurements. *J. of Geoph. Res.*, **105**, 11,925-11,933.

Morcrette J-J and Y. Fouquart, 1985: On systematic errors in parametrized calculations of longwave radiation transfer. *Quat. J. of Roy. Met. Soc.*, **111**, 691-709.

Picon L. R. Roca, S. Serrar, J-L Monge and M. Desbois, 2002: A new Meteosat "Water Vapor" archive for climate studies. *Accepted in J. of Geoph. Res.*

Roca R., L. Picon, M. Desbois, H. Le Treut and J-J Morcrette, 1997: Direct comparison between Meteosat water vapor channel and GCM results. *Geophy. Res. Let.*, **24**, 147-150.

Roca R. and L. Picon, 1999: Evaluation of convection and upper level moisture and their links using Meteosat water vapor channel data. *AMIP II Diagnostic Subproject 34*.

Roca R., 2000: Validation of GCMs cloudiness using Meteosat observations. ECMWF/EuroTRMM Workshop on the Assimilation of precipitation and cloud radiances in NWP. Reading, UK, 6-9 November, pp 185-205.

Roca R. H. Brogniez, L. Picon and M. Desbois, 2001: High resolution observations of free tropospheric humidity from Meteosat over the Indian Ocean. MEGHA-TROPIQUES 2nd Scientific Workshop. Paris, France, 2-6 July.

Roca R., H. Brogniez, L. Picon and M. Desbois, 2002: Free Tropospheric Humidity observations from Meteosat water vapor data. Proceeding for the AMS conference, San Diego, USA, Feb 2003.

Rossow W. and L. Garder, 1993: Validation of ISCCP cloud detections. *J. Climate*, **6**, 2370-2393.

Schmetz J. and co-authors, 1995: Satellite observation of upper tropospheric relative humidity, clouds and wind field divergence. *Beitr. Phys. Atmosp.*, **68**, 345-357.

Soden B. and F. Bretherton, 1993: Upper Tropospheric Humidity from the GOES-6.7 μm channel: Method and Climatology for July 1987. *J. of Geoph. Res.*, **98**, 16,669-16,688.

Spencer R. and W. Braswell, 1997: How dry is the tropical free troposphere? Implications for global warming theory. *Bull. of Am. Met. Soc.*, **78**, 1097-1106.

The Polar Climate in AMIP Simulations

V.M. Kattsov[1], J.E. Walsh[2], W.L. Chapman[2], and S.V. Vavulin[1]

(1) Voeikov Main Geophysical Observatory, St.Petersburg, Russia;
(2) Department of Atmospheric Sciences, University of Illinois, Urbana, IL, USA
e-mail: kattsov@main.mgo.rssi.ru; walsh@atmos.uiuc.edu

1. INTRODUCTION

This paper presents some findings of the AMIP-II Diagnostic Subproject No.9 "Polar processes and sea ice" with a focus on the atmospheric fields affecting air-sea-ice coupling in the both hemispheres. Goals of the study included (1) assessments of the systematic errors and across-model variance of the polar fields of basic climate variables (surface air temperature, precipitation, evapotranspiration, sea level pressure, cloudiness, radiative fluxes, etc.); and (2) a comparison of AMIP-II and AMIP-I model performances in the polar regions for a set of the models that participated in the both phases of the project. The study is an extension of that by Walsh et al. (2002), which contains the list of references used here.

2. RESULTS

As compared against NCEP/NCAR reanalysis, in the Arctic, AMIP-II models generally oversimulate surface air temperature (SAT) by several degrees during the greater (cold) part of the year. AMIP specification of the open water fraction within sea ice is one of possible causes of the oversimulation. In summer, if the models are ranked in order of increasing cloudiness, SAT biases averaged over the Arctic Ocean tend to decrease from positive to negative values (Fig.1). In winter, the tendency is not pronounced. The inter-model scatter in simulating SAT is high for the northern polar region, and even higher in the Antarctic (Fig.2), where additional variance is introduced by the difference in model resolutions of the orographic gradients.

As compared to the AMIP-I, AMIP-II models on the average show a moderate improvement in the annual cycle of precipitation over the Arctic Ocean in the sense of decreasing the biases and the inter-model scatter throughout the year (not shown). However, with the exception of the summer months, precipitation is still generally oversimulated by the models: the AMIP-II 16-model mean annual precipitation is 0.87 mm/d over the Arctic Ocean poleward of 70^0N, which is 0.02 mm/d lower than the AMIP-I estimate, but still too high compared with available observational estimates of 0.78 mm/d (Bryazgin, 1976; cf. Khrol, 1996), 0.75 mm/d (Legates-Willmott, 1990b), and 0.76 mm/d (Xie-Arkin, 1998). The lack of reliable observational data on precipitation for the Southern polar region prevents definite conclusions on the corresponding systematic errors of the AMIP models.

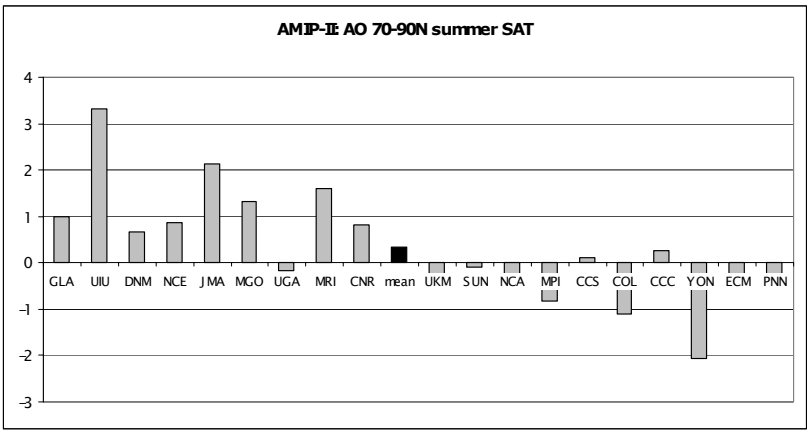

Figure 1. Biases, with respect to NCEP/NCAR reanalysis, of AMIP-II simulations of summer mean SAT averaged over the Arctic Ocean within 70^0N. The models are ranked in order of increasing total cloudiness averaged over the same region. The black bar is for the 19-model mean bias.

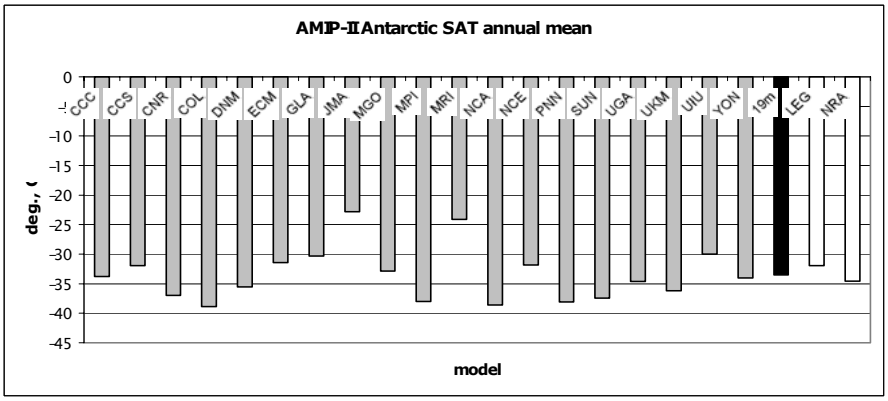

Figure 2. Annual mean SAT averaged over the terrestrial Antarctic. The black bar shows the 19-model mean; the white bars are for Legates-Willmott (1990a) climatology (LEG) and NCEP/NCAR reanalysis (NRA).

Annual mean precipitation minus evapotranspiration (P-E) averaged over terrestrial watersheds of the Arctic Ocean is a good measure of a major component of the ocean freshwater budget – the river water discharge. For the Asian watershed (Fig.3), if compared against the Bryazgin-Shver/Zubenok (1976) estimate of 0.55 mm/d, the AMIP-II 17-model mean (0.56 mm/d) is improved with respect to the same subset of the AMIP-I models (0.65 mm/day). For the North-American watershed, the P-E estimates both for AMIP-I and AMIP-II coincide with each other and the observationally-derived value of 0.60 mm/d.

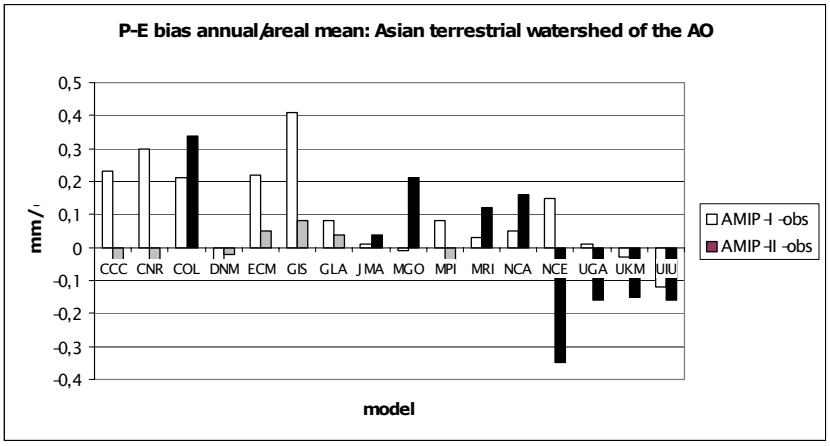

Figure 3. Biases, with respect to the Bryazgin-Shver/Zubenok (1976) estimate, of AMIP-I (white bars) and AMIP-II (gray and black bars) simulations of the annual mean P-E over the Asian terrestrial watershed of the Arctic Ocean. The gray bars mark an improvement, the black ones a deterioration, of model results.

Among the most notable systematic errors of AMIP models is a bias in the pattern of sea level pressure over the Arctic Ocean with respect to NCEP/NCAR reanalysis (Fig.4). The bias has moderately improved in the AMIP-II relative to AMIP-I. The bias has the potential to contaminate the wind forcing of sea-ice/ocean currents in the fully coupled atmosphere-ocean models. Attempts undertaken with the MGO model (AMIP-II version) to establish causes of the bias were of limited success. Varying sea-ice specification (continuous constant-depth slab vs. concentration/thickness distribution); atmospheric diffusion and some other coefficients; horizontal resolution (T42 vs. T30); introducing "enveloped" orography; replacing the AMIP temporally smoothed lower boundary conditions – interpolated SST/sea-ice monthly means – with observed daily fields resulted in changes only of the details, but not the first-order bias.

Other findings include indications of improvements in the seasonal cycle of Arctic clouds in some models, significant scatter (more than 100 W/m^2) between the minimum and maximum (summer) incoming surface short wave radiation, and considerable scatter in turbulent fluxes.

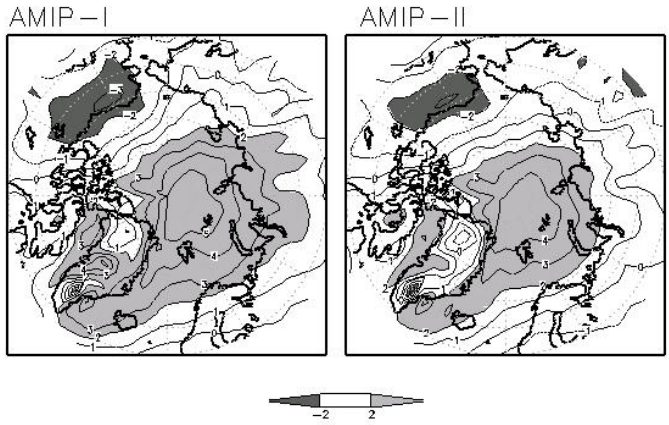

Figure 4. Biases (mb) relative to NCEP/NCAR reanalysis, of the annual mean sea level pressure in the Arctic composited over 17 AMIP-I (left) and AMIP-II (right) models.

3. CONCLUSIONS

Highlights of the findings presented in this paper include a pervasive systematic error in the pattern of sea-level pressure over the Arctic Ocean, indications of improvements in the seasonal cycle of Arctic clouds in some models, and a gradual convergence of the simulated and observational estimates of annual mean precipitation over the Arctic Ocean. While the model-to-model scatter in simulations of the polar atmospheric variables have generally decreased in AMIP-II if compared to AMIP-I, they still remain substantial and potentially important for model coupling. Another obvious problem facing modellers is the insufficiency and inconsistency (scatter) of existing validation datasets in high latitudes, especially in the Antarctic. Because of space limits, this paper includes only a limited portion of results obtained within this study.

ACKNOWLEDGEMENTS

The MGO portion of this study was supported by the Russian Foundation for Basic Research through Grant 02-05-65242, and the Illinois portion by the International Arctic Research Center.

REFERENCES

Walsh, J.E., V. Kattsov, W. Chapman, V. Govorkova, and T. Pavlova, 2002: Comparison of Arctic climate simulations by uncoupled and coupled global models. *J.Climate*, 15, 1429-1446.

Evaluation of AMIP-2 Snow Cover Simulations

Allan Frei[1], James Miller[2] David Robinson[3], Ross Brown[4], Andrew Grundstein[5], Thomas Mote[6]

[1]Hunter College, City University of New York Email: afrei@geo.hunter.cuny.edu
[2]National Snow and Ice Data Center, University of Colorado
[3] Rutgers University
[4]Meteorological Service of Canada,
[5]University Georgia

We present results from fifteen AMIP-2 simulations (table 1) whose simulations of snow covered area (SCA) and snow water equivalent (SWE) are being evaluated. Frei and Robinson (1998) evaluated SCA simulations from twenty-seven AMIP-1 GCMs, finding that at continental to hemispheric scales there were biases in the mean annual snow cycle, including underestimated fall and winter SCA over North America and overestimated spring SCA over Eurasia. The models also failed to reproduce observed interannual variability of SCA.

The principal data set used for estimating historical large-scale SCA is based primarily on visible-band satellite imagery. This weekly data set, produced by the National Oceanic and Atmospheric Administration (NOAA), covers the period from 1967 to present (see climate.rutgers.edu/snowcover). In addition, for AMIP-2 simulations, two new data sets based on combinations of station observations and snow pack models are used to evaluate simulated SWE over North America. Brown et al. (2002) have developed a gridded dataset of SWE over North America specifically for use in evaluating AMIP-2 models. Approximately 8000 snow depth observations per day, obtained from US and Canadian stations, are used in an iterative spatial interpolation routine along with a snow pack model to estimate SWE values on a lat-lon grid of approximately 0.3° resolution. We focus on the region south of 55N, as few stations are located farther north. Grundstein et al. (2002) have developed a 1°x1° gridded SWE data set over the northern Great Plains of the US. Their data set was developed using more sophisticated snow pack modeling, but less sophisticated spatial interpolation, compared to the Brown et al data set. In addition, we use the gridded temperature and precipitation data set of Willmott and Matsuura (2001) to identify causes of regional snow cover biases.

Northern Hemisphere SCA The seasonal biases identified in AMIP-1 models are no longer apparent in AMIP-2 (Frei et al. 2002). Figure 1 shows boxplots of monthly mean SCA over Northern Hemisphere lands from fifteen AMIP-2 models along with observed values (asterisks). Figure 2 (left panel) shows mean winter (DJF) SCA values from observations and from each model. Models are generally within 5% of observed values. Also shown in figure 2 (right panel) are simulated and observed ranges of winter SCA values. AMIP-2 models tend to underestimate variability in SCA, but less severely than AMIP-1 models.

LAT/LON

	ACRONYM	RESEARCH INSTITUTE	GRID
1	**CCCMA**	Canadian Centre for Climate Modelling and Analysis	3.8 x 3.8
2	**CCSR**	Center for Climate System Research	2.8 x 2.8
3	**CNRM**	Centre National de Recherches Meteorologiques	2.8 x 2.8
4	**DNM**	Department of Numerical Mathematics	3.9 x 5.0
5	**ECMWF**	European Centre for Med-Range Weather Forecasts	2.0 x 2.0
6	**GLA**	Goddard Laboratory for Atmospheres	3.9 x 5.0
7	**JMA**	Japanese Meteorological Agency	1.9 x 1.9
8	**MRI**	Meteorological Research Institute	2.8 x 2.8
9	**NCAR**	National Center for Atmospheric Research	2.8 x 2.8
10	**PNNL**	Pacific Northwest National Laboratory	2.8 x 2.8
11	**SUNYA**	SUNY, Albany	2.8 x 2.8
12	**UGAMP**	The UK Universities' Global Atm Mod Programme	2.5 x 3.8
13	**UIUC**	University of Illinois at Urbana-Champaign	3.9 x 5.0
14	**UKMO**	United Kingdom Meteorological Office	2.5 x 3.8
15	**YONU**	Yonsei University	3.9 x 5.0

Table 1. Models included in this analysis of AMIP2 snow simulations.

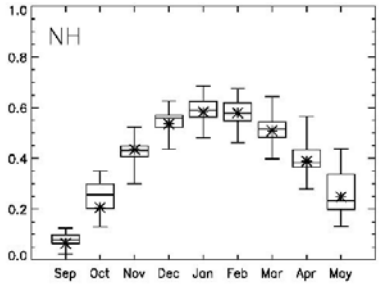

Figure 1. Observed and modeled monthly mean SCA over the Northern Hemisphere. Box and whiskers show results from 15 AMIP-2 models; asterisks indicate observed values. SCA is expressed in fraction of land area north of 20N.

Consistent biases in SCA over large regions (>15 degrees longitude) are prevalent near the southern boundary of the winter snow pack over Eurasia. The region with the largest bias is eastern Asia, including the Tibetan Plateau and eastern China, where models overestimate SCA by $>10^6$ km^2 in January. Over western Asia (30-60E) models understimate SCA, but the magnitude of the bias is approximately half of the bias over eastern Asia. Figure 3 illustrates the bias in one representative model. While these biases in SCA are consistent with model biases in temperature and precipitation when compared to Willmott and Matsuura (2001), there is little correlation between the magnitude of temperature or precipitation biases and the magnitude of SCA biases. Over North America models also have biases, but for large regions (>15 degrees longitude) they are not consistent between models.

North American SWE and SCA Over smaller regions we do find consistent biases over North America. Over the northern Great Plains of the US the models tend to underestimate SWE and overestimate SCA (figure 4). The models tend to deposit a snow pack that is more shallow,

but spatially more extensive, than observations indicate. The overestimation of SCA is particularly apparent in winter and spring.

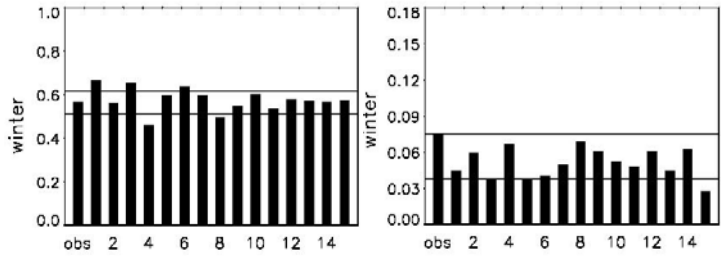

Figure 2. Observed and simulated mean (left panel) and range (right panel) of winter SCA over Northern Hemisphere lands. SCA is expressed in fraction of land area north of 20N.

Over the northern Great Plains models are not capturing the magnitude of large SWE events that are occasionally experienced in this region. As cold air masses tend to dominate, a deep snow pack will persist subsequent to large events, resulting in large monthly SWE values compared to the median. This occurs in almost half of the observed Januaries during the AMIP-2 time domain. Modeled SWE in this region is much less variable (figure 4).

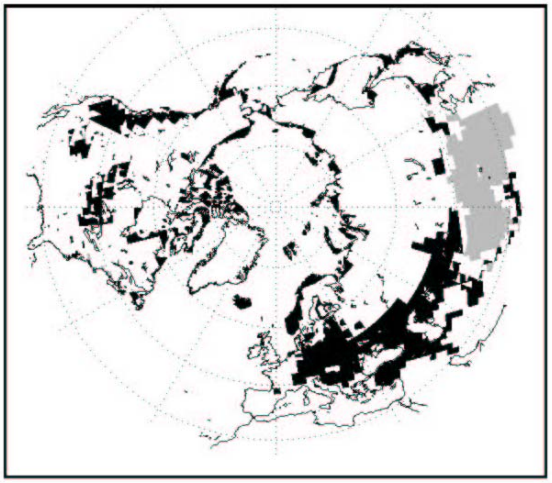

Figure 3. Spatial distribution of bias in mean winter SCA for the MRI AMIP-2 model. Regions of model underestimation >25% are shown in black; model overestimation >25% shown in gray. SCA is expressed in fraction of land area north of 20N.

The underestimation of SWE is not isolated to one small region. Over North America as a whole there is a tendency for models to underestimate SWE. The largest, as well as the most consistent, biases are found over the Pacific coast where orographically induced precipitation associated with maritime air masses result in deep snow packs. All models underestimate SWE in this region.

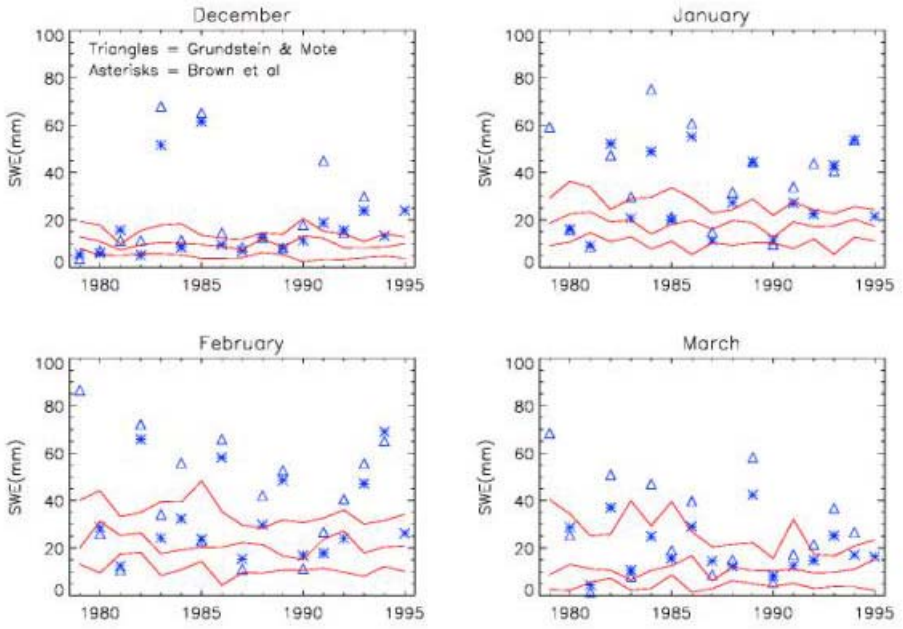

Figure 4. Northern US Great Plains monthly mean SWE (mm) for observed values (asterisks and triangles) and AMIP-2 models. Solid lines indicate bottom quartile, median, and upper quartile of the 15 AMIP-2 models.

References

Brown, R. D., B. Brasnett, D. A. Robinson (2002). "Gridded North American monthly snow depth and snow water equivalent for GCM evaluation." *Atmosphere-Ocean* 40: in press.

Frei, A., J. A. Miller, D. A. Robinson (2002). "Improved simulations of Snow Extent in the Second Phase of the Atmospheric Model Intercomparison Project (AMIP-2)." *Journal of Geohpysical Research, Atmospheres*: submitted.

Frei, A. and D. A. Robinson (1998). "Evaluation of snow extent and its variability in the Atmospheric Model Intercomparison Project." *Journal of Geophysical Research* 103(D8): 8859-8871.

Grundstein, A., T. Mote, D. J. Leathers (2002). "A Hybrid Climatology of Snow Water Equivalent over the Northern Great Plains of the United States." *Polar Geography*: submitted.

Willmott, C. J. and K. Matsuura (2001). Terrestrial Air Temperature and Precipitation: Monthly and Annual Time Series (1950 - 1999), Center for Climatic Research, Department of Geography, University of Delaware.

HYDROLOGICAL CYCLE AND LAND SURFACE PROCESSES

Moisture Cycle Quantities Over the United States and Globe from AMIP-2 Models

David A. Salstein and Richard D. Rosen
Atmospheric and Environmental Research, Inc., Lexington, Massachusetts
salstein@aer.com

INTRODUCTION

Under Diagnostic Subproject 27 we are assessing how well AMIP-2 models simulate precipitable water (W) and moisture divergence over the United States on seasonal and interannual times scales. Seasonally, the summer increase in W and anomalous moisture divergence are reasonably well captured, less so than interannual signals. Considering the North American Monsoon Experiment (NAME) region centered on the Southwest US/Mexico, we find that the models tend as a group to simulate the seasonal progression of moisture reasonably well, although some models appear to be more successful than others in capturing the northward advance and southward retreat of the monsoon. The intensity of the monsoon circulation in a model seems tied to its land-surface scheme, among other characteristics. Globally, the models appear to yield different estimates for the rate at which moisture cycles through the atmosphere.

MOISTURE AND ITS DIVERGENCE OVER NORTH AMERICA

The simulation of atmospheric moisture over North America was examined in individual models, as well as in the ensemble mean. The mean values show the expected general decrease in moisture from south to north with low values in the desert Southwest (Fig. 1). The model means are moister than reanalysis over most of the continent, but in summer models are considerably drier in the Southwest. There is a fair amount of spread in the seasonality of W, as was the case in AMIP-1 (Gaffen et al. 1997). The difference in W over the conterminous US, for example (Fig. 2), between Jun/Jul/Aug and Dec/Jan/Feb is 17 mm for reanalysis, which is spanned by model values ranging from 11 to 25 mm.

Moisture divergence may be determined either directly from horizontal fluxes or by the use of the water balance equation from the difference between evaporation and precipitation (E-P, assuming negligible changes in atmospheric water storage). AMIP protocols did not require all moisture fluxes to be archived, and so the model moisture divergence is computed here from E-P.

Figure 1
Precipitable Water

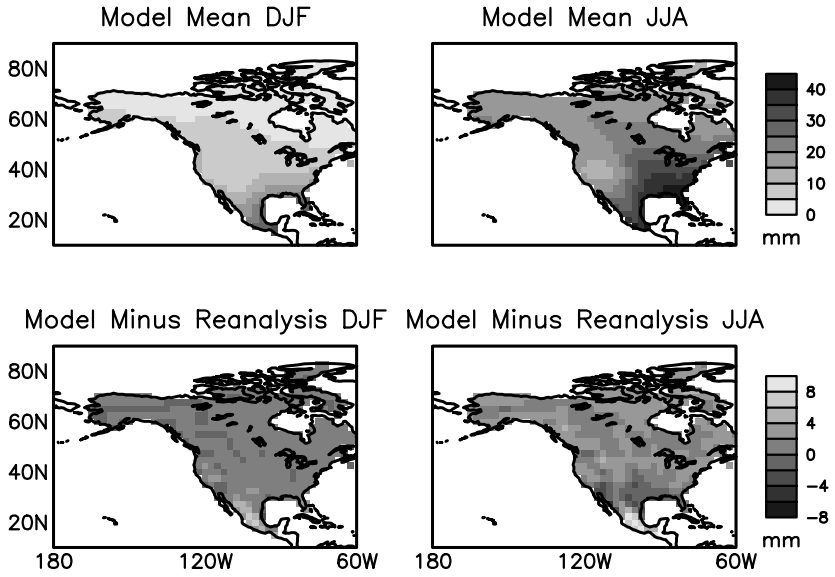

Figure 2
Seasonality of Precipitable Water (JJA minus DJF)

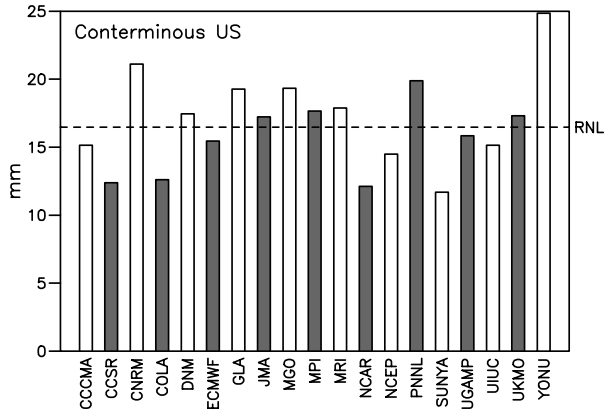

When estimated over the conterminous US (Fig. 3), the seasonal cycle is reasonably well reproduced. Note that the negative sign for most of the year indicates moisture convergence, but during summer divergence over the continent indicates that it is a source of moisture (E>P). Models, however, have both smaller spring convergence and summer divergence than reanalysis. The largest spread among models, given as one standard deviation about the mean, occurs in July. Interannually, the U.S. moisture divergence (Fig. 4) has strong signals related to the phase of ENSO. During the warm events in early 1983, and to a lesser extent, 1987, moisture convergence over the US was most intense. The models capture this signature, though with a fair spread. Moreover, model simulations of both P and E individually possess an ENSO-related signature (Fig. 5, for the Mississippi basin).

Figure 3

Seasonal Cycle of Moisture Divergence over US

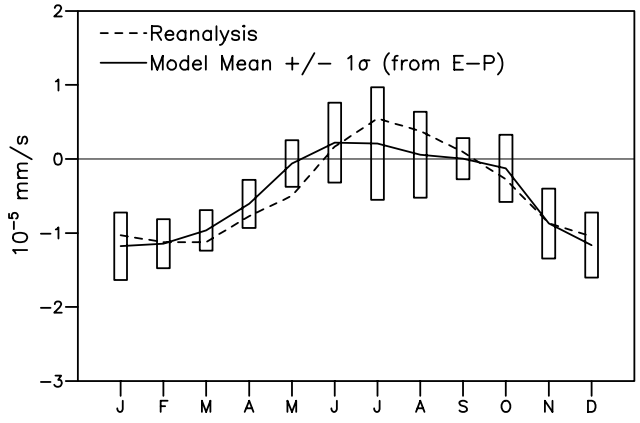

Figure 4

Interannual Signal of Moisture Divergence over US

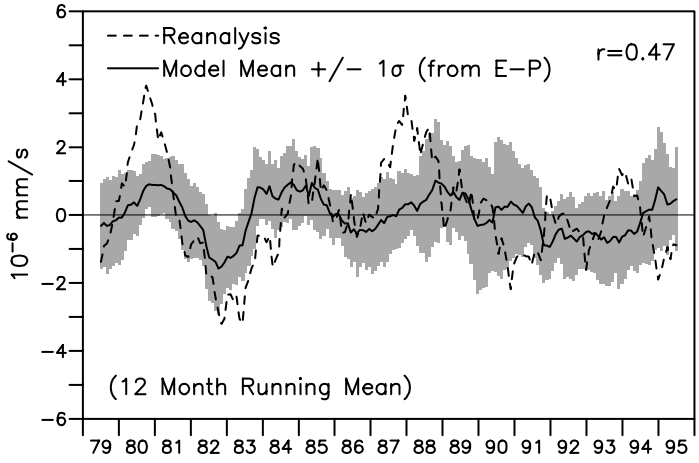

Figure 5

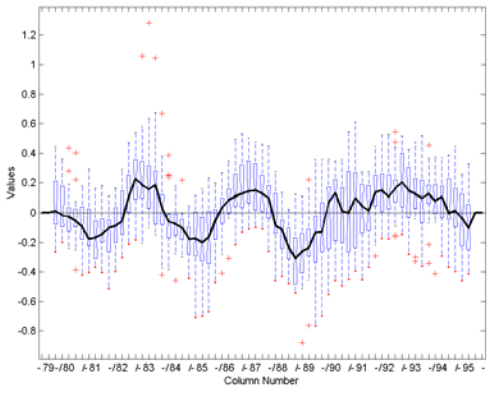

Precipitation

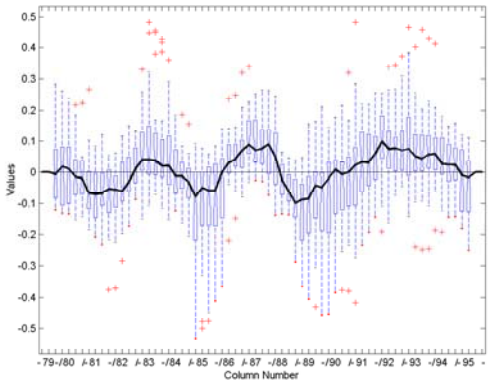

Evaporation

MOISTURE DIVERGENCE IN THE NORTH AMERICAN MONSOON

Three nested regions have been defined by the NAME to study aspects of seasonal moisture variability over much of the US (Higgins et al. 1997). The core NAME region 1 is limited to northwest Mexico and southern Arizona and New Mexico, with NAME regions 2 and 3 covering ever greater parts of the continent (Fig. 6). The seasonal cycle of the monsoon signal is characterized by moisture convergence starting in springtime in the lowest NAME latitudes, advancing farther north as the warm season progresses. The northernmost extent of the largest convergence occurs during August. (This region, unlike the US as a whole, is not a source region for moisture in the summer, but rather receives it from elsewhere.) The monsoonal moisture signal retreats by mid-autumn. Models fall into three categories in reproducing the strength the monsoon (Fig. 7 for NAME region 2): Weak with a small seasonal signal (CCSR, COLA, GLA, MRI, NCEP, UGAMP, UIUC, and UKMO); Moderate, most similar to the NCEP-NCAR reanalysis (CCC, CNRM, DNM, ECMWF, JMA, MPI, SUNYA, and YONU); and more Intense than observed (MGO, NCAR, PNNL). Interannual anomalies in the models are somewhat more difficult to categorize in this fashion, yet there are similarities with the seasonal assignments. Based on these categories, we note that land-surface schemes can be associated with the intensity of the monsoon. For example, UGAMP and UKMO, two Weak models (in the NAME2 region), use the Meteorological Office Surface Exchange Scheme. Also generally in the Weak category are models using SiB. The Moderate models typically have "bucket" and ISBA schemes, and the Intense use the LSM or BATS schemes. (Abbreviations are identified in AMIP documents.)

Figure 6

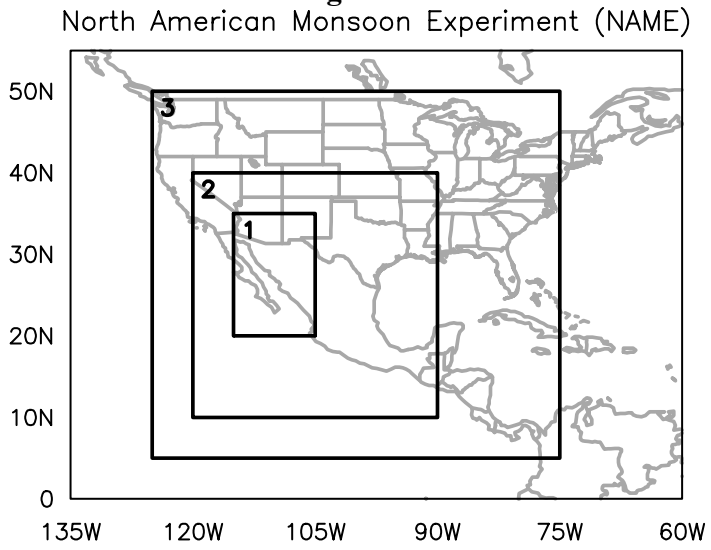

Figure 7

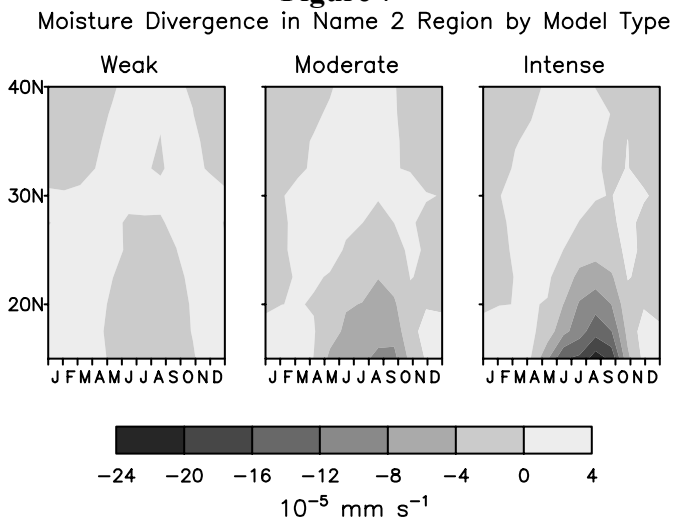

GLOBAL RECYCLING

AMIP-2 models were also analyzed to estimate global atmospheric moisture residence times (Salstein et al. 2003). Defined as the ratio of either W/P or, equivalently, W/E, values between 7 and 10 days are estimated by the models. Such differences indicate that models are cycling water at considerably different rates through the atmosphere. Interestingly, though, the models do tend as a group to possess an ENSO signal in residence time, which is longer during warm events.

REFERENCES

Gaffen, D.J., R.D. Rosen, D.A. Salstein, J.S. Boyle, 1997: Evaluation of tropospheric water vapor simulations from the Atmospheric Model Intercomparison Project. *J. Climate*, **10**, 1648-1661.

Higgins, R. W., Y. Yao, and X. Wang, 1997: Influence of the North American Monsoon System on the US summer precipitation regime. *J. Climate*, **10**, 2600-2622.

Salstein, D.A., R.D. Rosen, and H. Kanamaru, 2003: Model-based estimates of moisture cycling over the US and globe. Extended abstract, Symposium on Observing and Understanding the Variability of Water in Weather and Climate. Amer. Meteor. Soc.

ACKNOWLEDGMENTS. Grant NA06GP0349 from NOAA/Office of Global Programs to AER supported the work reported here. We thank H. Kanamaru who performed the calculations for Fig. 5 at Boston University.

Atmospheric Transports into the Continents of Energy and Water Simulated with AMIP Models

Ho-Jeong Shin[1], Il-Ung Chung[2], Jeong-Woo Kim[1]

[1]Department of Atmospheric Sciences and Global Environment Laboratory, Yonsei University
[2]Department of Atmospheric & Environmental Sciences, Kangnung National University

1. Introduction

In this study, atmospheric energy and water transports not only into the global land but also into each of the six continents are analyzed for their annual mean and variation with AMIP II standard simulations

The energy budget at the top-of-atmosphere calculated from AMIP II simulation by YONU AGCM Tr7 results in the net downward radiation over the ocean and the net upward radiation over the land. This result implies that the ocean-to-land energy transport should necessarily occur in atmosphere for satisfying the global energy balance. This transport has a magnitude of 2.2PW, which is a sum of latent heat transport and dry static energy transport. Latent heat transport estimated from the surface freshwater flux (that is, precipitation minus surface evaporation) balances surface runoff (energy equivalent) within 10% difference, and it shows a larger amount of 3.5PW and the same direction compared to the total energy transport. Dry static energy transport estimated from the difference between total and latent energy transport is 1.3PW in land-to-ocean direction. From the facts that the ocean-to-land energy transport on the global scale is dominantly related to the latent energy transport and the two components of the total energy transport have the opposite direction against each other, a question is raised if such characteristics of the ocean-to-land energy transport would also be shown on the continental scale.

2. Annual Mean

On the global scale, AMIP II model ensemble shows the similar feature as the results from YONU AGCM so that total ocean-to-land energy transport of 2.4PW consists of latent heat transport of 3.2PW in the same direction and dry static energy transport of 0.8PW in the opposite direction (Fig. 1). However, as shown in Fig. 1, this feature is not shown for any continent. The six continents can be classified into two groups in terms of their characteristics of the energy transport. Eurasia, North America and Antarctica belong to the first group, in which total energy and dry static energy are transported into the continents. On the contrary, in the second group including South America, Africa and Oceania, they are transported out of the continents. In both groups, the direction of total energy transport follows that of dry static energy transport. Latent energy is transported into all continents to balance surface runoff.

3. Annual Variation

Most of the continents experience the seasonal reverse in direction of the total energy transport in relevance to monsoonal circulation (Fig. 2a). Therefore, in the hemispheric continents such as Eurasia, North America, Oceania and South America, the annual variation of energy transport is relatively large, and in both hemispheres, the land-to-ocean transports occur during summer. Africa, in particular, shows the smallest annual variation. On the global scale, the annual

variation of total energy transport seems to be dominated by the pattern for the northern hemispheric continents. The pattern of seasonal change of dry static energy transport into each continent, as shown in Fig. 2b, is quite similar to that of total energy transport. As a result, the annual variation of the total energy transport can be largely explained by that of the dry static energy transport while the annual mean of the transport on the global scale can be largely explained by latent heat transport. From Fig. 2c, two salient features in the annual variation of the latent heat transport into continents can be pointed out: One is that seasonal reverse of the transport does not occur for every continent, and the other is that the magnitude of annual variation of the latent heat transport is much smaller than that of the dry static energy transport. Compared Fig. 2c with 2d, it is found that these continental scale water transports do not balance monthly but annually with phase differences.

The annual variations of the ocean-to-land energy transports are analyzed from Taylor diagram as shown in Fig. 3. In these diagrams, the ensemble mean of AMIP II simulations is used as a reference data, and the standard deviation for each model result is normalized by that for the ensemble mean. Compared to ensemble mean, Fig. 3a indicates that most of the models have a high correlation of 0.9 or more and small pattern-difference with respect to the annual variation of total energy transport. This result is probably interpreted by way that the uncertainty of total energy transport is relatively low due to energy conservation. In this figure, it should be noted that the model-to-model variance for African continent is significantly larger than that for the other continents. In case of the dry static energy transport shown in Fig. 3b, each model has lower correlation and larger pattern difference with the model ensemble mean, compared to case of the total energy transport. These two diagrams, however, retain a high similarity, as we can easily expect from the discussion above. From Fig. 3c and 3d, the distinguished features in the comparison of continental scale water transports are the great inter-model difference and its significant variance between continents.

4. Conclusive Remark

Annually, total energy and dry static energy transports into the global land are in the opposite direction. However, on every continent, they are in the same direction. Dry static energy is transported into Eurasia, North America and Antarctica, while transported out of South America, Oceania and Africa. Further analysis and discussion will have to be done to explain the reasons of the differences in the energy transports between continents.

Latent energy is transported into all continents during the whole year to balance surface runoff, and the balance maintains on annual average with monthly differences in phase of annual variation between latent energy and surface runoff. The large inter-model differences should be taken into account to be reduced in pursue of model improvement.

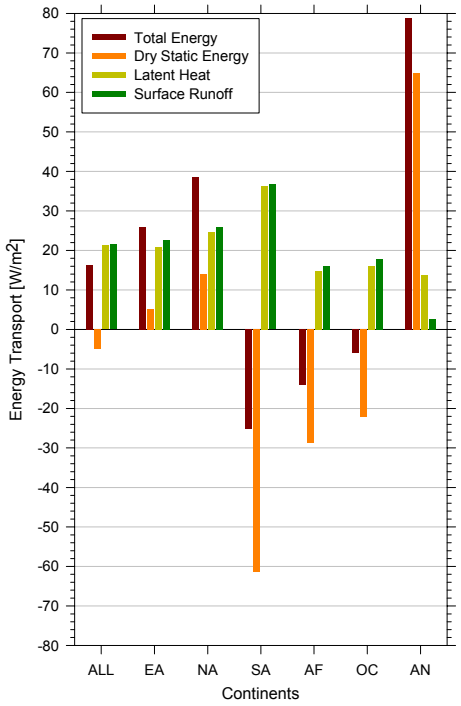

Fig. 1. The annual mean ocean-to-land energy transport per unit area (in Wm^{-2}) determined by ensemble mean of 17 AMIP II models. EA, NA, SA, AF, OC and AN represents Eurasia, North America, South America, Africa, Oceania and Antarctica, respectively, and ALL is for the entire continents.

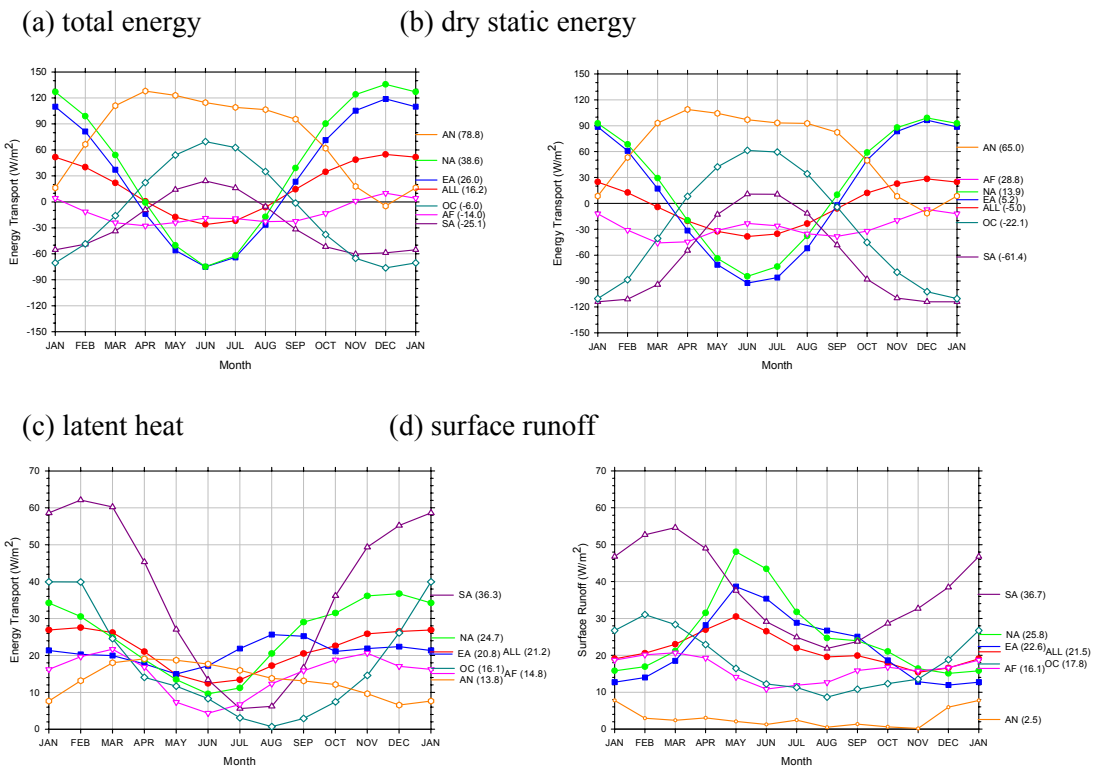

Fig. 2. The annual variation of ocean-to-land energy transport per unit area (in Wm^{-2}) determined by ensemble mean of the 17 AMIP II models. Each panel is for total energy (a), dry static energy (b), latent heat (c) and surface runoff (d), respectively.

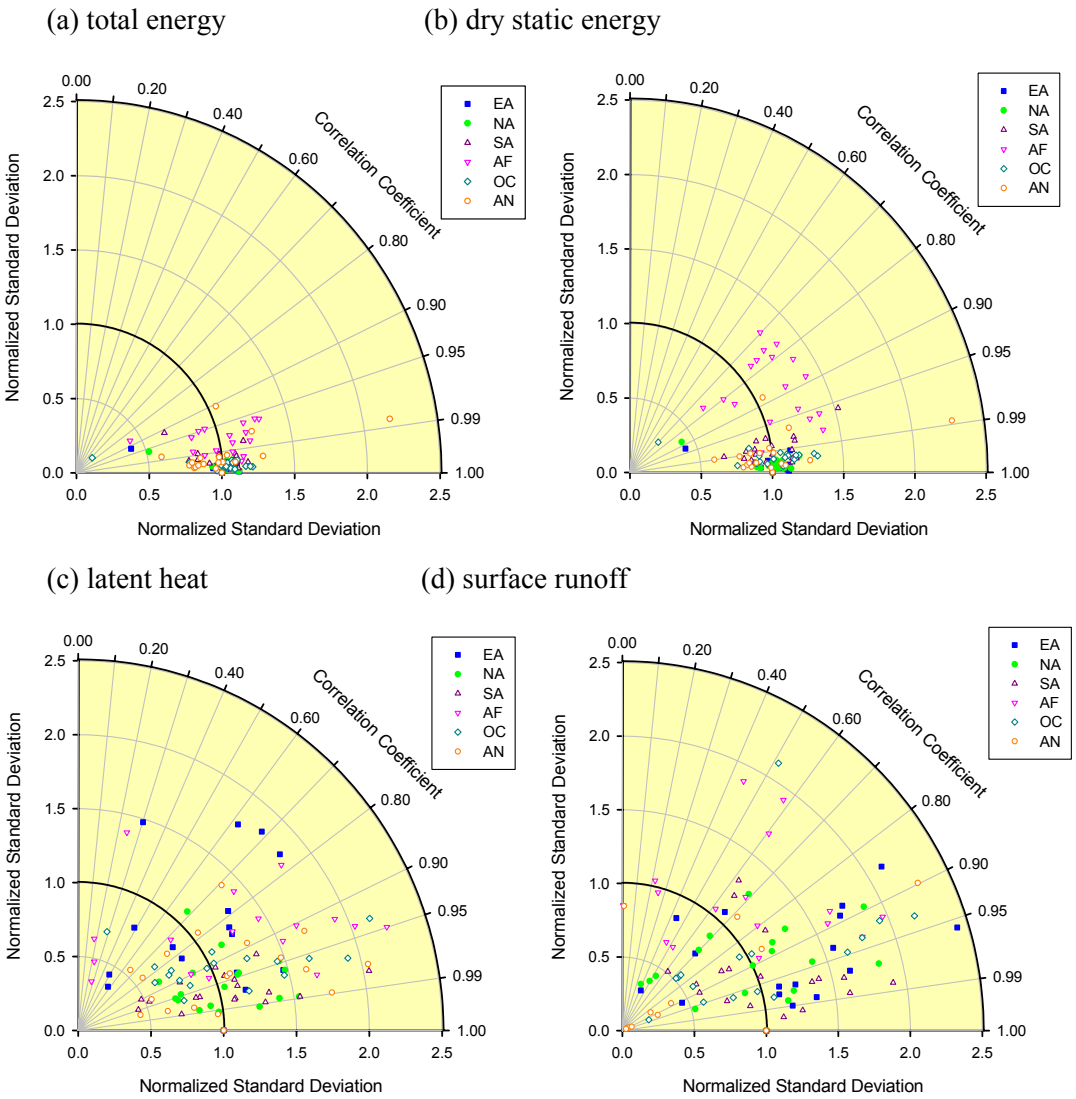

Fig. 3. Taylor diagrams for annual variation of ocean-to-land energy transports simulated by 17 AMIP II models. Each panel is for total energy (a), dry static energy (b), latent heat (c), and surface runoff (d).

GLASS-Sponsored Activities Relevant to AMIP

Randal Koster
Global Modeling and Assimilation Office
Code 900.3, NASA Goddard Space Flight Center
Greenbelt, Maryland, USA
randal.d.koster@nasa.gov

1. Introduction: What is GLASS?

GLASS (Global Land-Atmosphere System Study) is a subpanel of the GEWEX (Global Energy and Water Cycle Experiment) program, which itself is a component of the World Climate Research Program. GLASS focuses on the improved modeling of land surface processes and their interaction with the atmosphere. GLASS research currently proceeds along four lines:

(1) *"Offline local-scale" activities*. This is essentially the new home of the offline thrust of the Project for the Intercomparison of Land-Surface Parameterization Schemes (PILPS), a project that for a number of years has focused on the analysis and validation of land surface models (LSMs). Through PILPS, LSMs have been driven with observations-based forcing data, and their responses (evaporation, runoff, etc.) have been compared directly to observations.

(2) *"Offline large-scale" activities*. This effort encompasses the Global Soil Wetness Project, a project in which a number of LSMs are forced with realistic global distributions of rainfall, radiation, and other forcing to produce global distributions of soil moisture, evaporation, and other land surface fields. GSWP is entering its second phase, in which ten years (1986-1995) of surface data will be generated.

(3) *"Coupled local-scale" activities*. In this effort, land surface models are coupled to single column representations of local atmospheric processes to examine the feedback processes associated with land-atmosphere coupling. One emphasis is on the use of such simple coupled systems to aid in land data assimilation.

(4) *"Coupled large-scale" activities*. Here, land-atmosphere coupling at the global scale, as represented by atmospheric general circulation models, is examined with detailed experiments. One of the foci is on seasonal prediction, i.e., on the determination of how the knowledge of land moisture conditions contributes to seasonal forecast skill.

More information on GLASS is available from its website, (http://hydro.iis.u-tokyo.ac.jp/GLASS). Many of the activities in the fourth GLASS effort are highly relevant to the AMIP project. The remainder of this paper addresses these activities.

2. GLACE

The list of published AGCM land-atmosphere interaction studies is extensive. Necessarily missing from single-AGCM experiments, however, is an analysis of the model-dependence of the experimental results. Model dependence in land-atmosphere interaction can bias results tremendously. In one AGCM, the atmosphere may respond strongly to anomalies in land surface state, and in another, the atmosphere may have an internal variability that overwhelms any land surface signal. The two AGCMs would yield contradictory conclusions about the importance of initializing soil moisture in forecast simulations, about the degree to

which deforestation affects climate, and perhaps even about the need for a realistic treatment of land surface processes in climate simulations.

The degree to which the atmosphere responds to land surface anomalies, particularly at hourly to monthly timescales, is hereafter loosely referred to as the ``land-atmosphere coupling strength''. Coupling strength is not easy to quantify. It is not explicitly prescribed or parameterized, being instead a net result of complex interactions between numerous complex process parameterizations in the AGCM, such as those for evapotranspiration, boundary layer development, and moist convection. The great majority of AGCM land-atmosphere interaction studies appear to take a given model's implicit coupling strength on faith, never attempting to quantify it or to compare it against that of other models. This arguably hinders the evaluation of climate sensitivity experiments.

The quantification and documentation of land-atmosphere coupling strength is indeed the goal of GLACE (Global Land-Atmosphere Coupling Experiment). GLACE will *not* be able to address the realism of simulated large-scale coupling strength, since the necessary direct measurements are not available. The project will, however, show the extent to which the coupling strength varies between models, and it will allow individual models to be characterized as having a relatively strong, intermediate, or weak coupling, for later use in interpreting results obtained with those models. The range of coupling strengths uncovered by GLACE will serve to quantify the uncertainty inherent in our understanding of land-atmosphere coupling and our ability to model it.

GLACE is a broad follow-on to the four-model intercomparison study of Koster et al. (2002), hereafter referred to as K02. K02 describes a numerical experiment performed by four AGCM modeling groups: the NASA Seasonal-to-Interannual Prediction Project (NSIPP) AGCM, the Center for Ocean-Land-Atmosphere Studies (COLA) AGCM, the National Center for Atmospheric Research Community Climate Model Version 3 coupled to the Biosphere-Atmosphere Transfer Scheme (CCM3/BATS), and the Hadley Centre, Met Office AGCM (HadAM3). In the first part of the experiment, the AGCM, fully coupled to its own land surface model (LSM) but forced by prescribed sea surface temperatures (SSTs), was run over July. At each time step in this simulation (hereafter labeled simulation W1), the values of all land surface prognostic variables at every grid cell were recorded into a special data file. The one-month experiment was then repeated 15 more times, using 15 different sets of atmospheric and land surface initial conditions, to obtain an ensemble of 16 one-month (July) simulations (simulations W1-W16)

.

The second part of the experiment consisted of another 16-member ensemble of one-month (July) simulations, using the same prescribed SSTs. At every time step of each of these simulations, the updated values of all land surface prognostic variables were discarded and then replaced by the corresponding values for that time step from the data file written in Simulation W1. Thus, in this ensemble, all member simulations (simulations R1-R16) were forced to maintain precisely the same time series of geographically-varying land surface states.

The resulting precipitation data from the two ensembles were processed into a diagnostic Ω_P, which reflects the degree to which the sixteen precipitation time series generated in each ensemble are similar. In essence, Ω_P is a useful measure of land-atmosphere coupling strength, being essentially the ratio of land-explained precipitation variance to total precipitation variance. (See K02 for more details.) Plots of Ω_P for the four AGCMs show a wide disparity in the diagnostic between the models. Land-atmosphere coupling strength is clearly largest for the NSIPP model. The COLA and CCM3/BATS models have similar coupling strength distributions, with Ω_P values of 0.2 or less almost everywhere, and the HadAM3 model has what appears to be the weakest coupling strength.

The K02 study was a first step in the right direction. GLACE aims to extend the analysis substantially:

a. *Participation From a Wider Range of Models*. The intriguing intermodel variations found in K02 are presumably indicative of the broad range of coupling strengths implicit in today's AGCMs. The goal of GLACE is to establish this range more precisely and, more importantly, to generate a comprehensive ``table" of AGCM coupling strengths, a table that can help in the interpretation of the published results of a wide variety of climate models.

b. *Separation of the Effects of "Fast" and "Slow" Reservoirs*. The experimental set-up used in K02 was limited; the prescribed diurnal surface temperature variations had as much an effect on Ω_P as anything else. Since diurnal variations in temperature and storage in ``fast" moisture reservoirs (e.g., canopy interception) have little potential for seasonal prediction, the noted differences in K02 may have limited practical application. Of much greater relevance to the general question of land impact on climate is whether some of the ``slower" state variables (in particular, soil moisture in the root zone and lower reservoirs) affect the evolution of weather. This aspect of coupling strength will be examined in GLACE through some simple modifications to the experimental plan.

c. *Effect on Air Temperature*. K02 focused on how the land surface boundary affects the generation of precipitation. Also of interest is the control of the land boundary on air temperature fluctuations, particularly when only root zone (and lower) soil moisture is prescribed. GLACE will provide the means to address this issue.

Complete details regarding the experimental plan are available at both the GLACE website (http://glace.gsfc.nasa.gov) and the GLASS website (http://hydro.iis.u-tokyo.ac.jp/GLASS). Participating AGCM groups are given 6 months to complete the GLACE experiments; the current due date is the end of August, 2003. The processing and analysis of the submitted AGCM data will then take about 3 months, at which time a a summary journal paper, co-authored by all participants, will be written.

3. "Poor Man's LDAS" Experiment

A second experiment proposed for the GLASS "large-scale coupled" initiative has a more direct bearing on the issue of seasonal predictability. In essence, the experiment directly determines the degree to which land moisture initialization affects the seasonal prediction of precipitation and temperature.

A pilot study with the NSIPP AGCM has been performed. For each boreal summer during 1997-2001, two 16-member ensembles of 3-month simulations were generated. The first, ``AMIP-style" ensemble establishes the degree to which a perfect prediction of SSTs would

contribute to the seasonal prediction of precipitation and temperature over continents. The second ensemble is identical to the first, except that the land surface is also initialized with ``realistic'' soil moisture contents through the continuous prior application (within GCM simulations leading up to the start of the forecast period) of a daily observational precipitation data set and the associated avoidance of model drift through the scaling of all surface prognostic variables. By comparing the output from the two ensembles, the impact of land initialization on the forecasted precipitation is isolated.

The pilot study shows that land initialization has a statistically significant impact on summertime precipitation over only a handful of continental regions. These regions agree, to first order, with those that satisfy three conditions: (1) a tendency toward large initial soil moisture anomalies, (2) a strong sensitivity of evaporation to soil moisture, and (3) a strong sensitivity of precipitation to evaporation. The impact on temperature prediction is more spatially extensive. The degree to which the initialization increases the *skill* of the forecasts is mixed, reflecting a critical need for the continued development of model parameterizations and data analysis strategies.

This "Poor Man's LDAS" experiment, which is described in detail by Koster and Suarez (2003), requires a substantially larger commitment of participants' computer resources than the GLACE experiment. The design of the multi-model intercomparison version of this experiment is still in its planning stages. It is not yet known how many modeling groups would be willing to participate.

4. Memory Analysis

Recently, Koster and Suarez (2001) applied water balance considerations at the soil surface to derive an equation that relates the autocorrelation of soil moisture in climate models to (1) seasonality in the statistics of the atmospheric forcing, (2) the variation of evaporation with soil moisture, (3) the variation of runoff with soil moisture, and (4) correlation between the atmospheric forcing and antecedent soil moisture, as perhaps induced by land-atmosphere feedback. Geographical variations in the relative strengths of these factors, which can be established through analysis of model diagnostics, lead to geographical variations in simulated soil moisture memory. Koster and Suarez (2001) successfully demonstrated the relevance and usefulness of the equation with data from the NSIPP modeling system.

The equation should, in fact, be applicable to any AGCM-LSM system. All that is needed is information on soil water holding capacity, instantaneous soil moisture contents, and monthly-averaged evaporation, net radiation, precipitation, and runoff amounts. Presumably all of these data already exist amongst the standard data archived for AMIP. Thus, without any new effort from AMIP participants, AMIP and GLASS could collaborate on an intercomparison study focusing on soil moisture memory. Such a study is being considered by the GLASS panel.

5. Closing Words

The "large-scale coupled" effort of GLASS can benefit greatly from interaction with the AMIP community. The modeling groups needed to perform the GLASS intercomparison studies described above are, for the most part, already participating in AMIP. Conversely, AMIP

modeling groups can glean benefit from participation in GLASS experiments. These experiments will give a participating group a much stronger understanding of its model's land-atmosphere coupling. This improved understanding is important, given the importance of the coupling in defining the model's overall behavior.

References:

Koster, R. D., and M. J. Suarez, 2001: Soil moisture memory in climate models. *J. Hydrometeorology*, **2**, 558-570.

Koster, R. D., P. A. Dirmeyer, A. N. Hahmann, R. Ijpelaar, L. Tyahla, P. Cox, and M. J. Suarez, 2002: Comparing the degree of land-atmosphere interaction in four atmospheric general circulation models. *J. Hydrometeorology*, **3**, 363-375.

Koster, R. D., and M. J. Suarez, 2003: Impact of land surface initialization on seasonal precipitation and temperature prediction, *J. Hydrometeorology*, **4**, 408-423.

The GEWEX Atmospheric Boundary Layer Study (*GABLS*)

Albert A.M. Holtslag,
Meteorology and Air Quality Section, Wageningen University, the Netherlands (NL)

The overall objective of the GEWEX Atmospheric Boundary Layer Study (*GABLS*) is to improve the understanding and the representation of the atmospheric boundary layer in regional and large-scale climate models. *GABLS* aims to provide a platform in which scientists working on boundary layers at different scales will interact. Such activity is important in itself and also very relevant for other activities in GEWEX and more generally for the activities within WCRP and IGBP (Holtslag and Randall, 2001).

The first focus of *GABLS* is on the representation of the stable atmospheric boundary layer (SBL). It appears that much of the warming predicted by climate models is during stable conditions over land (either in winter or at night). This is documented in the latest IPCC report (see for example figure 9.10, pages 546-548 in Cubasch and Meehl, 2001). At the same time it is realized that the understanding and parameterization of the SBL is still rather poor, and that progress is slow (e.g. Beljaars and Holtslag, 1991). As an example, Figure 1 shows the difference in the temperature at a height of 2 meters for January 1996 as calculated from two model runs with the same forcings, but with (slightly) different stability functions in the mixing scheme of the ECMWF model in stable conditions (after Viterbo et al, 1999). The scheme with more mixing, leads to higher temperatures over continental areas in winter. To obtain the same synoptic evolution in the two simulations, gentle relaxation towards the analysis is applied above 500 m above the surface. Also the same prescribed values for the sea surface temperature are used (see Viterbo et al, 1999 for more details). Notice that the differences in the mean temperatures over the land areas can take values up to 10K!

To review our understanding and to discuss future directions on Stable Boundary Layers, a workshop was held at the European Center for Medium-Range Weather Forecasting (ECMWF) in Reading, UK, on March 25-27, 2002. The workshop agenda covered the following topics: Modeling and parameterization experiences at the large-scale modeling centers, Progress in theory and understanding of SBLs, Large-Eddy Simulation (LES), and Observational data sets (Cabauw, CASES, ARM, Lindenberg, and others). Discussion sessions were held on each of the above topics, and a planning session concluded the meeting. In total about 20 presentations were given by leading scientists and about 30 people attended the workshop (see Figure 2 for a photo of the attendees).

At the ECMWF-workshop many questions were raised, such as: Why do (most) models like enhanced mixing in stable cases? What is the role of the Atmosphere - Land Surface coupling for SBL's (see also Van der Wiel et al, 2002a en b)? How do models compare with the new data available (such as from CASES-99; see Poulos et al, 2002)? How important is model vertical resolution, et cetera? Subsequently, the GABLS plans were presented at a meeting during the AMS 15th Symposium on Boundary Layers and Turbulence in Wageningen, the Netherlands (Evening of 16 July 2002). About 80 conference participants joined that meeting and overall very positive feed back was received.

Initially a case study of a night in the CASES-99 data set (Poulos et al, 2002) was prepared for a bench-mark study of one dimensional column and LES models over land (prepared by staff members at the Meteorology and Air Quality Section of Wageningen University, NL). However,

it became clear that a bench-mark case for a stable boundary layer over land is rather complex to start with and to compare the skills of LES and single column models. Therefore, it has been decided to first focus on a case for a SBL with less complexity. This case is based on the results presented in a study by Kosovic and Curry (2000). As such the boundary layer is driven by an imposed, uniform geostrophic wind, with a specified surface-cooling rate, which attains a quasi-steady state SBL. The case for the LES inter comparison is prepared and convened by Malcolm MacVean (Meteorological Office, UK). In addition, Joan Cuxart Rodamilans (University of the Balearic Islands at Mallorca) convenes the inter comparison of the single-column models for this case.

The selected case has already been distributed for a LES inter comparison, where the basic aim is to contribute towards a quantification of the reliability of stable boundary layers in LES. About 10 groups have already agreed to participate in this exercise. The purpose of this single-column inter comparison is to check the performance of any turbulence or vertical diffusion scheme for this shear-driven stably stratified case. The basic philosophy of this exercise is to make a run with every single-column model at exactly the same conditions as the LES, including physical setup and vertical resolution. This will make the comparison to the LES outputs more trustable. Single-column versions of operational models (either weather forecast or climate studies) are very welcome to participate.

The outcome of the model inter comparison study will be presented at a workshop which is planned to be held in Mallorca in the period of September 22 until 25, 2003 (as hosted by the University of the Balearic Islands). We strongly encourage the large-scale modeling centers to take part in the 1D model inter comparisons studies, as well as motivate their scientists to contribute and take part in the proposed activities.

In the future we hope that GABLS may also present an important opportunity for the set up of adequate datasets to be collected and for the consistent analysis of existing data for the improvement of stable atmosphere parameterizations in various conditions. Such improvements are of utmost importance to the study of regional and global climate change scenarios, among other important modeling uses. This issue will also be addressed in the fourth coming workshop.

If you like to participate in the model inter comparisons and/or in the workshop please send an email to Bert Holtslag (Bert Holtslag@wur.nl) for general information, to Joan Cuxart Rodamilans (joan.cuxart@uib.es) for the single-column model study or to Malcolm MacVean (malcolm.macvean@metoffice.com) for the LES inter comparison. Please also consult http://www.gewex.org/ or http://www.met.wau.nl/ for updates on GABLS activities in the near future.

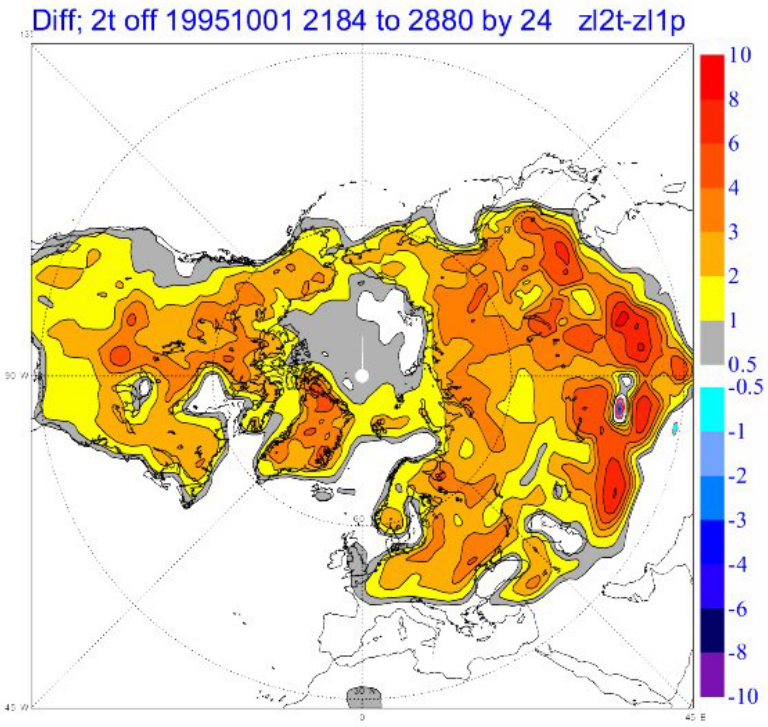

Figure 1
Difference of the *mean* temperatures at a height of 2 meters for January 1996 between calculations with two versions of the stable boundary layer parameterization in the ECMWF model. Note that areas over land with differences less than 0.5 K are indicated as 'white' in the figure, while larger differences are according to the scale at the right hand side of the figure (Courtesy Anton Beljaars, ECMWF).

Acknowledgements
This is a community effort, which needs the activity and creativity of many people to make real progress! As such I like to thank all participants at the various meetings for their inputs and comments. In particular I would like to acknowledge Ric Cederwall, Anton Beljaars, Malcolm MacVean, Joan Cuxart Rodamilans, Greg Poulos, and my staff members at the Meteorology and Air Quality Section of Wageningen University for their help and comments. This text also appeared in the GEWEX newsletter, 13, May 2003

References

Beljaars, A.C.M., and A.A.M. Holtslag, 1991: Flux parameterization over land surfaces for atmospheric models. J. Appl. Meteor., 30, 327-341.
Cubasch, U. and G.A. Meehl (and many contributing authors), 2001: Projections of Future Climate Change, Chapter 9 in 'Climate Change, The scientific basis', IPCC, Cambridge UP.
Holtslag, A.A.M. and D.A. Randall, 2001: New Boundary Layer Study. GEWEX news, 11, p. 6.

Kosovic, B. and J.A. Curry, 2000: A large eddy simulation study of a quasi-steady, stably stratified atmospheric boundary layer. J. Atmos. Sci., 57, p. 1052-1068.

Poulos, G.S., W. Blumen, D.C. Fritts, J.L. Lundquist, J.L. Sun, S.P. Burns, C. Nappo, R. Banta, R. Newsom, J. Cuxart, E. Terradellas, B. Balsley, and M. Jensen, 2001: CASES-99, A comprehensive investigation of the Stable Boundary layer. B. Am. Meteorol. Soc., 83, p. 555-581.

Viterbo, P, A.C.M. Beljaars, J.-F. Mahfouf, and J. Teixeira, 1999: The representation of soil moisture freezing and its impacts on the stable boundary layer. Q.J. Roy. Meteorol. Soc, 125, p. 2401-2426.

Wiel, B.J.H. van de, R.J. Ronda, A.F. Moene, H.A.R. de Bruin, and A.A.M. Holtslag, 2002: Intermittent turbulence and oscillations in the stable boundary layer over land - Part 1: A bulk model. J. Atmos. Sci., 59, 942-958. Part 2: A system dynamics approach. J. Atmos. Sci., 59, 2567-2581.

Large-Scale Validation of AMIP2 Land-Surface Simulations

T.J. Phillips[1], A. Henderson-Sellers[2], P. Irannejad[2], K. McGuffie[3], S. Sharmeen[2], H. Zhang[4]

[1] PCMDI/LLNL, Livermore, California, USA (e-mail: phillips@pcmdi.llnl.gov)
[2]ANSTO Environment, Sydney, Australia
[3]University of Technology, Sydney, Australia
[4]Bureau of Meteorology Research Centre, Melbourne, Australia

INTRODUCTION

Diagnostic Subproject 12 (DSP 12) on Land-surface Processes and Parameterizations is one of several AMIP-related efforts to analyze the effectiveness of current climate models in simulating continental processes. DSP 12's particular objectives are 1) to validate large-scale AMIP2 continental simulations against available global reference data sets; 2) to verify continental energy/moisture conservation and diagnose related land-surface processes in the AMIP2 models; and 3) to formulate hypotheses on putative connections between AMIP2 simulation performance and the complexities of the respective land-surface schemes (LSSs) that might be tested by further numerical experimentation.

This paper outlines DSP 12's large-scale validation work, while companion papers by Henderson-Sellers et al., Irannejad et al., and Zhang et al. briefly present our analysis of other facets of AMIP2 land-surface simulations.

METHODOLOGY

In validating AMIP simulations of continental climate on the large (continental to global) scale, we examine both coupled atmospheric forcings (e.g. precipitation) and surface responses (e.g. latent heat flux). We choose a reference data set that offers a "best current estimate of truth" for each land-surface process, but we also consider alternative choices of validation data, in recognition of the existing large observational uncertainties. Because of the present dearth of direct observations of many continental processes on the global scale, we utilize "synthetic" data sets such as:

- merged gauge-satellite precipitation products such as the Climate Prediction Center Merged Analysis of Precipitation (CMAP) or the Global Precipitation Climatology Project (GPCP) data sets;
- simulations of latent heat flux obtained by off-line forcing of a particular LSS with observed estimates of precipitation such as that of the Variable Infiltration Capacity (VIC) simulation of global continental climate for the period 1979-1993 (Nijssen et al. 2001 *J. Climate*).
- climate reanalyses such as that of the ECMWF ERA15, and the NCEP R1 (aka NCEP/NCAR) and R2 (aka NCEP/DOE) reanalyses.

Figure 1: Taylor diagram of integrated spatio-temporal variabilities of continental precipitation from alternative validation data sets-- CMAP and VIC observational estimates, and ERA15 ('ERA'), NCEP R1 ('NR1') and R2 ('NR2') reanalyses--where these are normalized by the variability of the chosen GPCP reference data set. The plotted points denote values of the respective normalized variabilities when integrated over all land surfaces on a common 2.5x2.5-degree grid and over all seasons in the period 1979-1993 of data set overlap.

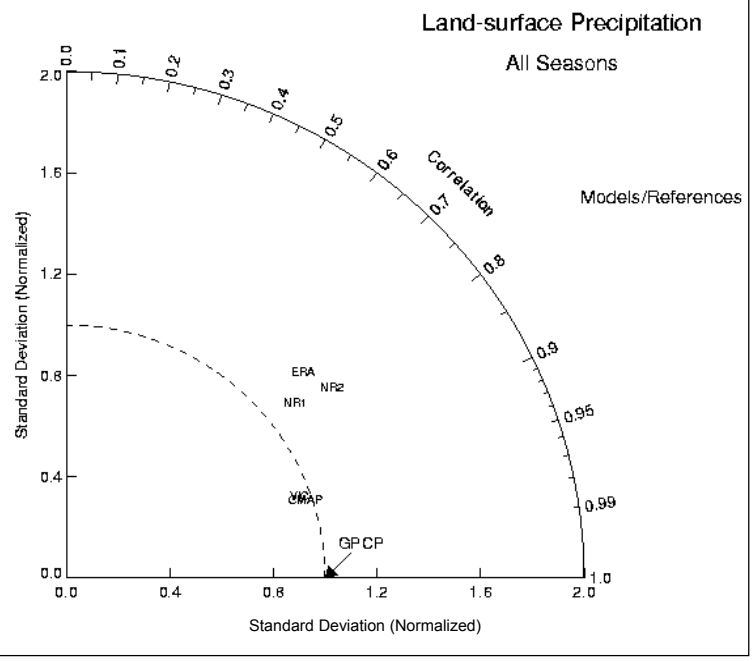

In comparing AMIP2 simulations against alternative validation data, we compute summary statistics so as to objectively measure the current observational uncertainties in specific land-surface processes, as well as to assess where the AMIP2 simulations fall relative to these uncertainties. We have employed Taylor diagrams (Taylor, 2001 *J. Geophys. Research*) as *one* means of making such evaluations. For instance, the Taylor diagram of Figure 1 illustrates that the structure of the spatio-temporal variability (about annual-mean, global-mean values) of the CMAP and VIC precipitation data exhibit substantially greater similarity to the chosen GPCP reference (and to one another) than do the reanalyses' estimates of precipitation variability. In particular, the root-mean-square (RMS) differences (proportional to the distance from the GPCP reference point) of the CMAP and VIC precipitation are considerably less than those for the three reanalyses. Moreover, these lesser RMS differences correspond to a close match in the amplitude of precipitation variability (as indicated by their similarity in radial displacements in this polar plot or their proximity to the dashed-line inner circle passing through the GPCP reference point), and the lesser RMS differences also are associated with their good agreement in "phase" of variability (as shown by spatio-temporal correlations ~ 0.95 that are indicated along the azimuthal scale).

SELECTED RESULTS FROM AMIP2 LAND-SURFACE SIMULATIONS

The Taylor diagram of Figure 2 compares the variability structure of 23 AMIP2 simulations against the GPCP reference data during Northern summer, when global land-atmosphere coupling is strongest. (The AMIP2 spatio-temporal variabilities are normalized by that of the reference data in order to allow consistent comparison with other land-surface processes, e.g. as shown by Figure 3.) Relative to the GPCP reference, it is seen that continental precipitation is generally not well-simulated by the AMIP2 models: sizeable phase differences are universal, and the amplitude of the simulated precipitation variability is also excessive in

many cases. Similar structural characteristics are also manifested by the precipitation variabilities of the ERA15, NCEP R1, and NCEP R2 reanalyses (see Figure 1).

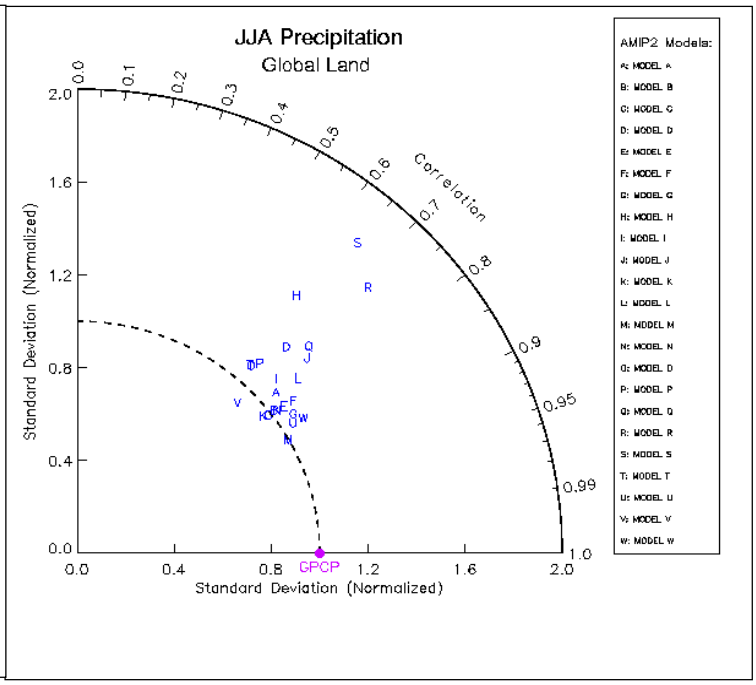

Figure 2: As in Figure 1, except that the integrated normalized spatio-temporal variabilities of continental precipitation from 23 AMIP2 simulations (designated 'A', 'B', … , 'W') are displayed. The plotted points denote values of the normalized variabilities that are integrated spatially over all land points on a common 4x5-degree grid, but that are temporally integrated only over the June-July-August (JJA) seasons in the period 1979-1995.

The analogous Taylor diagram for JJA continental latent heat flux is shown in Figure 3. It is seen that the precipitation amplitude bias of many of the AMIP2 simulations does not carry over to the continental latent heat flux, as estimated by the VIC off-line simulation with precipitation forcing comparable to that of the GPCP data set (Figure 1). This result is presumably due to the constraints on evapo-transpiration imposed by vegetation effects (e.g. stomatal resistance) that are represented with varying degrees of complexity in the AMIP2 models.

There also are preliminary indications that the complexity with which vegetation effects are simulated may not be of paramount importance, *at least at seasonal climatic time scales.* Model B, for example, which includes a "bucket" land-surface hydrological scheme that is modified simply by imposing a spatially constant minimum stomatal resistance, appears to produce a simulation of seasonal latent heat flux that is "competitive" with models having substantially more complex representations of vegetation canopies. It is likely, however, that this outcome is also due in part to Model B's relatively good performance in simulating continental precipitation variability (Figure 2).

Figure 3: As in Figure 2, except for the integrated JJA spatio-temporal variabilities of continental latent heat flux from 23 AMIP2 simulations, normalized by the variability of this flux in the VIC off-line simulation (of the period 1979-1993), which was forced by precipitation comparable to the GPCP data set (see Figure 1). Note the generally reduced variability amplitudes of the AMIP2 simulations of latent heat flux compared with those of continental precipitation in Figure 2. Note also the relatively "competitive" performance of Model B which includes a modified "bucket" land-surface hydrology scheme.

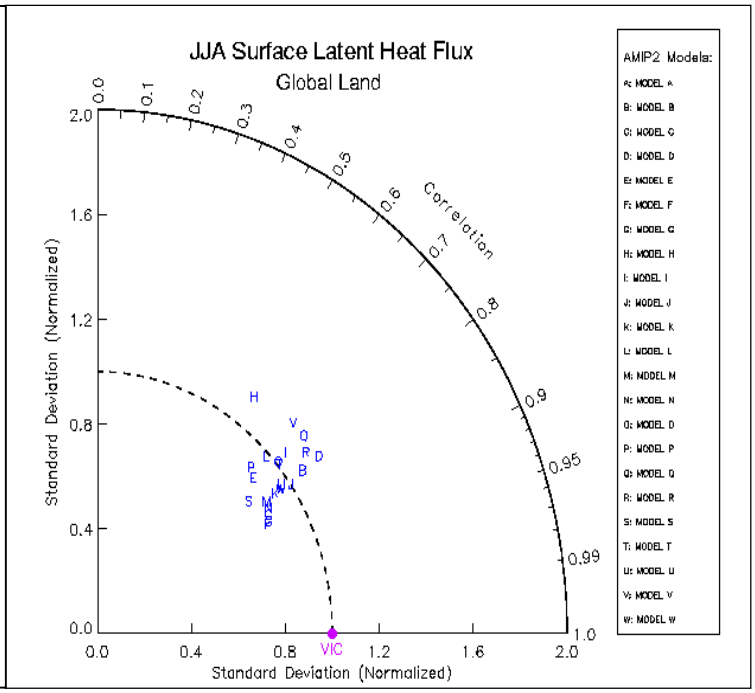

ACKNOWLEGMENTS: This work was performed under the auspices of the U.S. Department of Energy by the University of California Lawrence Livermore National Laboratory under Contract No. W-7405-ENG-48.

Evaluation of Land Surface Energy Budet of AMIP II Global Climate Models

A.Henderson-Sellers1, P. Irannejad1, K. McGuffie3, S. Sharmeen1, T.J. Pillips2 H. Zhang4 and A. J. Pitman5

1. Environment ANSTO, PMB 1 Menai NSW 2234, Australia
2. PCMDI, Lawrence Livermore National Laboratory, USA
3.Dept. Applied Physics, UTS, Sydney, Australia
4.BMRC, Bureau of Meteorology, Melbourne, Australia
5. Dept. of Physical Geography, Macquarie University, North Ryde, Australia

Address for Correspondence:
Associate Professor K. McGuffie
Department of Applied Physics
University of Technology, Sydney
P.O. Box 123
Broadway
NSW 2007
Australia
E-mail: Kendal.McGuffie@uts.edu.au
Tel.: +61 2 9514 2072
Fax: +61 2 9514 2219

ABSTRACT

The partitioning of the surface net available energy into latent and sensible heat fluxes for 20 AMIP II AGCMs is analysed and compared to reanalyses. Surface energy and Taylor plots reveal two clusters of land-surface schemes (LSSs): 'bucket' schemes and 'SiBlings'. Six characteristics appear: (i) SiBlings simulate evaporation closest to global estimates; (ii) AGCMs simulate evaporation better in drier and more humid climates than in intermediate climates; (iii) in wet climates, both models and reanalyses overestimate latent heat compared to the best estimates and, compared to reanalyses, AGCMs underestimate latent heat and overestimate sensible heat; (iv) 1-layer soil models with vegetation resemble complex LSSs, while 2-layer soil models without vegetation mimic buckets; (v) spatio-temporal correlation for latent heat is worst (and with largest intra-model differences) for dry climates and improves with increasing humidity; and (vi) buckets' and SiBlings' latent and sensible climate trajectories in spatio-temporal correlation space differ significantly.

Introduction: AMIP II diagnostic subproject 12

Following Love *et al.* (1995), the AMIP II protocol increased emphasis on the importance of adequate initialisation/spin-up of continental moisture stores; focussed attention on the conservation of land-surface energy and moisture; and requested a more extensive set of required land-surface output variables. These improvements plus the greater spectrum of land-surface scheme (LSS) complexity represented in AMIP II AGCMs than in AMIP I (Phillips, 1999) allow a more thorough investigation of the relationship between AGCM land-surface simulations and land-surface parameterisation schemes. The DSP12 purpose is hindered by the lack of high

quality observed global datasets of land-surface variables; itself arising because many (e.g. evapotranspiration) are not directly observable at scales appropriate to atmospheric models. An alternative is to use reanalyses data (Roads and Betts, 1999) e.g. ECMWF (Gibson *et al*., 1997), NCEP-NCAR (Kistler *et al*., 2001) and NCEP-DOE (Kanamitsu *et al*., 2000).

Evaluation of global predictions is aided by stratification of the data. Here, the de Martonne (1948) aridity index in the form $I_a = \bar{P}/(\bar{T}+10)$ ($\bar{P}$ = mean annual precipitation (mm); $\bar{T}$ = mean air temperature (°C)) is used. To avoid an infinite solution, the climate is defined as Polar below temperatures of -5°C (Henderson-Sellers *et al.,* 2002). Classification is derived from the 1979-1995 precipitation from Xie and Arkin (1997) and the average of the three reanalyses near-surface air temperature.

2. Energy partition at the land surface

The simulated 17-year mean latent heat flux (LH) and sensible heat flux (SH) of 20 AMIP II AGCMs (letters A-T) are compared globally (GLS) and for the de Martonne climate zones with the three reanalyses in Figure 1. The diagonal lines show the geometric location of the mean LH+SH of all models (solid) and the reanalyses (dashed). Scatter along the diagonal is due to differences in partitioning the surface available energy (E_a) into LH and SH. Scatter to the sides of the diagonals is caused by the reanalyses and the AMIP II AGCMs predicting different E_a. Arrows at the top of each diagram show the mean LH simulated by the VIC land-surface scheme (Liang *et al.*, 1994) forced by observed precipitation and tuned to capture the mean stream flow of the world's large rivers. Because of these constraints, it is expected that VIC's long-term mean LH is the best estimate of the real LH (Maurer *et al*., 2000; Irannejad *et al*. 2000).

For the global average (GLS), 11 of the AGCMs have a value of E_a within the range of the reanalyses. However, this number varies in different climates mainly in response to changes in the reanalyses' E_a range. Most models' LH lies outside the reanalyses' range in Mediterranean to Humid climates because the reanalyses agree very well. The AMIP II models generally show better agreement with the ECMWF reanalysis in wetter and cold climates and better consistency with the NCEP-DOE reanalysis in the drier climates.

The horizontal lines in Figure 1 corresponding to each model's (LH, SH) point show the magnitude of the energy residual (dE_a) of the model assuming that the net 17-year change in the surface energy store is negligible, i.e.:

$$dE_a = (R_{net} - S_m H) - (LH + SH) \qquad (1)$$

where R_{net} is surface net radiation and $S_m H$ snow melt equivalent energy. The magnitude of the surface energy residual is different in different climates, e.g. AGCM R's dE_a is about -3.3 W m^{-2} in the Arid climate, while it is about 3.2 W m^{-2} in the Extremely Humid climate. Some of the residual energy (dE_a) might be due to loss or gain of energy at the lower boundary of the soil layer but this hypothesis could not be tested here due to the lack of information about the lower boundary conditions of the models' soil layer. For three AGCMs (L, G & P), dE_a is larger than anticipated in DSP12. For AGCM P, which fails to close its surface energy budget everywhere,

LH and SH agree with reanalyses and some other AGCMs but ($R_{net} - S_m H$) is considerably greater than all the reanalyses. Investigation shows P's mean longwave downward radiation is around 30 W m^{-2} greater than the AMIP II average corresponding to an atmospheric temperature deviation of about 6K not found in P's reported fields.

The relative position of the AMIP II AGCMs compared to each other and to the reanalyses varies with climate (Figure 1). However, compared to reanalyses there are some models that tend to systematically underestimate LH (e.g. M), underestimate available energy (e.g. O) or overestimate sensible heat flux (e.g. Q). Closer inspection reveals that M, Q and E frequently lie towards the top left (small LH, large SH) and that O, P and G consistently lie towards the lower part of the distribution (small SH). E and M use SiB (Sato *et al.*, 1989); Q uses SSiB (Xue *et al.*, 1991); G uses a SVAT (Pan and Mahrt, 1987); while both O and P use buckets (Manabe, 1969). Thus, all but one (G – which has problems) of the LSSs identified in Figure 1 as outliers fall into two groups: a bucket hydrology or a SiB-based (Sellers *et al.*, 1986) LSS (here termed SiBlings). It is also noted that Model L's LSS is also a SiBling (SSiB: Xue *et al.*, 1991). The relatively small LH predicted by SiBlings can be attributed to the high sensitivity of the canopy resistance of the scheme to atmospheric humidity (Sato, 1995 personal communication). SiBlings tend to simulate LH closest to VIC in most climates. Bucket model O simulates LH better than many other models in all climates, except the Extremely Humid. However, such an uncharacteristic behaviour of this 'bucket' seems to be due to its abnormally small surface available energy. Compared to VIC, the models overestimate LH especially in intermediate climates probably due to the complications in calculating surface resistance and the evaporation scaling factor for medium soil wetness. Variations among the models' LH and SH are relatively smaller in wetter climates than in drier ones. Reanalyses agree more with each other in intermediate climates, but all highly overestimate LH compared to VIC. The bucket model including canopy resistance (A) simulates LH similarly to most SVATs, while a two-layer soil model with no explicit canopy (S) behaves like a simple bucket by simulating high LH in almost all climates.

3. Spatio-temporal analysis

The modified Taylor diagram (Taylor, 2001) in Figure 2(a) shows the ranges of spatio-temporal statistics of LH simulated by the 20 AMIP II models compared to the ensemble reanalysis. The spatio-temporal statistics of 20 AGCMs are shown as box-whisker plots for the two most extreme climates (Arid and Extremely Humid) with numbered cross marks for the median values for the other 6 climates.

Compared to the average of the three reanalyses, the AGCMs perform less well (smaller coefficient of correlation, larger deviation from unit of normalised standard deviation and larger normalised root mean square error) in dry climates than in wet for LH. The inter-model differences of the statistics are also greater in dry climates and become smaller (better inter-model agreement) in wetter areas, which is coherent with PILPS 2(b) off-line findings (Shao and Henderson-Sellers, 1996). For SH, the temporal and spatial distributions in drier climates are closer to those of the ensemble reanalyses than in wetter regimes (Figure 2(b)). The inter-model range in correlation coefficient (arc whiskers) is larger for SH than for LH. This is because the models' evaporation is limited by the availability of moisture at the surface due to precipitation.

4. Clusters of LSS types

To exclude the impact of differences in models' and reanalyses' E_a, SH and LH have been scaled against the reanalysis ensemble E_a (Figure 2(c)). While NCEP-NCAR has similar LH to NCEP-DOE in the two wettest climates (Figure 1), its scaled LH is smaller than NCEP-DOE in all climates. The AMIP II AGCMs are scattered around the NCEP-DOE reanalysis in dry climates; around the NCEP-NCAR reanalysis in the Mediterranean to Humid climates (only Sub-humid is shown); and around the ECMWF reanalysis in the Very Humid (not shown) and Extremely Humid climates (Figure 2(c)).

The AGCMs that use the bucket hydrology scheme with a variable (O) or constant (P) water holding capacity predict the scaled LH greater than the range of reanalyses in all climates (O) or in drier (Arid to Sub-humid) climates (P). AGCMs E, L, M and Q, which use variants of the SiB scheme (Sellers *et al.,* 1986), are among the least evaporating models in almost all climates. The evolution of spatio-temporal statistics of LH and SH from a representative bucket and SiBling LSS (O and M respectively) shows that LH agreement with the ensemble reanalysis improves when moving from dry to more humid climates (Figure 2(d)). In all climates, and especially in drier ones, the SiBling LSS predicts LH better than the bucket. Similar but complementary trajectories for SH also show the SiBling to be superior to the bucket, which has very much smaller variability than the reanalyses.

Overall, the results presented here show that the values and relative partitioning of surface available energy varies for the 20 AMIP II models and three reanalyses by climate. The process of validation is hindered by the lack of observed 'truth' and disagreement among the three re-analyses. The AMIP II models agree better with different reanalyses in different climates. Over all land surfaces, the sum of the two fluxes lies within the range of the reanalyses for 11 of these 20 AMIP II models. However, the surface energy is partitioned differently from the reanalyses so that only two AGCMs simulate both LH and SH in the range of the three reanalyses. When scaled against the surface available energy, the AMIP II models that use variants of the SiB scheme (Sellers *et al.,* 1986) are among the least evaporating models in all climates and the traditional buckets (Manabe, 1969) among those evaporating the most. The Siblings' LH is closer to the best estimate (VIC off-line simulations) than other models.

Overall, these AMIP II results are encouraging because, compared to AMIP I, surface energy residuals are smaller and plausible for all but three AGCMs and the models' land-surface simulations are converging. It is clear that challenges still exist for evaluation due to the lack of agreement amongst available validation data. Despite this lack of an agreed land-surface 'truth', the results presented here demonstrate that land-surface parameterisation schemes can capture the expected wide range of behaviours but that not all schemes are currently simulating all characteristic climate behaviours equally well.

Acknowledgements

We thank the PCMDI AMIP II team and all AMIP II & PILPS participants.

References

De Martonne, E., 1948, *Traité de Geographie Physique*, 7th ed., Librairie Armand Colin, Paris.

Gates, W. L., 1992, The atmospheric model intercomparison project, *Bull. Amer. Meteor. Soc*., 73, 1962-1970.

Gibson, J. K., P. Kallberg, S. Uppala, A. Hernandez, A. Normura, E. Serrano, 1997, ERA description, *ECMWF Re-Analysis Project Report Series, 1,* 72pp. ECMWF Reading,UK.

Henderson-Sellers, A., Irannejad, P., Sharmeen, S., McGuffie, K. and Phillips, T.J., 2002, Evaluation of AMIP II global climate model simulations of the land-surface water budget and its components over the GEWEX-CEOP Regions, submitted to *Journal of Hydrometeorology*

Irannejad P., A. Henderson-Sellers, T. Phillips and K. McGuffie, 2000: Analysis of AMIP II models' simulation of land surface climates, *GEWEX News*, **10**, 5-8.

Kanamitsu, M., W. Ebisuaki, J. Woolen, J. Potter, and M. Fiorino, 2000. An overview of NCEP/DOE Reanalysis-2. *Second WCRP International Conference on Reanalyses Proc*. WCRP 109.

Kistler, R., E. Kalnay, W. Collins, S. Saha, G. White, J. Woollen, M. Chelliah, W. Ebisuzaki, M. Kanamitsu, V. Kousky, H. van den Dool, R. Jenne, and M. Fiorino, 2001: The NCEP-NCAR 50-Year Reanalysis: Monthly Means CD-ROM and Documentation. *BAMS,* **82,** 247-268.

Liang, X., D.P. Lettenmaier, E.F. Wood and S.J. Burges, 1994: A Simple Hydrologically Based Model of Land Surface Water and Energy Fluxes for General Circulation Models. *J. Geophys. Res.,* **99(D7)**,14,415-14,428.

Love P.K., Henderson-Sellers A. and Irannejad P., 1995, AMIP diagnostic subproject 12 (PILPS Phase 3): Land surface processes, *Proceedings of the First International AMIP Scientific Conference*, Monterey, California, USA, 15-19 May 1995, WCRP-92, WMO/TD-No. 732,

Manabe, S., 1969, Climate and ocean circulation: 1. The atmospheric circulation and the hydrology of the earth's surface, *Mon. Wea. Rev*., **97**, 739-774.

Maurer E.P., B. Nijssen and D.P. Lettenmaier, 2000: Use of reanalysis land surface water budget variables in hydrologic studies, *GEWEX News*, **10**, 6-8.

Pan H.-L. and Mahrt L., 1987, Interaction between soil hydrology and boundary-layer development, *Boundary-Layer Meteorol.,* **38**, 185-202.

Phillips, T.J., 1999, AMIP II model features documentation, Accessible online at www-pcmdi.llnl.gov/modeldoc/amip2/.

Roads, J., and A. Betts, 1999, NCEP/NCAR and ECMWF Reanalysis Surface Water and Energy Budgets for the Mississippi River Basin, available on line http://ecpc.ucsd.edu/gcip/9906gcip.htm.

Sato N., Sellers P.J., Randall D.A., Schneider E.K., Shukla J., Kinter II J.L., Hou Y-T., and Albertazzi E., 1989, Effects of implementing the Simple Biosphere Model in a general circulation model. *J. Atmos. Sci.*, **46**, 2757-2782.

Sellers P.J., Mintz Y., Sud Y.C., Dalcher A., 1986, A Simplified Biosphere Model (SiB) for Use within General Circulation Model. *J. Atmos. Sci.*, **43**, 505—531.

Shao, Y. and Henderson-Sellers, A., 1996, Modeling soil moisture: a Project for Intercomparison of Land Surface Parameterization Schemes Phase 2(b), *J. Geophys. Res. (Atmospheres),* **101(D3),** 7227-7250

Taylor K.E., 2001, Summarizing multiple aspects of model performance in a single diagram*, J. Geophys. Res.*, **106**, 7183-7192.

Xie, P. and P.A. Arkin, 1997: A 17-year monthly analysis based on gauge observations, satellite estimates, and numerical model outputs, *Bull. Amer. Meteor. Soc*., **78**, 2539-2558.

Xue, Y., P.J. Sellers, J.L. Kinter, and J. Shukla, 1991: A simplified biosphere model for climate studies. *J. Climate*, **4,** 345-364.

Figure Legends

Figure 1 17-year mean SH and LH of 20 AMIP II models (A-T) and three reanalysis products for all land surfaces (GLS) and the different de Martonne climates. Diagonal lines are the geometric location of the average LH+SH of all models (solid) and the reanalyses (dashed). Horizontal lines show the surface energy residuals where they are non-zero. Arrows at the top of each panel show the best LH estimate as simulated off-line by the VIC land-surface scheme.

Figure 2 Modified Taylor diagrams for LH (a) and SH (b) showing spatio-temporal statistics of 20 AGCMs against the average (ensemble) of the three available reanalyses as box plots. Filled boxes (10%-90% percentiles) and whiskers (all data) are plotted for the two extreme climates (Arid and Extremely Humid). Median values for the other climates are numbered 2-6 (and 8 for Polar). (c) Partitioning of surface energy between scaled SH and LH (ratioed to the average of the three reanalyses) of 20 AMIP II AGCMs (A-T) and three reanalyses for three climates (Arid, Sub-humid and Extremely Humid). (d) two LH and SH climate trajectories (excluding Polar) of spatio-temporal statistics for AGCM O (bucket) and AGCM M (SiBling).

FIGURE 1

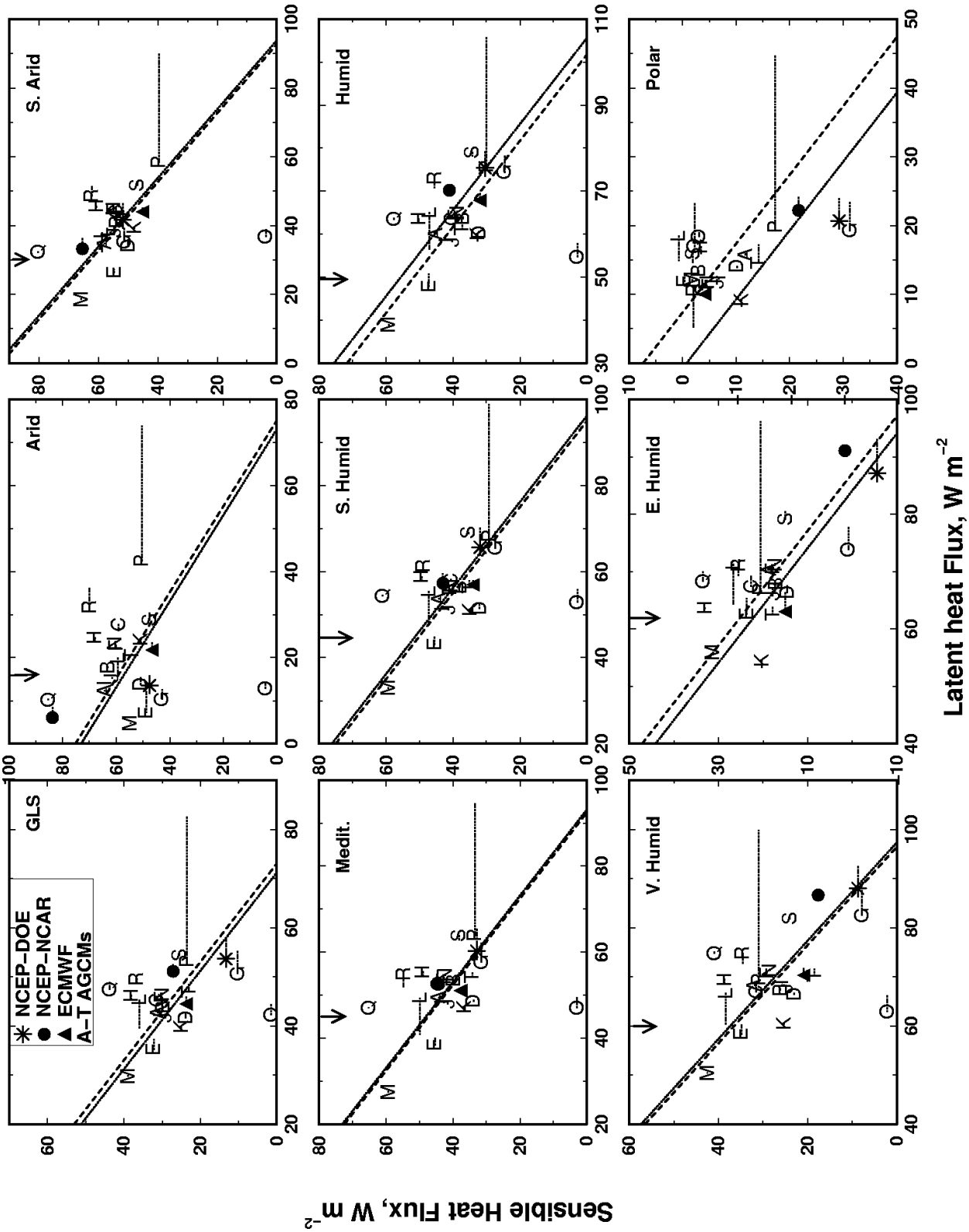
NCEP–DOE
NCEP–NCAR
ECMWF
A–T AGCMs
GLS
Arid
S. Arid
Medit.
S. Humid
Humid
V. Humid
E. Humid
Polar
Sensible Heat Flux, W m-2
Latent heat Flux, W m-2

FIGURE 2

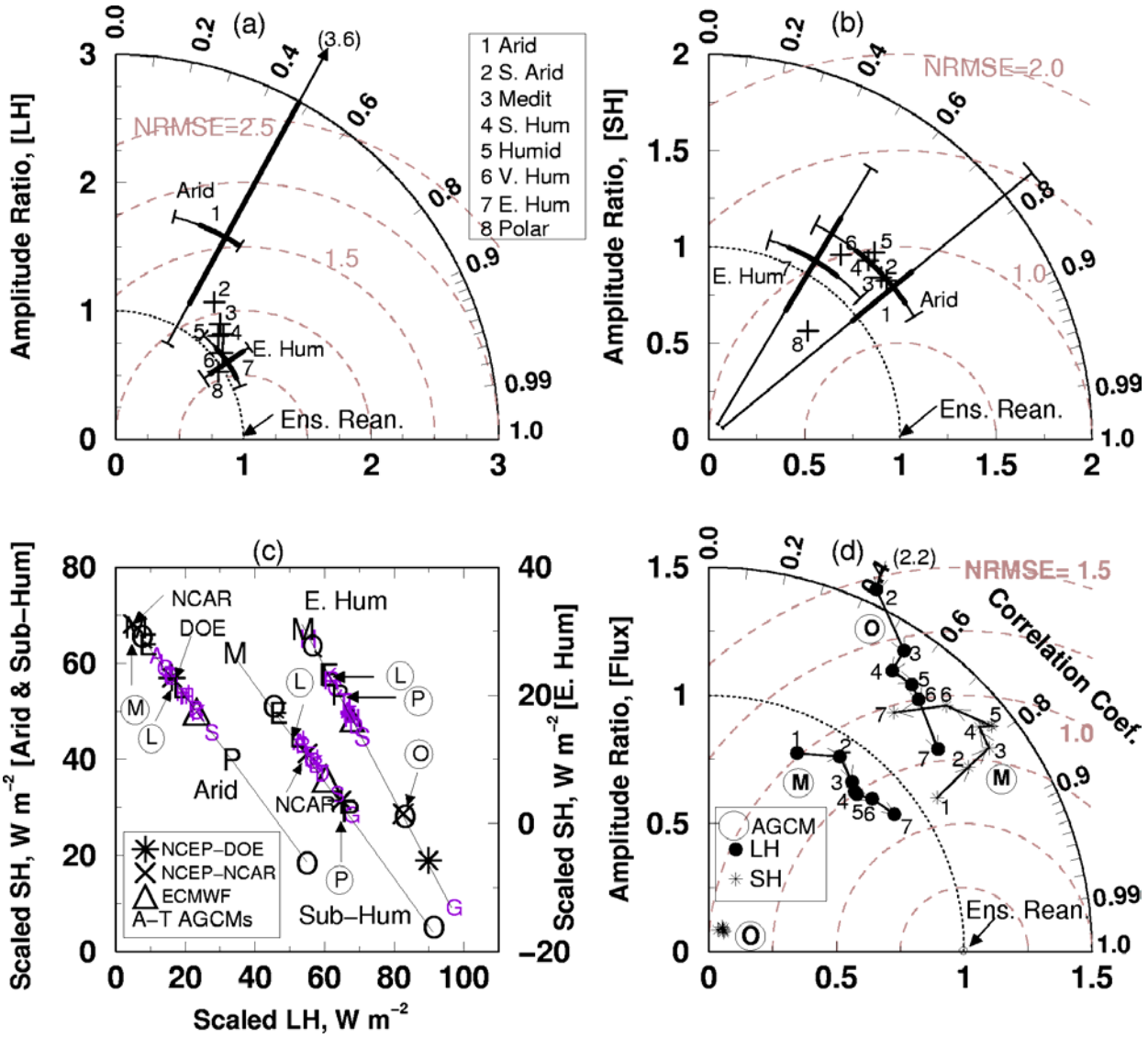
(a)
(3.6)
NRMSE=2.5
1 Arid
2 S. Arid
3 Medit
4 S. Hum
5 Humid
6 V. Hum
7 E. Hum
8 Polar
Arid
E. Hum
Ens. Rean.
Amplitude Ratio, [LH]
(b)
NRMSE=2.0
E. Hum
Arid
Ens. Rean.
Amplitude Ratio, [SH]
(c)
NCAR
DOE
E. Hum
Arid
NCAR
Sub–Hum
NCEP–DOE
NCEP–NCAR
ECMWF
A–T AGCMs
Scaled SH, W m^{-2} [Arid & Sub–Hum]
Scaled SH, W m^{-2} [E. Hum]
Scaled LH, W m^{-2}
(d)
(2.2)
NRMSE= 1.5
Correlation Coef.
AGCM
LH
SH
Ens. Rean.
Amplitude Ratio, [Flux]

Analysis of Land-surface Water Budget in the AMIP II Global Climate Models over the GEWEX-CEOP Regions

P. Irannejad1*, A. Henderson-Sellers1, S. Sharmeen1, T.J. Phillips2, K.McGuffie3 and H. Zhang4

1Environment, ANSTO, PMB 1, Menai, NSW 2234, Australia
2PCMDI, LLNL, Livermore, CA, USA
3Dept. Applied Physics, UTS, Sydney, Australia
4Bureau of Meteorology Research Centre, Melbourne, Victoria, Australia
*Email: pix@ansto.gov.au

1. Introduction

The surface water balance simulated by 20 AMIP II AGCMs for the period 1979-1995 are analysed over global land surfaces (GLS) and in seven GEWEX-CEOP regions: BALTEX, CATCH, GAME-Siberia, GCIP, LBA, MAGS, MDB. The estimated runoff from Global Runoff Data Center (GRDC) and precipitation from Climate Prediction Center (CMAP) along with three reanalysis products (NCEP-DOE, NCEP-NCAR, ECMWF-ERA15) and one set of global off-line land surface simulations by the Variable Infiltration Capacity (VIC) land-surface scheme (LSS) have been used for model evaluation.
The surface water balance equation for each AGCM and evaluation sets are solved:

$$Pr - Ev - Ro - \frac{dW}{dt} = 0 \qquad (1)$$

where t is time, Pr is precipitation rate, Ev is evapotranspiration rate and Ro is runoff (surface+subsurface+drainage) rate and W is the surface water storage (soil moisture+canopy storage+snow/ice cover). The information needed to calculate $\frac{dW}{dt}$ is not provided by AMIP or is reported with non-standard definitions and/or units by many AGCMs. Therefore, we assume that over a long period of time the rate of change of the surface storage in (1) is negligible ($dW/dt \to 0.0$ as $dt \to \infty$). For the 17-year AMIP II period we conservatively assume that a change in the surface water storage a $\frac{dW}{dt} = \pm 0.1$ mm d^{-1} is an acceptable range.

2. Surface Water Balance

The 17-year mean surface water balance of the reanalyses, VIC and AMIP II AGCMs reveals that NCEP reanalyses do not close their surface water balance, presumably due to the soil moisture nudging. VIC conserves the surface water everywhere. Because VIC simulation is constrained by observed precipitation and tuned for large river flows, we may expect that VIC provides a reliable surface water simulation, at least when averaged over large basins and a long period of time. Most of the AMIP II models close surface water balance within the acceptable range globally (GLS) and in most of the CEOP basins. Among the models that have problem closing the budget three (G, M, R) have incorrectly reported their runoff component. Of the 17 models with no obvious reporting error, six models (A, C, F, N, P, S) fail to conserve surface water over the global land surfaces within the ±0.05 mm d^{-1} and only one (C) within the ±0.1 mm

d^{-1}. Six models (C, D, H, K, L, S) fail within the ±0.1 mm d^{-1} in the MDB, one model (D) in the CATCH and the LBA and one (L) in the MAGS. All of the 17 models close their balances in the other CEOP basins. AGCM F reported negative runoff (probably due to a sign error) in the first two years of simulations. These two years are excluded from calculations for Model F.

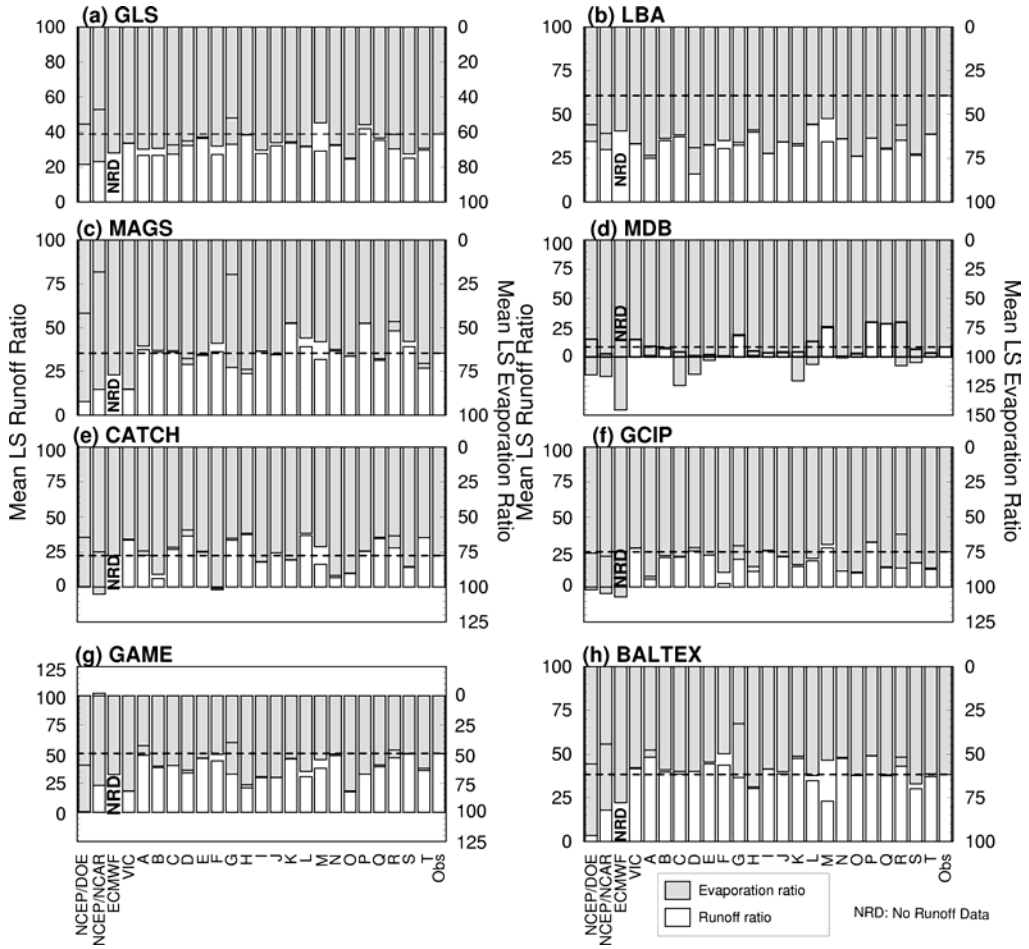

Figure 1 17-year mean runoff ratio (Ro/Pr) and evaporation ratio(Ev/Pr) for GLS and seven CEOP regions. 'Obs' is observations based on GRDC runoff and CMAP precipitation.

3. Partitioning of Available Surface Water

Figure 1 shows the mean runoff and evapotranspiration ratios of the reanalyses and AMIP II models globally and in the GEWEX-CEOP regions. When the two bars meet each other with no overlap the surface water balance is closed. The overlap shows the percentage of excessive surface water loss by evaporation plus runoff to water gain by precipitation. 'Obs' shows the runoff ratio calculated using mean GRDC runoff and CMAP precipitation. Evaporation ratio is calculated as the residual from the surface water balance equation.

Globally and in all the CEOP regions NCEP reanalyses have the sum of the two ratios greater than 100%; in MDB the imbalance, caused mainly by soil moisture nudging and a decrease in

surface water storage (Figure 2), is as large as 65% of the mean precipitation. ECMWF may have similar problem. However, we were not able to assess it because we could not acquire its runoff data (NRD). The non-closure of the surface water budget and very different evaporation and runoff ratios from observations suggest that reanalyses are not appropriate tools for evaluating the AGCMs' simulated surface water budget components.

VIC and almost all of the AGCMs simulate a runoff ratio smaller than observations over the GLS. However, this is not a general rule, with many models overestimating runoff ratio in CATCH and BALTEX. Reanalyses and AMIP II models are especially doing poorly in the MDB, where all reanalyses and seven (out of 17) AGCMs produce mean evaporation ratios of greater than 100%, to some extent, due to the poor initialisation of the soil moisture and problematically long spin-down period of the models (Figure 2).

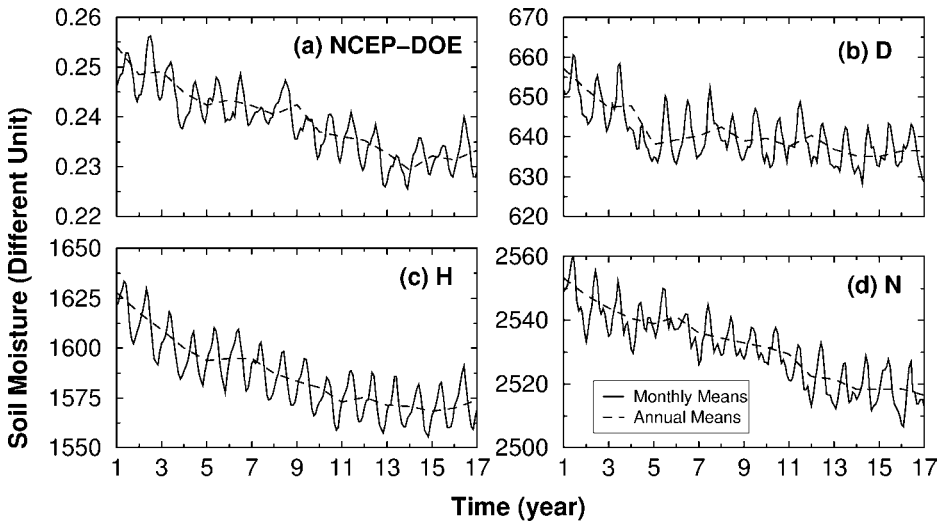

Figure 2. 17-year soil moisture trend for NCEP-DOE and three AMIP II models.

In the LBA all reanalyses and AMIP models underestimate runoff ratio compared to observations. Considering the relatively high available energy and dense vegetation canopy of the catchment, an observed mean runoff ratio of about 61% is arguably too high. Investigation reveals that the GRDC mean runoff over some areas of LBA is greater than the CMAP mean precipitation (Figure 3(a)). Comparing GRDC with the GCPC and Legates and Willmott precipitation climatologies provides similar results. Comparison of the mean seasonal cycles of runoff and precipitation for areas of $Ro \geq Pr$ (Figure 3(b)) shows that excess runoff to precipitation is especially large during the high precipitation period when it is expected that some of the precipitation to be stored in the soil to supply evaporation and slow drainage in the relatively drier months.

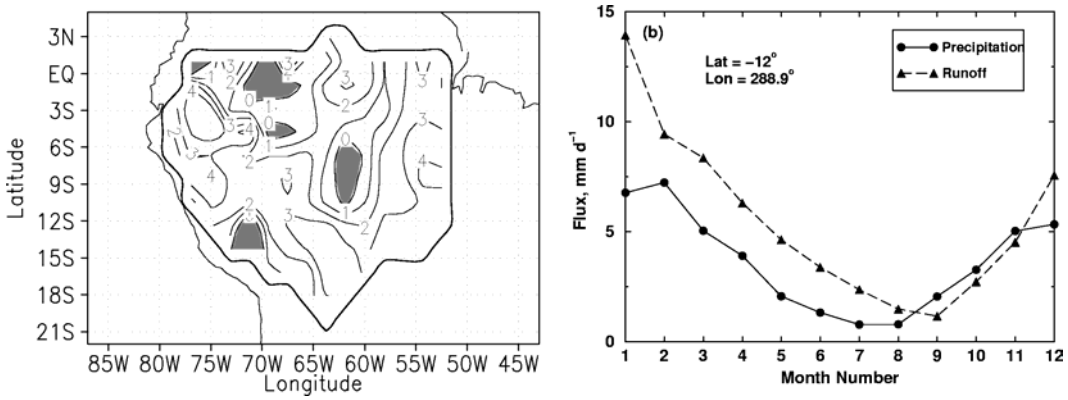

Figure 3 (a) Geographical distribution of the mean Pr-Ro in the LBA (Ro>Pr in the shaded area) and (b) the mean seasonal cycle of Pr and Ro for one grid square in the shaded area.

4. Summary

From the analysis performed we found that:

- Most AMIP II AGCMs close surface water budget within an acceptable range-- some of the models have not followed the AMIP protocol for reporting values of the required variables.
- Magnitudes of water imbalance are different in different regions (6 models fail in MDB).
- Despite the emphasis in the AMIP II protocol, soil water initialisation is still a problem, especially in MDB and probably for other arid and semi-arid regions.
- 17-year mean Ev is greater than Pr, especially in MDB (seven models) to some extent due to poor soil water initialisation.
- Problem concerning the lack of reliable global observations for evaluating land-surface simulations persists.
- Reanalyses are not appropriate for the evaluation of simulated surface water components,
- GRDC runoff data is problematic (e.g. in Amazon), and at best is not consistent with precipitation data.
- Due to constrained atmospheric forcing, off-line land-surface schemes' results, such as VIC, can provide appropriate tools for the evaluation of AGCMs' surface water simulations.

Preliminary Analysis of Sixteen AMIP2 Model Simulations over the Australian Region

H. Zhang[1], A. Henderson-Sellers[2], P. Irannejad[2], S. Sharmeen[2], T. Phillips[3], K. McGuffie[4]

[1]Bureau of Meteorology Research Centre, Melbourne, Australia
[2]ANSTO Environment, Sydney, Australia
[3]PCMDI, Livermore, CA, USA
[4] Applied Physics, University of Technology, Sydney, Australia

INTRODUCTION

This report presents preliminary analyses of sixteen models from the Atmospheric Model Intercomparison Project II (AMIP2) over the Australian region. There are two main goals: (a) to deliver an evaluation of current AGCMs' simulations of observed climate over this region; and (b) to try to establish whether, and potentially, how, land-surface processes and parameterization affect the model predictability of climate anomalies on seasonal and longer time scales. There is a great variety of land-surface complexities in the sixteen models, ranging from simple Manabe-type bucket hydrology models with no explicit canopy related processes to schemes with fully parameterised canopy processes and incorporated carbon-cycles. Such diversity in complexity in land-surface schemes provides a good opportunity to study the role of land-surface parameterization in climate simulations. The detailed analyses of the model results have been described by Zhang et al. (2002) thus only some selective results are presented here.

MODEL SIMULATIONS OF SURFACE CLIMATOLOGY

In this preliminary analysis, the Australian Bureau of Meteorology (BoM) observational rainfall, temperature and surface evapotranspiration datasets are used in validating surface climatologies simulated by the models. The area-averaged root-mean-square-errors (RMSEs) of the model precipitation and monthly mean daily maximum surface temperature climatologies over the continent are shown in Figure 1. Simulations from a "poor-man's ensemble", generated by simply averaging all the model simulations throughout the 17-year period as a set of new simulations, are also included for comparison. RMSEs are generally higher in the austral summer season, with model P being the significant outlier for precipitation, as well as O and H for Tmax. As found by many other studies, poor-man's ensembles give the best overall RMSE results.

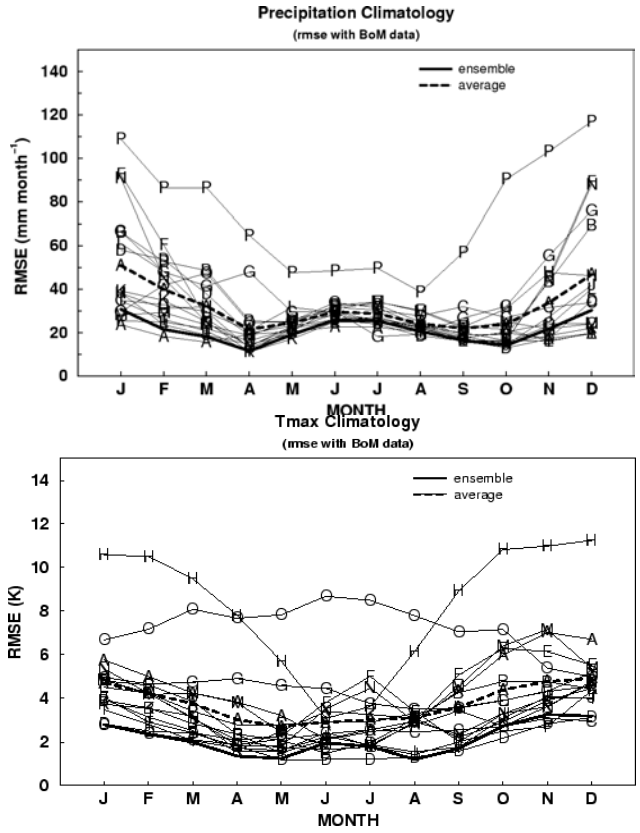

Figure 1: (a) Root-mean-square-error (RMSE) of precipitation climatology simulated by 16 AMIP2 models against the BoM observations (mm month^{-1}) over the Australian region. The heavy dash line represents the averaged RMSE of all the 16 models. The heavy solid line represents the RMSE of results from by the poor-man ensembles of the 16 models. (b) As (a) but for monthly averaged daily Tmax.

MODEL SIMULATIONS OF SURFACE CLIMATE VARIABILITY

The Linear Error in Probability Space (LEPS) score is calculated in assessing the skill of the models in simulating surface climate anomalies for the 17-year period (1979 to 1995). Figure 2 shows the model skill in simulating monthly precipitation anomalies against the BoM observational data. Model simulated anomalies are referred to the 17-year climatology from the model simulations. Most of the models exhibit rather limited skill in simulating rainfall anomalies in DJF. There is also no coherence about regions where most models have (or do not have) skill. The majority of the models do not show skill in simulating rainfall variations in north and northeast where the Australian summer monsoon dominates. In the austral winter season (not shown), the model skill is better than that in DJF.

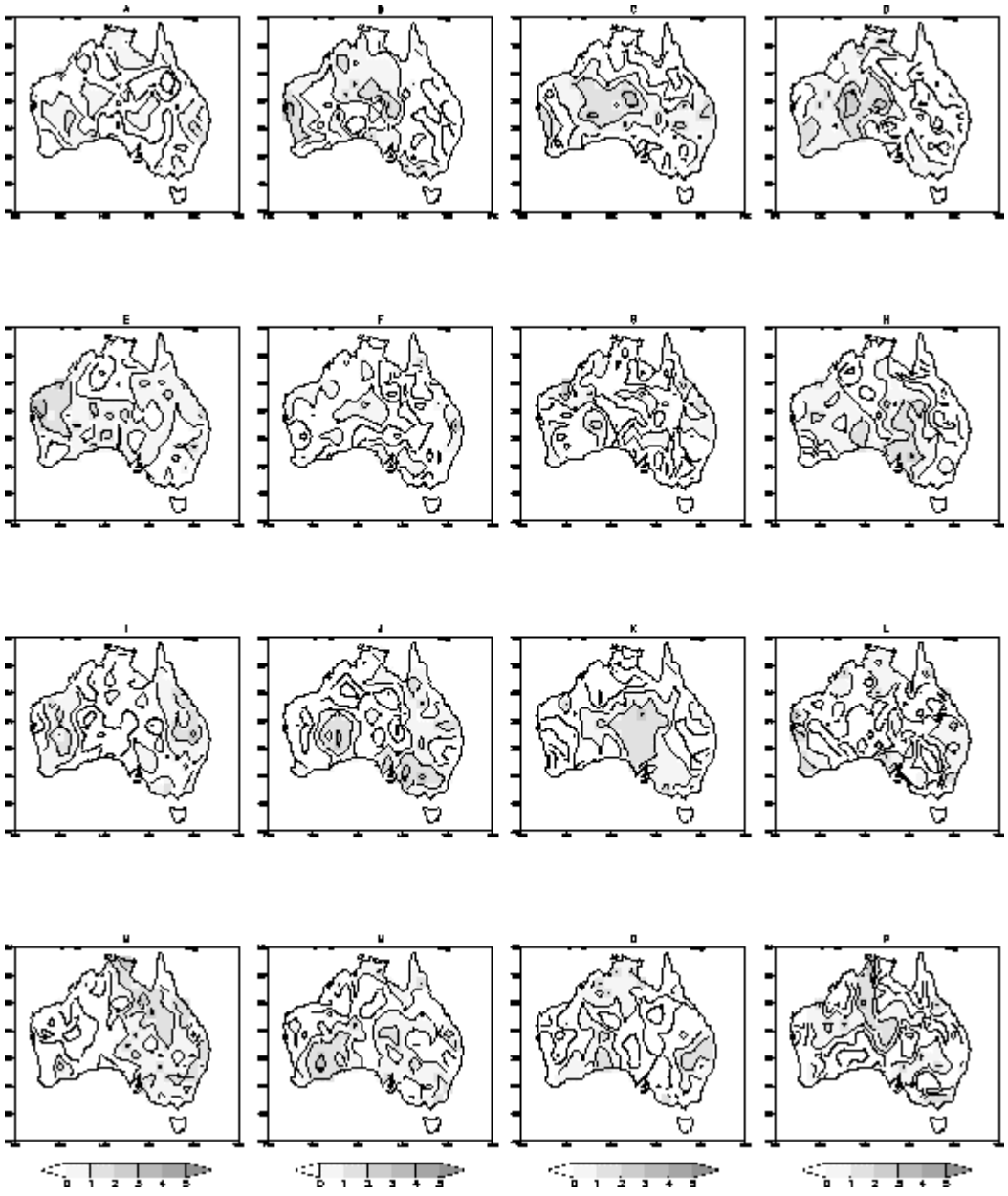

Figure 2: LEPS score of 16 AMIP2 models in simulating precipitation anomalies (DJF) in the 17-yr (1979-1995) period. The BoM observational dataset (1950 to 1999) is used in the calculation. LEPS score in the diagram is divided by 10 with a range of –10 to 10.

POTENTIAL IMPACTS OF LAND-SURFACE MODELLING ON MODEL PREDICTABILITY

Preliminary lag-correlation analysis is conducted in this study to assess the potential impacts of land-surface modelling on model predictability. Results reveal that "climatic memory" derived from land-surface processes (e.g. soil moisture) has different features in the sixteen models: some models show rapid feedback processes between land-surface and the overlying atmosphere, while others show slowly varying processes in which anomalous surface conditions have impacts on the model integrations on longer time-scales (Figure 3a). It is found that models with simple bucket scheme (Model O and P) tend to have a more rapid decay rate in the retention of soil moisture anomalies, and therefore, soil moisture conditions have a weaker influence on forecasting surface climate anomalies (Figure 3b). This study suggests that land-surface modelling has the potential to influence AGCM predictability on seasonal and longer time scales.

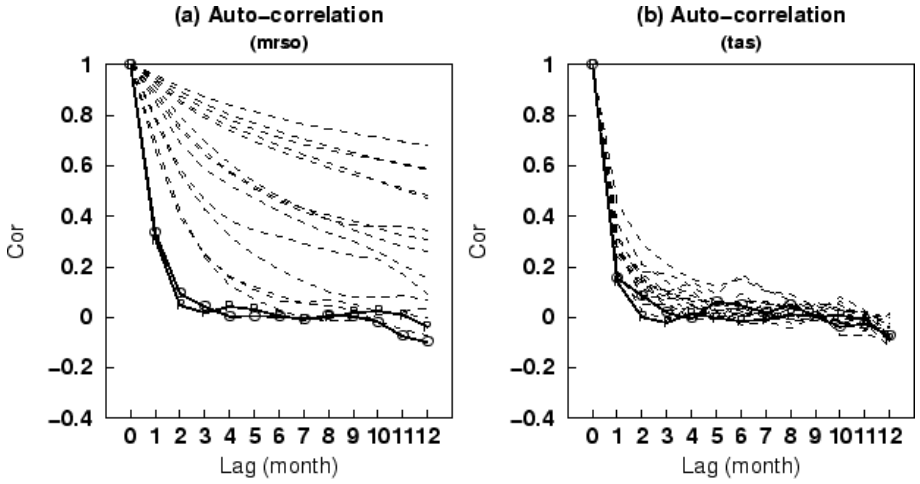

Figure 3: Area-averaged auto correlations of soil moisture (a) and surface air temperature (b). Only Model O and P are identified and other models are represented by dashed lines.

DISCUSSION AND CONCLUSIONS

This report has presented the results of analysing 16 AMIP2 models over the Australian region. It has focused on assessing the surface climate simulations. This study has quantified the skill of the model simulations using the measurements including biases, RMSE and spatial correlations. A range of model differences have been described and some can be linked to the complexity in the model's land-surface schemes. Lag-correlation analysis has revealed that the characteristics of climatic "memory" from land-surface processes (e.g. soil moisture) differ among the sixteen models and land-surface modelling has the potential to affect AGCM predictability on seasonal and even longer time scales.

REFERENCE:

Zhang, H. and A. Henderson-Sellers, P. Irannejad, S. Sharmeen, T. Phillips, and K. McGuffie, 2002: *Land-surface Modelling and Climate Simulations: Results over the Australian Region from Sixteen AMIP2 Models*, Bureau of Meteorology Research Centre Report, No. 89.

AMIP Simulations of the Heat and Water Budgets over Major River Watersheds

V.P.Meleshko, T.V. Pavlova and V.A. Govorkova

Voeykov Main Geophysical Observatory
St.Ptersburg, Russian Federation

The aim of the study is to assess performance capability of the AMIP-II GCMs in simulation of the seasonal cycle of surface heat and water budget over major watersheds of the world. The progress was also evaluated in terms of the quantities considered with regards to development of GCMs for the last decade on the basis of simulations conducted during the first and second phases of AMIP. Seventeen models were selected for comparison that participated in both phases of AMIP and their data were available for analysis: CCCma, CNRM, COLA, DNM, ECMWF, GISS, GLA, JMA, MGO, MPI, MRI, NCAR, NCEP, SUNYA, UGAMP, UKMO, UIUC. And eight watersheds were considered in the study: Amazon, Baltic basin, Congo, Mississippi, Volga, Ob, Enisei, and Lena.

For comparison with observation the following data sets were utilized: monthly means of surface air temperature (Legates and Willmott, 1990a; New et al., 1999), monthly means of precipitation (Legates and Willmott, 1990b; Xie and Arkin, 1996), and evaporation derived from ECMWF and NCEP/NCAR re-analyses (Gibson et al., 1997; Kalnay et.al., 1996). The radiation fluxes at the surface and the top of the atmosphere, and runoff were also analyzed and compared with observation.

The first panel of figures 1, 2 and 3 shows the spread of seasonal cycle of surface air temperature, precipitation and evaporation for Volga and Enisei watersheds, as simulated in AMIP-I and AMIP-II phases. The light and heavy shadings define spreads of seasonal cycles for appropriate variables. The spread was determined from 50% models that produce the least deviation from the computed monthly means that obtained in its turn from ensemble of 17 models. The second panel of the figures shows annually means and RMS differences between computed and observed values of appropriate quantities for each AMIP-II model. Slim bars imply annually averaged RMSE for every AMIP-II AGCM, and all models are ranked in order of RMSE increase. Thick bars imply annually mean differences between computed and observed values. The observed variables shown in the first panels of the figures by full lines are used for calculation of the mean differences and RMSE.

Comparison with observation indicates that AMIP-II models are more successful in simulation of seasonal absorption of the solar radiation at the earth surface and surface air temperature at the majority of watersheds as compared to AMIP-I models. Spread of the seasonal cycle for surface air temperature among the models is largest in winter when the snow cover is present over the watershed. One can notice that surface air temperature spread is distinctly reduced in AMIP-II models.

Spread of seasonal cycles of precipitation was also reduced in AMIP-II models, although the improvement is not so apparent as for the surface air temperature. Correlation of computed precipitation fields with observation is generally less than that for temperature. Despite some decrease of spread in AMIP-II simulation of seasonal cycle, the AMIP-I and AMIP-II models mostly underestimate amount of precipitation over Amazon basin and overestimate them over Enisei basin. It is important to note that precipitation climatology produced from different

sources differ significantly and over some watersheds observed differences between observations are of the same magnitude or even larger than the difference among model simulations.

Seasonal evaporation computed from AMIP-I and AMIP-II models is in better agreement with ERA than that with NCEP/NCAR reanalysis for majority of watersheds. The AMIP-II models show smaller seasonal spread of evaporation than AMIP-I models. However, due to uncertainty in determination of climatic evaporation, quality of computed evaporation from current GCMs requires further validation against other independent data sets.

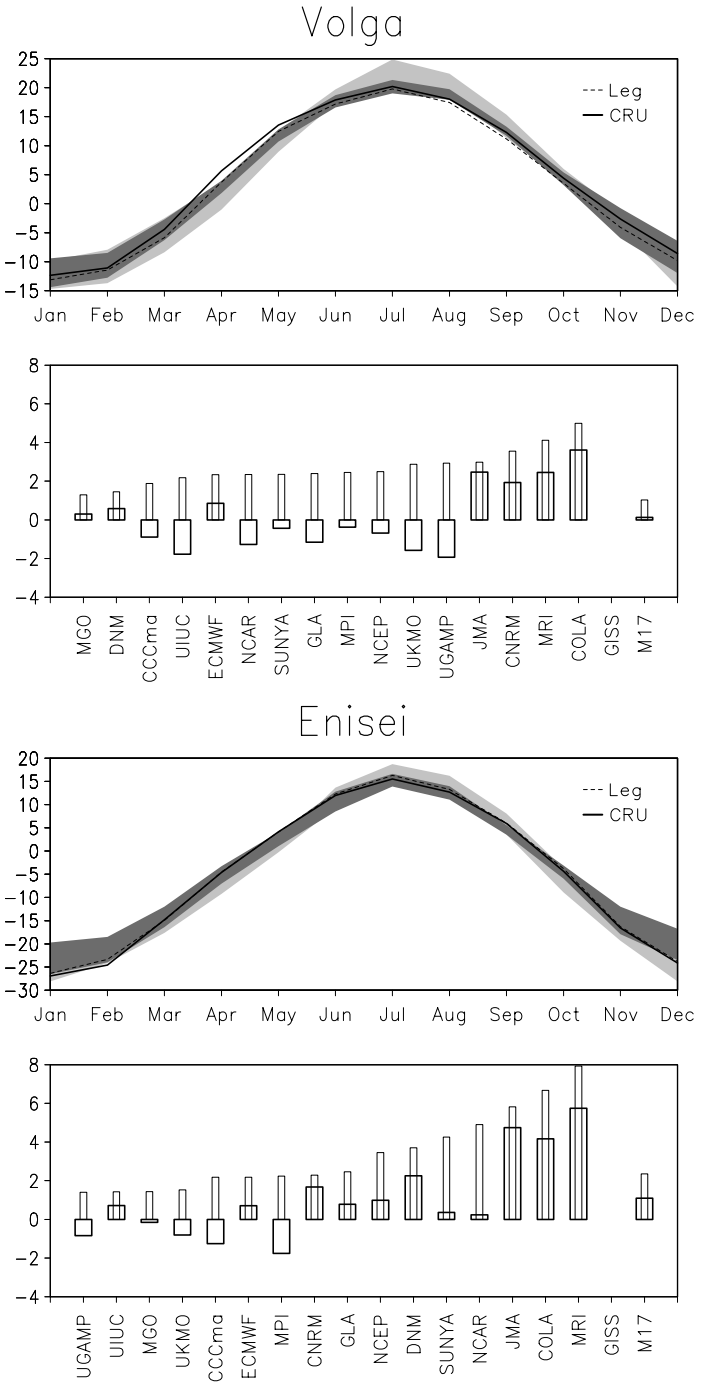

Figure 1. Upper panel: seasonal variation of surface air temperature in AMIP-I and AMIP-II simulations at Volga and Enisei watersheds. Bottom panel: annually mean RMSE and difference between computed and observed surface air temperature in AMIP-II simulations for the same watersheds. Further explanations are given in the text.

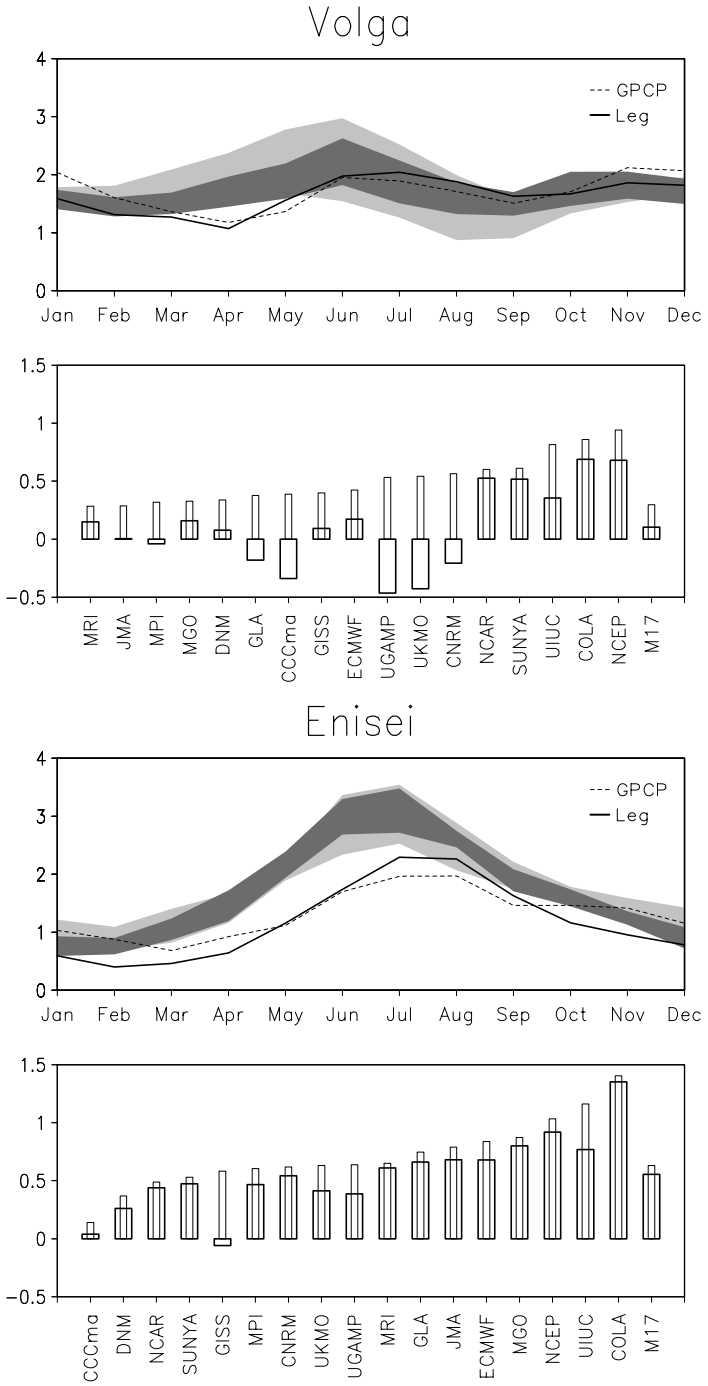

Fig.2 The same as Fig.1, but for precipitation

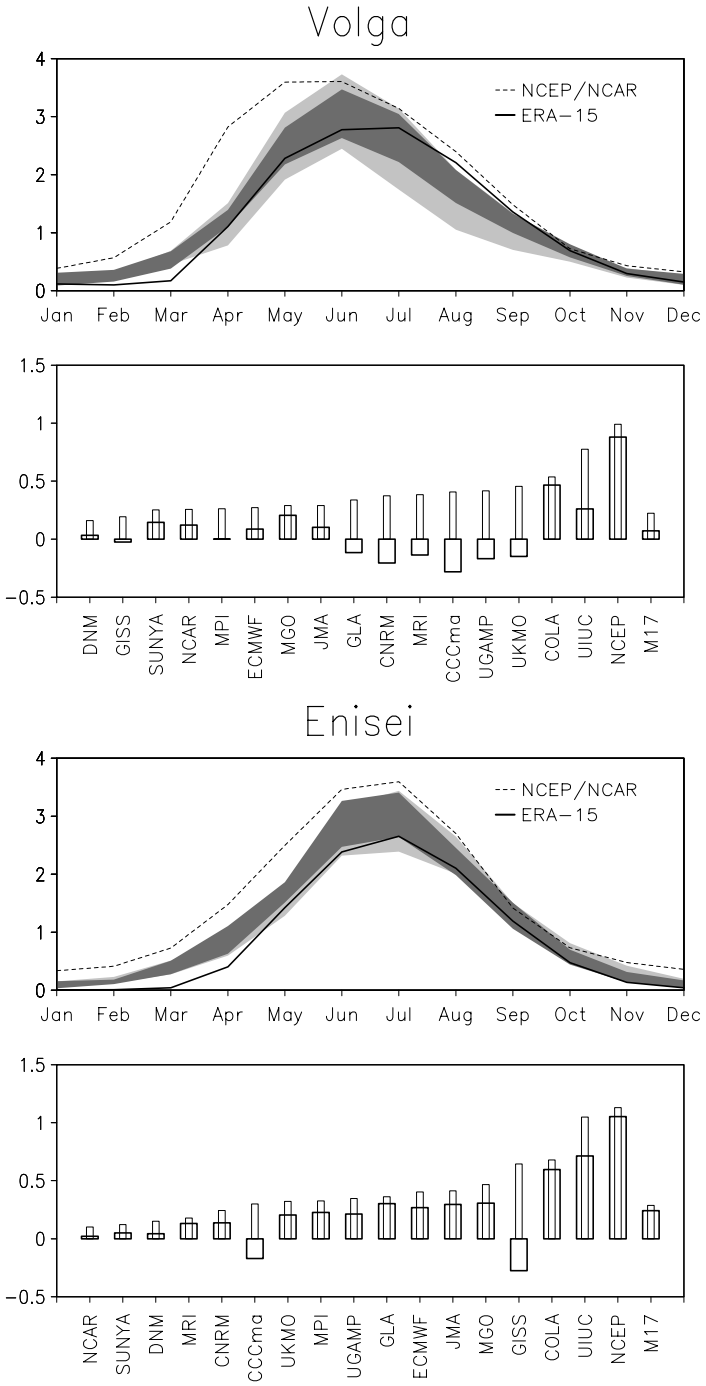

Fig.3. The same as Fig.1, but for evaporation.

References

Gibson, J.K., P.Kalberg, S.Uppala, A.Nomura, A.Hernandez, E.Serrano, 1997: ERA Description, *ECMWF re-analysis project report series*, 1.

Kalnay E., M.Kanamitsu, R.Kistler, W.Collins, D.Deaven, L.Gandin, M.Iredell, S.Saha, G.White, J.Wollen, Y.Zhu, M.Chelliah, W.Ebisuzaki, W.Higgins, J.Janowiak, K.C.Mo, C.Ropelewski, J.Wang, A.Leetma, R.Reynolds, R.Jenne and D.Joseph, 1996: The NCEP/NCAR 40-year reanalysis project. *Bull.Am.Meteorol.Soc.*, 77, 437-471.

Legates D.R., and C.L.Willmott, 1990a: Mean seasonal and spatial variability in global surface air temperature. *Theor.Appl.Clim.*, **41**, 11-21.

Legates D.R., and C.L.Willmott, 1990b: Mean seasonal and spatial variability in gauge corrected global precipitation. *Int.J.Clim.*, **10**, 111-133.

New M., M.Hulme and P.D.Jones, 1999: Representing twentieth century space-time climate variability. Part I: development of a 1961-90mean monthly terrestrial climatology. *J.Climate*, **12**, 829-856.

Xie P., and P.A.Arkin, 1996: Analysis of global monthly precipitation using gauge observations, satellite estimates, and numerical model predictions. *J.Climate*, **9**, 840-858.

Intercomparison of Stationary Waves in AMIP-2 GCMs and their Maintenance Mechanisms

Renu Joseph and Mingfang Ting
Department of Atmospheric Sciences
University of Illinois at Urbana-Champaign
Urbana, Illinois
renu@atmos.uiuc.edu

INTRODUCTION:

The atmospheric stationary waves depict the regional features of the atmospheric circulation and are thus closely linked to regional climate. For example, upper level stationary wave troughs and ridges are often related to precipitation and surface temperature changes with stationary ridges in general being less cloudy and warmer than stationary wave troughs, especially in the extratropics. Though, stationary waves are the zeroth order temporal and first order spatial variability in the atmosphere and should be expected to be simulated well by all GCMs, differences in model physics and numerics can cause different models to produce varying atmospheric stationary wave patterns. It is therefore crucial to assess and understand how well climatological stationary waves are simulated in the various models and the sensitivity of stationary wave simulation to different parameterization schemes. Due to the fact that the AMIP GCMs are often used in assessing the effect of global and regional climate changes, it is necessary to understand the climatological stationary wave simulations in these models and the sensitivity of the stationary waves to model physics.

In this study, the seasonal cycle of the stationary waves in AMIP-2 GCMs is studied with special focus on January and July. The stationary waves in the atmospheric GCM simulations are then compared to those simulated by a nonlinear baroclinic stationary wave model in order to understand the role of different forcing terms in maintaining the stationary wave changes. This research is aimed at answering the following questions.

- How well is the seasonal cycle of stationary waves in the various AMIP-2 GCMs simulated in comparison to that in the NCEP/NCAR reanalysis?
- If the stationary wave pattern and amplitude are well simulated in a model, is the maintenance mechanism of the stationary waves in the model similar to that in nature?

DATA AND MODEL DESCRIPTION:

The climatological stationary wave in seven AMIP-2 GCMs are compared with those in the NCEP/NCAR reanalysis climatology (1948-99). The nonlinear baroclinic stationary wave model developed by Ting and Yu (1998) is used to diagnose the maintenance mechanism of the stationary waves. Forcings in the nonlinear model include orography, diabatic heating and transient vorticity and heat convergences. Transient forcing in this study has been parameterized by a linear damping.

RESULTS AND DISCUSSION:

We first compare the climatological stationary wave simulations in the seven AMIP-2 models to the NCEP/NCAR reanalysis. The stationary waves are reasonably simulated by all models considered, although most of them overestimate the Northern winter extratropical stationary waves except in two models. Two statistical indices were used to quantify the evaluation of the seasonal cycle of the stationary waves. The spatial pattern correlation between the different models at all vertical levels were calculated to determine the ability of the GCMs in simulating the climatological stationary wave pattern as compared to the NCEP/NCAR reanalysis (not shown). Correlations were above 0.6 in most models with the transitional seasons having the weakest correlation. In general, the correlations were the highest in the upper troposphere (where the stationary wave amplitudes are the largest) and in the solsticial seasons. The correlation coefficients do not assess the strength of the stationary waves, however. Hence, the area weighted mean of the global streamfunction amplitude squared at every vertical level was compared (not shown here). The strength of the stationary wave field in the reanalysis shows a strong seasonal cycle in the upper troposphere and a less pronounced seasonal cycle in the lower troposphere. All except two models overpredicted the strength of the stationary wave amplitudes in July.

The nonlinear baroclinic stationary wave model is utilized to diagnostically examine the effects of different forcings in producing the stationary wave changes in all seasons. In general, the nonlinear model with the forcings of diabatic heating and orographic forcing with transient forcing parameterized captures the stationary waves in all models fairly well (Fig. not included). We then decompose the effects of the individual forcings of heating and orography. The main contributor to the stationary waves in the tropics is diabatic heating. The contributions of orographic forcing are comparable to those of diabatic heating in the extratropics. This indicates that the overprediction of all stationary waves in the tropics in July or in general, the differences between the NCEP/NCAR reanalysis stationary waves and the individual models in the tropics is primarily caused by differences in the diabatic heating in the models.

The nonlinear model results due to diabatic heating alone in January is shown in Fig. 1 as an example. Here we see that in all except two models, the tropical centers of stationary waves due to heating are predicted reasonably well. However, all the models in this month underpredict the stationary waves in the Northern Hemisphere extratropics compared to the NCEP/NCAR reanalysis. The residually derived diabatic heating was used in the case of the NCEP/NCAR reanalysis. It should be noted that all models have underrepresented the effects of the diabatic heating in the storm tracks region compared to the residually derived heating in the NCEP/NCAR reanalysis.

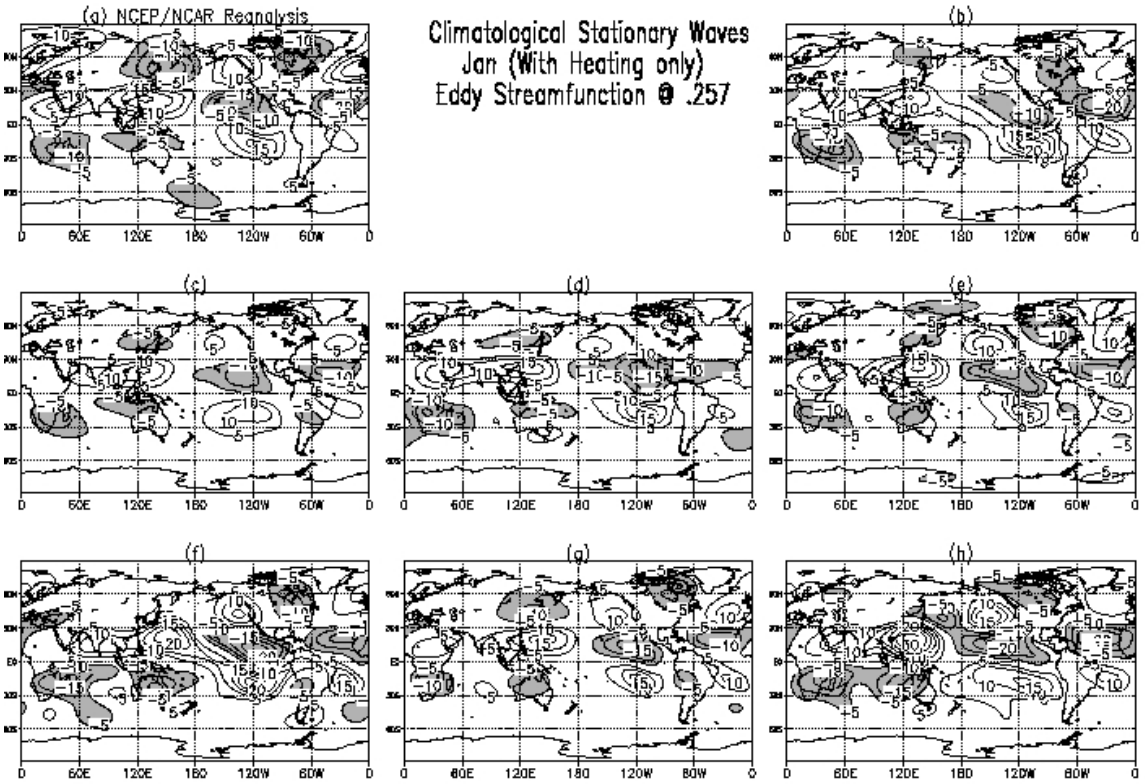

Fig. 4 Upper level Stationary wave streamfunction (sigma=0.257) in the nonlinear model with forcing from diabatic heating only for (a) NCEP/NCAR reanalysis and seven AMIP-2 models. Contour interval is 5×10^6 $m^2 s^{-1}$. Negative contours are shaded.

Figure 2 shows the nonlinear model results due to orographic forcing in January. Most of the stationary wave patterns in the Northern hemisphere extratropics in this month are overrepresented in January when compared to the NCEP/NCAR reanalysis. The cause for the overprediction of the effect of orography seems to be the unrealistically strong low level zonal mean zonal flow in these models.

Thus in the AMIP 2 intercomparison, we find that 1) In general, stationary waves are simulated reasonably well in all the models considered; 2) Differences in diabatic heating is one of the main causes of the differences in stationary wave prediction in the tropics in most models; 3) In the extratropics, the effect of orographic forcing is comparable to that of the diabatic heating and that models overestimate the effect of orographic forcing in the northern hemispheric winter due to the over-prediction of the zonal mean wind at the surface.

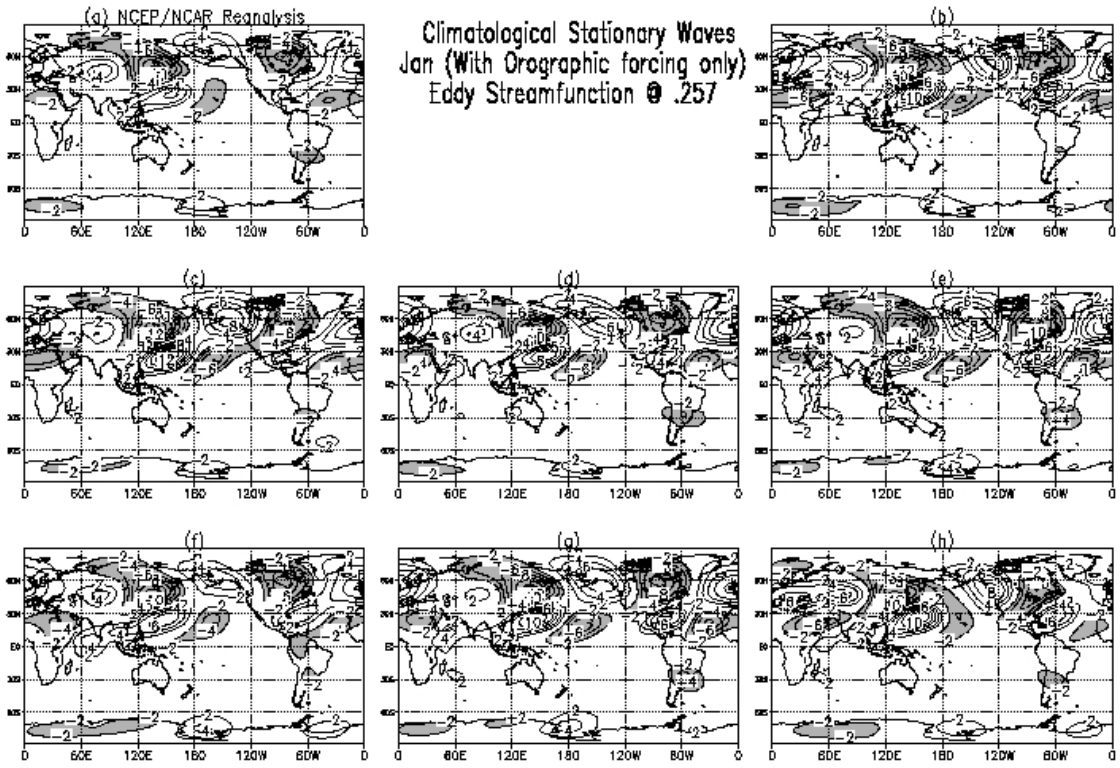

Fig. 2 Upper level Stationary wave streamfunction (sigma=0.257) in the nonlinear model with forcing from orographic uplifting only for (a) NCEP/NCAR reanalysis and seven AMIP-2 models. Contour interval is $2x10^6$ m^2s^{-1}. Negative contours are shaded.

Acknowledgements: This research was supported by the National Science Foundation grant ATM 00-00585 grant.

REFERENCES:

Ting, M. and L. Yu, 1998: Steady response to tropical heating in wavy linear and nonlinear baroclinic models. *J. Atmos. Sci*., 55, 3565-3581.

Intercomparison of Surface Air Temperature and Precipitation Extremes in AMIP-2 Simulations

Viatcheslav V. Kharin,[1] Francis W. Zwiers,[1] and Xuebin Zhang[2]

[1]Canadian Centre for Climate Modelling and Analysis,
Meteorological Service of Canada,
Victoria, British Columbia, Canada
[2]Climate Monitoring and Data Interpretation Division,
Meteorological Service of Canada,
Downsview, Ontario, Canada

The extremes of near surface temperature and 24-h and 5-day accumulated precipitation rates are examined in simulations performed with atmospheric general circulation models (AGCMs) participating in the second phase of the Atmospheric Model Intercomparison Project (AMIP-2; Gleckler 1996). The extremes are evaluated in terms of 20-yr return values of annual extremes estimated by fitting a Generalized Extreme Value (GEV) distribution to a sample of annual extremes at every grid point (Zwiers and Kharin 1998; Kharin and Zwiers 2000). The temperature warm and cold extremes are evaluated for 12 AGCMs. The precipitation extremes are examined for 16 AMIP-2 simulations. Extremes are estimated at the original model grids with resolutions ranging from 72×45 to 192×96 with a median grid size of 128×64. For intercomparison purposes, estimated extreme value statistics are bi-linearly interpolated onto a common 128×64 Gaussian grid.

The model results are validated against reanalyses from the European Centre for Medium-Range Weather Forecasts (Gibson et al. 1997; Simmons and Gibson 2000) and National Centers for Environmental Prediction (Kalnay et al. 1996; Kanamitsu et al. 2002) and station data. Precipitation extremes are also validated against the pentad Climate Prediction Center (CPC) Merged Analysis of Precipitation (CMAP) (Xie et al. 2003) which is a blend of rain gauge observations, satellite data and model output.

A general conclusion of the study is that there are various degrees of consistency in the way current atmospheric models simulate the annual extremes of temperature and precipitation. On the whole, the AGCMs appear to simulate temperature extremes reasonably well as compared to the reanalyses. Smallest disagreements between the models are generally found for warm extremes. Model discrepancies are somewhat large for cold extremes, particularly over sea-ice and snow covered areas and in wet cloudy regions. Precipitation extremes are less reliably reproduced by the models and reanalyses.

Figure 1 displays 20-yr return values of warm and cold annual extremes estimated from the 1979-95 NCEP–DOE AMIP-II (NCEP2) reanalysis, and the corresponding 12-model ensemble means and inter-model standard deviation. On average, the considered 12 AMIP-2 models tend to produce slightly warmer extremes of T_{max} than those in NCEP and ECMWF reanalyses. The NCEP2 reanalysis has substantially colder annual extremes of T_{min} than most of the considered AMIP-2 models, particularly over land. The inter-model standard deviation is quite a bit larger for cold extremes than that for warm extremes. Cold extremes are less reliably simulated over snow and sea-ice covered areas and in wet and cloudy regions in the tropics. Many models also

exhibit an exaggerated clustering behaviour for temperatures near the freezing point of water (not shown).

There is less consistency in the ability of the AMIP-2 models to simulate extremes of 24-h and 5-day precipitation rates (Figure 2). Major disagreements are found in the tropics where the parameterization of deep convection plays a crucial role in generating daily precipitation extremes. It is difficult to be more specific than that because tropical precipitation variability, and by its extension its extremes, can be very sensitive to the tuning of the deep convection parameterization (e.g., Scinocca and McFarlane 2004). There is a weak tendency for extremes to be more intense in higher resolution models, but this dependence is not very robust in the tropics.

A common theme throughout this and other model intercomparison studies (e.g. Lambert and Boer 2001) is that while individual models may disagree with the available observations quite dramatically, the ensemble average of the climate statistics from many models typically provides one of the best matches to the observations. Since no single model can be selected as the clear favorite for all quantities that have been evaluated, the present study supports the importance of the multi-model ensemble approach to the simulating the present day climate and, perhaps, possible future climate changes.

Unfortunately, we have not be able to associate the model formulations and key characteristics with their performance in simulating climate extremes. Modern climate models are very complex and employ a variety of parameterization packages to represent the effect of unresolved physical processes. The models are often "tuned" to match the observed mean climate. The climatic extremes are rarely used for model validation. We can only hope that the results that we have presented will stimulate the discussion of the model's ability to simulate climate extremes in the respective modelling groups.

REFERENCES

Gibson, J. K., P. Kalberg, S. Uppala, A. Hernandes, A. Nomura, and E. Serrano, 1997: ECMWF Reanalysis Report Series 1 – ERA Description. ECMWF, Reading, UK, 72 pp.

Gleckler, P., 1996: Atmospheric Model Intercomparison Project Newsletter, No. 8. [Available online at http://www-pcmdi.llnl.gov/amip/NEWS/index.html.]

Kalnay, E., and Coauthors, 1996: The NCEP/NCAR 40-Year Reanalysis project. *Bull. Amer. Meteor. Soc.,* **77,** 437–471.

Kharin, V. V., and F. W. Zwiers, 2000: Changes in the extremes in an ensemble of transient climate simulations with a coupled atmosphere-ocean GCM. *J. Climate,* **13,** 3760–3788.

Lambert, S. J., and G. J. Boer, 2001: CMIP1 evaluation and intercomparison of coupled climate models. *Clim. Dyn.,* **17,** 83–106.

Kanamitsu, M., W. Ebisuzaki, J. Woollen, S.-K. Yang, J. J. Hnilo, M. Fiorino, and G. L. Potter, 2002: NCEP–DOE AMIP-II Reanalysis (R-2). *Bull. Amer. Meteor. Soc.,* **83,** 1631–1643.

Simmons, A. J., and J. K. Gibson, 2000: The ERA-40 project plan. ECMWF ERA-40 Project Report Series No. 1, 63 pp.

Scinocca, J. F. and N. A. McFarlane, 2004: The variability of modelled tropical precipitation. *J. Atmos. Sci.* (accepted for publication).

Xie, P., J. E. Janowiak, P. A. Arkin, R. Adler, A. Gruber, R. Ferraro, G. J. Huffman, and S. Curtis, 2003: GPCP pentad precipitation analyses: an experimental dataset based on gauge observations and satellite estimate. *J. Climate,* **16,** 2197–2214.

Zwiers, F. W., and V. V. Kharin, 1998: Changes in the extremes of the climate simulated by CCC GCM2 under CO_2 doubling. *J. Climate,* **11,** 2200–2222.

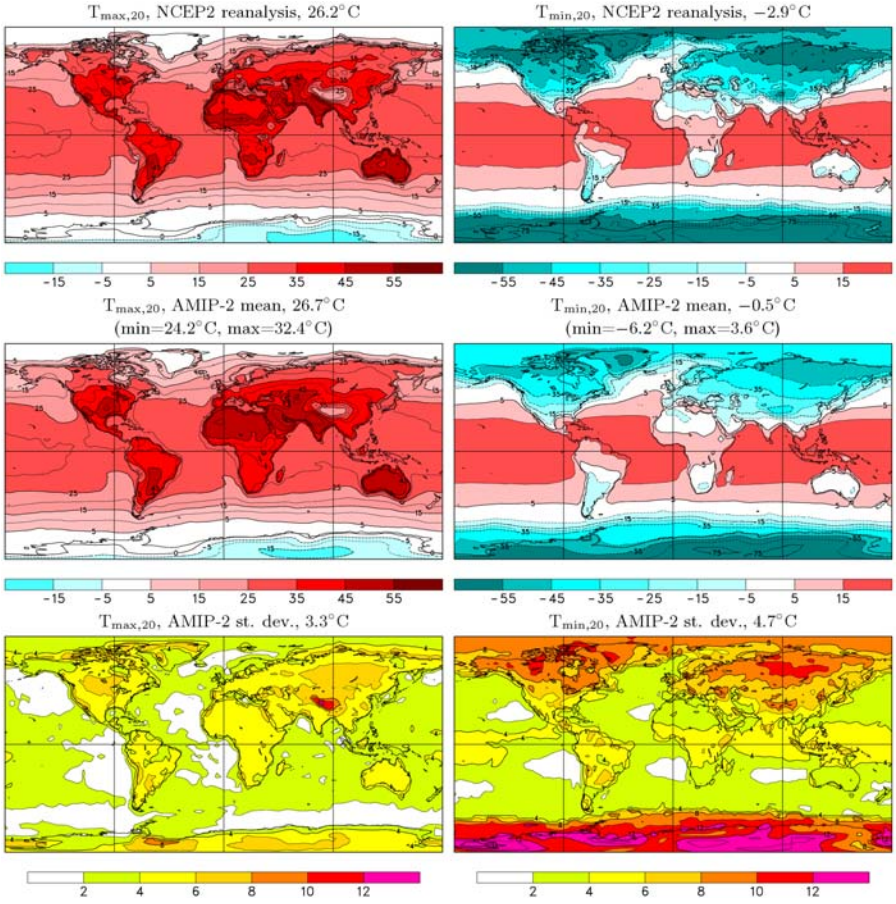

Figure 1: Twenty-year return values of annual extremes of T_{max} (top left) and of T_{min} (top right) estimated from the 1979-95 NCEP2 reanalysis, and the corersponding AMIP-2 ensemble means (middle panels) and inter-model standard deviations (bottom panels). All units are °C. Global averages are indicated in the plot titles.

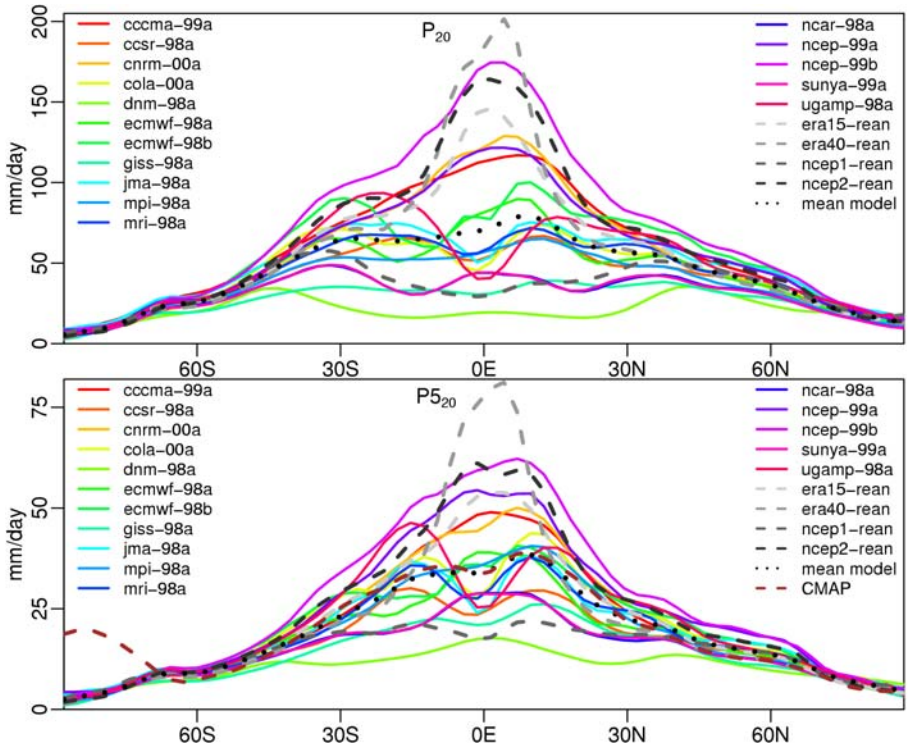

Figure 2: Zonally averaged 20-yr return values of annual 24-h (top panel) and 5-day (bottom panel) precipitation rate extremes simulated by the 16 AMIP-2 models, in the reanalyses and as estimated from the CMAP dataset. Units are mm/day.

Feature Based Diagnostics from ECMWF/NCEP Analyses and AMIPII: Model Climatologies

Kevin Hodges
University of Reading, U.K.
http://www.nerc-essc.ac.uk/~kih/AMIP2/era_results_new.html
(The contribution below is taken from the main page of this website. Refer to the website for interactive results.)

1. Processing Methodology

1a. Storm Tracks

The data used in this study are instantaneous fields every 6 hours. Since we are interested in the synoptic spatial scales the following pre-processing has been performed on each field before applying the tracking algorithm. Because we want to explore a wide range of fields at multiple levels, synoptic scale features can be identified consistently in these fields if we first remove the large scale, slowly varying planetary scales. So each field is spectrally decomposed using spherical harmonics and the coefficients for total wave numbers n<=5 are set to zero before converting back to grid point space. In addition the fields are spectrally truncated to T42 and some smoothing in the form of a tapering of the spectral coefficients is applied.

The tracking algorithm is applied to both the positive and negative anomalies in the filtered fields and to individual seasons for each year; December, January February (DJF); March, April, May (MAM), June, July, August (JJA), September, October, November (SON). This is performed for each hemisphere. A limited Eulerian analysis is also performed for comparison with the feature based statistics, thus mean fields, STD and 2-6 day bandpass filtered variance are computed for the spatially filtered fields. These results my be presented as well if requested.

1b. Tropical Easterly Waves

The processing for the EW activity is also performed at the T42 resolution for all models except those that are already at lower resolution. This is the only pre-processing performed (i.e. no planetray wave removal or additional smoothing) to prevent the degredation of the already weak waves. The period covered is from May to November (7 months) for the tropical region ~5S - 40N. Additionaly seasonal cycle statistics are computed but are not displayed here.

1c. Statistics

Before computing the statistics the track ensembles for each season for each year are filtered. Since we are only interested in the most coherent systems the ensembles are filtered to retain only those tracks that have lifetimes >= 2 days and which travel further than 1000Km. This may appear some what arbitrary but is used to exclude systems that are semi-stationary (which may be important in their own right and which may be explored later) or short lived secondary activity (again the nature of this activity may be explored later).

The track ensembles for each year are then combined into total ensembles for each season for the calculation of the climatological statistics presented below. Statistics are in the form of distribution densities and mean attributes. All densities have been scaled from probability density functions to number density per unit area per season, where the unit area is equivalent to a 5^0 spherical cap (~10^6 Km^2). By per season we mean that the densities have been normalized by the number of contributing track ensembles for that season. The mean attribute statistics are suppressed (not plotted) in regions where the feature or track densities are low as these will have a lower statistical significance than where the densities are high (confidence maps could be computed but this would increase the number of plots significantly and with additional computational cost). This gives some of the plots a rather ragged appearance. Smoother plots can be produced but this may give the wrong impression of the mean attributes. The thresholds used are again arbitrary but can be changed easily.

The climatological results presented here will be updated as more become available, particularly from AMIPII integration's. Also, results exploring the variability in the statistics with teleconnections will be made available later together with the methodology for the calculation.

2. Results

Note: The track density statistic is now defined in its more traditional form as opposed to the results previously found here. See Storm Track Paper for further details.

2a. Storm Tracks:-

Field Identification.

Summary table of available storm track results

Data Type:	☐ Model Info	☐ Planetary Scales	☑ Statistics (Clim.)
Statistic (Densities):	☐ Feature Density	☑ Track Density	☐ Genesis Density
Statistic (Mean Attributes):	☐ Intensity	☐ Growth/Decay Rate	☐ Speed/Velocity
Hemisphere:	☑ Northern Hemisphere	☐ Southern Hemisphere	
Anomaly type:	☑ Positive	☐ Negative	
Season :	☑ DJF	☐ MAM	☐ JJA

(Note: Anomaly and Statistic type options have no effect for Info or Planetary Waves, Season option only affects the Teleconnections statistics.)

Note: Teleconnection statistics are very incomplete and are broken down in terms of season. At the moment there are only really results for ECMWF (ERAOP) and NCEP for the NH, DJF, more to follow. Files are multi-page graphics.

Models

- ERA Analyses (79-93)
- Operational Analyses (94-2001)
- ERA+Operational Analyses (79-2001)
- NCEP Re-Analyses
- NCEP-DOE Re-Analyses
- GEOS1 Re-Analyses
- NCAR
- JMA

Field Type

- Mean Sea Level Pressure
- 500hPa Omega
- 330K Potential Vorticity
- PV=2 Potential Temperature
- 250hPa Temperature
- 500hPa Temperature
- 850hPa Temperature
- 200hPa Meridional Wind

Return File Type:- (•) **Postscript** ( ) **PDF**

PDF option now working again!!

SUBMIT RESET

2b. Tropical Easterly Waves:-

These results are double page gziped postscript files of a range of statistics for each model for the 850hPa Vorticity only.

Models

- ERA+Operational Analyses (79-2001)
- NCEP Re-Analyses (79-99)
- NCEP Re-Analyses (48-99)
- NCEP-DOE Re-Analyses
- GEOS1 Re-Analyses
- NCAR
- JMA
- CCSR

Return File Type:- (•) **Postscript** ( ) **PDF**

SUBMIT RESET

3. Further Information

This work forms part of an ongoing study of synoptic scale features in forecast analyses, model and satellite data using feature based methods. Work on the ECMWF Re-analyses is being conducted in collaboration with Brian Hoskins at Reading. Work on an Atmospheric Model Intercomparison Project (AMIP) II diagnostic sub-project is also currently being undertaken with

the Program for Climate Model Diagnosis and Intercomparison (PCMDI) (http://www-pcmdi.llnl.gov/). The main contact for the AMIP II project is James Boyle at PCMDI.

Further information on the AMIP II diagnostic sub-project can be found at http://www-pcmdi.llnl.gov/old/amip/DIAGSUBS/sp3.html For any suggestions or comments on the results presented here please contact me at kih@mail.nerc-essc.ac.uk

Should We Expect Climate Models to Converge When We Increase Resolution?

V D Pope and R A Stratton
Met Office, Hadley Centre for Climate Prediction and Research, UK
Email: vicky.pope@metoffice.com

One of the questions that climate modellers should address is whether their models have sufficient spatial resolution to represent the physical processes affecting climate. We have addressed this issue using the Hadley Centre climate model, HadAM3 (the climate version of the Met Office's Unified Model) and report the results in Pope and Stratton (2002). The model is run in AMIP II mode with 4 horizontal resolutions ranging from N48 (2.5 x 3.75 deg) to N144 (0.833 x 1.25 deg). An inherent assumption in this approach, and in numerical modelling of the atmosphere generally, is that models will converge towards an ideal solution as resolution is increased - provided we stay within the range for which the parametrizations are valid. We have shown that this assumption is not always justified. For example, the plot of zonal mean temperatures and differences shows that the warming in the troposphere when resolution is increased is largely converged at N96 (1.25 x 1.875 deg) whereas the cooling around the tropopause at the north pole is only apparent at N144. In principle, undesirable resolution dependencies in physical parametrizations can be removed. However, many processes, and in particular intermittent processes such as convection, are inherently non-linear making resolution dependency inevitable.

We used a range of techniques to identify the processes that affect convergence. For example, dynamical core tests with a smooth uniform land surface everywhere, were used to isolate dynamical processes. 'Spin-up' tendencies were used to diagnose the contribution of individual physical parametrizations and the dynamics scheme. The tendencies are produced by running a series of 1 day integrations starting from operational analyses scattered evenly through the period 1/12/98 to 21/2/99. The analyses use an assimilation system based on the forecast version of HadAM3. Spin-up tendencies are produced by taking the accumulated increments for each of the basic model fields from the dynamics and physical parametrization schemes and averaging them for all the runs. The dependency of the results on particular details of the model were also investigated to see how general the results are.

We showed that non-linearity in both the hydrological cycle and the dynamics play an important role in the lack of convergence. Non-linearity in convection and the response of vertical motion to increased resolution affected the convergence of the tropical circulation, assocated precipitation and the Madden Julian oscillation. They also affected mid-latitude storms. Non-linear dynamics affected the convergence of the tropopause temperature in the full model and the surface pressure in the dynamical core. The general resolution dependency of the results and the particular lack of convergence of some fields mean that it is important to explore the ability of the global model to simulate climate and the signals of climate change at a range of resolutions.

Pope V D and R A Stratton, 2002: The processes governing resolution sensitivity in a climate model. Climate Dynamics, to appear.

Impact of resolution changes on zonal mean temperatures (K)

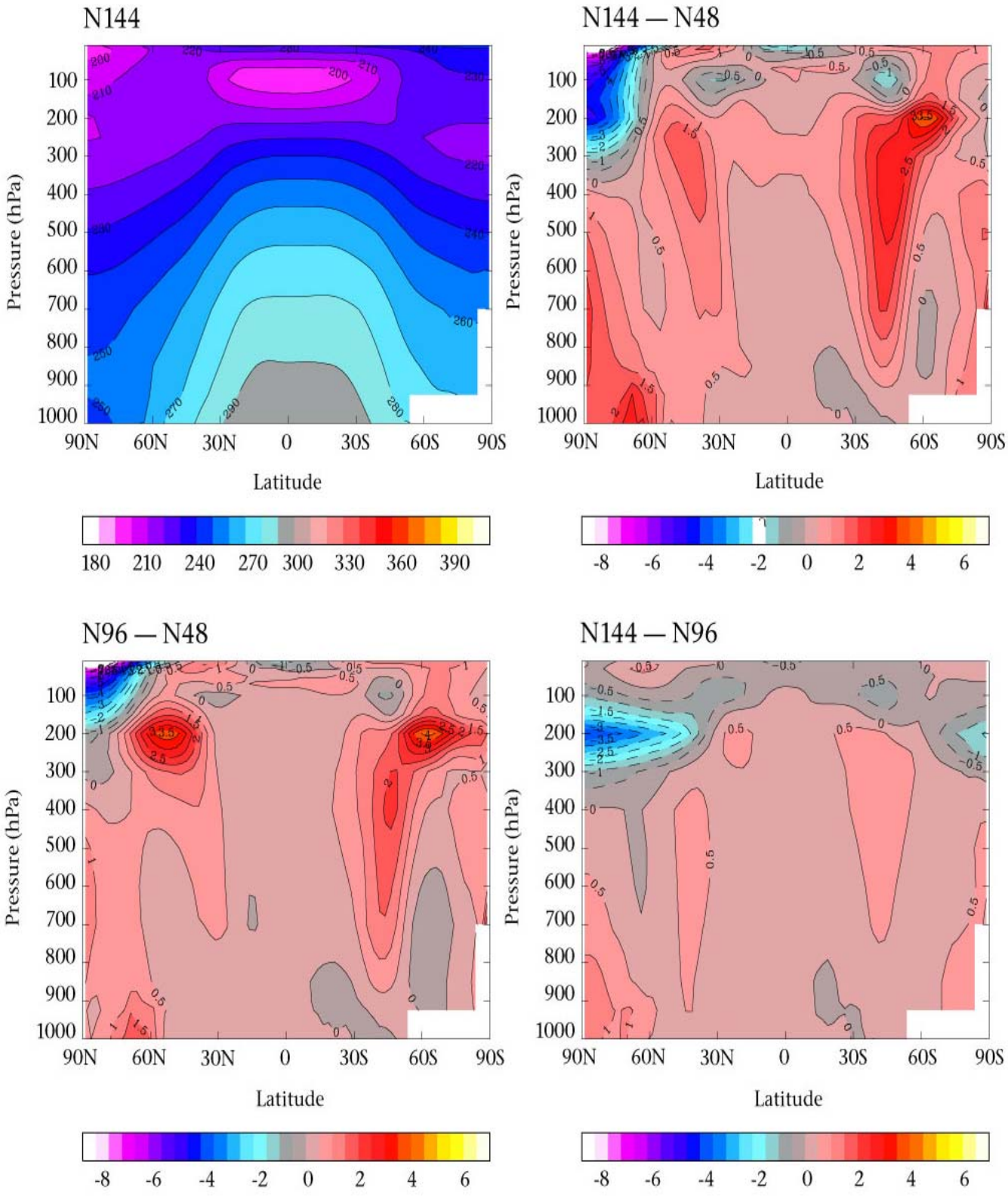

Modelling the Climatology of Storm Tracks – Sensitivity to Resolution

R A Stratton and V D Pope
Hadley Centre, Met Office.

1. Introduction

Standard climate models do surprisingly well in modelling the basic climatology and characteristics of storm tracks, even though they cannot represent the structure of individual storms because of their low resolution. This study uses a series of AMIP 2 integrations done with the Hadley Centre's climate model HadAM3 (Pope et al 2000) to investigate the impact of doubling horizontal resolution from N48 (2.5° latitude x 3.75° longitude) to N96 (1.25° x 1.875°) and increasing vertical resolution in the troposphere and lower stratosphere by increasing the number of levels from 19 to 30.

Storm tracks for the northern hemisphere winter are analysed using feature tracking for model fields and fields from ERA15 reanalyses (Gibson et al 1997) covering a 15 year period from 1979 to 1993.

2. Storm tracks

In recent years methods of analysing the climatology of storm tracks have become increasingly sophisticated. We use one of the most sophisticated techniques, namely the feature tracking developed by Kevin Hodges of Reading University (Hoskins and Hodges 2002). The suite of programmes he has developed allows aspects of the life cycle of the storms to be analysed statistically as well as the tracks themselves. We used 6 hourly mean sea level pressure data for our analysis. Figure 1 shows plots of track density calculated from instantaneous mean sea level pressure output every 6 hours. Comparing panels 1a and 1c indicates that increasing horizontal resolution improves the position and strength of the storm tracks. In the Atlantic it is generally moved poleward, and between Greenland and Norway it is strengthened. In the Pacific, it is strengthened in the mid Pacific and weakened in the east Pacific. Comparing panels 1b and 1c, on the other hand, shows that increasing vertical resolution has a more mixed impact. In particular, it has a detrimental effect in the Pacific where the storm track moves south. Overall at the highest resolution analysed the track density for mean sea level pressure is in good agreement with ERA (fig 1c) over the Atlantic but is too far equatorward over the Pacific.

Fig 1 Cyclone track density for djf 1979–93

Figures 1 and 2

(a) N96L30 minus N96L19

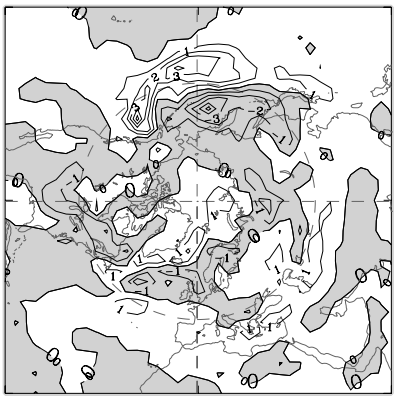

(b) N96L30 minus N48L30

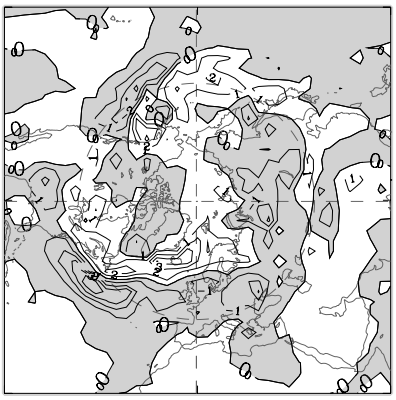

(c) N96L30 minus ERA

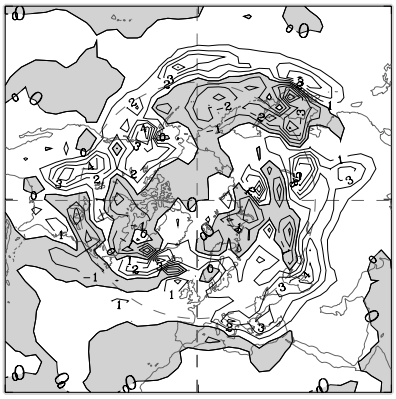

(d) ERA

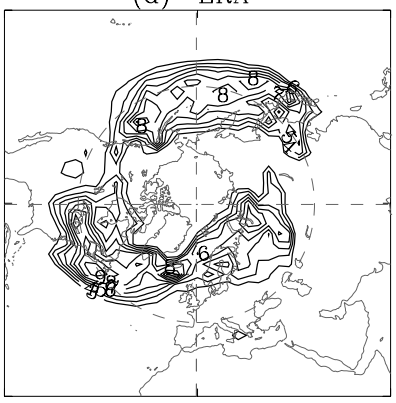

Fig 2 vT at 700hPa and E vectors at 200hPa for djf 1979–93

(a) N96L30 minus N48L30

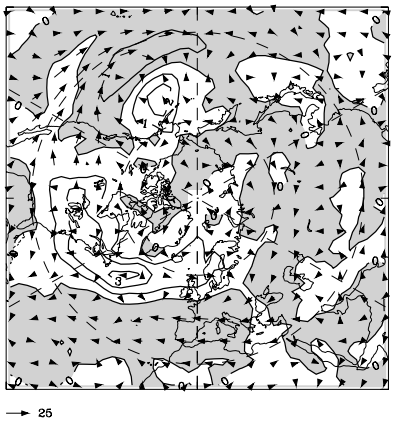

(b) ERA

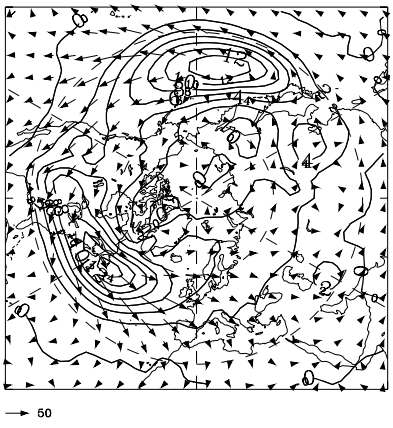

3. PHYSICAL PROCESSES INVOLVED

Many of the changes identified above are simply associated with changes in the position and strength of the mean jet, which can be linked to changes in the large-scale structure of the atmospheric circulation. Of course these changes are partly due to changes in the storm tracks as well, so the argument could be regarded as somewhat circular. Two examples of the impact of changes in the mean are the poleward shift in the Atlantic storm track on increasing horizontal resolution and the equatorward shift in the Pacific storm track on increasing vertical resolution. Both these changes coincide with shifts in the position of the climatological mean jet (Pope and Stratton (2002) and Pope et al (2001)). When horizontal resolution is increased there are increased transient vertical velocities and a more active hydrological cycle (Pope and Stratton, 2002). At mid latitudes in particular, more water vapour rises and condenses releasing latent heat. Also water droplets fall more quickly and evaporate less quickly also producing net heating. The resulting change in the mean temperature structure is associated with the poleward sift in the mean jet. When vertical resolution is increased the changes in temperature a little more complex (Pope et al., 2001) but are generally beneficial. However, the resulting equatorward shift of the jet is detrimental.

E-vectors derived from quasi-geostrophic baroclinic theory allow us to make some analysis of how the storms evolve and interact with the mean (Hoskins et al 1983). Figure 2 shows E-vectors from the model and ERA calculated from winds and temperatures filtered on the timescale of synoptic-scale features i.e. 2.5-6 days. We use a band pass filter described by Doblas-Reyes and Deque (1998). The contours show the vertical component of the E-vector (v'T') at 700 hPa. The arrows show the horizontal component of the E-vectors as 200 hPa, where most of the eddy convergence takes place. Where these converge (diverge) indicates that eddies are weakening (strengthening) the mean westerly flow. Figure 2b shows the typical observed pattern with the strongest upward propagation at the beginning of the storm tracks. Propagation across the oceans with some storms converging over northern Europe and north western America and others diverging towards the equator. Figure 2a shows that increasing horizontal resolution gives increased vertical propagation of storms all the way along the Atlantic storm track. This is an indication that storms are being generated at more locations at higher resolution and not just over the eastern seaboard of the US. Further analysis of other diagnostics (the subject of a more detailed study) indicates that storms are too long-lived and travel too far in the low resolution model. At higher resolution they are more transient as well as being generated at more locations. Essentially the storm evolution is more realistic in that secondary developments are being generated along the storm tracks. Hence although individual storms do not travel as far the storm track extends further into Europe thus producing a more realistic simulation. It would seem that the changes in the Atlantic storm track are consistent with changes in the corresponding E-vectors. The shift in the position of the Pacific storm track is also broadly similar to the shift in the pattern of the upward component of the E-vectors.

4. Summary

The results from this study suggest that increasing horizontal resolution improves the simulation of storm tracks. Increasing vertical resolution is less obviously beneficial, although the main detrimental effect is the equatorward shift of the storm tracks which is associated with a corresponding shift in the jet. This in turn is associated with temperature changes which are beneficial. Increasing horizontal resolution shifts the storm tracks poleward and increases their strength. The shift in location is linked to the changes in jet which is in turn linked to the changes in tropospheric heating - possibly partly associated with better resolution of the storms. At higher horizontal resolution storms have a more realistic lifecycle, generating secondary developments along the storm track. Individual storms are therefore more short-lived and are generated at a more wider range of locations along the main storm track.

References

Doblas-Reyes F J and Deque M (1998) A flexible bandpass filtering procedure applied to midlatitude intraseasonal variability. Mon Wea Rev 126: 3326-3335.

Gibson K J , Kallberg P, Uppala S, Nomura A, Hernandez A, Serrano E (1997) ERA description, ECMWF re-analysis project report series 1, ECMWF, Reading, UK.

Hoskins B J, James I N and White G H (1983) The shape, propagation and mean-flow interaction of large-scale weather systems. J Atmos Sci 40: 1595-1612.

Hoskins B J and Hodges K I (2002) New perspectives on the Northern Hemisphere winter storm tracks. J Atmos Sci 59: 1041-1061.

Pope V D, Gallani M L, Rowntree P R and Stratton R A (2000) The impact of new physical parametrizations in the Hadley Centre climate model Had AM3. Clim Dyn 16:123-146.

Pope V D, Pamment J A, Jackson D R, Slingo A (2001) The representation of water vapour and its dependence on vertical resolution in the Hadley Centre climate model. J Clim 14: 3065-3085.

Pope V D, Stratton R A (2002) The processes governing horizontal resolution sensitivity in a climate model. Clim

Diagnostics of Climate Variability and Trend Using Potential Vorticity Maps

Ming Cai
Department of Meteorology, University of Maryland, College Park, MD 20742, USA
cai@atmos.umd.edu

1. Introduction

The largest day-to-day variability in the extratropics occurs along the pathway of fronts that separate warm air from cold air. There is a net poleward heat transport associated with synoptical disturbances that warms the higher latitudes. On average, the net poleward heat transport by extratropical weather system is as large as that by quasi-stationary waves (Peixoto and Oort, 1992). Therefore, it is quite conceivable that the climate variations of extratropical frontal activity could be equally important as variations in quasi-stationary waves and they collectively are responsible for variations between warmer (hotter) winters (summers) and colder (milder) winters (summers) in the extratropics. In the context of the global warming debate, the largest observed warming trend in the last 25 years takes place in the extratropics [Jones et al., 2001, IPCC, 2001]. It is natural to ask whether changes in extratropical frontal circulation system can explain part of the much-amplified warming trend in high latitudes.

It is known that interannual/decadal variations of the winter season surface temperature are related to several prominent climate circulation variations, such as ENSO [e.g., Ropelewski and Halpert, 1986; Trenberth and Hurrell, 1994; Zhang et al., 1997] and AO/NAO [e.g., Trenberth and Hurrell, 1994; Hurrell, 1995; Thompson and Wallace, 2000; Baldwin and Dunkerton 2001, Thompson et al. 2002]. Furthermore, the recent upward trend of the AO index, reflecting a general reduction of sea level pressure over the polar cap, is coincident with a warming trend of the wintertime surface temperature in high latitudes, particularly over the continents in Northern Hemisphere [e.g., Hurrel.1995; Thompson and Wallace;1998, Thompson et al. 2000]. In contrast, it is much less clear what the impact of day-to-day frontal activities is on climate variations of the surface temperature. The primary objective of this study is to seek answers to these two questions: Is there a significant amount of interannual and decadal variability of frontal activities? If so, can climate variations/trend of frontal activities be related to the observed climate variations/trend in the surface temperature over the extratropics?

2. Data and Method

Following Morgan and Nielsen-Gammon [1998], daily (00Z) pressure (topography) maps on a constant potential vorticity (PV) surface (PV = 2.5 PVU, 1 PVU = 10^{-6} $m^2s^{-1}Kkg^{-1}$) are obtained using the surface pressure and potential temperature, the PV and temperature analyses on 11 isentropic surfaces derived from the NCEP/NCAR reanalysis II dataset [Kalnay et al., 1996; Kistler et al., 2001] for the period of 1979 to 2000. For brevity, the *pressure field on the 2.5 PVU surface* is denoted as "*P2.5*" hereafter. Morgan and Nielsen-Gammon [1998] referred to a constant PV surface with a PV value from 1 to 3.5 PVU as the "dynamic tropopause". They demonstrated the utility of diagnosing various weather phenomena such as cyclogenesis, PV folding/intrusion associated with frontogenesis, and development of upper level trough systems

along the dynamic tropopause. The objective of this study is to derive indices that gauge climate variability of upper level frontogenesis using daily P2.5 maps. The daily (00Z) air temperature field at the lowest σ level is also analyzed to relate these indices to the changes in the surface air temperature (denoted as "SAT"). For the sake of convenience, the data on February 29th in the 6 leap years from 1979 to 2000 are excluded. Therefore, there are total of 8030 maps for each of the P2.5 and SAT fields.

The climate annual cycle is obtained by first averaging data on each calendar day across all years from 1979 to 2002, which yields a series of 365 maps. Then a 31-day running mean operator is applied to the 365 consecutive maps to obtain smoothly varying annual cycle. The annual cycles of the P2.5 and SAT fields are denoted as "$P2.5^{annual}$" and "SAT^{annual}", respectively. The daily anomaly maps can be obtained straightforwardly by taking out the annual cycle from the original daily maps. The annual cycle of daily standard deviation maps of the two fields, denoted respectively as "SD_P2.5" and "SD_SAT", can be then derived from the anomaly maps with same procedure stated above.

Shown in Figure 1a is a typical P2.5 map taken at 00Z, March 12, 1993. On average, a constant PV surface tilts from low pressure (higher elevation) in lower latitudes to high pressure (lower elevation) in higher latitudes. On day-to-day maps, high pressure (low elevation) regions correspond to the area where large-amplitude of cyclonic PV anomalies reside. The border of the low elevation portion of the PV surface, as outlined by a selected isobar line (say P2.5 = 300 hPa), is highly curved, snaking up and down along meridians and latitudes alternately. The equator side of the low elevation regions can be regarded as an upper level front where the PV surface slopes steeply and descends meridionally towards higher latitudes.

A Boolean type function varying with location (x, y) and time (t) is defined to measure upper level PV intrusion events:

$$\mathrm{PVI300}(x,y,t)=\begin{cases}1, \text{ if } \mathrm{P2.5}(x,y,t) > \mathrm{P2.5}^{annual}(x,y,day) + 0.5\,[\mathrm{SD\_P2.5}(x,y,day)] \\ \qquad\qquad \text{and} \quad \mathrm{P2.5} > 300 \text{ hPa} \\ 0, \text{ otherwise}\end{cases} \tag{1}$$

where (x, y) are longitude and latitude; t = (year – 1979)365 + day, year = 1979, 1980, …, 2000 and day = 1, 2, … 365; "[]" denotes the zonal mean averaging operator. The colored area in Figure 1b represents the area where PVI300 = 1 for the P2.5 map shown in Figure 1a. Clearly, these regions are the places where the PV surface would have a much steeper slope compared to the climatological PV surface slope, implying a much stronger horizontal PV gradient. From the point of view of weather, these regions correspond to PV intrusion zones associated with upper level frontogenesis where PV surfaces descend. Typically, below these PV intrusion zones cold surface temperature anomalies are observed (Figure 1c).

Note that one could use local standard deviation instead of the zonal mean value in (1). The criterion for counting PV intrusion events is more uniform along longitude by using the zonal mean standard deviation. Because $P2.5^{annual}$ itself is nearly zonally symmetric (not shown here), it makes little difference if one uses the zonal mean of $P2.5^{annual}$ in (1) instead of the local value. The second criterion, namely, P2.5 > 300 hPa, is helpful to differentiate loosely the PV intrusion events over extratropics from the PV intrusion events occurring in subtropical and tropical regions. The results presented below are not sensitive to the choice of this elevation criterion as long as it is in the range from 250 hPa to 350 hPa.

A useful index (denoted as PVI) that can be readily derived from daily PVI300 maps is the time series of the percentage area of PVI300 = 1 in the Northern Hemisphere, measuring the

general level of upper level frontogenesis associated with polar fronts. Mathematically, it is defined as

$$\mathrm{PVI}(t) = \frac{100}{2\pi}\int_0^{\pi/2}\int_0^{2\pi}\mathrm{PVI300}(x,y,t)\cos(y)\,dx\,dy\,. \qquad (2)$$

For the PVI300 map shown in Figure 1b, PVI = 14.4, implies that at 00Z on March 12, 1993, 14.4% area in the Northern Hemisphere experiences upper level frontogenesis as measured by the PV intrusion index.

3. Results

The unfiltered time series of daily PVI index (Figure 2a) has a dominant annual cycle signal as well as noticeable interannual variability. The PVI index is larger in winter season and smaller in summer. On a typical day in winter (summer) season, the PVI index is about 13.5 (8.5). Within a season, the day-to-day variability of PVI is about half of the seasonal cycle. The day-to-day variability within a season varies from year to year. For example, it is seen that in the winter of 1999/2000, the PVI index varies from 10.5 to 14 whereas it varies from 13 to 16 in the winter of 1998/1999. In this sense, the winter of 1998/1999 can be regarded as a high PVI index winter with more frequent occurrences of upper level frontal activities and the winter of 1999/2000 correspond to a low PVI index winter with much suppressed frontogenesis activities.

To elucidate the interannual variability and long time climate trends of the PVI index, we have applied a 365-day running mean filter to the time series shown in Figure 2a and the result is plotted in Figure 2b. It is seen that the year-to-year variability of the PVI index varies from 11 to 12, which is about 1/3 of the day-to-day variability within a season. Therefore, it is quite indisputable that the interannual/decadal variability shown in Figure 2b is statistically significant. The year-to-year variability of the PVI index clearly exhibits a quasi-biennial signal. The horizontal line with alternating black and red colored segments in Figure 2b marks the mean value of the PVI index. The black (red) portions correspond to the easterly (westerly) phase of the QBO index derived from the NCEP equatorial zonal mean zonal wind at 50 hPa (http://www.cpc.ncep.noaa.gov). With the assistance of the colored segments, it is easy to see that the PVI index tends to intensify during the easterly and weaken in the westerly phase of the QBO. The apparent exceptions are the winter of 1989/1990 and spring/summer of 1994 for the easterly phase and 1998 for the westerly phase. Therefore, from 1979 to 2000, there are 7 of 9 easterly phases showing an amplifying PVI index and 8 out of 9 westerly phases coinciding with a weakening PVI index. In additional to the QBO-like interannual variability, the PVI index also exhibits notably decadal scale climate tends. Particularly, the PVI index has a downward trend from 1985 to 1996 and a sharp rebounding upward trend since then.

Table 1. Indices measuring extreme cold/warm weather events

$\mathrm{EX\_COLD}(t) = \frac{100}{A_{40}\,2\pi/9}\int_0^{\pi/2}\int_0^{2\pi} T_{EC}\cos(y)\,dx\,dy\,,\ T_{EC} = \begin{cases}1, & \text{if } \mathrm{SAT}^{\mathrm{anomaly}}(x,y,t) < -\mathrm{SD\_SAT}(x,y,\mathrm{day})\\ 0, & \text{otherwise}\end{cases}$
$\mathrm{EX\_WARM}(t) = \frac{100}{A_{40}\,2\pi/9}\int_0^{\pi/2}\int_0^{2\pi} T_{W}\cos(y)\,dx\,dy\,,\ T_{W} = \begin{cases}1, & \text{if } \mathrm{SAT}^{\mathrm{anomaly}}(x,y,t) > \mathrm{SD\_SAT}(x,y,\mathrm{day})\\ 0, & \text{otherwise}\end{cases}$

A_{40} is the total area of the Earth surface north of 40 °N. t = (year – 1979)365 + day, year = 1979, 1980, …, 2000 and day = 1, 2, … 365.

Table 1 lists definition of two additional indices, denoted as "EX_COLD" and "EX_WARM". If the observation stations were placed equally in space, EX_COLD is the percentage number of stations in the region north of 40 ºN that would report their surface air temperature below the daily climatological value by one standard deviation at a given time t.

Likewise, EX_WARM is that for one standard deviation above . Plotted in panels (c) and (d) of Figure 2 are the 365-day running mean time series of the EX_COLD and EX_WARM indices, respectively. In comparison with Figure 2b, it appears that more extreme cold events and less extreme warm events coincide with higher values of the PVI index and vice versa. In term of relation to the equatorial stratosphere QBO, it is seen that more extreme cold temperature episodes in the area north of 40ºN are observed during the easterly phase of QBO and less cold temperature episodes in the westerly phase. The correlation between the two time series plotted in panels (b) and (c) is 0.52 and –0.31 between panels (b) and (d).

It is of interest to point out both EX_COLD and EX_WARM indices show a generally continuous warming trend (less and less extreme cold and more and more extreme warm temperature episodes) since 1985. The PVI index, on the other hand, exhibits a seemingly upward trend after 1995, reversing from the general downward trend between 1985 and 1995. Nevertheless, the EX_COLD and EX_WARM indices still follow the PVI index at the interannual scales. For example, the EX_COLD index was high in 1996 and 1999, consistent with a high PVI index in these two years. The EX_COLD index was low the winter 1997/1998 to the spring of 1998, coinciding with a relatively low PVI index.

4. Summary

This paper proposes a potential vorticity intrusion index (denoted as PVI) as an alternative diagnostic tool to study the observed climate variability/trend of the surface temperature. The PVI index is defined as the percentage area of upper lever PV intrusion in the extratropics at any given time. More (fewer) outbreaks of extreme cold surface air temperature in high latitudes take place when the PVI index is high (low). The interannual variability of the PVI index exhibits a strong QBO- like signal. The high (low) PVI index prevails when the equatorial zonal mean zonal wind at 50 hPa is easterly (westerly). The PVI index also exhibits a strong interdecadal variability. Between early 1980s and middle 1990s, the PVI index shows a downward trend, accompanied with which is a warming trend in both cold/warm surface air temperature anomalies. During last 5 years of 1990s, the PVI index shows an upward trend, but the surface air temperature continuous to exhibit a warm trend. This effectively is an inconsistency between trends in upper level circulation and in surface air temperature [Van den Dool et al., 1993].

References

Baldwin, M. P., and T. J. Dunkerton, Stratospheric harbingers of anomalous weather regimes. *Science*, **294**, 581-584, 2001.

Blackmon,. L., J. M. Wallace, N. C. Lau, and S. L. Mullen, An observational study of Northern Hemisphere wintertime circulation. *J. Atmos. Sci.*, *34*, 1040-1053, 1977.

Cai, M. and H. M. van den Dool, Low-frequency waves and traveling storm tracks. Part I: Barotropic component. *J. Atmos. Sci.*, *48*, 1420-1436, 1991.

Kalnay, E. and Coauthors, The NMC/NCAR 40-year reanalysis project. *Bull. Amer. Meteor. Soc.*, *77*, 437–471, 1996.

Kistler, R. and co-authors, The NCEP/NCAR 50-year Reanalysis. *Bull. Amer. Meteor. Soc.*, *82*, 247–268, 2001.

Hurrell, J. W., Decadal trends in the North Atlantic oscillation region temperature and precipitation. *Science*, *269*, 676-679, 1995.

IPCC, Climate 2001, The Scientific Basis. J. T. Houghton et al. Eds., *Cambridge Univ. Press*, *Cambridge,* 881 pp.

Jones, P. D., T. J. Osborn, K. R. Briffa, C. K. Folland, E. B. Horton, L. V. Alexander, D. E. Parker, and N. A. Rayner, Adjusting for sampling density in grid box land ocean surface temperature time series. *J. Geophys. Res.*, *106*, 3371-3380, 2001.

Morgan, M. C. and J. W. Nielsen-Gammon, Using tropopause maps to diagnose midlatitude weather systems. *Mon. Wea. Rev.*, *126*, 2555-2579, 1998.

Peixoto, J. P. and A. H. Oort, Physics of Climate. *American Institute of Physics*, *New York*, 520pp, 1992.

Reed, R. J., A study of a characteristic type of upper level frontogenesis. *J. Meto.*, *12*, 226-237, 1955.

Ropelewski, C. F., M. S. Halpert, North American precipitation and temperature patterns associated with the El Niño, and the PNA pattern. *Mon. Wea. Rev.*, *114*, 2352-2362, 1986.

Thompson, D. W. J., and J. M. Wallace, The Arctic oscillation signature in the wintertime geopotential height and temperature fields. *Geophys. Res. Lett.*, *25*, 1297-1300, 1998.

Thompson, D. W. J., and J. M. Wallace, Annual modes in the extratropical circulation. Part I: Month-to-month variability. *J. Climate*, *13*, 1000-1016, 2000.

Thompson, D. W. J. , J. M. Wallace, and G. C. Hegerl, Annual modes in the extratropical circulation. Part II: Trends. *J. Climate*, *13*, 1018-1036, 2000.

Thompson, D. W. J., M. P. Baldwin, and J. M. Wallace, Stratospheric connection to Northern Hemisphere wintertime weather: Implications for prediction. *J. Climate*, *15*, 1421-1428, 2002.

Trenberth, K. E. and J. W. Hurrell, Decadal atmosphere-ocean variations in the Pacific. *Clim. Dyn.*, *9*, 303-319, 1994.

Van den Dool, H. M., E. A. O'Lenic, and W. H. Klein, Consistency check for trends in surface temperature and upper level circulation: 1950-1992. *J. Climate*, *6*, 2288-2297, 1993.

Zhang, Y., J. M. Wallace, and D. S. Battisti, ENSO-like interdecadal variability: 1900-93. *J. Climate*, *10*, 1004-1020, 1997.

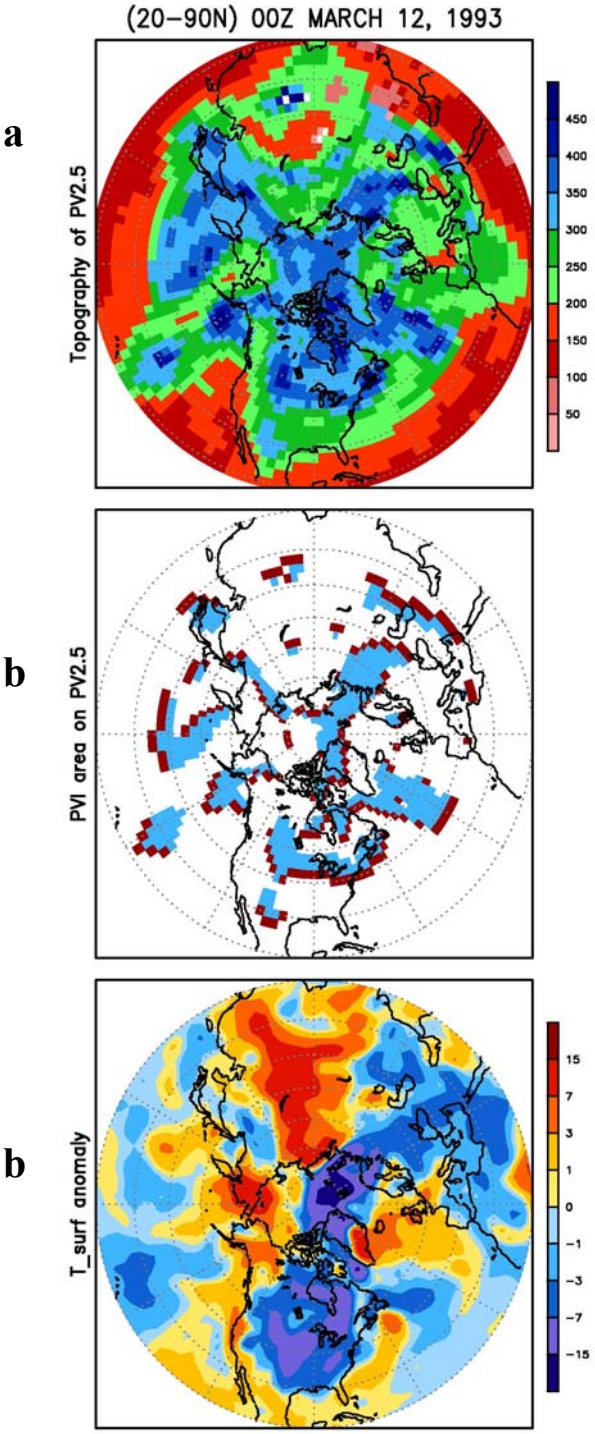

Figure 1. Snapshot maps of (a) P2.5 in unit of hPa, (b) PVI300 (PVI300 = 1 for colored areas and otherwise PVI300 = 0), and (c) $SAT^{anomaly}$ in unit of ºC at 00Z on March 12, 1993. The red-colored pixels in panel (b) approximately represent the locations of PV fronts.

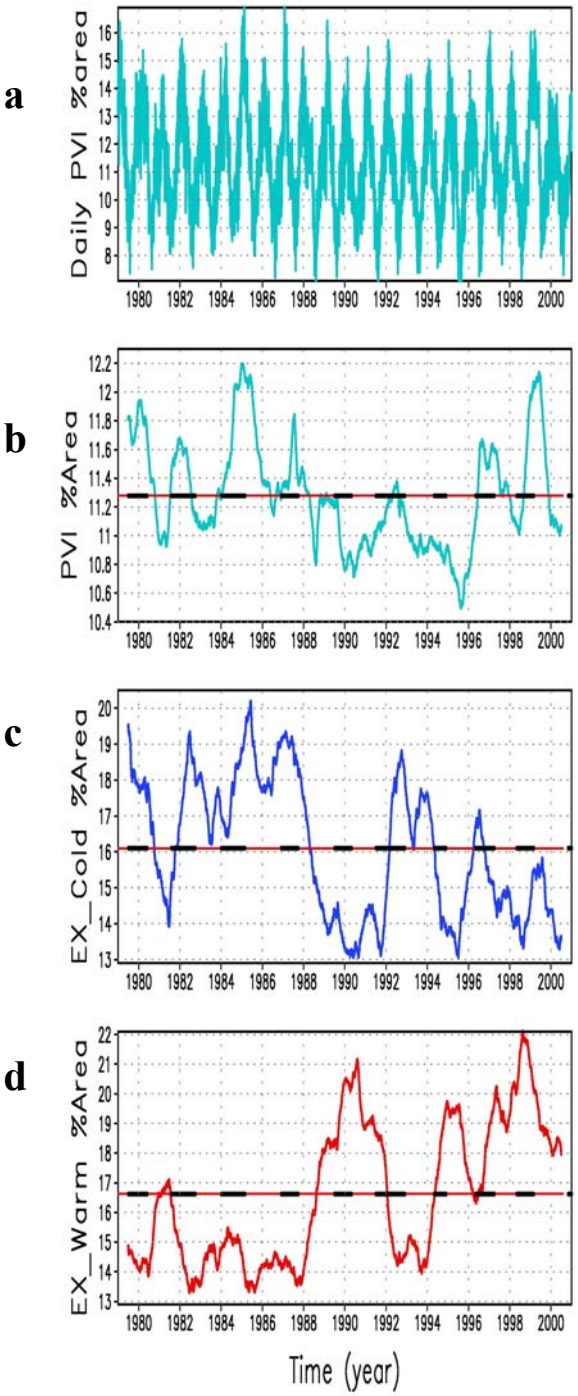

Figure 2. Time series of (a) unfiltered daily PVI index, (b) 1-year running mean PVI index, (c) 1-year running mean EX_Cold index, and (d) 1-year running mean EX_Warm index. The horizontal line in the middle of each panel is the mean value of the curve. The black and red portions of the line indicate the easterly and westerly phases of the QBO, respectively.

SELECTED ACTIVITY AT SOME MODELING CENTERS

MPI-ECHAM5: Resolution Dependence of Systematic Errors

E. Roeckner, G. Bäuml, M. Esch, M. Giorgetta, S. Hagemann, I. Kirchner, L. Kornblueh, E. Manzini[1], A. Rhodin, U. Schlese, U. Schulzweida and A. Tompkins[2]

Max Planck Institute for Meteorology, Hamburg, Germany
[1] Current affiliation: Istituto Nazionale di Geofisica e Vulcanologia, Bologna, Italy
[2] Current affiliation: European Centre for Medium Range Weather Forecasts, Reading, UK

1. THE MODEL

Compared to the previous model (ECHAM4; Roeckner et al., 1996: MPI f. Meteor., Rep. No. 218, 90 pp.), the following processes have been changed in ECHAM5:

- Advective transport: flux-form semi-Lagrangian scheme for positive definite variables like water vapor, cloud liquid water, cloud ice (Lin and Rood, 1996: MWR, 124, 2046-2070).

- Cloud cover: prognostic-statistical scheme applying a propability density function (PDF) for the total water content derived from a cloud resolving model. The moments of the (Beta)-distribution are obtained from prognostic equations for variance and skewness (Tompkins, 2002: JAS, 59, 1917-1942).

- Cloud microphysics: rain formation by coalescence and accretion, aggregation of ice crystals to snow flakes, sedimentation of cloud ice, phase changes (Lohmann and Roeckner, 1996: Clim.Dyn., 12, 557-572).

- Longwave radiation: The 'Rapid Radiative Transfer Model" (RRTM; Mlawer et al., 1997: JGR, 102D, 16663-16682) has been adopted from ECMWF. The model is based on the correlated-k method with the k-distributions directly attained from a line-by-line model. The scheme has a higher spectral resolution (16 bands instead of 6 in ECHAM4) and it is computationally more efficient at high vertical resolution because the CPU-time increases linearly with the number of layers compared to a quadratic dependence in ECHAM4.

- Solar radiation: The number of spectral bands has been increased from 2 to 4. This practically eliminates the 'cloud absorption bias' in ECHAM4. Options are (a) high resolution in the UV for calculating photolysis rates (Landgraf and Crutzen, 1998: JAS, 55, 863-878) and (b) Beta weighted two stream approximation to account for cloud inhomogeneities.

- Land surface: implicit coupling of atmosphere and land surface so that prognostic variables and surface fluxes are calculated synchroneously at the same time level. Main advantage compared to the semi-implicit scheme in ECHAM4 is energy conservation in the new scheme (Schulz et al., 2001: J.Appl.Met., 40, 642-663).

- Snow on the canopy: obtained from a prognostic equation including interception of snowfall, sublimation, melting and unloading due to wind (Roesch et al., 2001).

- Surface albedo: depends on the specified background albedo, a specified snow albedo (function of temperature), the area of the grid box covered with forest, the snow cover on the ground (function of snow depth and slope of terrain) and the snow cover on the canopy (Roesch et al., 2001: Clim.Dyn., 17, 933-946).

- Lakes: a simple mixed-layer model is used for calculating temperature and ice thickness.

- Land surface data: vegetation ratio, leaf area index, forest ratio and background albedo have been derived from a global 1km-resolution dataset (Hagemann, 2002: MPI f. Meteor., Rep. No. 336, 21 pp).

- Ozone: prescribed as a function of month, latitude (zonal means) and height according to ozone sonde profiles and satellite data (Fortuin and Kelder, 1998: JGR, 103D, 31709-31734).

- Domain/resolutions (currently): top levels at 30km or 80km. Horizontal resolutions from T21 to T106, 19 or 31 layers for 30km version, and 39 or 90 layers for 80km version.

2. EXPERIMENTS AND RESULTS

Ten AMIP2 simulations (1978-1994) have been performed with the standard version of ECHAM5 (top level at 30km) at different horizontal resolutions (T21, T31, T42, T63, T85, T106) and two vertical resolutions (L19, L31). The L31 experiments were performed for T42, T63, T85 and T106 only. Seasonal root mean square (rms) errors with respect to ECMWF reanalyses (ERA15) were computed for temperature, geopotential height and zonal wind at three pressure levels (200, 500 and 850 hPa) and for sea level pressure as well. In the L19 simulations, the rms errors decrease with increasing horizontal resolution. This improvement is systematic between T21 and T63, but marginal only between T63 and T106. On the other hand, in the L31 simulations, the impact of increased horizontal resolution is evident up to T106, especially for temperature and geopotential height in the middle and upper troposphere. Compared to L19, the L31 simulations improve at higher horizontal resolutions (T63, T85, T106) but deteriorate at moderate horizontal resolution (T42).

A comparison between the L19 and L31 simulations at high horizontal resolution (T106) is shown in Figure 1. In all cases, the L31 errors (right column) are significantly smaller than those in the L19 simulations (left column). This applies not only to the total errors of 500 hPa geopotential height (upper panels) and sea level pressure (lower panels), but also to the zonally asymmetrical part of 500 hPa geopotential height (middle panels), especially in the Pacific sector and over the Rocky Mountains. These error patterns are typical for the T63 and T85 simulations as well (not shown). However, as indicated above, the T42 response to increased vertical resolution is different, and the errors are systematically higher than in the L19 simulation.

3. CONCLUSIONS

Increasing the vertical resolution from L19 to L31 is beneficial at 'high enough' horizontal resolution (T63, T85 and T106). The opposite effect is found for moderate horizontal resolution

(T42). This result, indicating that horizontal and vertical resolutions should not be chosen independently, is consistent with quasi-geostrophic theory (Lindzen and Fox-Rabinovitz, 1989: MWR, 117, 2575-2583) and idealized numerical experiments (Fox-Rabinovitz and Lindzen, 1993: MWR, 121, 264-271).

Atmospheric GCM Development Issues at GFDL: Impact of Aerosols

William Stern
Geophysical Fluid Dynamics Laboratory
wfs@gfdl.noaa.gov

1. Introduction

Recent atmospheric general circulation model (AGCM) development at GFDL has been primarily directed toward the goal of producing a credible atmospheric component for a coupled GCM, suitable for climate predictions on time scales ranging from seasons to centuries.

The major thrust of this AGCM development effort at GFDL involves the flexible modeling system (FMS). The model participating in AMIP2 uses a B-grid core with a horizontal resolution of 2.5 x 2.0 longitude - latitude and 18 vertical hybrid coordinate levels (N45L18). Some of the physics, such as relaxed Arakawa-Schubert (RAS) convection, orographic gravity wave drag and the Mellor-Yamada boundary layer have evolved from the older GFDL-DERF model (AMIP2 submission is named derf-98a), while newer parameterizations for radiation (including aerosols), fully prognostic cloud prediction and a new land model, have been introduced in the GFDL-FMS AM2 GCM (AMIP2 submission is named gfdl-02a).

A number of sensitivity studies have been conducted as part of the model development process. One study of interest is a comparison with and without aerosols, which is the focus of this report.

2. Discussion

As part of the FMS AGCM development effort at GFDL, aerosols were included to provide a more accurate radiative forcing. Figure 1 shows the geographical short wave signature of the aerosols averaged over the AMIP2 period for DJF and JJA, respectively. In these figures, clear sky downward short wave at the surface is plotted for the difference of AM2 with aerosols (AM2amip2v2) and without aerosols (AM2amip2). The plots show several regional maxima in aerosol related (negative shortwave) forcing. For DJF in the mid-latitudes across Europe, northeast China and the eastern U.S., which are presumably due to sulfates and across west-central Africa, which is primarily from dust. In JJA there is a large area of dust related aerosol forcing across northern Africa extending eastward across Saudi Arabia into western India. The impact of including aerosols on the annual mean surface short wave budget is a significantly smaller difference when compared with observations (ERBE) than in the GCM simulation without aerosols, i.e., 2 w/m^2 versus nearly 7 w/m^2. An additional more remote sensitivity appears in precipitation over the tropical western Pacific. A significant difference is apparent (not shown) in the western SPCZ during DJF, where the case with aerosols shows a large reduction in previously excessive precipitation rates, closer to the observed.

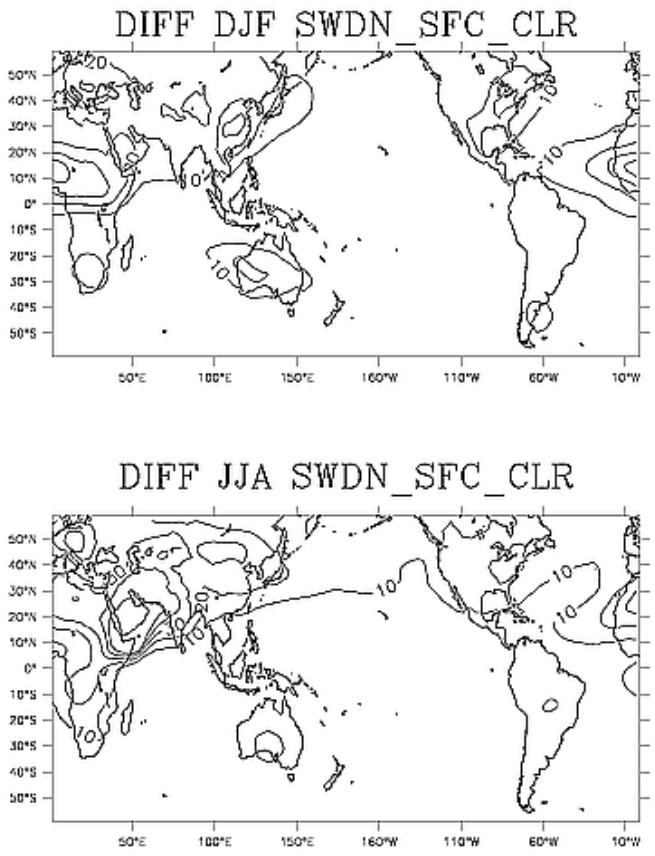

Fig 1. Downward clear sky short wave at the surface for AM2 simulation without aerosols minus simulation with aerosols. DJF (Top) and JJA (Bottom). Contours range from 10 to 50 w/m^2 with an interval of 10.

The addition of aerosols to AM2amip2v2 did not produce unanimous improvement. In the northern hemisphere mid-latitude upper troposphere the aerosol forcing appears to exacerbate an already warm bias by about 3 Deg K in the zonal mean. This can be seen in Figure 2, which shows 200 hPa zonal mean temperature plots. It is speculated that the current aerosol dataset has too much sulfates during DJF in the Northern Hemisphere mid-latitudes, particularly over Europe. In addition, the vertical distribution of dust is also being looked at for possible errors. A newer aerosol dataset will be available soon and it is hoped that it will alleviate some of this upper tropospheric warm error. However, as noted above, this accounts for only about 3 degrees of a 10 degree warm error (see figure 2). In this regard additional experiments are being conducted using an improved vertical advection scheme for specific humidity (and other tracers) i.e., piece-wise parabolic method (ppm), and modifications to the RAS convection scheme. One such experiment, AM2p10, used the ppm and included cumulus momentum transport plus a lower limit on entrainment in RAS. Its zonal mean 200 hPa temperature profile is plotted along with the other experiments in Figure 2 and shows an overall cooling of from 4 to 6 degrees at all latitudes, which reduces the northern hemisphere extra-tropical rms error significantly, but produces a cold tropical and southern hemisphere upper troposphere. It is hoped that the new aerosol dataset combined with further modifications to the convection will be able reduce these errors. The AM2 GCM is currently being used as the atmospheric component for several coupled

model experiments. Feedback from these coupled experiments will also serve to direct future development of the AM2 GCM.

Finally, a parallel AGCM development track is being pursued at GFDL, denoted as AM3. This involves new parameterizations for convection, orographic gravity wave drag and boundary layer physics, as well as enhancements to the stratosphere. It is expected that an AM3 based GCM will eventually replace the AM2 based GCM as the atmospheric component to the coupled GCM.

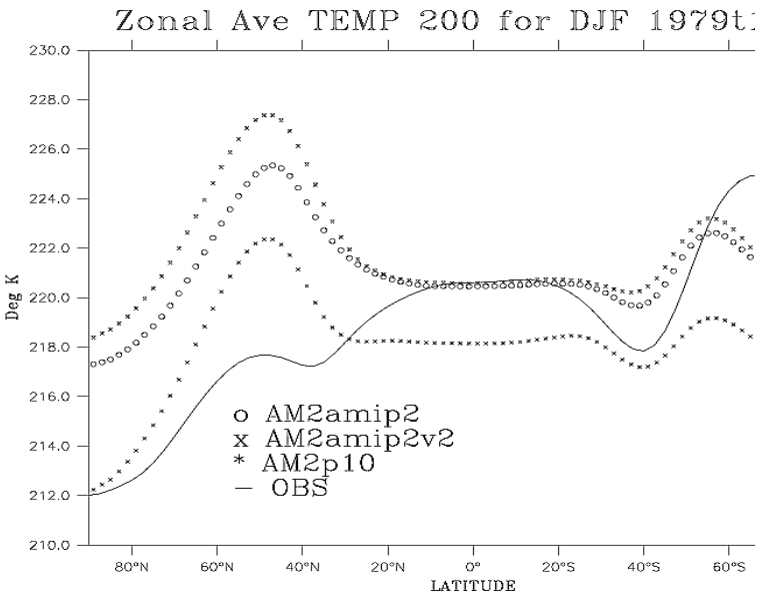

Fig. 2. Zonal mean temperature (Deg K) at 200 hPa during DJF for AM2 with aerosols (x), without aerosols (o), AM2 with aerosols + v.adv + RAS (*) and Observations (black line).

Model Activities at MGO

Matyugin V.A.
Voeikov Main Geophysical Observatory
St. Petersburg, Russian Federation

1. AMIP-II VERSION OF THE MGO AGCM

AMIP-II version of the MGO AGCM is rather similar to that used in AMIP-I. Its full description is given in the number of recent publications (Phillips 1994; Shneerov et al., 1997; Shneerov et al., 2001). Computational algorithm and space resolution is kept the same in both runs. The model uses spectral representation of the main prognostic variables ζ, D, T, q, ln p. Horizontal resolution is spectral triangular 30 (T30), roughly equivalent to 3.75 x 3.75 degree latitude/longitude grid. Vertical resolution is presented by 14 unequally spaced □-levels. The model T30L14 includes parameterization of all major physical processes: spectral treatment of solar and infrared radiative transfer in the cloudy atmosphere, vertical turbulent heat, moisture, and momentum exchange in the boundary layer and free atmosphere, deep and shallow convection, cloud prediction and precipitation formation, gravity wave drag forcing and land surface processes.

Meanwhile further refinements of certain physical processes were undertaken and after extensive validation in multi-year runs appropriate changes were incorporated in the new version of the model MGO-2. The major changes related to the following physical processes:

- radiation code has been modified and absorption by minor greenhouse gases and aerosols were included;
- new schemes of layer cloud prediction at the top of the boundary layer and cloud optical properties;
- diurnal cycle of solar radiation;
- Tiedtke deep and shallow cumulus convection;
- New scheme of land surface processes accounts for effect of vegetation cover and spacially varying field capacity of the soil on surface radiation balance, evaporation and runoff;
- Active soil layer is described by four model layers of 3 m depth.

2. USE OF THE MGO GCM IN THE CLIMATE INVESTIGATIONS AND WEATHER FORECASTS

The GCM has been used in the following studies:

- cloud-radiative, water vapor and sea-ice feedbacks in MGO GCM coupled to mixed-layer ocean in simulation of equilibrium climate with CO_2 doubling (Meleshko et al., 2000);
- variability of hydrological cycle in the northern hemisphere and its impact on water balance over Volga watershed and sea level variability of the Caspian sea in second half of the 20^{th} century (Pavlova et al., 2001);

- simulated variability of tropical atmosphere and its dependence on parameterization of deep cumulus convection in the MGO GCM (Meleshko et al., 2001c);
- role of sea-ice cover in variability of extra-tropical atmosphere (Kattsov at al., 1997);
- assessment of climate change over Russia in the 21st century due to CO_2 increase (Meleshko et al., 1999);
- evaluation of potential seasonal predictability in the northern hemisphere and over Russia due to influence of surface boundary condition and memory in initial state of the atmosphere (Meleshko et al., 2001b);
- development of ensemble prediction system for one-month over Russia (Meleshko et al., 2001a);

At present the version of the model T42L14 with similar package of physical parameterizations is used in operational prediction for one month.

3. EVALUATION THE PERFORMANCE CAPABILITY OF THE MODEL

Some impression on current status of the model based on AMIP-II simulation can be drawn from figures 1 and 2.

Figure 1. MGO AGCM performance : AMIP-II vs. AMIP-I

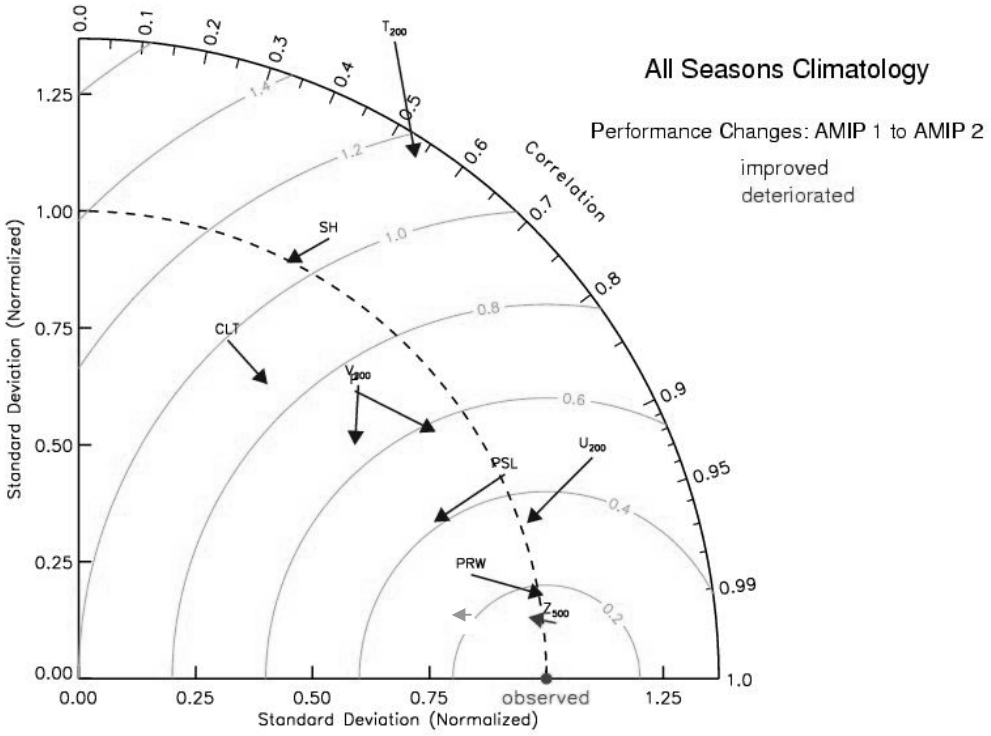

Figure 2. Annual RMSE of precipitation (PRC), precipitable water (PRW), surface air temperature (TAS), sea-level pressure (SLP), and mean of all variables (MN) computed from AMIP II GCMs for the Northern Hemisphere.

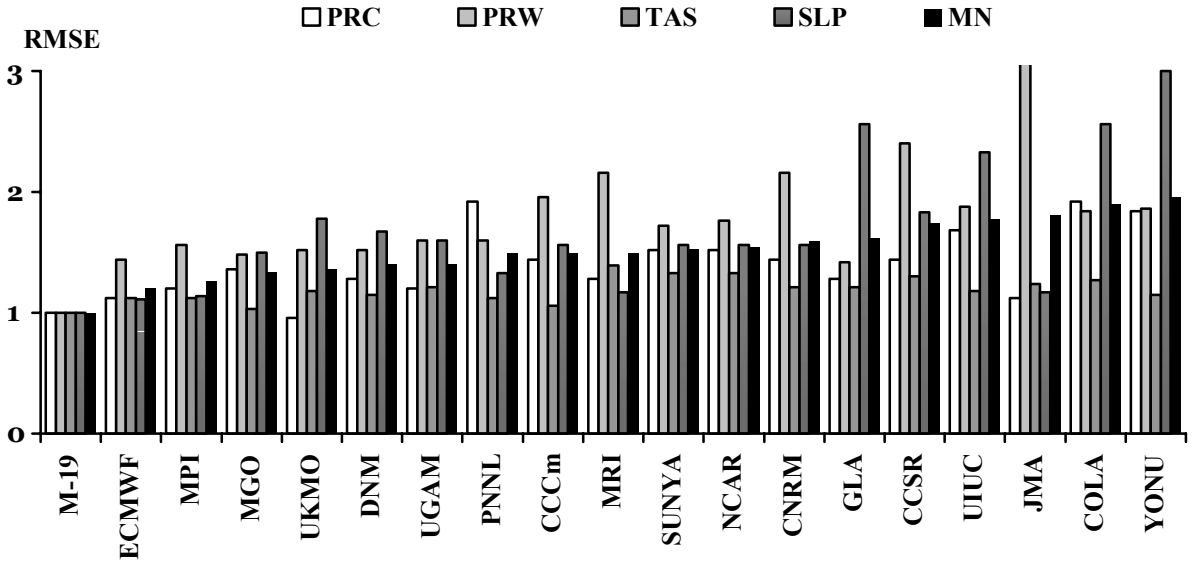

All errors are normalized on the appropriate averaged RMSE from 19 AMIP-II models (M-19). GCMs are ranked in order of RMSE increase for MN (black bars).

4. Further development of the MGO AGCM

Currently the higher resolution version of the MGO GCM is being tested. It will also incorporate:

- hybrid vertical coordinate system implemented on 21 irregularly spaced levels
- Shape-preserving semi-Lagrangian transport scheme for advecting water vapor and other scalar fields

References

Kattsov, V.M., V.P. Meleshko, G.V. Alekseev, V.A. Matyugin, B.E. Shneerov, V.M. Gavrilina, 1997: Impact of sea-ice concentration on high-latitude atmospheric variability. *Meteor. Gidrologia (Russian Meteorology and Hydrology)*, No.4, 43-54.

Meleshko V.P., Gavrilina V.M., Matyugin V.A., Mirvis V.M., Pichugin Yu.A., Vavulin S.V., 2001a: Application of the MGO GCM to long-range forecasting. *MGO Proceedings*, No.550, 127-154.

Meleshko V.P., Gavrilina V.M., Pichugin Yu.A., Shneerov B.Ye., 2001b: On assessment of potential seasonal predictability of atmospheric circulation in the northern hemisphere. *MGO* ***Proceedings, No.550, 166-178.***

Meleshko V.P., Randall D.A., Vavulin S.V., Shkolnik I.M., 2001c: Dependence of the MGO GCM reproduced atmospheric circulation upon the convection parameterization. *MGO Proceedings*, No.550, 44-84.

Meleshko, V.P., V.M. Kattsov, P.V. Sporyshev, S.V. Vavulin, and V.A. Govorkova, 2000: Climate system response to anthropogenic forcing: water vapour, clouds and radiation interaction. *Meteor. Gidrologia (Russian Meteorology and Hydrology)*, No.2, 22-45.

Meleshko, V.P., V.M. Kattsov, P.V. Sporyshev, S.V. Vavulin, and V.A. Govorkova, 1999: MGO climate model sensitivity to atmospheric CO_2 change. In: *Contemporary investigation at Main Geophysical Observatory (on the occasion of 150th anniversary of its foundation),* Hydrometeoizdat, 3-32.

Shneerov, B.E., V.P. Meleshko, A.P. Sokolov, D.A. Sheinin, V.A. Lyubanskaya, P.V. Sporyshev, V.A. Matyugin, V.M. Kattsov, V.A. Govorkova, and T.V. Pavlova, 1997: MGO Global atmosphere general circulation model coupled to mixed layer ocean. *MGO Proceedings*, No.544, 3-123.

Shneerov B.Ye., V.P.Meleshko, V.A.Matyugin, P.V.Sporyshev, T.V.Pavlova, S.V.Vavulin, I.M.Shkol'nik, V.A.Zubov, V.M.Gavrilina, V.A.Govorkova, 2001: The new version of the MGO global model of general circulation of the atmosphere (version MGO-2). *MGO Proceedings*, No.550, 3-43.

Pavlova T.V., Meleshko V.P., Govorkova V.A., 2001: The components of heat and water balances as computed by the MGO GCM within the framework of the AMIP I and AMIP II over the large rivers watersheds. *MGO Proceedings*, No.550, 85-109.

Phillips, T. J., 1994: A summary documentation of the AMIP Models. PCMDI Report No. 18, LLNL, UCRL-ID-116384, CA, 343 pp. For the most up-to-dateversion see WWW address: http://www-pcmdi.llnl.gov/modeldoc/amip

HadGEM1 – The New Hadley Centre Global Environment Model

V. Pope, T. Johns, G. Martin & HadGEM1 Development Team
Met Office, Fitzroy Road, Exeter EX1 3PB

The Hadley Centre in the Met Office has undertaken an ambitious programme of model development to produce their next generation of climate models. The atmospheric component of the model includes the same schemes as the Met Office's weather forecast model, but with parameter choices and some further developments to make it suitable for coupled modelling on climate timescales. Compared with the previous model, HadCM3, the new climate model includes substantially improved representations of physical processes in the atmosphere, new sea ice representation and some improvements in the ocean. It also includes increased functionality and higher resolution. Major improvements are the use of semi-Lagrangian instead of Eulerian dynamics to advect both dynamical and tracer fields, new boundary layer, gravity wave drag and microphysics schemes, and major changes to the convection, land surface (including tiled surface characteristics) and cloud schemes. Also included is representation of dynamic sea ice and improved thermodynamic properties of the sea ice. Processes available in the standard version of the model for the first time include the direct and first indirect radiative effects of aerosol, the sulphur cycle, atmospheric chemistry and dynamic vegetation.

The model performs well, and in many aspects it improves upon the previous version. Long standing errors common to many climate models have been substantially reduced, notably the cold and moist biases in the upper troposphere are much smaller (see Fig. 1), cloud-radiative properties, boundary-layer properties and the representation of tracers are all improved. The winds (particularly in the tropics) are generally improved at low levels, although they are rather worse at upper levels. The exception at low levels is in an increased bias in near-surface equatorial easterlies, particularly over the Pacific. These are associated with the development of cold equatorial SSTs in the coupled model and with deficiencies in convection over the equatorial Pacific, convection being confined to the Indonesian region (Fig. 2). These errors are linked to an original deficiency in convection over Indonesia in the atmosphere-only model.

There are considerable improvements in the representation of cloud in HadGAM1 compared with HadAM3. Perhaps the most significant development is the much greater consistency between the cloud and radiation budget fields in HadGAM1 – comparisons with satellite observations demonstrate that the developments included in the new model lead to a much better representation of the different ISCCP cloud types (e.g. Fig. 3), while at the same time providing a generally more reliable simulation of the top-of-atmosphere radiation budget and the cloud radiative forcing.

Several aspects of variability are improved. Transient eddy activity is increased and the storm tracks strengthened. This is partly a result of the change to semi-Lagrangian dynamics and partly due to the increased horizontal resolution. Analysis of synoptic variability over Europe indicates that both HadGAM1 and HadGEM1 produce a realistic distribution of weather regimes. The frequency and distribution of northern hemisphere blocking events are improved in HadGAM1, although blocking over the Pacific is reduced considerably in HadGEM1 compared

with HadGAM1. This is thought to be related to the development of tropical SST and precipitation errors and the related tropical and subtropical wind errors.

Intraseasonal variability of convection near the equator is generally stronger and closer to observations in HadGAM1/GEM1. However, as in HadAM3, there is limited convective variance coincident with the equatorial wave modes. Simulation of the Madden-Julian Oscillation is improved in the coupled model: HadGEM1 produces several eastward-propagating events with comparable magnitude to observations (Fig. 4). However, as in HadCM3, there is limited extent of eastward propagation due to a systematic error in low-level winds along the equator. Also in the tropics, interannual variability is worse, in particular the ENSO signal is very weak and there is little response of the Walker circulation to El Nino events. The tropics remain an area of concern in the new model.

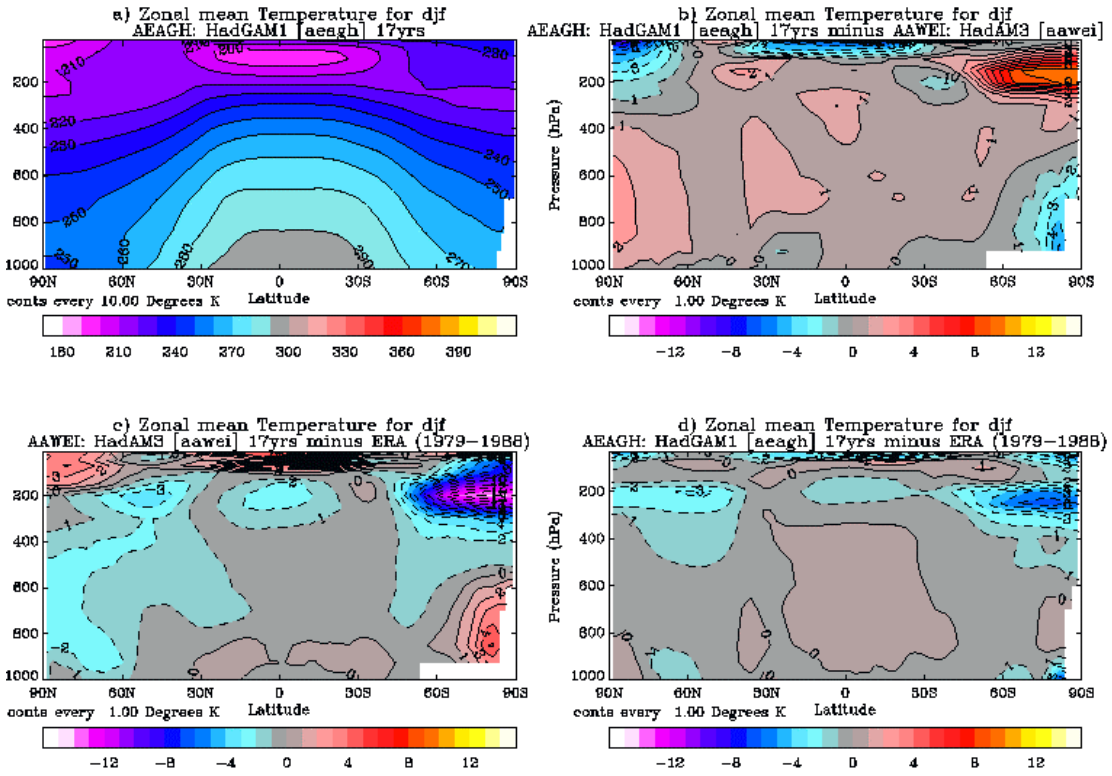

Figure 1: Zonal mean temperature in HadGAM1 compared with HadAM3 and ERA-15

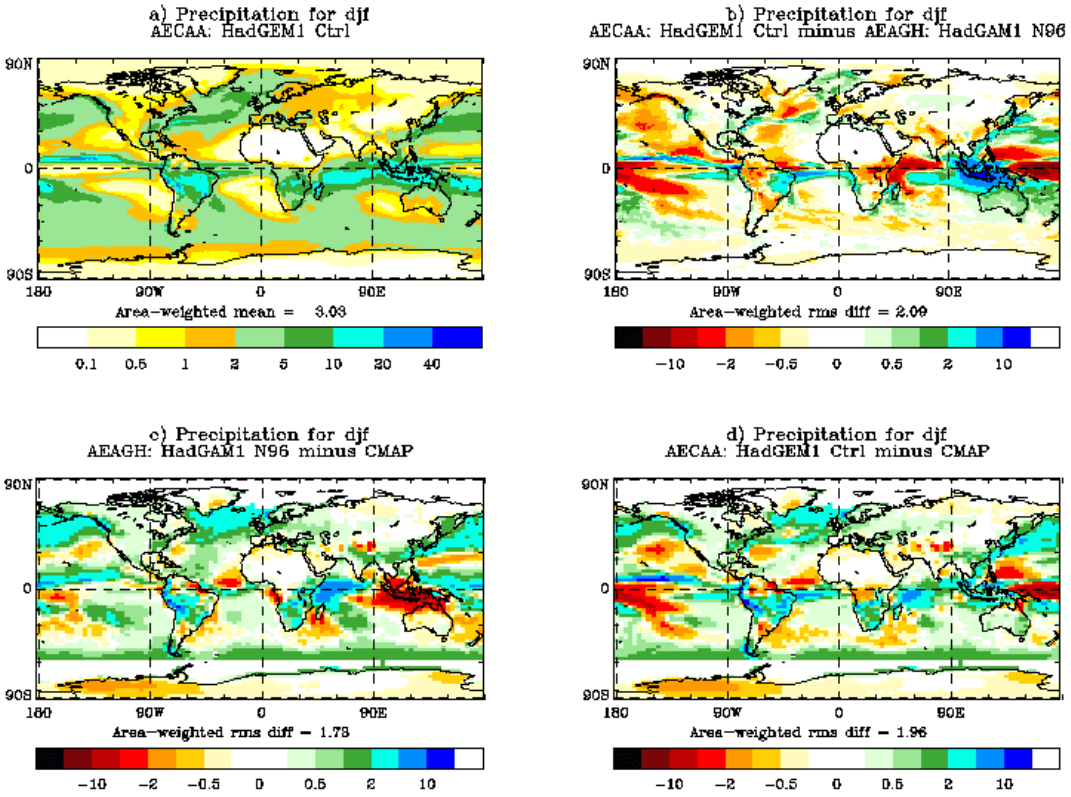

Figure 2: Precipitation in HadGEM1 compared with HadGAM1 and CMAP/O climatology

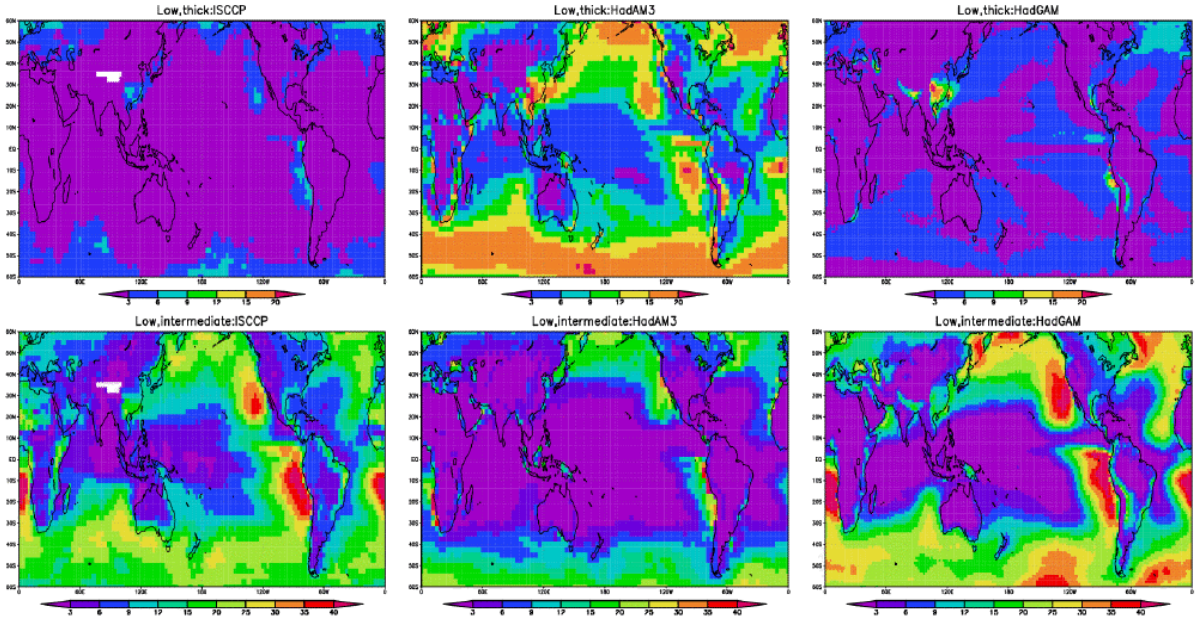

Figure 3: Comparison of annual mean ISCCP low -level thick (top) and intermediate (bottom) optical depth clouds with HadAM3 and HadGAM1

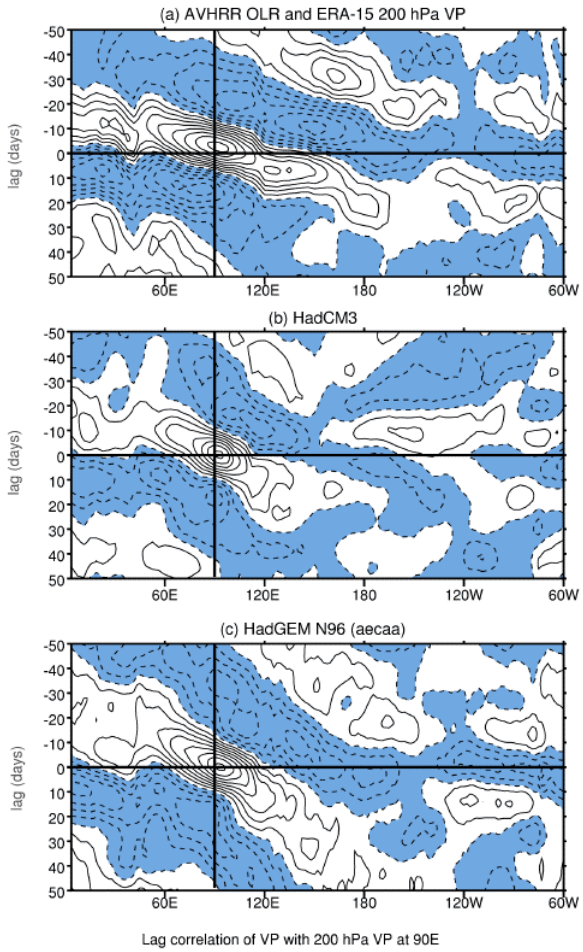

Figure 4: Lag-lead correlations of band pass filtered (20-100 day) OLR with an upper tropospheric velocity potential index defining the active phase of the MJO at 90^0E.

Inter-annual Variability of Tropical Precipitation and Associated Extra-tropical Atmospheric Response in the MRI/JMA AGCM

Tomoaki OSE, Masato SUGI and Akio KITOH
Nagamine Tsukuba Ibaraki 305-0052 JAPAN
e-mail: ose@mri-jma.go.jp

1. INTRODUCTION

Inter-annual variability of precipitation in the tropical Western Pacific (WP) has been know as one of the key issues for the seasonal prediction over Japan during its winter (DJF) and summer (JJA). I report the predictability of the tropical precipitation, especially in the tropical WP. Then, I like to show the statistical study on how the successful/unsuccessful simulation of inter-annual precipitation variability is related to SST anomalies.

2. MODEL AND EXPERIMENTS

The MRI/JMA AGCM (Shibata et al., 1999) used here is based on the old-version of the JMA short-term prediction model with some schemes incorporated and some improvements made for a climatic model. Ensemble integrations with six members are made during January 1949 – December 1998 under the observed SST and sea ice (HadISST1). Analysis is focused on the 6-member ensemble average for December-January-February (DJF) and June-July-August (JJA) during 18 years from DJF 1980 (December 1979-February 1980) to DJF 1998 and from JJA 1980 to JJA 1998. The NCEP2 reanalysis data and Xie-Arkin precipitation data are used for the verification. Note that the WP domain is referred to as (130-150E, 5-15N) for DJF study and (130-150E, 10-20N) for JJA study.

3. RESULTS

3.1.1 GCM performance about tropical Western Pacific (WP) precipitation

The inter-annual variability of the tropical WP precipitation is shown in Fig.1a and Fig.2a for each member of the integrations, the ensemble average and the observation. The observed precipitation variability is within the uncertainty estimated from the diversity of six members, almost perfectly for DJF. The ensemble integration for a few of JJA cases misses to capture the observation within their diversity.

The observed tropical WP precipitation has different relationship with SST between DJF and JJA. The WP SST variability is plotted as well as the WP precipitation for DJF and JJA in Fig. 1b and Fig. 2b, respectively. The DJF WP precipitation is closely related to the WP SST variability. On the other hand, the JJA WP precipitation is not related to the WP SST.

Fig.1-4 from left to right. In Fig.1 and Fig. 2 (a), empty circles for GCM members, filled circles for GCM average and squares for OBS. In Fig.1 and Fig.2 (b), squares for precipitation and circles for SST. In Fig.3 and Fig.4, circles for WP SST and squares for Nino3.4 SST. (a) GCM, (b) OBS. See the details in the text.

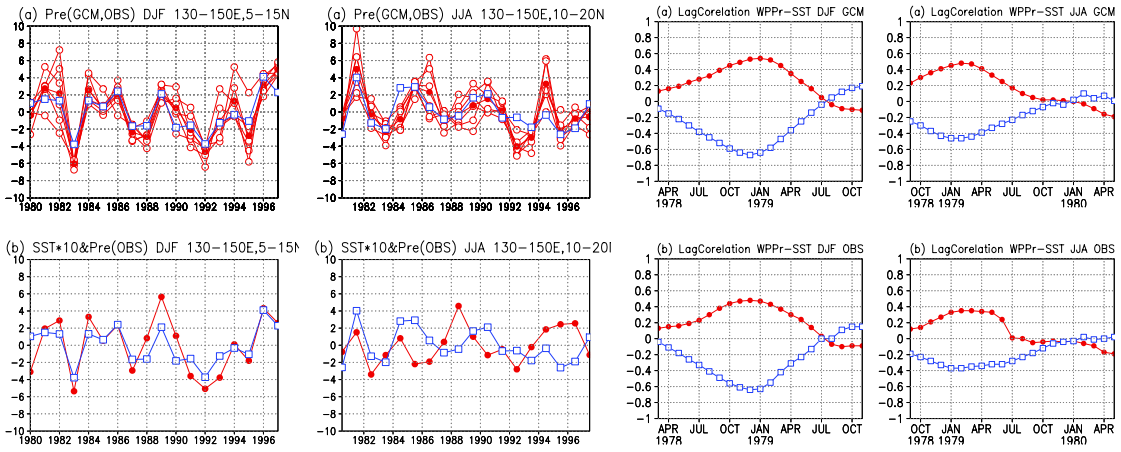

How about the relationship between the WP precipitation and the El-Nino SST? Fig. 3 shows the lagged correlation of WP precipitation for DJF with WP SST and Nino3.4 SST in the GCM simulation (a) and in the observation (b). Fig. 4 is the same but for JJA. First, I like to confirm that the GCM produces almost the same lagged correlation plots qualitatively and quantitatively. The DJF WP precipitation is well related not only to the WP SST positively but also the El-Nino SST negatively in DJF. These are the simultaneous relationship. For JJA, the WP precipitation is related to the WP SST and the El-Nino SST for the previous DJF, a half year ago. The GCM simulations get real history only from the observed SST and sea ice. The memory about the previous DJF must be left in other SSTs or sea ice coverage.

3.2 Why is the JJA WP precipitation related to the El-Nino SST in the previous DJF?

The simultaneous correlation of the WP precipitation with the global SST is shown in Fig. 5 for JJA. Significantly large correlated (> 0.8 or < -0.8) SST area is not found, including the WP SST. This fact indicates that any single SST area does not control the WP precipitation. Relatively large correlations (> 0.6 or < -0.6) are found in the Indian Ocean and the southern off-equatorial Pacific.

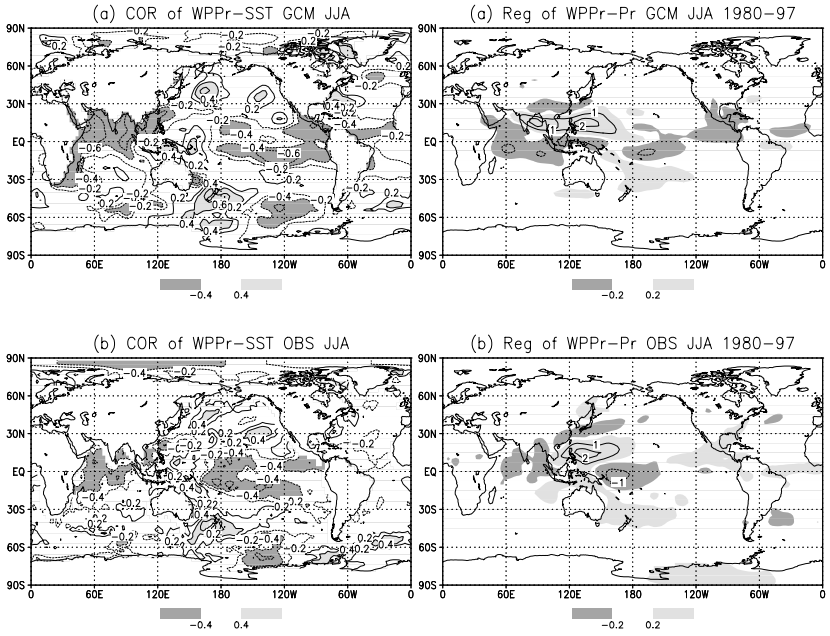

Fig. 5-6 from left to right. In Fig.5-6, (a) GCM and (b) OBS. See the details in the text.

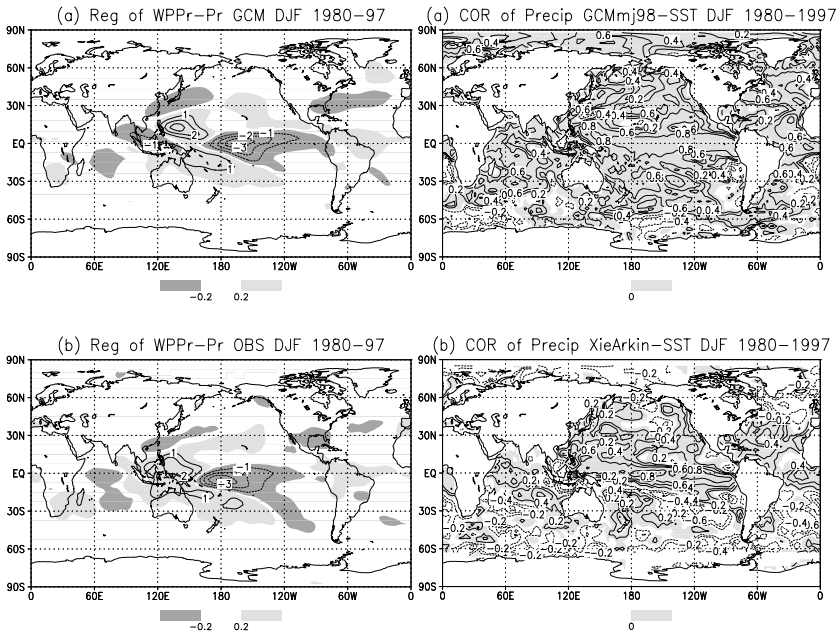

Fig. 7-8 from left to right. In Fig.7-8, (a) GCM and (b) OBS. See the details in the text.

Fig. 6 is the regression map of precipitation by the tropical WP precipitation for JJA. The regression pattern for the simulated precipitation is similar to the observed one with some exceptional area in the northern Indian Ocean and the eastern North Pacific. The regressed precipitation for JJA have negative anomaly in the Indian Ocean and the central Pacific around the equator. They are common for the GCM and the observation. If we connect these negative anomalies of precipitation to the SST anomalies in the Indian Ocean and the southern off-equatorial Pacific, both regional SST and precipitation variability is considered as the cause for the real simulation of the JJA WP precipitation. Actually, the JJA SST in the Indian Ocean and the southern off-equatorial Pacific keeps the memory of the DJF Nino3.4 SST.

3.3 DJF precipitation variability in the eastern Indian Ocean

The regression map of the DJF precipitation by the DJF WP precipitation is shown in Fig. 7. The simulated precipitation successfully captures the characteristics of the observed pattern over most regions. The major exception is the negative anomalies from the maritime continents through the eastern Indian Ocean.

Generally, the precipitation anomalies in the AGCM tend to be positively correlated with the local SST. The correlation between precipitation and local SST at the same place for DJF is shown in Fig. 8. Positive correlations are extended from the WP region through the equatorial Central and Eastern Pacific in the observation. Negative correlations are also found in the observation from the South China Sea and around the maritime continents through the southern Pacific. The AGCM does not seem to reproduce the similar correlation map. Particularly, a large contrast is found from the maritime continents through the eastern Indian.

4. SUMMARY

The MRI/JMA AGCM (Shibata et al., 1999) integration with the observed SST successfully simulates the variability of the tropical Western Pacific precipitation for both DJF and JJA.
The relationship between the tropical Western Pacific precipitation and the local SST variability is different for DJF and JJA. High correlation is clear for DJF, but almost no correlation for JJA. The tropical Western Pacific precipitation for JJA tends to be related with the El Nino SST for the previous DJF. The JJA SSTs over the Indian Ocean and the central Pacific off the equator keep the memory of the previous DJF El Nino3.4 SST to some extent. The JJA precipitation over the above two regions may play a role to create the JJA precipitation over the Western Pacific related with the El Nino SST for the previous DJF.

The simulated precipitation over the eastern Indian Ocean for DJF is positively related to the local SST anomaly. The observed relationship is opposite. Generally, the inter-annual variability of precipitation in the AGCM tends to be positively related to the local SST variability at each oceanic region on the whole. On the other hand, that local relationship in the observation differs from region to region. The above difference between the AGCM and the observation appears most clearly in the eastern Indian Ocean for DJF. The question about why is left.

REFERENCES

Shibata, K., H. Yoshimura, M. Ohizumi, M. Hosaka and M. Sugi, 1999: A simulation of troposphere, stratosphere and mesosphere with an MRI/JMA98 GCM. Papers in Meteorological Research Institute, Vo. 50, No.1, pp.15-53.

The Performance of an Atmospheric General Circulation Model (R42L9/LASG)

Tongwen Wu, Guoxiong Wu, Rucong Yu, Zaizi Wang, and Yiming Liu
LASG, Institute of Atmospheric Physics, Chinese Academy of Sciences, China
twwu@lasg.iap.ac.cn

1. **Brief description of model**

State Key Laboratory of Atmospheric Sciences and Geophysical Fluid Dynamics, Institute of Atmospheric Physics (LASG/IAP) have contributed great efforts on developing a comprehensive general circulation model (GCM) suitable for climate studies over the Asian monsoon area. In 1991, a nine-level GCM model from Simmonds (1985) was introduced. It is a spectral model rhomboidally truncated at zonal wave number 15 (hereafter R15L9). Wu et al. (1996) made a number of significant changes and reconstructed it to R15L9/LASG model formulation. They successfully adapted the unique dynamic framework by subtracting "a standard atmosphere" from the set of governing equation. Despite its coarse horizontal resolution (approximately 7.5^{o}lon×4.5^{o}lat.), the R15L9/LASG model was capable of simulating the climate mean states, such as sea level pressure, precipitation, and wind fields and was successful in simulating monsoon onset and some inter-annual variability as well. In the recent years, K-distribution radiation scheme which is originally developed by Shi (1981), cloud fraction diagnose method (Slingo, 1987), and the simplified simple biosphere (SSiB) model (Xue et al., 1996) have gradually been adapted to the R15L9/LASG model. However, due to its coarse horizontal resolution, the model is inefficient in simulating the interannual variability of the climate system. In 2001, its horizontal resolution is enhanced from zonal wave number 15 to number 42 (hereafter R42L9/LASG). This new version of the model has approximately 2.8125^{o}long×1.66^{o}lat resolution.

The purpose of this study is to evaluate the performance of the R42L9 model in simulating climate in comparison with observations. The model climatology is based on the last 30-year results of a 40-yr integration that employs 30-years (1971-2000) averaged climatological monthly mean sea surface temperature and sea-ice fractional concentration which are generated from the Program for Climate Model Diagnosis and Intercomparison (PCMDI).

2. Simulated climate

In comparison with the observations, the seasonal mean climates of geographical distributions of the sea level pressure, precipitation, 500-hPa geopotential height, 850- and 200-hPa zonal wind fields averaged for the 30-year integration of the R42L9 model are analyzed. Results show that the model well reproduces the observed basic patterns of observed SLP, such as the Aleutian and Icelandic low pressure and Mongolia high pressure systems in boreal winter (December to February, DJF), the subtropical high pressure over Pacific and Atlantic in summer (June to August, JJA), and the intertropical convergence zone ITCZ) and a belt of subtropical high pressure with the centers in each of Pacific, Atlantic, and Indian oceans in both seasons. The R42L9 model captures two major troughs off the east coasts of Eurasian continent and North

American continent, two major ridges over the western coast of North America and the eastern Atlantic, and a band of high geopotential height over the tropic and subtropic in boreal winter. During JJA, the R42L9 model successfully reproduces the observed large-scale zonal symmetries of 500-hPa geopotential height and the northern subtropical high over Pacific and Atlantic. Comparing with its coarse resolution (R15L9/LASG), the simulation of regional climate, especially regional precipitation in Asian monsoon area was partly improved in this version of model.

Fig. 1 shows the JJA mean precipitation over the Asia-Pacific region. The large rainfall is mainly distributed along the equator and the Asian monsoon area. The observed pattern of precipitation over the Asian monsoon region with the largest precipitation center over the Bay of Bengal and a secondary maxima of precipitation over Philippine is simulated by the R42L9 model (Fig. 1a). R15L9 (Fig. 1b) fails to capture the feature of regional precipitations because of the limitation of its coarse horizontal resolution. When comparing with Xie-Arkin's climatology, regional biases of precipitation from R42L9 model are still obvious. The precipitation maximum over the Bay of Bengal extends too northward and eastward and is obviously larger than the observation.

The R42L9/LASG model reproduces the interseasonal variation of Asian monsoon precipitation. The seasonal cycles of precipitation averaged for the East Asia (105^{o}-140^{o}E, 22.5^{o}-45^{o}N) and Indian monsoon region (60^{o}-150^{o}E, 5^{o}-30^{o}N) from R42L9 and R15L9 simulations and Xie-Arkin's observations are shown in Fig. 2. During the prevailing period of summer monsoon (May to August), the simulated and observed rainfall amounts over East Asian monsoon region are almost identical. The seasonal cycle of Indian summer precipitation is simulated by the R42L9 model as well as by the R15L9 model. In Fig. 2b, the magnitude of region-averaged precipitation in the R42L9 model is closer to the Xie-Arkin's estimates than that in R15L9 model.

In order to further improve the simulation of SLP and the atmospheric circulation, enhance the regional simulation, reduce biases with the observations, we must improve the simulation of atmospheric temperature in the future and improve the parameterization of model physical processes. In addition, increased vertical resolution is required and will be a part of the future version.

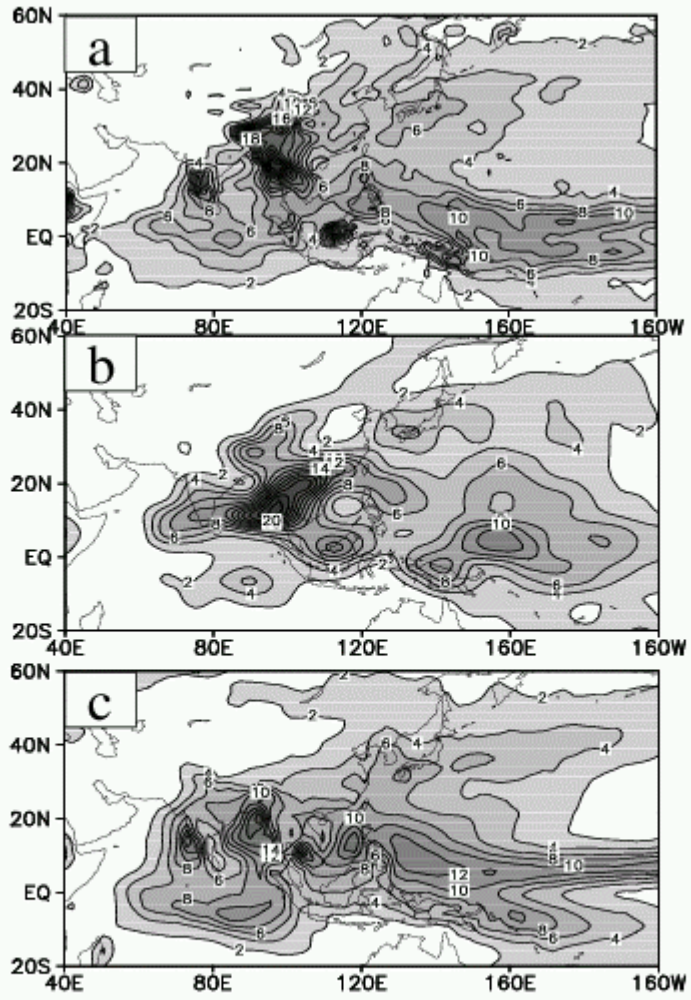

Figure 1. The mean JJA precipitation (mm/day) for (a) R42L9/LASG, (b) R15L9/LASG, and (c) the 22 yrs (1979-2000) Xie/Arkin observational climatology.

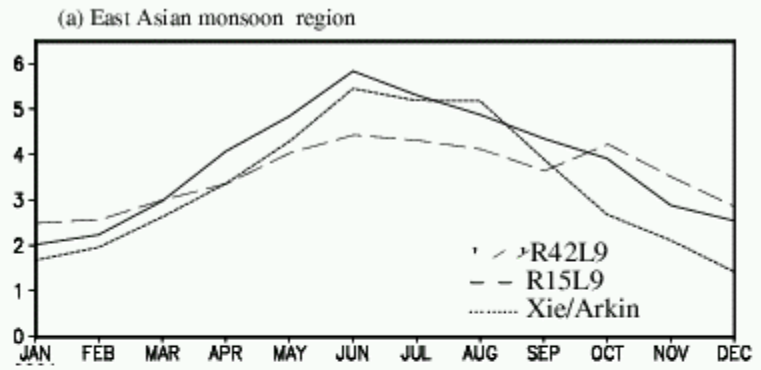

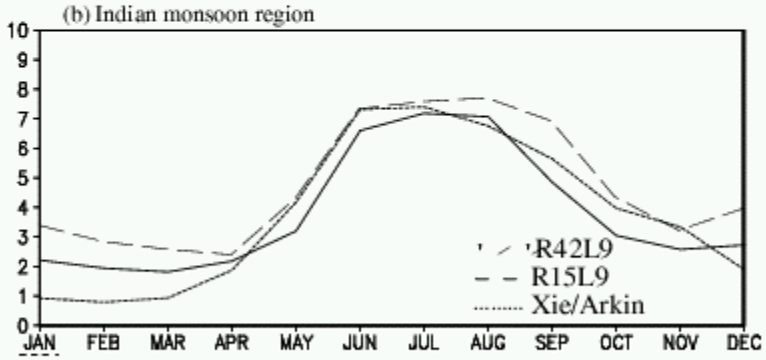

Figure 2. Seasonal cycle of precipitation (mm/day) over the East Asia (105°-140°E, 22.5°-45°N) and Indian Monsoon Area (60°-105°E, 5°-30°N) from R42L9, R15L9, and the 22 yrs (1979-2000) Xie/Arkin climatology.

References

Shi, G.Y., 1981: An accurate calculation and representation of the infrared transmission function of the atmospheric constitutes, Ph.D. Thesis, Dept. of Sci., Tohoku University of Japan, 191 pp.

Simmonds, I., 1985: Analysis of the "spinning" of a global circulation model, *J.Geophys.Res.*, **90**, 5637-5660.

Slingo, J.M., 1987: The development and verification of a cloud prediction scheme for the ECMWF model, *Quart. J. Roy. Meteor. Soc.*, **113**, 899-927.

Wu, G.-X., H. Liu, Y.-C. Zhao, and W.-P. Li, 1996: A nine-layer atmospheric general circulation model and its performance, *Adv.Atmos.Sci.*, **13**, 1-18.

Xue, Y., P. J. Sellers, J.J. Kinter, and J. Shukla, 1991: A simplified biosphere model for global climate studies, *J.Climate*, **4**, 345-364.

Past, Present and Future of LASG Climate System Model

Rucong Yu and Tongwen Wu
(LASG, Institute of Atmospheric Physics, Chinese Academy of Sciences, China)
yrc@lasg.iap.ac.cn

1. Past of LASG climate system model

The national key Laboratory of numerical modeling for Atmospheric Sciences and Geophysical fluid dynamics (LASG) was established in 1985. Since then, LASG was continually awarded as excellent Laboratory in the four times national assessment in China. The current scientific focus is the climate related research. The climate model, the powerful tool in climate studies, definitely is paid many attentions. In the international model comparisons, such as AMIP and CMIP, LASG climate model was almost the unique one from the developing countries. Same as world climate development, LASG developed own individual AGCM and OGCM, air-sea coupled GCM and climate system model, step by step.

A global ocean-atmosphere land system model (GOALS) has been developed and continually improved in LASG since 1995. Up to now, the GOALS model has several versions. The evaluations of GOALS model show that, in general, different versions of GOALS model are all able to reproduce the basic characteristics of current observed climate in many aspects reasonably, especially for the large scale features and seasonal cycle. The model data have been broadly used to study the climate variability and climate change induced by CO2 concentration increasing. The GOALS model, as one of the nineteen CGCMs developed by fifteen institutions around the world, joins in CMIP 1 and 2.

2. Present of LASG climate system model

The atmospheric component of GOALS has been improved in model resolution and physical parameterization and the simulating ability of current version is much better than previous version (Fig. 1).

In addition, a new grid AGCM is being developed in LASG. The dynamical framework has been developed based on a series of advanced numerical methods which include following features. (1) explicit finite difference scheme with exact linear and quadratic conservations; (2) weighted equal-area coordinates along the latitude for reducing the model instability at the poles; (3) flexible leaping-grid method along the longitude for further reducing the model instability at the poles; (4) a two-step shape-preserving advection scheme for water vapor transport; (5) the reduction of the standard atmosphere. This dynamical framework can exactly conserve the total available energy and the total mass of the dynamical system, and can be well stable without any filtering and smoothing. The water vapor can be well shape-preserving and economically computed.

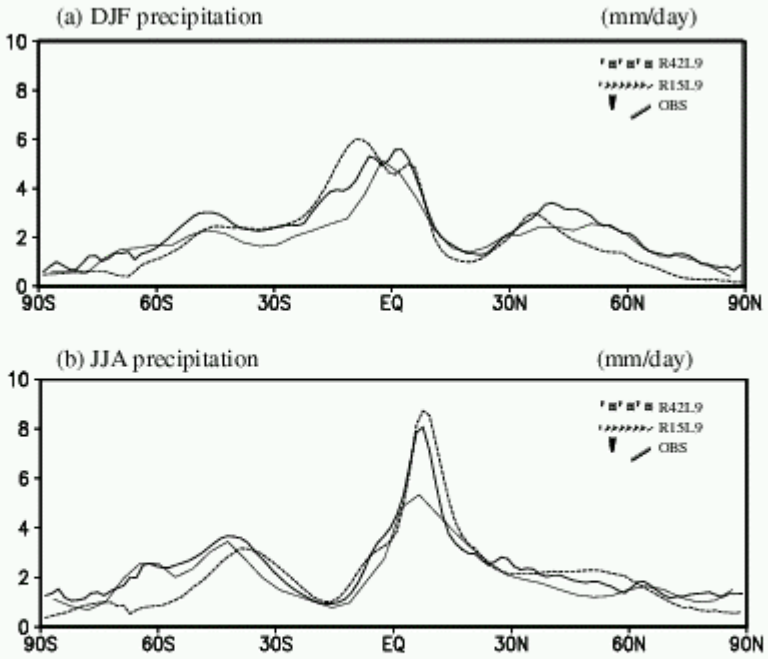

Figure 1. Zonal-mean DJF (a) and JJA (b) precipitation rate (mm/day) for the R42L9/LASG, R15L9/LASG, and the observational climatology.

The resolution of LASG OGCM has been enhanced to uniform 0.5°×0.5° grids horizontally and 30 layers in vertical. Under the circumstances the main straits and passages in the Indonesian Archipelago can been resolved. The model has been integrated for 45 years forced by climatological monthly data, and a 15 year-long experiment has been conducted using ERA15 daily wind stresses. The speed of Equatorial Undercurrent (EUC) in the high resolution model is much larger than that in previous version, and also the North Equatorial Counter Current (NECC). The high resolution model can simulate the "W" pattern of South Equatorial Current, which low resolution model can't. The simulated pathway and the water source of ITF are both coincident with the observation.

To develop climate system model at the state of the art, the NCAR CSM framework was introduced to LASG in 2000. By replacing the oceanic component of the NCAR CSM with LASG L30T63 OGCM, a flexible coupled general circulation model (FGCM) is being developed. The preliminary version of FGCM has been integrated for 60 years without significant climate drift. Most of climatological features in FGCM0 are very similar with that in NCAR CSM.

2. Future of LASG climate system model

LASG's new version of AGCM, R42L26, will replace the CCM3 to set up FGCM1. We are developing the LASG CSM toward state of the art model by modularizing and standardizing the LASG CSM. For physical parameterization, we will focus on the stratiform cloud related physical processes. In addition, many attentions will be paid to improve understanding of many of the component processes in climate system, including cloud physics; radiative transfer; atmospheric chemistry, including aerosol chemistry, boundary-layer processes, and biogeochemical processes, and understanding the interactions among the physical, chemical, and biogeochemical subsystems.

APPENDIX I

AMIP Workshop Program
Toward Innovative Climate Model Diagnoyunstics

12-15 November, 2002
Meteo-France, Toulouse

PROGRAM OVERVIEW

Tues 12 Nov: Overview and General Circulation
Wed 13 Nov: Tropical Variability and Monsoons
Thu 14 Nov: Fluxes, Clouds and Radiation
Workshop discussion: Refining the AMIP Experimental Protocol
Fri 15 Nov: Hydrological Cycle and Land Surface Processes
Phenomena and Extra-Tropical Variability
Action Item Discussion

Tuesday, 12 November

Workshop Registration: 8:45-9:30AM

AMIP OVERVIEW AND GENERAL CIRCULATION

Chair: M. **Déqué**

Meteo-France Welcoming Remarks: D. Cariolle
WGNE Remarks: D. Williamson
Model Intercomparison: Reflections and Challenges: L. Gates 9:40-10:00
Background and Workshop Objectives: P. Gleckler 10:00-10:20
Evaluating Model Performance: K. Taylor 10:20-10:40
Workshop Logistics: M**. Déqué**

BREAK **AND CONTINUED REGISTRATION** 10:45-11:15

Chair: L. Gates

KEYNOTE: The ERA40 Project and its use for model evaluation: M. Miller 11:15-11:50

On the limitations of prescribing Sea Surface Temperatures in AGCM Experiments: C. Cassou, J. Hurrell, S. Brown and A. Phillips 11:50-12:10

Use of an Ensemble of short AMIP Runs in Support of Numerical Weather and Climate Prediction: S. Saha 12:10-12:30

LUNCH 12:30-13:45

Chair: B. McAvaney

Annual Cycle of Potential Seasonal Predictability in an Ensemble of Multidecadal GCM Simulations: C.-T. Chen 13:45-14:05

Predictability studies in an idealized AMIP-type ensemble experiment: L. Li and S. Conil 14:05-14:25

Atmospheric Transports and Energetics: G. Boer and S.Lambert 14:25-14:45

Assessment of atmospheric angular momentum parameters in AMIP-2 simulations: D. Salstein, R. Rosen, S. Marcus, J. Dickey 14:45-15:05

BREAK 15:05-15:25

Chair: D. Williamson

KEYNOTE **Dynamical Diagnostics: New approaches:** B. Hoskins 15:25-16:00

HadGEM1 - The new Hadley Centre Climate model: V. Pope, R. Stratton and others 16:00-16:20

Using AMIP Simulations with the FSU Super-ensemble Modeling of Seasonal Climate Predictions: W. Yun and T. Krishnamurti 16:20-16:40

Chair: P. Gleckler
Oral Introductions to Poster Session (2 minutes each) 16:40-17:10

POSTER SESSION AND ICE-BREAKER 17:15-19:00

Wednesday, 13 November

TROPICAL VARIABILITY AND MONSOONS

Chair: K. Sperber

KEYNOTE Analysis of the West African Monsoon in forced and coupled simulations: J.-F. Royer, H. Douville, F. Chauvin 9:00-9:35

Water and Energy Budgets in the AMIP Simulation with the JMA GCM: H. Kitagawa 9:35-9:55

Application of Maximum Potential Intensity Techniques for Tropical Cyclone Intensity to AMIP Simulations: K. McGuffie, G. Holland 9:55-10:15

The Australasian Region Wintertime Double Jet as Simulated in AMIP: M. Harvey and B. McAvaney 10:15-10:35

BREAK 10:35-10:55

Linearity in ENSO's Atmospheric Response: S. Nigam and E. DeWeaver 10:55-11:15

The mid-cloud cover in the east of Tibetan Plateau: R. Yu 11:15-11:35

The Performance of LASG AGCM New Version (R42L9): T. Wu, P. Liu, Z. Wang, Y. Liu, R. Yu, and G. Wu 11:35-11:55

Diagnosis of Diabatic Heating Errors in the NCMRWF Global Model Simulations: S. Kar, G. Iyengar, S.V. Singh and S. Nigam 11:55-12:15

The Madden-Julian Oscillation in GCMs: K. Sperber, J. Slingo, P. Inness, S. Gualdi, W. Li, P. Gleckler, C. Doutriaux 12:15-12:45

LUNCH 12:45-14:00

Chair: H. Douville

KEYNOTE The GEWEX CEOP Project: K. Koike 14:00-14:35

Analysis of propagating modes in the tropics in an Ensemble of Short AMIP Runs: H. van den Dool 14:35-14:55

Evaluating Tropical Diurnal Variations in AGCMs: A BMRC Experiment: Z.-J. Wu, Huqiang Zhang and Bryant McAvaney 14:55-15:15

BREAK 15:15-15:35

Chair: F. Zwiers

Simulation of the Quasi-Biennial Oscillation in ECHAM5:
M. Giorgetta 15:35-15:55

Diagnostics of Variability and Trends Using Potential Vorticity Maps:
M. Cai 15:55-16:15

Snow Cover, Soil Moisture, and the Asian Summer Monsoon: A. Robock and M. Mu 16:15 -16:35

Thursday, 14 November

FLUXES, CLOUDS AND RADIATION

Chair: M. Miller

KEYNOTE The GEWEX Cloud System Study (GCSS): S.Krueger 9:00-9:35

Using the ISCCP Simulator to Evaluate Midlatitude Cloud Regimes: M. Webb 9:35-9:55

Evaluation of radiative fluxes in AMIP-type GCM experiments based on surface observations: M. Wild 9:55-10:15

Large Scale Systematic Errors in Shortwave Cloud Forcing - Results from AMIP I and II: G. Potter 10:15-10:35

BREAK 10:35-11:00

Chair: D. Salas

Comparisons of AMIP II Clouds with Global Observations: B. Weare 11:00-11:20

KEYNOTE Using ARM for model diagnostics: J.-J. Morcrette 11:20-11:55

The Sensitivity of Implied Ocean Heat Transports to Dominant Surface Heat Fluxes: P.Gleckler 11:55-12:15

First results of the AMIP-II GCMs evaluation using METEOSAT Water Vapor data: H. Brognez, R. Roca and L. Picon 12:15-12:35

LUNCH 12:35-13:50

Chair: J. Potter

The Polar Climate in AMIP Simulations: V. Kattsov, J. Walsh, W. Chapman, and S. Vavulin 13:50-14:10

Evaluation of Snow Cover Simulations in AMIP Simulations: A. Frei, J. Miller , D. Robinson , R. Brown , T. Mote , A. Grundstein 14:10-14:30

WORKSHOP DISCUSSIONS: REFINING THE AMIP EXPERIMENTAL PROTOCOL 14:30-17:25

Chair: K. Taylor

This session will include short introductions, each followed by discussion. After the introductions, there will be a general discussion with the time remaining. The chairperson will determine an appropriate point to take a short break.

The value of AMIP and CMIP for the IPCC: B. McAvaney

Refining the AMIP Experimental Protocol: P.Gleckler

Climate Impacts Diagnostics: F. Zwiers

Status of the WGNE Standard Variability Diagnostics: D. Williamson

Cloud and Radiation diagnostics, guided by the GEWEX GCSS:S. Krueger

Land Surface Diagnostics, Guided by the GEWEX GLASS: J. Polcher

Additional Covariances Needed: G. Boer

AMIP forcing: Inclusion of tropospheric and stratospheric aerosols and greenhouse gases: A. Robock

WORKSHOP DINNER

Friday, 15 November

HYDROLOGICAL CYCLE AND LAND SURFACE PROCESSES

Chair: V. Kattsov

KEYNOTE A Poor man's land data assimilation: R. Koster 9:00-9:35

GEWEX Gewex Atmospheric Boundary layer Study: B. Holtslag 9:35-9:55

Moisture cycle quantities over the United States and globe from AMIP models: D. Salstein , R. Rosen, and H. Kanamaru 9:55-10:15

Atmospheric Transports into the Continents of Energy and Water Simulated with AMIP Models: J.-W. Kim, H.-J. Shin and I.-U. Chung 10:15-10:35

BREAK 10:35-11:00

Chair: J. Polcher

Large-scale Validation of AMIP II Land-surface Simulations: T. Phillips, A. Henderson-Sellers, P. Irannejad, K. McGuffie, S. Sharmeen, H. Zhang 11:00-11:20

Evaluation of Land Surface Energy Budget of AMIP II Global Climate Models: A. Henderson-Sellers, P. Irannejad, K. McGuffie, S. Sharmeen, T. J. Phillips and H. Zhang 11:20-11:40

Analysis of Land-surface Water Budget in the AMIP II Global Climate Models over the GEWEX-COEP Regions: P. Irannejad, A. Henderson-Sellers, S. Sharmeen, T.J. Phillips, K.McGuffie and H. Zhang 11:40-12:00

Analysis of Sixteen AMIP2 Model Simulations over the Australian Regions: H. Zhang, A. Henderson-Sellers, P. Irannejad, S. Sharmeen, T. Phillips, K. McGuffie 12:00-12:20

AMIP simulations of the heat and water budgets over major river watersheds: V. Meleshko, T. Pavlova, V. Govorkova 12:20-12:40

LUNCH 12:40-13:55

Chair: K. Puri

The impact of a new land surface scheme on the MRI/JMA98 AGCM: M. Hosaka, A. Kitoh 13:55-14:15

PHENOMENA AND EXTRA-TROPICAL VARIABILITY

Stationary Waves in AMIP GCMs and their Maintenance Mechanisms
R. Joseph and M. Ting 14:15-14:35

Extreme Events in AMIP: F. Zwiers 14:35-14:55

Feature Based Analysis of Re-Analyses and AMIP II Integrations: K. Hodges and J. Boyle 14:55-15:15

Modelling the Climatology of Storm Tracks - Sensitivity to Resolution: R. Stratton and V. Pope 15:15-15:35

ACTION ITEM DISCUSSION AND WORKSHOP CONCLUSIONS 15:35-16:00

Tuesday Poster Session:

AMIP simulations in different resolutions with ARPEGE: M. Déqué
Current state of GEM climate simulations at RPN: B. Dugas
Model development of ECHAM5 at MPI: S. Hagemann
Model activities at BMRC: B. McAvaney
Coupled and Atmospheric Model Development at CCCCma: F. Zwiers
Model activities at LASG: Y. Rucong, T. Wu
Model activities at NCMRWF: S.C. Kar
Model activities at GFDL: B. Stern
Model activities at MRI-JMA: A. Kitoh and M. Hosaka
Model development at Yonsei University: H.-J. Shin, I.-U. Chung, J.W. Kim
Model activities at MGO: V. Matyugin

Ocean-driving and atmosphere-driving anomalies in the reanalysis data and possible implications on predictability: M. Pena, E. Kalnay, and M. Cai

Validation of Cloud-resolving Models and GCM Cloud Parameterizations Using CERES/TRMM Data: Z. Eitzen, K.-M. Xu, B. Wielicki, T. Wong, and L. Parker

Interannual Variability of Tropical Precipitation and Associated Extra-tropical Atmospheric Response in the MRI/JMA AGCM: T. Ose, M Sugi and A. Kito

Feedbacks affecting the response of the thermohaline circulation to increasing CO2: A study with a model of intermediate complexity: I. Kamenkovich , A. Sokolov and P. Stone

Investigating Water Recycling Processes in the Amazon using 20 AMIP II Models and Isotopes: A. Henderson-Sellers, K. McGuffie, H. Zhang, S. Sharmeen, S. Chambers

Lower Northern Hemisphere carbon sink implied by improved atmospheric model Resolution: J. Orr, B. Govindasamy, P. Duffy, and J. Taylor

A case study on the use of a modern computer language in the analysis of climate data: PyClimate J. Saenz, J. Fernandez and J. Zubillagas

The PCMDI open-source open-science software system: C. Doutriaux, D. Williams, B. Drach